THE NORWEGIAN UNIVERSITY OF
SCIENCE AND TECHNOLOGY
DIVISION Of APPLIED MECHANICS,
THERMODYNAMICS AND FLUID DYNAMICS

MODELLING OF TURBULENCE AND COMBUSTION FOR SIMULATION OF GAS EXPLOSIONS IN COMPLEX GEOMETRIES

BY
BJØRN JOHAN ARNTZEN

THESIS FOR THE DR. ING. DEGREE
MAY 1998

Abstract

This thesis analyses and presents new models for modelling of turbulent reactive flows for CFD simulation of gas explosions in complex geometries like offshore modules.

The most important aspects determining the course of a gas explosion in a complex geometry are the development of turbulence and the corresponding increase in the combustion rate during the explosion. To be able to model the process it is necessary to use a CFD code as a starting point, provided with a suitable turbulence and combustion model. The modelling and calculations are done in a 3D finite volume CFD code, where complex geometries are represented by a porosity concept, which gives porosity on the grid cell faces, depending on what is inside the cell.

The turbulent flow field is modelled with the k-ε turbulence model. The turbulent flow field behind obstructions, which should produce turbulence, is not resolved for smaller geometry. Subgrid models are therefore used for production of turbulence from geometry not fully resolved on the grid. Results from LDA measurements around obstructions in steady and transient turbulent flows have been analysed and the turbulence models have been improved to handle transient, subgrid and reactive flows.

The combustion is modelled with a burning velocity model, and a flame model which incorporates the burning velocity into the code. Two different flame models have been developed. SIF, which treats the flame as a interface between reactants and products, and the β-model where the reaction zone is resolved with about 3 grid cells.

The flame normally starts with a quasi laminar burning velocity, due to flame instabilities, modelled as function of flame radius and laminar burning velocity. As the flow field becomes turbulent, the flame uses a turbulent burning velocity model, based on experimental data presented by Bradley, as function of turbulence parameters and laminar burning velocity. The extrapolation of these data is evaluated. The laminar burning velocity is modelled as function of gas mixture, equivalence ratio, pressure and temperature in reactant.

Pressure/time curves from a range of hydrocarbon gas explosion experiments have been compared with simulations, which in most cases shows good agreement. In simulation of these experiments a range of parameters have been varied, as gas mixture, congestion, obstructions, confinement, scale and grid resolution.

Acknowledgements

I have received a scholarship from the Norwegian Research Council (NFR) for 30 months. The research have also been financed by the EU research programs MERGE and EMERGE, and the Gas Safety research Programs (GSP) at CMR, sponsored mainly by BP, Elf, Exxon, Gas de France, HSE, Mobil, NPD, Phillips and Statoil.

The work was carried out at Christian Michelsen Research (CMR) Departement of Process and Safety, in Bergen, where my models were implemented in the gas explosion flow simulator, FLACS. I am very grateful to my colleagues at CMR for support, valuable discussions, experimental results and help in implementation of models and visualization of results.

I am also grateful to the GSP sponsors and participants of the EU projects for valuable discussions and experimental results, and to my supervisor Professor B. F. Magnussen for introducing me to the field of turbulence and combustion.

This thesis will be submitted for the degree:

Doktor Ingeniør (Dr. ing.)
Doctor of Engineering

at the Norwegian University of Science and Technology, NTNU, Trondheim, Norway

Bergen, May 1998

Bjørn Johan Arntzen

Contents

Nomenclature

Latin letters

A	Area
A	mole ratio oxygen/fuel
$A(c)$	pdf of the reaction rate, $w(c)$
C	mole ratio carbondioxid/fuel
C_P	constant pressure specific heat capacity
C_μ, $C_{\varepsilon 1}$, $C_{\varepsilon 2}$	constants in the k-ε turbulence model
c	sonic speed
c	mass fraction of products
c_q	minimum c where $w>0$
D	diffusion coefficient
D, d	diameter or dimension of obstruction
d	coefficient of the pressure-difference term
1D, 2D, 3D	one, two and three dimensional
E	equivalence ratio
F	convective volume and mass flows
f	volume fraction of products
f_{mix}	mixture fraction
g	gravity constant
h	enthalpy
K	equilibrium constant
K	strain rate (dimensionless)
k	turbulent kinetic energy
L_i	Dimension of obstruction in direction i
Le	Lewis number
l_I	turbulent integral length scale
l_m	turbulent mixing length scale
l_t	turbulent length scale, used in presentation of FLACS results
M	molecule weight
N	mole ratio nitrogen/fuel
n	mole fraction
P	pressure
P_k	production rate of turbulent kinetic energy
P_ε	production rate for dissipation of turbulent kinetic energy
R	gas constant
Re	Reynolds number
S	burning velocity
S_ϕ	source term for variable ϕ
T	temperature
T_i	subgrid area blockage in direction i, used in turbulence and flamefolding models
U	flow velocity and flow velocity in x-direction
u'	turbulent velocity fluctuation
V	flow velocity in y-direction
V	volume or volume fraction
W	reaction rate (dimensionless)
w	reaction rate
Y	mass fraction

Greek letters

α	thermal diffusivity
α	fraction of CO in products
α	temperature exponent
β_i	porosity in grid cell and on cell face in direction i
β	fraction of H_2 in product
β	Zel'dovich number
β	pressure exponent
γ	fraction of unburned fuel in products
Γ_ϕ	diffisuvity coefficient for variable ϕ
δ	flame thickness
δ_{ij}	Kronecker delta, =1 if $i=j$, and 0 else
Δ	grid cell size
Δx	grid cell size in x direction
Δt	time step length
ε	dissipation rate of turbulent energy
η	fraction evaporated water in products
Λ	burning velocity eigenvalue
λ	Taylor length scale
λ	thermal conductivity
μ_t	turbulent eddy viscosity
ν	kinematic viscosity
ρ	density
τ	expansion ratio, density ratio between reactant and product
τ_c	chemical timescale
χ	fraction of O_2 in products

Subscripts and superscripts

B, b	bottom point and bottom cell face
E, e	east point and east cell face
L	laminar
N, n	north point and north cell face
nb	neighbouring grid points
P	main node point
P	products
R	reactants
S, s	south point and south cell face
T	turbulent
T, t	top point and top cell face
W, w	west point and west cell face
0	reference position
i, j	flow directions
$*$	most recently updated value

Abbreviations

CFD	computational fluid dynamics
CMR	Chr. Michelsen Research
FLACS	FLame ACcelerator Simulator
LDA	laser Doppler Anemometer
pdf	probability density function
RMS	root mean square
SIF	Simple Interface Flame
TDMA	tri-diagonal matrix algorithm

1 Introduction

1.1 Motivation for the Thesis

The strength of a gas explosions depends on a range of parameters. Some are related to the geometry, like size, the degree of confinement and amount of turbulence generating obstructions. Other are related to the gas mixture, like composition, location and quantity. The ignition location and presence of any blast reducing components like blast walls and water deluge systems are also important parameters. The overpressures from explosions are needed for blast propagation, structural response and risk calculation.

Explosion experiments can be used to find pressures for a given set of parameters. Simulation of an explosion can be much faster and cheaper than an experiment, and the input parameters can easily be changed. Simulation of explosions are therefore used in design of offshore oil and gas installations to obtain maximum blast which they can withstand

A range of the sub models used for calculations of gas explosions is not well suited to give a representative description of the process. The models for representation of combustion and turbulence have a large grid dependence which should be minimized. Other problems are related to calculation in new different geometries and lack of experimental data for different gas mixtures.

The main objective of the present work is to improve the models describing a gas explosion so they give a sound physical description of the process. The models should handle most fuel mixtures (nearly any possible hydrocarbon type, including water deluge and dust clouds).

1.2 Modelling of Turbulence and Combustion

The models mostly used for representation of combustion and turbulence, are combustion models of eddy break-up type and the k-ε turbulence model. In calculation of gas explosions with these models the results depend strongly on the grid size and initial values for turbulence field chosen. This dependence must be minimized before the models could give accurate predicting of gas explosions in new geometries.

The combustion modelling should give a representation of the flame which includes localization and area of flame. The flame in an explosion will normally be thinner than the grid used in the calculations. Flame models, as the SIF and β flame models are therefore needed to represent the flame, instead of combustion models. The flame model needs burning velocity models which describe the propagation velocity of the flame into a specified reactant.

The strength of an explosion depends on how fast the flame burns and the expansion of the gas through the flame. This density ratio depends through thermodynamics on the product composition, which is controlled by equilibrium chemistry. The product composition is however in most explosion codes wrongly based on an assumption of complete combustion.

The burning rate depends largely on the turbulence field. Turbulence models are normally for steady non reactive flows and may therefore give transient turbulence fields which are very dependent on grid and initial conditions. The turbulence modelling most therefore be modified to give representative turbulence field in transient reactive flows, as gas explosions, independent of grid and initial conditions.

1.3 Previous/other Work

MEGGE, the Model Evaluation Group Gas Explosions, have made a protocol for EU, Vasey (1995) with guidelines for evaluation of gas explosion models. The models evaluated were divided into four classes:

- Empirical models, like venting guidelines based on geometry volume and venting area.
- Phenomenological models, as described by Phillips (1994), like the TNT equivalence method, the TNO multi-energy method, the British Gas COBRA method and the Shell SCOPE method.
- CFD models, as FLACS, which are most fundamentally based and solves the underlying equations governing the gas flow, turbulence and combustion process. They have high accuracy when the turbulence and combustion is modelled well.
- Experimental scaling, where the reduction in scale is compensated with a more reactive fuel, normally by adding extra oxygen.

The work in this thesis is on CFD modelling of gas explosions. The CFD code used by the author is the FLACS (FLame ACellerator Simulator) code. Hjertager (1982 and 1986) had early a presentation with suggestion for models for calculation of gas explosion with CFD codes. An overview of available CFD codes for calculation of gas explosions in semi-confined space such as an offshore module is presented by Lees (1996). He lists the codes FLACS, CLISHE, EXSIM and REAGAS. Review of explosion codes and models are presented by Gardner et al. (1993) and more recently by Hjertager et al. (1996)

In the EU sponsored projects MERGE (Modelling and Experimental Research in Gas Explosions) and EMERGE, participants representing the four most widely used explosion codes have worked together to improve the models, Popat et al. (1996). These four codes are the FLACS code from CMR, the REAGAS code from TNO, the EXSIM code from Tel-Tek, described by Sæter (1995), and the COBRA code from British Gas, described by Catlin et al. (1995). Bakke (1990) gives a description of FLACS-89, and shows the status of FLACS before the author started development and implementation of models. Wingerden et al. (1993) describes FLACS-93 where some of the contributions from the author are included.

An evaluation of gas explosion models and their ability to predict gas explosions is presented by Selby and Yassin (1996). The Blast and Fire Engineering project, SCI (1996) may be seen as a world championship for the different codes for prediction of gas explosions, since the simulations were performed first and the experiments were done later, as were also done in the MERGE and EMERGE projects.

1.4 Present Contribution

The main contributions of this thesis are:

- Implementation of equilibrium chemistry, for improved temperature calculations.
- Enhancement of the k-ε turbulence model, so it also can handle transient flows, reactive flows and coarse grid flows.
- Improvements in modelling of turbulence generation from subgrid geometry.
- Analyses of combustion models of eddy break-up type.
- Development of the β flame model, where the flame has a fixed thickness of about three grid cells.
- Development of the SIF flame model, where the flame is represented as an interface between reactants and products.
- Enhancement of the SIMPLE algorithm so the code can handle reactive compressible flows and satisfy the equation of state.
- Evaluation and development of laminar, quasi-laminar and turbulent burning velocity models, as function of flame radius, turbulence field, gas mixture, temperature and pressure.
- Introduction and development of flame folding models which describe the flame area not represented on the numerical grid.
- Validation of the models through comparison between simulations and experiments.

1.5 Survey of the Thesis

Chapter 2	presents the gas explosion process and the FLACS code, with the governing equations and representation of geometry.
Chapter 3	presents enthalpy and density ratio from thermodynamics based on calculation of equilibrium chemistry. It also includes these effects from water spray and dust explosions. Compounds in the reactant as CO, CO_2 and H_2S are added to the code.
Chapter 4	presents the turbulence modelling. Simulated results are compared with cold and steady flows. Reactive transient flow experiments and simulations are evaluated. The models are improved to handle transient, subgrid and reactive flows.
Chapter 5	evaluates combustion models of eddy break-up type and presents the β flame model which was developed as a solution on the problems with the evaluated models.
Chapter 6	presents the flame model SIF and enhancement of the SIMPLE algorithm.
Chapter 7	presents models for laminar, quasi-laminar and turbulent burning velocities in addition to flame folding models.
Chapter 8	presents experimental and simulated results from a range of explosion experiments. A validation procedure for explosion codes and some limitations of the explosion code are also shown.
Chapter 9	give conclusions and suggestions for further work.

1.6 Application of the work

The models described and developed for this thesis are implemented in the gas explosion code FLACS. Some of the models, like the β flame model and the burning velocity models have been applied in FLACS since 1993. The new enthalpy model has been applied since 1996. The SIF model and the improvements in the turbulence and the burning velocity modelling will be the standard in forthcoming versions of FLACS.

The FLACS code has been used in the design and explosion risk control in over 400 platforms and process areas, offshore and land based, world wide. It has also been used for post accident investigation of Piper Alpha and West Vanguard offshore, the Beek onshore process plant in Holland and the TWA-flight-800 accident in 96.

The sub models included in the explosion code FLACS do not include models which describe shock/compression ignition, transition to detonation or flame acoustics interactions. The code's ability to give a representative simulation of gas explosions where one or more of these phenomena are important, is therefore limited.

2 Gas explosions and FLACS

2.1 The gas explosion process

In an accidental gas explosion of a hydrocarbon-air cloud (ignited by a weak source as a spark) the flame will normally start out as a slow laminar flame with a velocity in the order of 3 m/s. If the cloud is truly unconfined and unobstructed (i.e. no equipment or other structures are engulfed by the cloud) the flame is not likely to accelerate to velocities of more than around 20 m/s, and the overpressure will be negligible if the cloud is not confined. The main reasons for the flame acceleration under these conditions are flame instabilities, turbulence generated in the atmosphere by wind and by the flame itself at the ground surface.

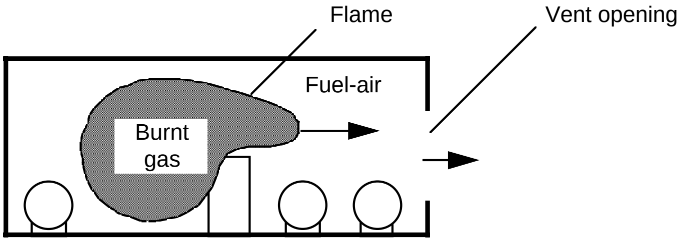

Figure 2.1 Gas explosion in a partly confined area with process equipment.

In a building or in an offshore module with process equipment as shown schematically in Figure 2.1, the flame may accelerate to several hundred meters per second. When the gas is burning the temperature will increase and the gas will expand by a factor of up to 8 or 9. The unburnt gas is therefore pushed ahead of the flame and a turbulent flow field is generated. When the flame propagates into a turbulent flow field, the effective burning rate will increase and the flow velocity and turbulence ahead of the flame increases further. This strong positive feedback mechanism is causing flame acceleration and high explosion pressures and in some cases transition to detonation.

In a confined situation, such as a closed vessel, a high flame velocity is not a requirement for generation of pressure. In a closed vessel there is no or very little relief (i.e. venting) of the explosion pressure and therefore even a slow combustion process will generate pressure.

The consequences of a gas explosion will depend on factors like:

- type of fuel
- size and fuel concentration of the combustible cloud
- location of ignition point
- strength of ignition source
- pre ignition turbulence, due to leaks or wind
- size, location and type of explosion vent areas
- location and size of structural elements and equipment
- mitigation schemes

Gas explosions may be very sensitive to changes in these factors. Therefore it is not a simple task to estimate the consequences of a gas explosion.

In general a gas explosion can be considered to be a mechanism where the flame front propagates at subsonic speed relative to the unburnt gas, immediately ahead of the wave. In a gas explosion the propagating velocity can span more than three orders of magnitude. The mechanism of flame propagation will be quite different in the different velocity regimes.

When a flame propagates through a premixed gas cloud there are two mechanisms causing pressure build-up. These are:

1) fast flame propagation
2) burning in a confined volume

In most accidental explosions a combination of these two effects causes the pressure build-up.

In a partly confined area with obstacles (i.e. process equipment, piping etc.) the flame may accelerate to several hundred meters per second during a gas explosion. The mechanisms causing the increased burning rate in turbulent deflagrations are the wrinkling of the flame front by large eddies and the turbulent transport of heat and mass at the reaction front. This turbulence is mainly caused by the interaction of the flow with structures, pipe racks, etc.

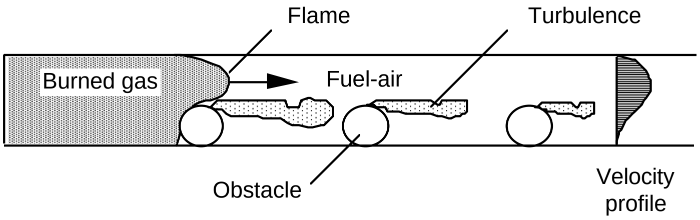

Figure 2.2 Turbulence generation in a channel due to repeated obstacles in an explosion

Figure 2.2 shows how turbulence is generated in the wake of obstacles in a channel. When the flame consumes the unburnt gas, the products will expand. This expansion can be up to 8-9 times the initial volume. The unburnt gas is therefore pushed ahead of the flame and a turbulent flow field may be generated. When the flame propagates into a turbulent flow field, the burning rate will increase dramatically. This increased burning rate will further increase the flow velocity and turbulence ahead of the flame. The increased burning velocity will cause the explosion pressure to rise.

The mechanism of flame acceleration due to repeated obstacles constitutes a strong positive feedback loop. This loop is shown in Figure 2.3. When a deflagration propagates through a region of obstacles and then ends up in an unobstructed region the flame speed will normally drop and adjust to the new environment.

This discussion shows that for a deflagration there are two mechanisms governing the pressure build-up in partly confined gas clouds, namely:

- Flame acceleration due to enhanced burning due to turbulence generated by flow past obstacles.
- Venting providing pressure relief or reducing the effect of the feedback mechanism described previously in this chapter.

These mechanisms have competing effects. The flame acceleration due to turbulence will increase explosion pressure, while venting will reduce the pressure. It is the balance between these two that is governing the pressure build-up.

Most simple models for prediction of explosion pressure such as venting guidelines for vented enclosures will not take the mechanism described above into account. Hence it is obvious that these types of simple models are inadequate for prediction of overpressure in congested environments and that they may in some cases generate overpressures that are wrong by orders of magnitude. The only models which can account for the effects of venting and equipment location on explosion overpressure are those based on solution of fluid-dynamic equations, CFD, such as FLACS.

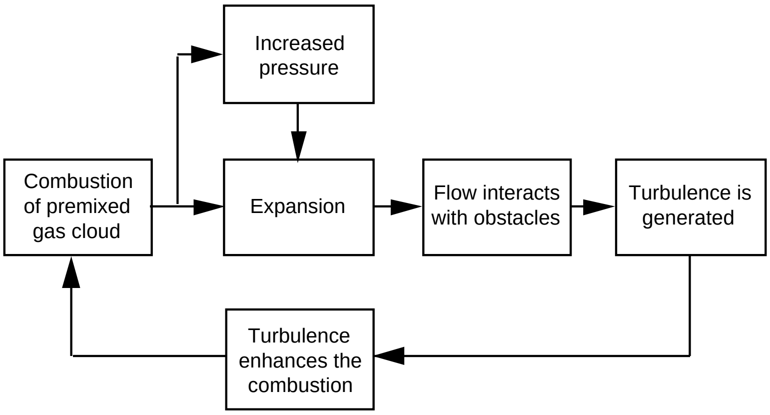

Figure 2.3 Positive feedback loop causing flame acceleration due to turbulence.

2.2 Application of FLACS

The FLACS tool is applied in connection with the consequences of a release of flammable liquid or gas. Considering the release of flammable material in general an event tree can be set up as shown in Figure 2.4. The figure shows all possible events after the accidental release of flammable gas or evaporating liquid into the atmosphere. If the gas cloud, formed from the release, is not within the flammability limits or if the ignition source is lacking, the gas cloud may be diluted and disappear. Ignition may occur immediately, or may be delayed by up to tens of minutes, all depending on the circumstances. In case of an immediate ignition (i.e. before mixing with air or oxidiser has occurred) a fire will occur.

The most dangerous situation will occur if a large combustible premixed fuel-air cloud is formed and ignites. The time from release start to ignition can be from a few seconds up to tens of minutes. The amount of fuel can be from a few kilograms up to several tons. The speed of a flame in a premixed fuel-air cloud is much higher than in a situation where the fuel and air are not mixed. Due to the speed of the flame (reaction) a pressure build-up may result, which is the main cause of damage to installations. These high speed reactions are referred to as gas explosions. The pressure generated by the combustion wave will depend on how fast the flame propagates and how the pressure can expand away from the gas cloud (governed by confinement). The consequences of gas explosions range from no damage to total destruction.

The pressure build-up due to the gas explosion can damage personnel and material or it can lead to accidents such as fires and BLEVES (domino effects). Blast waves generated by the pressure build-up in the explosive cloud and propagating into the surroundings can cause additional damage. Fires are very common events after gas explosions.

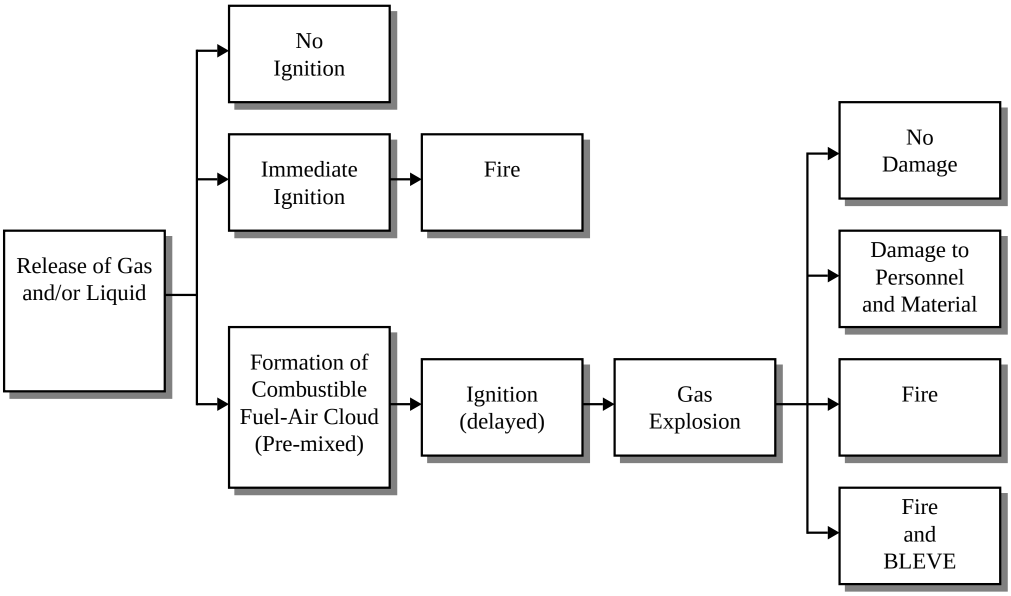

Figure 2.4 An event tree showing typical consequences of accidental releases of combustible gas or evaporating liquid into the atmosphere.

In the range of events illustrated in Figure 2.4 the FLACS tool can be applied for describing gas releases, the subsequent dispersion process and in case of an ignition the gas explosion process. With respect to gas explosion processes, FLACS only handles deflagration processes. Transition to detonation and detonation processes are <u>not</u> described by FLACS. FLACS can be used to predict blast pressures in the surroundings, i.e. at some distance from the area in which the explosion takes place, as well. The tool <u>cannot</u> be used to predict the processes and consequences of fires (radiation, direct heating).

The main outcomes of the FLACS tool, i.e. the results of the calculations, are concentration-profiles and fields when considering dispersion and the primary effects of gas explosions: static overpressure profiles and fields, dynamic overpressure profiles and fields both inside the flammable cloud and at some distance from this cloud (blast effects). In the next sections theoretical aspects of FLACS are described.

In many experimental setups one will find repeated obstacles of the same size. The basic research on gas explosions past many years now, has focused on the effect of such obstacle arrays, as e.g. the MERGE geometries, perhaps to a greater extent than on the effect of more realistic geometries. Both categories are important in order to be able to validate tools like FLACS. It is important to represent the vent openings of a semi-confined geometry properly. If obstacles close to the outer boundaries are adjusted to match the grid, the effective vent area may be affected.

2.3 Geometry representation

In order to have a good representation of the effect of obstacles it is important that they are well represented geometrically by the chosen grid. In most practical situations it will not be possible to represent the smaller obstacles on the grid, these should still be included since they may be treated by proper sub-grid models. Larger obstacles like the floor (or the ground), the ceiling, the walls and larger equipment are resolved on-grid. This means that they will be adjusted to match the grid lines.

The geometry is made by adding a range of simple objects, to represent the geometry. In the preprocessor CASD, two types of objects can be chosen, boxes and cylinders. Boxes have a location and a sizes (L_x,L_y,L_z) and area porosities (β_x,β_y,β_z). Cylinders have similarly a position, a diameter, *d*, a length, a direction and porosities. If all the specified sizes are greater than zero, the volume porosity β_v. must be specified. If this porosity is greater than zero a porous object has been specified and average distance between solids, which can be used as a characteristic length in turbulence generation must be given. The average distance should be changed to average diameter of solids, *d*, if the diameter is smaller than the distance, as for e.g. grated decks, since the turbulence then will be characterized by this diameter (wake flow instead of jet flow). Porous objects may also represent pipe bundles or other porous equipment.

2.3.1 Porosity at cell faces

The geometry is represented on the numerical grid, with area porosities on the grid cell faces and volume porosity in the grid cells. The geometry objects are presented either subgrid or ongrid, depending on the size of the objects and of the grid. Representation of subgrid geometry (objects which are smaller than the grid in at least one direction inside a grid cell), can be done by subgrid turbulence generation factors, T_i, typical diameter D_i, flame folding factors and drag factors, R_i, as shown by Sha et al. (1979).

If an object results in no porosity in direction *i* in a grid cell, and less than 50% porosity in the same direction in another grid cell, the area porosity in both grid cells will be calculated to zero. This is done since larger thin objects like walls are moved to the most nearby grid cell faces and one want to avoid unwanted openings in the geometry due to these movements. The calculation of these porosities and the turbulence and drag variables are done in the preprocessor CASD by a routine named PORCALC.

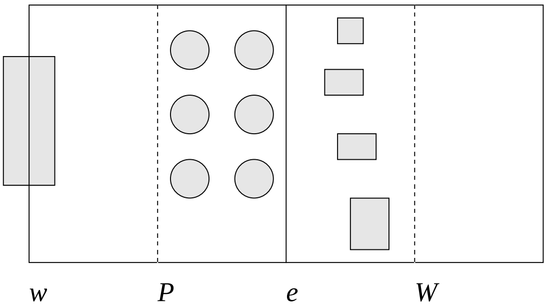

Figure 2.5 Two grid cells containing subgrid geometry

The porosity on the cell faces can be calculated in different ways, as is illustrated for cell face *e*, located between cell centres *P* and *W* in Figure 2.5.

- The actual porosity on the face (100%)
- The smallest porosity in any plane located between *P* and *W* (50%)
- The porosity when all objects between *P* and *W* are projected down to *e* (10%)

In the first alternative, subgrid objects have often no blocking influence on the flow field and in the third alternative, the blockage at the cell face can often be too large. The second alternative is therefore recommended and was chosen.

In FLACS-94, and earlier versions, cylinders were represented as boxes, with a diagonal equal to the cylinder diameter. This gave an acceptable representation of turbulence generation, since a cylinder has a thinner wake than a box of the same size, but the area blockage is of course too small. A too small area blockage results in too high flow rates and thereby too low pressures for situations with near sonic flows (obtained with pressures above 1 barg).

2.3.2 Subgrid turbulence generation and drag factors

The subgrid turbulence generation and drag factors represent the turbulence and drag generating area of a subgrid object. They were in earlier versions of FLACS located at the cell face between two cells, and for most objects calculated directly from the porosity

$$T_i = (1 - \beta_i) \tag{2.1}$$

The turbulence was generated in the cell downstream of the face. In Figure 2.5, the subgrid objects located between *P* and *E* will generate turbulence in cell *E* if the flow is from left, and in cell *P* if the flow is from right. Depending on the location of the object within the staggered cell, the turbulence field will then begin between a 1/2 grid cell upstream and downstream the object. Objects located closer than 1/2 grid cell from a solid wall will then give no turbulence production due to flows towards or from the wall

A subgrid object may have one side in one cell and the opposite side in another cell, due to the location of the object, as the object at face *w* in Fig. 2.5. The two sides may also be located in different cells since the object is several grid cells long in one (or two directions). Since turbulence is generated downstream obstacles, FLACS 96 was modified to use flow direction dependent subgrid turbulence generation factors. These six new T_i, one for each direction, are located in the cell centre instead of at the cell faces. If the turbulence is generated in the cell downstream, the turbulence field will then begin between 0 and 1 grid cell down stream the object, depending on the location of the object within the cell. Objects located closer than one grid cell from a closed wall will give no turbulence generation for flows towards the wall.

In the modified FLACS-96*, which includes improved turbulence modelling and SIF, the turbulence was choosed to be generated in the same cell as the factor is located. The turbulence field will then begin between 0 and 1 grid cell upstream the object, depending on the location of the object within the cell. All objects will here generate turbulence, independent of location near walls. In calculation of explosions with this concept, the turbulence fields from subgrid objects will be located too close to the ignition point, and the time to peak pressures will be to short. Calculations have been repeated with turbulence generated in the cell downstream, instead of the same cell. Similar peak pressures were observed, but of course the pressure peak occurred later.

For later versions of FLACS it is recommended that the turbulence and drag generation factors are located at cell faces, together with the area porosities, with generation in the cell downstream. The turbulence field will then begin on average just behind the objects, as it should. The modified FLACS-96* also includes a direction dependent dimension D_i of each object, which is used in the modified subgrid turbulence model to give more representative and grid independent turbulence field.

If objects result in zero porosity in direction *i* on a grid face, T_i from these objects should be zero in all grid cells, since the objects then are larger than the grid and turbulence generation (and flame folding) then will be handled by ongrid models. This is included in FLACS 96, but not in earlier versions of FLACS, where such large objects wrongly gave subgrid turbulence, since they often are represented with subgrid porosities at their edges. The turbulence factor from a real subgrid object, with wall pointing in positive *i* direction may typically be represented by

$$T_{i+} = \gamma \frac{a_{i+}}{A_i} \tag{2.2}$$

where a_{i+} and A_i are the area of the object inside the grid cell and area of the grid cell in positive *i* direction. γ is chosen equal to 0.7 if the object is a cylinder and 1.0 if the object is a box, to take into account differences in flows around boxes and cylinders. T_{i-} is calculated similar from object walls pointing in negative directions.

As for the area porosities at cell faces, there exist several ways to calculate turbulence generation factors in cells containing several subgrid objects, as shown below for positive direction in the cell located between *w* and *e* in Figure 2.5.

- The largest T_{i+} in any plane in the cell (50%)
- All T_{i+} between *w* and *e* projected down on *P* (65%)
- The sum of all T_{i+} in the cell (110%)

In FLACS 96 T_i is also used as the flame folding factor. The last alternative was therefore chosen here. The second (and thereafter the first) alternative will however, in the author’s opinion, give a more representative turbulence generation factor. The reason for this is that turbulence is generated in the wake of obstructions, so extra obstructions located in the wake will not lead to any significant increase in turbulence production. In the subgrid turbulence model a maximum *T* value is defined, which is used when *T* exceeds this maximum value

In FLACS 96, the turbulence generation factor in a direction for a grid cell is therefore the sum of this factor from all subgrid objects located in the control volume.

$$T_{i+}^{cell} = \sum_{cv} T_{i+} \tag{2.3}$$

If $(T_{i+} + T_{i-}) > 0$ in a grid cell, there exists subgrid objects and a need for a turbulence subgrid diameter. It is calculated as a T_i average, of D_i from all subgrid objects in the grid cell

$$D_i^{cell} = \sum_{cv} D_i max(T_{i+}, T_{i-}) / \sum_{cv} max(T_{i+}, T_{i-}) \tag{2.4}$$

It should be noted that 3D subgrid objects are treated as 2D round and square cylinders by the turbulence generation factors. Real representation of 3D subgrid object would require a much more advanced subgrid model and may not give any improved turbulent flow representation since the knowledge about 3D turbulent flows is more deficient.

2.4 Mathematical model (fluid flow equations)

During the last years, the development of computers has had a large impact on the feasibility of using CFD at large scales. Previously, many of the applications of CFD have been for research and scientific use only, but now this technology is being used on practical problems in the industry. However, there are still limitations on the computational resources which put severe restrictions on spatial and temporal resolution for realistic scenarios, the increase of computational power cannot alone bring CFD of today into industrial practise. A code then need built-in subgrid models which account for details which cannot be resolved on the numerical grid.

This section describes the mathematical model for compressible fluid flow used in FLACS. Conservation principles have been applied to the following quantities in order to derive the conservation equations:

- Mass
- Momentum
- Enthalpy
- Mass fraction of fuel (or products)
- Mixture fraction
- Turbulent kinetic energy
- Dissipation rate of turbulent kinetic energy

In the following sub-sections further details will be presented.

2.4.1 Governing equations

The governing equations used in FLACS are presented below. In later chapters the ability of equations to describe transient reactive flows is evaluated.

The equation of state is that of an ideal gas:

$$pW = \rho RT \tag{2.5}$$

where W is the molar weight of the gas mixture and R is the universal gas coefficient.

Conservation of mass is evaluated in chapter 6:

$$\frac{\partial}{\partial t}(\beta_v\rho) + \frac{\partial}{\partial x_j}(\beta_j\rho u_j) = \dot{m}/V \tag{2.6}$$

The conservation of momentum (2.7) secure that the relation between pressure and flow velocities is representative. It is evaluated in chapter 6 and is represented by

$$\frac{\partial}{\partial t}(\beta_v\rho u_i) + \frac{\partial}{\partial x_j}(\beta_j\rho u_j u_i) = -\beta_v\frac{\partial p}{\partial x_i} + \frac{\partial}{\partial x_j}(\beta_j\sigma_{ij}) + R_i + R_W + (\rho - \rho_0)g_i, \tag{2.7}$$

where R_i represents distributed resistance in i-direction due to subgrid obstruction,

$$R_i = -f_i A_i \rho |u_i| u_i \tag{2.8}$$

$$A_i = \frac{1-\beta_i}{\Delta x_i} \tag{2.9}$$

and f_i is a non-dimensional constant depending on type and orientation of the obstruction.

Conservation of enthalpy, *h*, is evaluated in chapter 3:

$$\frac{\partial}{\partial t}(\beta_v \rho h) + \frac{\partial}{\partial x_j}(\beta_j \rho u_j h) = \frac{\partial}{\partial x_j}\left(\beta_j \frac{\mu_{eff}}{\sigma_h}\frac{\partial h}{\partial x_j}\right) + \beta_v \frac{Dp}{Dt} + \dot{Q} \tag{2.10}$$

Conservation of mass fraction of a chemical specie, *Y*, is evaluated in chapter 5:

$$\frac{\partial}{\partial t}(\beta_v \rho Y) + \frac{\partial}{\partial x_j}(\beta_j \rho u_j Y) = \frac{\partial}{\partial x_j}\left(\beta_j \frac{\mu_{eff}}{\sigma_m}\frac{\partial Y}{\partial x_j}\right) + R_m \tag{2.11}$$

Conservation of mixture fraction, *f*:

$$\frac{\partial}{\partial t}(\beta_v \rho f) + \frac{\partial}{\partial x_j}(\beta_j \rho u_j f) = \frac{\partial}{\partial x_j}\left(\beta_j \frac{\mu_{eff}}{\sigma_f}\frac{\partial f}{\partial x_j}\right) \tag{2.12}$$

Turbulence equations are described and evaluated in chapter 4, and include conservation of turbulent kinetic energy

$$\frac{\partial}{\partial t}(\beta_v \rho k) + \frac{\partial}{\partial x_j}(\beta_j \rho u_j k) = \frac{\partial}{\partial x_j}\left(\beta_j \frac{\mu_{eff}}{\sigma_k}\frac{\partial k}{\partial x_j}\right) + P_k - \beta_v \rho \varepsilon \tag{2.13}$$

and conservation of dissipation rate of turbulent kinetic energy

$$\frac{\partial}{\partial t}(\beta_v \rho \varepsilon) + \frac{\partial}{\partial x_j}(\beta_j \rho u_j \varepsilon) = \frac{\partial}{\partial x_j}\left(\beta_j \frac{\mu_{eff}}{\sigma_\varepsilon}\frac{\partial \varepsilon}{\partial x_j}\right) + P_\varepsilon - C_2 \beta_v \rho \frac{\varepsilon^2}{k} \tag{2.14}$$

2.4.2 Equation solver

The differential equation for a general variable ϕ may be expressed as follows using standard symbols:

$$\frac{\partial}{\partial t}(\rho\phi) + \frac{\partial}{\partial x_j}(\rho u_i \phi) - \frac{\partial}{\partial x_j}\left(\rho \Gamma_\phi \frac{\partial}{\partial x_j}(\phi)\right) = S_\phi \tag{2.15}$$

where ϕ denotes a general variable, ρ is the gas mixture density, x_i is the coordinate in *i*-direction, u_i is the velocity component in *i*-direction, Γ_ϕ is the effective (turbulent) diffusion coefficient and S_ϕ is a source term. Note that the area porosities β_i and the volume porosity β_v used in FLACS have been omitted here in order to avoid complexity at this stage in the description.

The partial differential equation presented above is integrated over a control volume using the Gauss theorem. The integrated equation may then be written as follows:

$$\Delta(\rho V \phi)/\Delta t + \sum_{\text{faces}} (\rho u_i A_i \phi)_{\text{face}} - \sum_{\text{faces}} (\Gamma_\phi A_i \delta\phi/\delta x_i)_{\text{face}} = S_\phi V \tag{2.16}$$

When the linearized source term ($S_\phi = S_C + S_P\phi$) is large enough to dominate the solution, it is easy to see how to obtain a desired value for the dependent variable (ϕ). If all other terms in the original equation are small compared to $_\phi$ one can set $S_C + S_P\phi \approx 0$, which leads to the expression $\phi = -S_C/S_P$. Setting $S_C = L\phi_{\text{desired}}$ and $S_P = -L$, where is a number which is large enough to make $_\phi$ the dominant term, yields $\phi = \phi_{\text{desired}}$.

2.5 Boundary conditions

A subject which has received much attention by CFD researchers, is the modelling of the flow conditions at the outer boundaries of the numerical domain. This is known to be a problem area, especially for subsonic flows where local disturbances of the flow field are felt everywhere in the domain. Special care must be taken to ensure physically correct results and to obtain a good convergence rate. The best choice of locating the boundary may be in regions where little is happening. Limitations of memory and computing speed will restrict the size of the problem, and in most cases one is forced to compromise between quality and cost.

If the flame passes an outer open boundary, the speed of sound (maximum flow velocity) at the boundary will be two and a half times higher, since hot products is flowing instead of cold reactants. This will lead to an increase in the volume flow over the boundary which results in too low pressures in the calculations. A flame outside the calculation domain will also have combustion and corresponding expansion which is not included in the explosion calculation. This will also lead to underestimation of pressures in the calculations. The calculation domain must therefore be large enough to avoid the flame passing the outer boundaries during the explosion.

The boundary conditions should eventually be modified so the volume flow does not increase due to increased sound velocity when products reaches the boundary. Calculations would then (as they should) rather overpredict the pressures if the flame passes an outer boundary. It is important that an explosion code rather over predicts than under predicts the explosion pressures if the user uses a too small calculation domain. The user should not get a premium of lower pressures for using a too small calculation domain.

The boundary condition in FLACS on each of the six outer boundaries of the calculation domain can be chosen from the first five of the boundary conditions presented below:

EULER

Here the inviscid flow equations (Euler) are discretized for a boundary element, which means that the momentum and continuity equations are used on the boundary, however only in the case of outflow. The ambient pressure is used as the pressure outside the boundary. A nozzle formulation is used in the case of inflow and sonic outflow. The `EULER` condition may tend to give somewhat too low explosion pressures in unconfined situations, in such cases the boundaries should be extended (see also `PLANE_WAVE` below).

NOZZLE

Here a nozzle formulation is used for both sub-sonic inflow/outflow and sonic outflow. This condition is suitable for porous areas with small sharp edged holes or grids (e.g. louvres and grating). A discharge coefficient is calculated from the area porosity and a drag coefficient. This condition has shown to give somewhat higher explosion pressures than the `EULER` formulation but is more robust. The `NOZZLE` condition may tend to give somewhat too low explosion pressures in unconfined situations, in such cases the boundaries should be extended (see also `PLANE_WAVE` below).

PLANE_WAVE

This boundary condition was designed to reduce the reflection of the pressure waves at open boundaries which occurs when using the `EULER` or `NOZZLE` boundary conditions. The pressure wave reflection is caused by setting a fixed pressure at the boundary. The `PLANE_WAVE` boundary condition extrapolates the pressure in such a way that reflections are almost eliminated (for outgoing waves). The problem which then may occur is that the pressure stays at a slightly elevated level after an explosion. For low confinement scenarios it is recommended to use this boundary condition and to extend the grid so that the total volume is large compared to the volume of the gas cloud (thus avoiding the elevated pressure level after the expansion of the burnt gas has taken place). In semi-confined situations where the boundaries are close to the vents the `PLANE_WAVE` condition should not be used. In very unconfined situations it is advised to extend the grid and to use the `PLANE_WAVE` condition.

SYMMETRY

This is a boundary condition that can be used to reduce the size of the computational domain and thereby the simulation costs. It is applicable when a symmetry plane can be defined in the given geometry/scenario, like in the MERGE geometries. This symmetry plane will then become a computational boundary which will not, however, act as an ordinary wall e.g. as regards flow friction. The simulation results may be mirrored across the symmetry plane to give the results for the full geometry.

WIND

This is a boundary condition where the flow velocity perpendicular to an outer boundary and corresponding turbulence parameters may be given. In the current release it is not possible to enter time dependent wind parameters. However, to avoid strong transient responses the wind is increased from zero velocity to the specified velocity over a given time interval. Selecting WIND require the specification of the wind speed and direction and turbulent intensity and length scale.

SOLID WALL BOUNDARY

The solid wall boundary condition is used at all cell faces which are totally blocked. At a solid wall there will be zero velocities, both in the tangential and the perpendicular directions. And a zero gradient perpendicular to the boundary or a fixed value may be used for the scalar variables. Also the utilisation of so-called wall-functions may improve the modelling of the flow in near-wall regions (both at the outer boundaries and in the interior space). Wall functions is discussed in chapter 4.

PRESSURE_RELIEF_PANELS

Pressure relief panels are commonly used in the process industry as a mitigating device in the case of an explosion. When the pressure forces on the panel exceed a certain limit, the panel yields and the pressure is relieved. There are different opening mechanisms for the pressure relief panels employed in the industry. One opening mechanism is that each subpanel (the panel consists of subpanels mounted on a frame) turns on a hinge when it yields. Another opening mechanism is that each subpanel pops out when it yields and follows the flow field downstream. In addition to different types of pressure relief panels, a so-called inactive panel used to monitor variables, and a so-called plastic panel used to model plastic sheets on vent openings (commonly used in experiments), are incorporated in the FLACS code.

POROUS WALLS, LIKE GRATED DECKS AND LOUVRE_PANELS

Louvre panels and grated decks are common in offshore installations and also in land-based process industry. The louvre panels and grated decks are modelled in FLACS as they affect the flow field due to flow area, drag forces, turbulence production and deflection of the flow downstream panels and decks.

2.6 Initial condition

Various initial conditions may be specified for a FLACS job, but normally the default values should be applied. In addition to initial flow field conditions as wind fields and jet releases, the available parameters are listed below:

```
UP-DIRECTION
GRAVITY_CONSTANT
TEMPERATURE
TURBULENCE_INTENSITY
TURBULENCE_LENGTH_SCALE
```

These parameters may be set to modify the effect of buoyancy, to alter the initial temperature or to change the initial turbulence. Representative initial values for turbulence may be difficult to define and the values chosen may have a great influence on the results in the calculation. This problem is therefore evaluated in Chapter 4.

2.7 FLACS versions

The FLACS code has been improved over a range of years. Over these years several versions of FLACS have been issued. Due to improvements in the understanding of the explosion process, new sub-models which describe the process better have been implemented. Different versions contains therefore often different sub-models. The main differences between the different versions with respect to combustion and turbulence modelling are as follows.

- The first versions of FLACS was FLACS-86 and FLACS-89. Both contains the *H-M* combustion model. FLACS-86 can only handle methane and propane, whereas FLACS-89 was expanded to handle 8 fuels.
- In FLACS-93 the author replaced the *H-M* combustion model with the β flame model and burning velocity models, due the edifices with the *H-M* model, found in the evaluation described in subsection 5.2.1. FLACS-94 and 95 have similar combustion modelling as FLACS-93, but constants in some sub models were adjusted so simulations agreed more with experiments and the grid dependency was lowered. The effect of water deluge was also included.
- In FLACS-96 the thermodynamics is improved, as described in Chapter 3, and some more fuels is included. FLACS-97 is similar to FLACS-96, but constants in some submodels were adjusted, so simulations agree more with the SCI large scale experiments.
- FLACS-96*, is a special version of FLACS-96, where the β flame model is replaced by the SIF model (chapter 6), and the turbulence modelling is improved as described in Chapter 4.
- FLACS-98 will likely be similar to FLACS-96*, but will also include some of the improvements in turbulent burning velocity modelling suggested in chapter 7.

2.8 The MUSIC code

It can be interesting to see how other CFD codes behave in simulation of explosions with similar submodels as used in FLACS. Some of the submodels are used in other widely used explosion codes and they were compared in the MERGE and EMERGE projects as presented in the previous chapter. The MUSIC code is a 3D flow solver in general coordinates, developed at CMR, which was intended to be an alternative to FLACS as a code for calculation of gas explosions. Similar submodels for turbulence and combustion as in FLACS 93, as the β flame model, were implemented in the MUSIC code.

The author wasted a lot of time on the MUSIC code before he showed that the code is not usable for simulations which included subgrid geometry (and reactive flow). The attempt of replacing FLACS with MUSIC was then stopped.

In the MUSIC code, the velocities are located in the cell centre, instead of on the cell faces, as in FLACS. In this concept, the velocity in the flow through the cell face between two grid cells is an average found with the Rhie and Chow interpolation of the velocities in the two grid cells. Due to satisfaction of the continuity equation it is not feasible to have sub grid geometry, which gives a partly porous cell face, with this concept. The interpolation results in unphysical (high and oscillating) pressures around the partly porous faces. The subgrid geometry may however be represented only with turbulence generation, drag and no blockage when the flow velocities are low. However, in a gas explosion the velocities are often nearly sonic and then the blockage is very important. MUSIC can therefore only be used when the geometry is represented ongrid.

The volume expansion in the reaction zone causes similar problems as around partly porous faces. The thinner the flame as more faulty becomes the flow and pressure field around the reaction zone. The representation of the flame with an interface, as SIF, must therefore be avoided in codes with velocities located in the cell centre. The β flame model gives a wider reaction zone and hence a less faulty pressure and velocity field. The β model however, depends on an isobaric, precise velocity and density field to represent the flame and will therefore move the flame imperfect of the specified burning velocity.

The MUSIC code was also analysed in turbulent flow calculations. The turbulent flow simulations around a single cylinder, with different grid resolution of the cylinder on a cartesian grid, gave about the same results with MUSIC as with FLACS. The cylinder and the flow field were also represented on a curve linear grid. The result from this was that the flow followed the cylinder wall nearly to the backside of the cylinder, instead of separating at the side of the cylinder, as seen in experiments and flow simulations on cartesian grid. This resulted in a very thin wake and low turbulence intensity downstream the cylinder, shown in Figure 4.25, compared with experiments and cartesian grid simulations. Unless this problem is solved, round cylinders will be much better represented on a cartesian than a curve linear grid.

The conclusions from the exercise with the MUSIC code are that velocities in CFD codes should be located at cell faces and not in the cell centre, for calculation of reactive flows and flows with subgrid geometry. Curve linear grid may give a poor representation of turbulent flows.

2.9 Summary

A gas explosion process is a result of fast liberation of chemically bound energy due to combustion of premixed fuel-air clouds. Important factors in the gas explosion process have been described, together with a description on where a gas explosion CFD code like FLACS can be used.

The representation of geometry, ongrid and subgrid, for explosion calculations by FLACS in obstructed and confined volumes is described. The mathematical model with the governing equations, which describe the gas explosion process is presented briefly. Proper boundary and initial conditions are crucial for representative simulation of gas explosions.

The CFD code MUSIC was intended to replace FLACS as a gas explosion code, but could not do that since it failed in representing flows past subgrid geometry.

3 Equilibrium chemistry thermodynamics

The background for this work was some observations made from FLACS simulations. The first was that FLACS-95 gave too low temperature in the product for a given enthalpy release. The second was that the density ratio between reactant and product, which causes the volume expansion in combustion, had it's maximum for a stoichiometric mixture in FLACS. Experiments show that maximum density ratio generally occurs for mixtures richer than stoichiometric.

The density ratio is, together with the burning velocity, the driving force of an explosion. In a 1D situation, as shown in Figure 3.1, with a density ratio of 8, a flame with burning velocity of 1 m/s will move with 8 m/s (the flame velocity) and the flow ahead of the flame will move with 7 m/s.

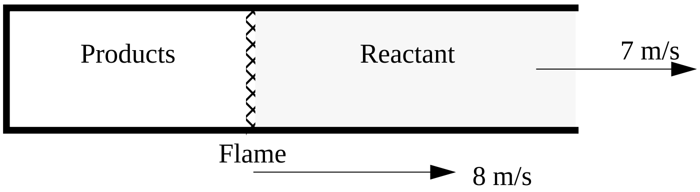

Figure 3.1 1-D flame propagation, burning velocity = 1 m/s, density ratio = 8

Stoichiometric propane- and methane-air mixtures have nearly the same burning velocity, but a difference of 6% in the density ratio, causes higher explosion pressures for propane than methane. This should show the importance of a correct density ratio.

In Table 3.1 the density ratios from the model in FLACS are compared with data from Baker (1983), which is also presented in the Gas explosion handbook (1993).

Table 3.1: Density ratio, ρ_R/ρ_P, with T_R=298K, P=1 atm

Gas	Methane	Ethylene	Propane			Acetylene		Hydrogen	
Eq. ratio, E	1.00	1.00	1.00	1.07	1.26	1.00	1.20	1.00	1.60
Baker (1983)	7.52	8.06	7.98	8.09	7.97	8.41	8.80	6.89	6.50
FLACS-95	7.30	8.01	7.81	7.67	7.47	8.56	7.90	6.62	6.51

Table 3.1 shows that FLACS-95 generally underpredicts the density ratio, due to weakness in the thermodynamical data. In section 3.1, the thermodynamical data are evaluated and improvements are suggested. The density ratio is calculated from the temperature ratio, which is calculated from thermodynamical data and mass fractions. The mass fraction models are evaluated in section 3.2.

The combustion process in FLACS 95, and earlier, is treated as a single step irreversible reaction between fuel and oxygen with CO_2 and H_2O as the only product. However, also other products are present. Models for estimating mass fractions of all relevant products are developed in section 3.3.

The FLACS code assumes the gas explosion to be adiabatic, no heat is lost to the surroundings. The background for the assumption is the short duration of the explosion. The reduction in temperature, due to this heat loss will decrease with scale, since heat is lost to an area and the energy content of the hot gas is proportional to volume.

The enthalpy equation in FLACS is

$$\frac{\partial}{\partial t}(\rho h) + \frac{\partial}{\partial x_j}(\rho u_j h) = \nabla \bullet \Gamma_h \nabla h + \frac{\partial}{\partial t} P + u_j \frac{\partial}{\partial x_j} P + S_h \tag{3.1}$$

S_h is an additional source term which may include such sources as radiation influences and viscous dissipation. In FLACS, S_h is set equal to zero. The increase in enthalpy due to turbulence dissipation and decrease in enthalpy due to radiation (important in rich mixtures due to soot formation) is therefore not included.

If the initial temperature in reactant is decreased, the temperature and density ratio will increase. The burning velocity will however decrease even more. In sum there will be a small decrease in the flame velocity.

3.1 Thermodynamical data

Thermodynamic data, which gives specific heat, C_p, and enthalpy of formation, H^0, as function of temperature is given in JANAF Thermochemical Tables as well as in the Chemkin thermodynamic database, Kee (1987). Since FLACS-95 seems to give too low temperature in the products, the thermodynamic data have been compared with the data from Chemkin.

In Chemkin C_p and H^0 are stored as polynomial fits:

$$\frac{C_p}{R} = a_1 + a_2 T + a_3 T^2 + a_4 T^3 + a_5 T^4 \tag{3.2}$$

$$\frac{H^0}{RT} = a_1 + \frac{a_2}{2} T + \frac{a_3}{3} T^2 + \frac{a_4}{4} T^3 + \frac{a_5}{5} T^4 + \frac{a_6}{T} \tag{3.3}$$

The relation between C_p and H is

$$C_p \equiv \left(\frac{dH}{dT}\right)_p \tag{3.4}$$

In FLACS, C_p and H as function of temperature is represented by a second order polynomial

$$C_p = a + bT \tag{3.5}$$

$$h = \int C_p dT = aT + \frac{1}{2} b T^2 \tag{3.6}$$

$$T = \frac{-a + \sqrt{a^2 + 2bh}}{b} \tag{3.7}$$

Expression (3.6) is however not correct since it assumes that the heat of combustion, as well as heat of formation, takes place at T_0=0 K. They take place at T_0=298.15 K and P=1 atm.

In testing of burning velocity models, the heat of combustion is often set to zero, to see if the flame burns with correct burning velocity when the expansion ratio (temperature increase) is zero. In FLACS-95, the temperature drops from 298 K in the reactant to 275 K in the products for a stoichiometric air-methane mixture in such tests.

The correct expression for enthalpy should be

$$h = h^0 + \int_{T_0}^{T} C_p dT = aT + \frac{1}{2}bT^2 - d \tag{3.8}$$

$$d = aT_0 + \frac{1}{2}bT_0^2 - h^0 \tag{3.9}$$

where h^0 is the standard heat of formation. When the heat of combustion is used in the enthalpy calculations (as in FLACS-95) h^0=0.

a, *b* and *d* are given for each component like H_2, H_2O, CO_2, CO, CH_4, C_2H_4, C_3H_8 in Table 3.2.

The coefficients *a*, *b* and *d* for a mixture of these components are averaged on basis of the mass fraction of each component

$$= \sum_{\alpha = 1}^{N} Y_\alpha a_\alpha \tag{3.10}$$

The temperature is then described in (3.11) by solution of the second order equation (3.9)

$$T = \frac{-a + \sqrt{a^2 + 2b(h + d)}}{b} \tag{3.11}$$

3.1.1 Evaluation of *a* and *b* used to represent $C_P(T)$ and *H(T)* in FLACS

The *a* and *b ‘s* used to represent the different gases in FLACS-95 are shown in Table 3.2. The specific heat capacity and enthalpy, as function of temperature, calculated by FLACS from these constants for available gases have been compared with similar data from Chemkin, calculated with (3.2) and (3.3).

The specific heat capacity of nitrogen from FLACS-95 gives a value around 40% too high for temperatures around 2300 K, compared with the true values found with Chemkin. Since enthalpy is a function of C_P, the enthalpy in FLACS-95 is also too high, as shown in Figure 3.1. The enthalpy data for nitrogen are the most important, since around 70% (on mass basis) of a normal gas air mixture is nitrogen.

The enthalpy data for the two other gases present in products, CO_2 and H_2O, agree well with the Chemkin data. Oxygen has, however like nitrogen a too high value for C_P at higher temperatures. As can be seen from Table 3.2, all fuels use the same enthalpy and specific heat. The Chemkin data in the table show, however, that they are far from equal (hydrogen should have a C_P 6 times higher at 300K).

The temperature calculated in products for a fuel air mixture with these (wrong nitrogen) data will typically be more than 100K too low and the density ratio will be 5% too low.

The calculations with FLACS-95, as shown in Table 3.1, show less difference since CO_2 and H_2O are not the only products, as will be discussed in the next section.

The values for *a* and *b* used in FLACS-95 are the same as implemented in FLACS-86, and are described by Hjertager (1986) and Bakke (1986). The values have been taken from Khalil et al. (1975), who have taken the data from Glasstone (1946). (This last reference has not been checked, since the correct values is known). The values for fuel are for a natural gas (81.3% CH_4, 14.4% N_2, 2.9% C_2H_6 and traces). As pointed out by Bakke (1986) heavier natural gases have lower specific heat than methane, but the error is considered negligible. With no fuel in the products, the values for fuels are irrelevant. If H_2 is present in the products, its value is important.

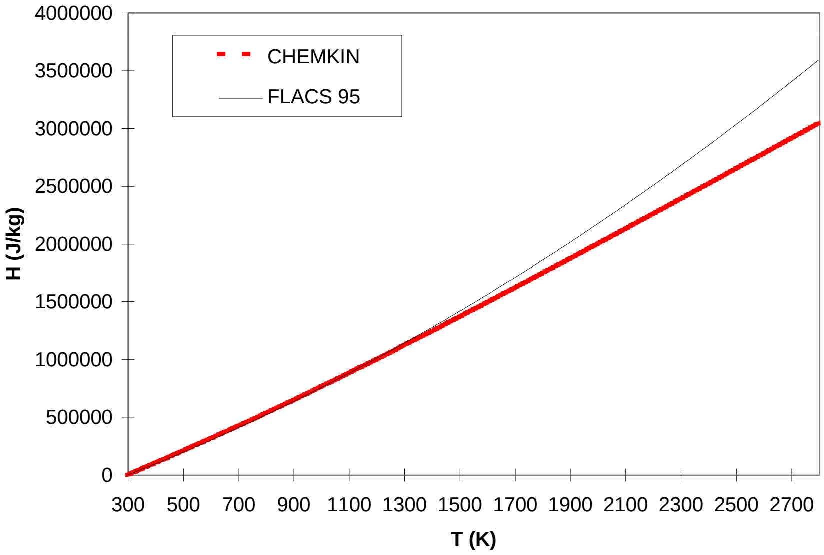

Figure 3.2 Enthalpy as function of temperature for nitrogen

3.1.2 Enthalpy of formation model, used in FLACS-96

Enthalpy of combustion, which is the enthalpy increase due to combustion when products are H_2O and CO_2 only, is used for temperature calculations in FLACS-95. As will be shown in section 2 and 3, additional products are present in a gas explosion. Enthalpy of formation, which is the enthalpy for each gas, are therefore used for temperature calculations in FLACS-96.

Enthalpy of combustion, Δh, is for a fuel equivalent to the difference in enthalpy of formation, h_f, between the reactants and products. This can easily be shown for hydrogen, with data from Table 3.2. Since each kg of H_2 produces 9 kg H_2O:

$\Delta h = h_{f,H2}+8h_{f,O2}-9h_{f,H2O}=0+0-9 * 13.44=121.0$ MJ/kg H_2

There are two advantages by switching to enthalpy of formation:

- The enthalpy will be equal for products and reactants

- Other products than CO_2 and H_2O can be formed (like CO, H_2, NO and OH)

Table 3.2: Gas data in FLACS, enthalpy of combustion as used in FLACS-95 and earlier, enthalpy of formation as used in FLACS-96 and later

		M g/mole	C	H	A	Δh 298 K MJ/kg	$h=aT+bT^2/2$		h_f 298 K MJ/kg	$h_f=aT+bT^2/2-d$		
							a	b		a	b	d 10^{-6}
Methane	CH_4	16	1	2	2	50.0	1000	4.11	-4.681	1200	3.40	5.19
Acetylene	C_2H_2	26	2	1	2.5	48.2			8.722	1340	1.40	-8.26
Ethylene	C_2H_4	28.1	2	2	3	47.2			1.867	740	2.85	-1.52
Ethane	C_2H_6	30.1	2	3	3.5	47.4			-2.786	700	3.70	3.16
Propylene	C_3H_6	42.1	3	3	4.5	45.8			0.486	690	3.10	-0.14
Propane	C_3H_8	44.1	3	4	5	46.3			-2.355	660	3.55	2.71
Butane	C_4H_{10}	58.1	4	5	6.5	45.7			-2.147	641	3.48	2.52
Hydrogen	H_2	2	0	1	0.5	120			0	13600	1.719	4.13
Hyd.sulfide	H_2S	34		1	1.5				-0.606	925	0.40	0.90
Sulphur dio.	SO_2	64							-4.64	765	0.14	4.87
Carb.m.ox.	CO	28	1	0	0.5				-3.951	1050	0.115	4.27
Carb. diox.	CO_2	44	1	0	0		1002	0.173	-8.957	1060	0.157	9.28
Water vapor	H_2O	18					1740	0.614	-13.43	1780	0.515	14.0
Water liquid	H_2O	18							-15.88	4000	0.550	17.1
Hydroxyl	OH	17							2.293	1620	0.200	-1.80
Nitric oxide	NO	30							3.010	1040	0.087	-2.7
Oxygen	O_2	32					888	0.195	0	950	0.112	0.29
Nitrogen	N_2	28					824	0.397	0	1036	0.118	0.31

The enthalpy of formation data from Chemkin (3.3) has been curve fitted with a second order polynomial fit of (3.8), with the coefficients *a*, *b* and *d* shown in Table 3.2 for a range of gases. The temperature can then be found with (3.11), if the enthalpy is known. Table 3.2 includes data for several new gases, like CO, OH and H_2O as liquid. It should be noted that CO, CO_2 and H_2 can be used both as fuel and as products. Other new products can be OH and NO.

Nitrogen, oxygen and all the other products are curve fitted for the temperature range 300 - 2800 K. The remaining fuels are curve fitted for 300 - 800 K. With these second order curve fits the accuracy of the temperature is within 10 K for a given enthalpy. This gives an accuracy on the density ratios better than 0.5%, which is acceptable. Better accuracy can be achieved using higher order polynomials as (3.3), but then the calculation of temperature will be time consuming.

For FLACS, inclusion of CO and CO_2 as reactants makes it necessary to specify also the number of oxygen molecules within the fuel molecule. This constant is called “O” and is 0.5 for CO and 1 for CO_2.

With these new models it is much easier than before to implement new gases as fuels. Generally, if sufficient information about the burning velocity (dependency of concentration, temperature and pressure), and the reaction equation is known, this can be done. For reactions including new gases like chloride, there would be some more work than by including new hydrocarbons (like pentane).

3.2 Gas composition in reactant and product

The mass fraction of each specie must be known for calculation of temperature.

The mole fraction of fuel, is the sum of the mole fractions of hydrocarbons (and hydrogen) in the reactant (mole fraction is equivalent to volume fraction).

$$n_{fuel} = \sum n_{C_xH_y} \tag{3.12}$$

The input to FLACS about the gas mixture in the reactant is the volume (mole) fractions, V_α, of each gas in the fuel, where the gases, α, are the first eight gases in Table 3.2.

$$\sum V_\alpha = 1 \tag{3.13}$$

In Table 3.3, each gas is listed with four parameters, M is the mole weight, C, H, and A are the mole fraction ratios between CO_2 and fuel, H_2O and fuel, and O_2 fuel and O_2

$$fuel + \mathrm{A}O_2 \rightarrow \mathrm{C}CO_2 + \mathrm{H}H_2O \tag{3.14}$$

These four constants:, C, H, A and M for the fuel are universal for this fuel, and are found from an average based on volume fractions of gases in the fuel, as shown for M.

$$M_{fuel} = \sum M_\alpha V_\alpha \tag{3.15}$$

The equivalence ratio, which is the ratio between fuel and oxygen, compared with that of a stoichiometric mixture, is the other input to FLACS.

$$E = \left(\frac{Y_{fuel}}{Y_{O_2}}\right) \Big/ \left(\frac{Y_{fuel}}{Y_{O_2}}\right)_{stoch} = \left(\frac{n_{fuel}}{n_{O_2}}\right) \Big/ \left(\frac{n_{fuel}}{n_{O_2}}\right)_{stoch} = \frac{n_{fuel}}{n_{O_2}} A \tag{3.16}$$

In the literature ϕ is often used instead of E as notation for the equivalence ratio.

The volume ratio between N_2 and O_2 is N/A. In air this ratio is 3.76, assuming air consists of O_2 and N_2 only. The mole factions of fuel and oxygen is then given by

$$n_{fuel} + n_{O_2} + n_{N_2} = 1 \tag{3.17}$$

$$n_{fuel}\left(1 + \frac{A}{E} + \frac{N}{E}\right) = 1 \tag{3.18}$$

$$n_{O_2} = n_{fuel}\frac{A}{E} \tag{3.19}$$

The mole weight of reactants is

$$M_R = \sum M_i n_i = M_{fuel} n_{fuel} + M_{O_2} n_{O_2} + M_{N_2} n_{N_2} \tag{3.20}$$

A_i C_i, H_i and N_i are equivalent to A, C, H and N, but on mass basis and calculated as

$$A_i = AM_{O_2}/M_{fuel} \tag{3.21}$$

mass fraction of fuel, as well as oxygen and nitrogen can be found from

$$Y_{fuel}(1 + Ai(1 + Ni)) = 1 \tag{3.22}$$

3.2.1 Mixture fraction and mass fractions in product

The gas mixture in FLACS can consist of regions with two different equivalence ratios, E_0 and E_9. Both of these are given as input, as well as the description of the region with E_0.

The two regions will mix and the mass fraction from region 0 in this mixture is called f_{mix}. A transport equation is solved for f_{mix}, so f_{mix} is known.

$$\frac{\partial}{\partial t}(\rho f) + \frac{\partial}{\partial x_j}(\rho u_j f) = \nabla \bullet \Gamma_f \nabla f \tag{3.23}$$

E in this mixture is a function of f_{mix} and is calculated from the mass fractions of fuel and oxygen in the two regions:

$$Y^R_{fuel} = f_{mix} Y_{fuel0} + (1 - f_{mix}) Y_{fuel9} \tag{3.24}$$

$$Y^R_{O_2} = f_{mix} Y_{O_2 0} + (1 - f_{mix}) Y_{O_2 9} \tag{3.25}$$

$$E = \frac{Y^R_{fuel}}{Y^R_{O_2}} Ai \tag{3.26}$$

The mass fraction of nitrogen is the same in both reactant and product

$$Y_{N_2} = 1 - Y^R_{O_2} - Y^R_{fuel} \tag{3.27}$$

The other mass fractions in the products are given in Table 3.3. The mass fractions of each compound are then known, as a function of f_{mix} only, since all the other variables are functions of E and constants

.

Table 3.3: Mass fractions in products, as functions of equivalence ratio, *E*

	$E < 1$	$1 < E$
Y^P_{fuel}/Y^R_{fuel}	0	$(E - 1)$
$Y^P_{CO_2}/Y^R_{fuel}$	C_i	C_i/E
$Y^P_{H_2O}/Y^R_{fuel}$	H_i	H_i/E
$Y^P_{O_2}/Y^R_{O_2}$	$(1 - E)A_i$	0

3.2.2 Temperature calculations in FLACS

The reaction zone, reactants and products are often described by the progress variable ***c***, where ***c*** is mass fraction of products, taking values ranging from zero in the unburnt reactants to unity in the fully burned products. The fuel mass fraction is then a function of ***c*** and the fuel mass fractions in reactant and product.

$$Y_{fuel} = Y^P_{fuel}c + Y^R_{fuel}(1-c) \tag{3.28}$$

The β flame model in FLACS solves a transport equation for $Y_{\mathrm{fuel.}}$

$$\rho\frac{DY_{fuel}}{Dt} = \nabla \bullet \rho D \nabla Y_{fuel} - Y_{fuel0}w \tag{3.29}$$

The SIF flame model, which is new in FLACS-96 and may be used instead of the β flame model, solves an algebraic equation for ***c***, instead of the transport equation for Y_{fuel}.

The temperatures in the reactant and product are calculated from the enthalpy, and the mass averaged constants *a* and *b*. Since *a* and *b* are calculated the same way, only *a* is shown.

$$a^R = a_{fuel}Y^R_{fuel} + a_{O_2}Y^R_{O_2} + a_{N_2}Y_{N_2} \tag{3.30}$$

$$a^P = a_{fuel}Y^R_{fuel} + a_{O_2}Y^R_{O_2} + a_{CO_2}Y_{CO_2} + a_{H_2O}Y + a_{N_2}Y_{N_2} \tag{3.31}$$

The temperature in control volumes in the reaction zone can be calculated under two different assumptions. The first is to assume that all energy released in combustion is used to heat the products. The mean temperature is then the mass average of the temperatures in reactant and product. This function is called TMIX2 in FLACS,

$$h^P = h^R + min(2-E, 1)Y^R_{fuel}\Delta h_{fuel} \tag{3.32}$$

$$T_2 = T(h^P, a^P, b^P)c + T(h^R, a^R, b^R)(1-c) \tag{3.33}$$

where the temperature functions T() is (3.7). The other assumption assumed that both products and reactants in the same grid cell have the same temperature.

$$a = a^R(1-c) + a^Pc \tag{3.34}$$

$$h = h^Pc + h^R(1-c) = h^R + \Delta h_{fuel}(Y^R_{fuel} - Y_{fuel}) \tag{3.35}$$

$$T_1 = T(h, a, b) \tag{3.36}$$

This function was first implemented in FLACS and is called TMIX. This assumption may be correct in calculation of a stirred reactor or when the temperature gradient is resolved in the flame (grid size 0.01 mm).

Both the β and SIF flame models are constructed based on the assumption that the flame is thin compared with the grid cell size. Assuming that pressure in a grid cell is equal in product and reactant, a volume expansion factor τ has been made

$$\tau + 1 \equiv \frac{\rho_R}{\rho_P} = \frac{T_PR_P}{T_RR_R} = \frac{T_PM_R}{T_RM_P} \tag{3.37}$$

$$\rho_R \equiv \rho(1 + \tau c) \tag{3.38}$$

The relation between pressure, density and temperature can be found from the ideal gas law

$$\rho RT = PM \tag{3.39}$$

where R=8.3144 is the gas constant. The molecular weight is

$$\frac{1}{M} = \frac{c}{M_P} + \frac{1-c}{M_R} \tag{3.40}$$

The ideal gas law is only satisfied when TMIX2 is used. Therefore only TMIX2 should be used.

In FLACS-96 where temperature calculations will be based on heat of formation, the enthalpy (under constant pressure) will be the same in reactant and products. The temperature is calculated as function of mass fractions (in product from Table 3.5) and heat of formation constants (from Table 3.2) with equation (3.11).

3.2.3 Improved enthalpy calculation in flame cells

In FLACS the enthalpy equation is modelled as

$$\frac{\partial}{\partial t}(\rho h) + \frac{\partial}{\partial x_i}(\rho u_i h) = \frac{\partial p}{\partial t} + u_i \frac{\partial p}{\partial x_i} + Q \tag{3.41}$$

where Q is a enthalpy source from heat fluxes or temperatures on walls, modelled through wall functions. For a closed adiabatic system with no enthalpy source:

$$\rho \frac{\partial h}{\partial t} = \frac{\partial p}{\partial t} \tag{3.42}$$

When the enthalpy is changed, due to isentropical compression or expansion, the enthalpy change is inverse proportional with density and will therefore be larger for products than for reactants.

$$\frac{\partial h}{\partial p} = \frac{1}{\rho} \tag{3.43}$$

The enthalpy change will therefore be much higher in products than in reactants. In a grid cell containing both reactant and products, the enthalpy will be unchanged and equal in reactants and products in a constant pressure process. When the pressure increases the enthalpy will be higher in products and when it decreases it will be higher in reactants. If one does the mistake of assuming equal enthalpy when the pressure has decreased, a too low temperature in reactant will be calculated. In situations with only a little reactant present, this enthalpy may give a calculated temperature in reactant below 0 K.

The initial enthalpy is a function of the mixture fraction and initial enthalpy in the two mixtures

$$h^0 = f_{mix} h_0 + (1 - f_{mix}) h_9 \tag{3.44}$$

The enthalpy in a cell is the sum of mass fraction and enthalpy in reactants and products

$$h = (1-c)h^R + ch^P \tag{3.45}$$

The change in enthalpy from the initial condition, is $\tau + 1$ times (the density ratio) larger in products than in reactants

$$h^P - h^0 = (1+\tau)(h^R - h^0) \tag{3.46}$$

Combining the two equations above gives the enthalpy in reactant and product

$$h^R = \frac{h + h^0\tau c}{1 + \tau c} \tag{3.47}$$

$$h^P = \frac{h(1+\tau) - h^0\tau(1-c)}{1 + \tau c} \tag{3.48}$$

The enthalpy is then the same as in reactant, for *c=0*, and the same as in product, for *c=1*.

The enthalpy are used in calculation of temperatures in reactant and product, Arntzen (1997), which are used in the update routine for calculation of the expansion ratio, defined as

$$\tau \equiv \frac{\rho_R}{\rho_P} - 1 = \frac{T_P R_P}{T_R R_R} - 1 \tag{3.49}$$

where the gas constants ratio is 1 for methane (but not e.g. for propane). A too low T_R will result in a too high (or negative) expansion ratio and it will not be possible to use the SIF model.

When the enthalpy is used only for average temperature calculations in a cell, as with the β flame model, the assumption that the enthalpy is equal in reactants and products is good enough, since an inaccurate temperature estimate in e.g. reactants occurs only when little reactants are present.

3.2.4 Improved model for compounds in the product

With the assumption that all products are either CO_2 or H_2O (as in FLACS) the maximum temperature will be for stoichiometric mixtures, since there will be unburnt fuel in rich mixtures and unburnt O_2 in lean mixtures.

A more likely result, than having unburnt fuel as product in a rich mixture, is that the products are H_2 and CO, or CO and CO_2, in addition to H_2O and N_2. Some will argue that not all fuel will be burned, due to inhomogenity in the rich mixture. This is however taken care of by the f_{mix} variable.

Lewis and von Elbe (1961) suggest to do the combustion of hydrocarbons in three steps. First CO and hydrogen are made (3.50). If more oxygen is available, hydrogen and oxygen reacts to water (3.51), and finally CO reacts with oxygen (3.52)

$$fuel + \frac{\mathrm{A}}{E}O_2 \rightarrow \mathrm{C}CO + \mathrm{H}H_2 \tag{3.50}$$

$$H_2 + O_2 \rightarrow 2H_2O \tag{3.51}$$

$$CO + \frac{1}{2}O_2 \leftrightarrow CO_2 \tag{3.52}$$

The oxygen available is expressed with the equivalence ratio, *E*. The *E* limits for which reaction takes place, depends on the constants A, C and O (from table 3.2) for the fuel mixture. If

$$\frac{2\mathrm{A}}{\mathrm{C}-2\mathrm{O}} < E \tag{3.53}$$

there is not enough oxygen to reaction (3.30). There will also be some fuel left and the reaction is

$$fuel + \frac{\mathrm{A}}{E}O_2 \rightarrow \gamma\mathrm{C}CO + \gamma\mathrm{H}H_2 + (1-\gamma)\,fuel \tag{3.54}$$

$$\gamma = \frac{2\mathrm{A}}{E(\mathrm{C}-2\mathrm{O})} \tag{3.55}$$

It should be noted that neither hydrogen nor CO can exist in this area when they are the only fuel, and most fuel air mixtures will be too rich to be combustible.

If the mixture is leaner,

$$\frac{2\mathrm{A}}{2\mathrm{A}-\mathrm{C}} < E \le \frac{2\mathrm{A}}{\mathrm{C}-2\mathrm{O}} \tag{3.56}$$

the products will be CO and a mixture of hydrogen and water vapour. The reaction is then

$$fuel + \frac{\mathrm{A}}{E}O_2 \rightarrow \mathrm{C}CO + \beta\mathrm{H}H_2 + (1-\beta)\mathrm{H}H_2O \tag{3.57}$$

$$\beta = 1 - 2\left(\mathrm{O} + \frac{\mathrm{A}}{\mathrm{E}}\right) \tag{3.58}$$

If the mixture is lean or only moderate rich

$$E \le \frac{2\mathrm{A}}{2\mathrm{A}-\mathrm{C}} \tag{3.59}$$

The products will be water vapour and a mixture of CO and CO_2

$$fuel + \frac{\mathrm{A}}{E}O_2 \rightarrow \alpha\mathrm{C}CO + (1-\alpha)\mathrm{C}CO_2 + \mathrm{H}H_2O + \chi O_2 \tag{3.60}$$

where the unknown variables will be described in next section. As also will be shown in the next section, there will always exist some CO in the products. All CO will not burn to CO_2, even in lean mixtures, due to a balance between CO, O_2 and CO_2 concentrations, given by an equilibrium constant.

3.3 Equilibrium constants

The assumption in FLACS that all fuel is burned to CO_2 if there is enough oxygen, give the highest density ratio for a stoichiometric mixture. This would have been a conservative approach if explosions would give maximum pressures for stoichiometric mixtures. Experiments often show that the highest pressures occur in rich fuel/air mixtures. FLACS will generally underpredict the pressures for overstoichiometric concentrations.

The assumption that a stoichiometric mixture of hydrocarbons and air will have only CO_2 and H_2O as products is according to Kuo (1986) appropriate only if the temperature in the products is low (T_P < 1200 K). The temperature in a gas explosion is usually much higher and a range of other compounds like NO, H, OH, O, N, NO,O_2 and CO are formed.

Temperatures and mass fractions of the product compounds behind a 1D constant pressure flame have been calculated with a chemical kinetics code. Such calculations can be done with the code Stanjan at: *http://adam.caltech.edu/tcc/*. With stoichiometric mixtures, pressure 1 atm. and T_R=298 K, the only important “new” compound seems to be CO (and O_2). The other compounds had mass fractions less than 0.2%. From the mass fractions for CO and CO_2, minimum values for α can be found, as shown in Table 3.4

.

Table 3.4: Products in stoichiometric mixtures, from a chemical kinetics code,T_R=298, P=1 atm

	Methane CH4	Acetylene C2H2	Ethylene C2H4	Ethane C2H6	Propane C3H8	Hydrogen H2
Y_{CO}	0.008	0.043	0.0194	0.0107	0.011	0
Y_{CO2}	0.139	0.17	0.168	0.1548	0.16	0
T	2245	2514	2390	2277	2289	2392
$\alpha = \frac{n_{CO}}{n_{CO} + n_{CO_2}}$	0.106	0.215	0.162	0.116	0.119	

As can be seen from the table, acetylene has a very large α. This will decrease the energy release and explains why FLACS calculates a too high density ratio (in Table 3.1), even with a too high C_p value. It should also be noticed that α increases with temperature.

The overall reaction and equilibrium constants which give α are:

$$2CO + O_2 \leftrightarrow 2CO_2 \tag{3.61}$$

$$K_p(T) = \frac{p_{CO}^2 p_{O_2}}{p_{CO_2}^2} = \frac{n_{CO}^2 n_{O_2}}{n_{CO_2}^2}P \tag{3.62}$$

After replacing the partial pressures with mole fractions, the following third order equation for α, as a function of *K(T)*, *E*, C, A, H and *P* (The pressure, *P*, has units atmospheres) is obtained.

$$K_P(T) = \left(\frac{\alpha}{1-\alpha}\right)^2 n_{O_2}^P P \tag{3.63}$$

where the mole fraction of oxygen in product is

$$n^P_{O_2} = \frac{\chi}{C + H + \chi + N/E} \tag{3.64}$$

$$\chi = n^P_{O_2}/n^R_{fuel} = \alpha\frac{C}{2} + A\left(\frac{1}{E} - 1\right) \tag{3.65}$$

The mass fractions in products are shown in Table 3.5. They are a function of E and α only, since the other variables are constant for the fuel mixture

Table 3.5: Mass fractions in product as function of Equivalence ratio and α

	$E \le \frac{2A}{2A - C}$	$\frac{2A}{2A - C} < E \le \frac{2A}{C-2O}$	$\frac{2A}{C-2O} < E$
$_{CO_2}/Y^R_{fuel}$	$(1 - \alpha)C_i$	0	0
$_{CO}/Y^R_{fuel}$	αC_{i2}	C_{i2}	γC_{i2}
${}^P_{O_2}/Y^R_{fuel}$	$\chi\frac{A_i}{A}$	0	0
$_{H_2O}/Y^R_{fuel}$	H_i	$(1 - \beta)H_i$	0
$_{H_2}/Y^R_{fuel}$	0	βH_{i2}	γH_{i2}
${}^P_{fuel}/Y^R_{fuel}$	0	0	$1 - \gamma$
α, β, γ	$\chi = \alpha\frac{C}{2} + A\left(\frac{1}{E} - 1\right)$	$\beta = 1 - 2(O + \frac{A}{E})$	$\gamma = \frac{2A}{E(C - 2O)}$
${}^R/M^P$	$\frac{E(C + H + \chi) + N}{E + A + N}$	$\frac{E(C + H) + N}{E + A + N}$	$\frac{2A}{C}\frac{(EC + C + H - 1)}{(E + A + N)}$
Eq. for reaction	(3.60)	(3.57)	(3.54)

3.3.1 The equilibrium constant, $K_P(T)$, for $2CO + O_2 \leftrightarrow 2CO_2$

$K_P(T)$ in tabulated form, from Sonntag and Wylen (1986) is shown in Table 3.7. The equilibrium constant can also be found from the JANAF tables, where $\log_{10}K_f$ of formation are tabulated as function of temperature. Strehlow (1979) gives the equilibrium constant for a specific reaction

$$(\log K_p)_{reaction} = \sum \upsilon_i(\log K_f)_i \tag{3.66}$$

$$(\log K_p)_{2CO + O_2 = 2CO_2} = 2(\log K_f)_{CO} + (\log K_f)_{O_2} - 2(\log K_f)_{CO_2} \tag{3.67}$$

The equilibrium constant for partial pressures is seen to be a function of temperature alone, Williams (1985). The equilibrium constant from Table 3.4, as well as from the JANAF tables and (3.67) can be expressed by

$$K_p(T) = 4.8 \times 10^8 e^{-66500/T} \tag{3.68}$$

in the temperature range 1400 to 2800 K. When the constant is known from (3.63), the corresponding temperature from (3.68) is:

$$T_{K_P} = \frac{66500}{20 - ln(K_P)} \tag{3.69}$$

Based on the equilibrium constant for CO, mass fractions can be calculated from Table 3.5. Then temperature and density ratios can be calculated. This has been done for the gas mixtures presented by Baker (1983) and the results are compared in Table 3.6.

Table 3.6: Density ratio, ρ_R/ρ_P, with T_R=298K, P=1 atm.

Gas	Methane	Ethylene	Propane			Acetylene		Hydrogen	
Equivalence ratio, *E*	1.00	1.00	1.00	1.07	1.26	1.00	1.20	1.00	1.60
Baker (1983)	7.52	8.06	7.98	8.09	7.97	8.41	8.80	6.89	6.50
Calculated with $K_{P,CO}$	7.55	8.11	8.00	8.11	7.91	8.51	9.08	7.23	6.55

The density ratios calculated with an equilibrium constant for CO are some what higher than those reported by Baker (1983). The difference also increases with temperature. This can be explained by the fraction of hydrogen, oxygen and other extra compounds in the products which increase in magnitude as the temperature increases.

3.3.2 Evaluation of multi compound equilibria

The following three reactions and their equilibria constants are most likely to be needed for accurate temperature calculations

$$H_2 + O_2 \leftrightarrow 2H_2O \tag{3.70}$$

$$_2 + 2OH \leftrightarrow 2H_2O \tag{3.71}$$

$$NO \leftrightarrow N_2 + O_2 \tag{3.72}$$

Table 3.7, from Sonntag and Wylen (1986), shows the equilibria constants for these three reactions, as well as the constant for CO, as a function of temperature. They are evaluated to find which must be included, and combined to find a relation between them.

Table 3.7: $K_{P2}(T)$ for the reaction $O_2 + 2H_2 \leftrightarrow 2H_2O$

T (K)	2000	2200	2400	2600	2800	3000	Value for FLACS-96
$ln(K_P) = ln\left(\frac{n_{CO}^2 n_{O_2}}{n_{CO_2}^2}P\right)$	-13.270	-10.240	-7.720	-5.602	-3.788	-2.222	
$ln(K_{P2}) = ln\left(\frac{n_{H_2}^2 n_{O_2}}{n_{H_2O}^2}P\right)$	-16.290	-13.536	-11.238	-9.296	-7.624	-6.172	
$ln(K_{P3}) = ln\left(\frac{n_{H_2} n_{OH}^2}{n_{H_2O}^2}P\right)$	-17.456	-14.296	-11.664	-9.438	-7.526	-5.874	
$ln(K_{P4}) = ln\left(\frac{n_{NO}^2}{n_{N_2} n_{O_2}}\right)$	-7.862	-6.866	-6.038	-5.342	-4.742	-4.228	
$\frac{n_{H_2}}{n_{H_2O}} \Big/ \frac{n_{CO}}{n_{CO_2}} = \sqrt{\frac{K_{P2}}{K_P}}$	0.221	0.192	0.172	0.157	0.147	0.139	0.17
$\frac{n_{OH}}{\sqrt{n_{O_2} n_{H_2}}} = \sqrt{\frac{K_{P3}}{K_{P2}}}$	0.558	0.684	0.808	0.931	1.202	1.16	0.80
$\frac{n_{NO}}{\sqrt{n_{O_2} n_{N_2}}} = \sqrt{K_{P4}}$	0.020	0.032	0.049	0.069	0.093	0.121	

Strehlow (1979) reports that the equilibrium constants are independent of each other, they can therefore be combined. Combining the equations in Table 3.7 gives the H_2 concentration through a simple relation between the variables α and β

$$\frac{n_{H_2}}{n_{H_2O}} \Big/ \frac{n_{CO}}{n_{CO_2}} = \frac{\beta}{1-\beta-\Gamma/2} \Big/ \frac{\alpha}{1-\alpha} \approx 0.17 \tag{3.73}$$

$$\beta \approx \frac{0.17\alpha}{1-0.83\alpha} \tag{3.74}$$

H_2 fractions around 20% of CO fractions are important and must be included

The mole fraction of OH

$$n_{OH} = 0.8\sqrt{n_{H_2} n_{O_2}} = 0.8\sqrt{\beta H \chi} \cdot n_{fuel}^R \tag{3.75}$$

is of same level as H_2 and O_2 fractions and must be included.

The NO concentration is a function of mole fractions of O_2 and N_2, as well as temperature, as seen from Table 3.7. n_{NO}=0.01 at *E*=1 and *T*=2500K (acetylene) or *E*=0.8 and *T*=2200K. Since NO has higher enthalpy of formation than O_2 and N_2 (Table 3.2), the temperature will drop around 15 K. This gives a reduction of the density ratio of only 0.6%, and possible NO-formation will therefore be neglected.

In oxygen enriched mixtures, n_{NO} can be larger and NO formation may then have to be included. Nitrogen can then no longer be treated as an inert gas.

3.3.3 Product model with equilibria constants for both CO, H_2 and OH

The products will be a mixture of hydrogen, water vapour, CO, CO_2, OH and O_2 (and SO_2 if H_2S is a part in the fuel) in addition to N_2, represented by the reaction

$$fuel + \frac{\mathrm{A}}{E}O_2 \rightarrow \alpha\mathrm{C}CO + (1-\alpha)\mathrm{C}CO_2 + \beta\mathrm{H}H_2 + (1-\beta-\Gamma/2)\mathrm{H}H_2O + \chi O_2 + \Gamma\mathrm{H}OH + \mathrm{S}SO_2 \tag{3.76}$$

$$\Gamma = 0.8\sqrt{\beta\chi/\mathrm{H}} \tag{3.77}$$

$$\chi = n^P_{O_2}/n^R_{fuel} \tag{3.78}$$

Conservation of oxygen give the mole ratio of oxygen in products, χ

$$\chi + 0.2\sqrt{\beta\mathrm{H}\chi} = \alpha\frac{\mathrm{C}}{2} + \beta\frac{\mathrm{H}}{2} + \mathrm{A}\left(\frac{1}{\mathrm{E}} - 1\right) \tag{3.79}$$

This is a second order equation for χ with solution

$$\chi = \Psi - \frac{\beta\mathrm{H}}{50}\left(\sqrt{1 + \frac{100\Psi}{\beta\mathrm{H}}} - 1\right) \tag{3.80}$$

$$\Psi = \alpha\frac{\mathrm{C}}{2} + \beta\frac{\mathrm{H}}{2} + \mathrm{A}\left(\frac{1}{\mathrm{E}} - 1\right) \tag{3.81}$$

The mole ratio of hydroxyl, Γ, can now be calculated with (3.77). The mole fraction of oxygen in products is then

$$n^P_{O_2} = \frac{\chi}{\mathrm{C} + \mathrm{S} + (1 + \Gamma/2)\mathrm{H} + \chi + \mathrm{N}/\mathrm{E}} \tag{3.82}$$

where equations (3.80) - (3.82) replace (3.64) and (3.65)

Table 3.8 shows the formulas needed to calculate the mass fractions in products (the right column is only for very rich mixtures).

Table 3.8: Mass fractions in product as function of Equivalence ratio, α and β

	$\mathrm{E} \le \frac{\mathrm{A}}{\mathrm{C}/2 + \mathrm{S} - \mathrm{O}}$	$\frac{\mathrm{A}}{\mathrm{C}/2 + \mathrm{S} - \mathrm{O}} < \mathrm{E}$
${}_{CO_2}/Y^R_{fuel}$	$(1-\alpha)\mathrm{C_i}$	0
${}_{CO}/Y^R_{fuel}$	$\alpha \mathrm{C_{i2}}$	$\gamma \mathrm{C_{i2}}$
${}_{SO_2}/Y^R_{fuel}$	S_i	$\gamma \mathrm{S}_i$
${}^P_{O_2}/Y^R_{fuel}$	$\chi\frac{\mathrm{A_i}}{\mathrm{A}}$	0
${}_{H_2O}/Y^R_{fuel}$	$(1-\beta-\Gamma/2)\mathrm{H}_i$	0
${}_{H_2}/Y^R_{fuel}$	$\beta \mathrm{H_{i2}}$	$\gamma \mathrm{H_{i2}}$
${}_{OH}/Y^R_{fuel}$	$\Gamma \mathrm{H}\mathrm{B}_i$	0
${}^P_{fuel}/Y^R_{fuel}$	0	$1-\gamma$
Γ, γ	$\Gamma = 0.8\sqrt{\frac{\beta\chi}{\mathrm{H}}}$	$\gamma = \frac{\mathrm{A}}{\mathrm{E}(\mathrm{C}/2 + \mathrm{S} - \mathrm{O})}$
${}^R/M^P$	$\frac{\mathrm{C} + \mathrm{S} + (1 + \Gamma/2)\mathrm{H} + \chi + \mathrm{N}/\mathrm{E}}{1 + (\mathrm{A} + \mathrm{N})/\mathrm{E}}$	$\frac{1}{\mathrm{E} + \mathrm{A} + \mathrm{N}}\left(\frac{\mathrm{A}(\mathrm{C} + \mathrm{S} + \mathrm{H} - 1)}{\mathrm{C}/2 + \mathrm{S} - \mathrm{O}} + \mathrm{E} + \mathrm{N}\right)$
Eq. for reaction	(3.76)	(3.54)

Table 3.9 gives the mass ratios between the different products and fuel, which are needed in the formulas in Table 3.8. The needed constants are calculated from Table 3.2

.

Table 3.9: Mass ratios between products and fuel

$B_i = \frac{M_{OH}}{M_{fuel}}$	$C_i = C\frac{M_{CO_2}}{M_{fuel}}$	${}_{i2} = C\frac{M_{CO}}{M_{fuel}}$	$H_i = H\frac{M_{H_2O}}{M_{fuel}}$	${}_{i2} = H\frac{M_{H_2}}{M_{fuel}}$	$S_i = S\frac{M_{SO_2}}{M_{fuel}}$

α seems to be a function mainly of *E*. During isentropic compression both pressure and temperature increase. K_P will then increase due to the temperature increase. α will however not change much because of it’s dependence on pressure through (3.63). α may therefore be tabulated as function of *E*. This α can then be used as a first guess.

A method for calculation of the product temperature is presented below:

```
Guess $\alpha$ (or use tabulated $\alpha(E)$)
Calculate $\beta$ from $\alpha$ with (3.74)
Calculate $\Psi$ from $\alpha$ and $\beta$ with (3.81)
If $\Psi<0$, $\alpha$ is too small, return to top, guess a $\alpha$ with higher value
Calculate $\chi$ from $\Psi$ and $\beta$ with (3.80)
Calculate $\Gamma$ from $\beta$ and $\chi$ with (3.77)
Calculate $n_{O2}$ from $\beta$ and $\chi$ with (3.82)
Calculate $K_P$ from $\alpha$ and $n_{O2}$ with (3.63)
Calculate $T_K$ from $K_P$ with (3.69)
Calculate mass fractions in product from $\alpha$, $\beta$, $\Gamma$ and $\chi$ with formulas from Table 3.8
Calculate $T_P$ from enthalpy and mass fractions, with (3.11)
If $(T_K-T_P) > 1K$, and $\Psi > 0.001$, return to top, guess a $\alpha$ with lower value
If $(T_P-T_K) > 1K$, return to top, guess a $\alpha$ with higher value
Else, $\alpha$ and $T_P$ are acceptable
```

The density ratio obtained with this scheme for hydrogen, shown in Table 3.10, agrees well with the data in Table 3.6, with a difference of only around 1%. In Table 3.6 the difference was 8% for E=1.

Table 3.10: Calculation of temperature and density ratio for hydrogen, with the scheme above

E	α	β	Ψ	χ	n_{O2}	Y_{O2}	Y_{OH}	Y_{H2}	T_P	ρ_R/ρ_P
1	0.226	0.05	0.023	0.017	0.006	0.004	0.006	0.001	2412	6.98
1.6	0.78	0.38	0.0003	0.0001	$6\ 10^{-5}$	$5\ 10^{-5}$	0.002	0.001	2224	6.54

3.3.4 Worst case equivalence ratio for FLACS

FLACS-96 would give better estimates of the pressures for overstoichiometric concentrations, than previous versions of FLACS did. The worst case equivalence ratio for a fuel mixture can be estimated from calculation of a flame velocity as the product of burning velocity and density ratio as function of E at the initial conditions. The E with highest flame velocity is also likely to give the highest pressures.

It should therefore be possible to choose “worst case Equivalence ratio” in a later version of FLACS. The code will then estimate this E for the fuel mixture as outlined above.

3.4 Water spray

Water sprays have proved to be effective to reduce the pressures in gas explosions. In FLACS, the effect of waterspray has only been modelled through a simple correction of the burning velocity (which will decrease due to water vapour present and may increase due to turbulence generated by the spray) The effect of volume expansion is not included.

A simple way of implementing this in FLACS is shown below. A more representative burning velocity can be found from the calculated temperature in products.

When water spray is present in the reactants, the temperature in products will decrease, since the water needs energy to be heated and evaporated. Under the assumption that the water vapour is evenly distributed and has the same temperature as the products, this new product temperature can be calculated if mass of water which will evaporate per volume gas in reactants, $\rho_{\text{water evaporated}}$ is known. The mass fraction of evaporated water in the products is then

$$\eta_{mass} = \frac{\rho_{water-evaported}}{\rho_{water-evaporated} + \rho_R} \tag{3.83}$$

The mass fraction of water in reactant may typically be 0.1. In the flame, η_{mass} may have a value of 0.03. This value will increase with time as more water is evaporated.

The formation enthalpy of the mixture with water, can be calculated from mass average of the enthalpy in the gas and in the water

$$h^w = h - \eta(h - h_{water}^{298K}) \tag{3.84}$$

The temperature in products, $T_P{}^w$, can be calculated from the formation enthalpy with equation (3.11) when the needed enthalpy constants *a*, *b* and *d* have been mass averaged, as shown for the constant a_P

$$a_P^w = a_P - \eta(a_P - a_{H_2O}) \tag{3.85}$$

The evaporated water will occupy a volume, equivalent to its mole fraction n_{vol}. The other products will have a partial pressure equivalent to the remaining mole fraction (1-n_{vol}). Both reactant and product should satisfy the ideal gas law and the pressure should be the same in both product (3.87) and reactant (3.86). The relation between mass and volume fraction of evaporated water is given by (3.88).

$$= \rho_R R T_R / M_R \tag{3.86}$$

$$P(1 - n_{vol}) = \rho_P R T_P^w / M_P \tag{3.87}$$

$$\frac{n_{vol}}{1 - n_{vol}} = \frac{M_P}{M_{H_2O}} \frac{\eta_{mass}}{(1 - \eta_{mass})} \tag{3.88}$$

With $M_P / M_{H_2O} \approx 28/18$, the volume expansion in terms of density ratios can be written as

$$\frac{\rho_R}{\rho_P} \approx \frac{T_P^w M_R}{T_R M_P}(1 + 1.6\eta_{mass}) \tag{3.89}$$

With η_{mass}=0.03, the temperature in a stoichiometric methane air mixture will drop from 2240 to 1880 K (it should be noted that nearly no CO will be left, due to the low temperature). Since M_R=M_P for methane, the volume expansion is reduced to 6.6, compared with 7.5 without waterspray.

The volume expansion will therefore decrease when waterspray is used.

The burning velocity will drop due to lower temperature in the reactant, but may in some situations have a larger increase due to turbulence generated by the droplets.

3.5 Dust explosions

The FLACS code has also been used for calculation of dust explosion. The calculation of representative volume expansion is as important as for gas explosions. The dust, which is solid, can in the code be treated as a gas with very high density (of order 10^3 kg/m^3). When treated as a gas, the density of the dust will depend on pressure, instead of being constant, but this error is not important since the dust occupies a very little fraction of the volume.

The enthalpy of formation of the dust should be known, for calculation of enthalpy and temperatures. Radiative losses are also significant in dust combustion, and will reduce the temperature and expansion of the products. In calculation of the expansion, a model for radiation may be necessary to calculate a representative temperature in the products. Dust explosions are described by Eckhoff (1991) and will in the near future be modelled and simulated by CMR in a similar way as for gas explosions.

3.6 Summary

The thermodynamics in the FLACS code has been evaluated with respect to enthalpy release due to combustion and temperature and density calculations.

FLACS-95, and earlier versions, use a too high specific heat for nitrogen. This results in underprediction of the temperature of products. In FLACS it is also assumed that fuel is converted only to H_2O and CO_2 during combustion. In the temperature range for products of an explosion, also CO, H_2 and OH will be formed. Neglection of this gives an overprediction of the temperature in products.

The fractions of CO, H_2 and OH in the products are mostly a function of temperature. FLACS therefore overpredicts the temperature when these are high (acetylene) and underpredicts it when the contents of these gases are low. For combustion of rich mixtures, FLACS-versions up to 95 have burnt all the oxygen, forming water vapour and carbondioxide. The rest of the fuel remains unburnt. This also leads to an underprediction of the temperature in rich mixtures.

Improvements and implementation of new models in FLACS, which have solved these problems, are described. Heat of combustion, as earlier used in FLACS, has been replaced by heat of formation since additional products to H_2O and CO_2 are made. Implementation of heat of formation data as function of temperature from Chemkin for actual gases in FLACS 96, secure correct temperature calculation when the products are known. The product composition of CO, H_2 and OH therefore need to be known. A model which gives the product composition, based on equilibrium constants, has been developed.

Three new gases have been included as fuels in FLACS-96, CO, CO_2 and H_2S. Gases like hydrogen, carbondioxide and carbonmonoxide can be present both in the reactants and the products. New possible products are SO_2 (when burning hydrogensulfide) and OH. When sufficient information is available for a gas (heat of formation and burning velocity) it is now quite easy to implement new gases in FLACS. Suggestions for better thermodynamics (temperature and density ratio) in calculations with waterspray are also presented. FLACS 96 is also able to handle mixtures with inert gases like nitrogen and carbondioxide.

4 Turbulence modelling

The turbulence field, described by turbulent intensity and length scale, are main factors determining the turbulent burning velocity of a flame. The strength of a gas explosion depends strongly on this burning velocity. In calculations of gas explosions with a CFD code, like FLACS, it is therefore important that representative transient turbulence fields are calculated, relatively independent of how the geometry is represented on the grid and the initial conditions of the turbulence field.

The turbulence field is calculated from the velocity field with a turbulence model. The main objective of the turbulence models is to represent the six Reynolds stresses (4.8) or the effective viscosity as (4.4) to be used in the three flow equations. The turbulence models are therefore not tailor made to give representative turbulence field to be used as input in burning velocities models in reactive flows.

The chapter starts with an overview of turbulence models and continues with a presentation of the k-ε turbulence model used in FLACS, and some of the deficiencies of the model. A overview of turbulent shear flows is followed by a presentation turbulent flows data from the EMERGE project. Thereafter follows suggestions for improvements of turbulence modelling for better handling of transient, reactive, near wall and subgrid flows. The last part of the chapter presents results from simulation of the turbulent flow experiments.

4.1 Overview of turbulence models

A review of turbulence models and their applications is given by Nallasamy (1987). Turbulence models can be classified in several ways. The most often used is that arranged in order of the number of differential equations solved for turbulence: Zero-, one-, two- and stress equation models as presented by Arntzen (1985).

- Zero equation models are mostly based on the eddy viscosity concept and give the shear stress as (4.21). They need a field of mixing length, which can be difficult to obtain in 3D complex flows.
- One equation models solves the equation for turbulent kinetic energy (4.1). They need a field of a turbulent length scale, for calculation of dissipation and effective viscosity. In rapid transient flows, one equation models with the length scale set proportional to the grid size may give more representative turbulence field than other models, as shown in Section 4.5.
- Two equation models are most widely used in present day engineering calculations. The length scale is here found from an algebraic relation with the solution of a second equation. The most popular two equation model is the k-ε model, presented in the next section.
- Stress equation models calculates the Reynolds stresses either through an algebraic relation with k, as the algebraic stress models, or by replacing the equation for k with equations for the Reynolds stresses.

4.2 *k*-ε turbulence models as used in FLACS

The convection, diffusion, production and dissipation of turbulence are most often, as in FLACS and the three other explosion codes, modelled by the *k*-ε model.

This model includes the equation for turbulent kinetic energy:

$$\frac{\partial}{\partial t}\rho k + \frac{\partial}{\partial x_i}\rho U_i k = \frac{\partial}{\partial x_i}\left(\frac{\mu_{eff}}{\sigma_k}\frac{\partial k}{\partial x_i}\right) + G_k - \rho\varepsilon \qquad (4.1)$$

and the equation for dissipation of turbulent kinetic energy:

$$\frac{\partial}{\partial t}\rho\varepsilon + \frac{\partial}{\partial x_i}\rho U_i\varepsilon = \frac{\partial}{\partial x_i}\left(\frac{\mu_{eff}}{\sigma_\varepsilon}\frac{\partial\varepsilon}{\partial x_i}\right) + G_\varepsilon - c_{\varepsilon 2}\rho\frac{\varepsilon^2}{k} \qquad (4.2)$$

where the turbulent viscosity is modelled by the Boussinesq eddy viscosity model, a relationship involving *k* and ε through:

$$\mu_t = c_\mu\rho\frac{k^2}{\varepsilon} \qquad (4.3)$$

The effective viscosity is set equal to the sum of the laminar and turbulent viscosity

$$\mu_{eff} = \mu + \mu_t \qquad (4.4)$$

The constants used in FLACS are given in the Table 4.1

Table 4.1: Constants used in the *k* ε model

$C_{\varepsilon 1}$	$C_{\varepsilon 2}$	C_μ	σ_k	σ_ε
1.44	1.92	0.09	1.0	1.3

These values are, unfortunately, not universal but have to be modified for other problems such as jets and wakes and recirculating flows. In the standard *k*-e model

$$G_k = P_k \qquad (4.5)$$

$$G_\varepsilon = c_{\varepsilon 1}\frac{\varepsilon}{k}P_k \qquad (4.6)$$

The shear generated production of turbulence

$$_k \equiv -\rho\overline{u_i u_j}\frac{\partial U_i}{\partial x_j} \qquad (4.7)$$

where the compressible Reynolds stresses in the *k*–ε model used in FLACS, is modelled as the rate of strain through the eddy-viscosity concept:

$$-\overline{\rho u_i u_j} = \sigma_{ij} = \mu_{eff}\left(\frac{\partial U_j}{\partial x_i} + \frac{\partial U_i}{\partial x_j}\right) - \frac{2}{3}\delta_{ij}\left(\rho k + \mu_{eff}\frac{\partial U_k}{\partial x_k}\right) \qquad (4.8)$$

which secure that

$$\overline{u_1^2} + \overline{u_2^2} + \overline{u_3^2} = 2k \tag{4.9}$$

The production of turbulence around obstacles occur in the shear layers downstream the objects, due to velocity gradients.

4.2.1 Deficiencies of the *k*-ε model

The *k*-ε model is not intended for use in chemical reactive flows, where large normal stresses occur, due to volume expansion from the heat release in the flame. The model is developed for steady flows and have therefore problems with transient flows as described in the next subsection. The geometry should also have a rather fine grid resolution. The *k*-ε model has therefore some limitations in a gas explosion code like FLACS, which simulates a chemical reactive very transient flow, with the geometry resolved on a coarse grid.

Due to the Reynolds hypothesis, two equation models, as the *k*-ε model have some deficiencies, Mohammadi (1994). One important deficiency is their inaccurate prediction of normal Reynolds stress anisotropies. The k-ε model does not produce secondary eddies near corners in channels with polygonal cross section (typical geometry in a module). The model is not able to distinguish between strain and shear. The turbulence in flows against a perpendicular wall (like upstream an obstacle/cylinder) is therefore overestimated. This last problem may be solved by replacing (4.7) and model the turbulence production as proportional to the product of strain and vorticity

$$P_k = \mu_{eff}\left|\frac{\partial U_j}{\partial x_i} + \frac{\partial U_i}{\partial x_j}\right|\left|\frac{\partial U_j}{\partial x_i} - \frac{\partial U_i}{\partial x_j}\right| \tag{4.10}$$

as outlined by Kato and Launder (1993), since the vorticity is zero in stagnation flows.

4.2.2 Initial conditions for *k* and ε

The initial values chosen on the turbulence field have shown to have a large influence on the development of turbulence fields in transient flows, calculated with the *k*-ε model. This model is however not made for transient flows. This difference in turbulence development also give calculated peak pressures in explosion calculations a large dependence on initial turbulence values, since the burning velocity is a function of turbulence field.

The initial turbulence field should be given representative values, as shown below. The calculated transient development should be made nearly independent of initial values. This can e.g. be done by inclusion of an extra transient term in the *k*-ε model, as presented in section 4.5. If free-stream turbulence effects are negligible, the turbulent intensity is of order 1% of the free stream velocity U_∞. k would then be $k \approx 10^{-4} U_\infty^2$ and ε should be set so the effective viscosity is of the same order as the laminar viscosity

$$\nu_t \sim 0(\nu) \sim 10^{-5}. \tag{4.11}$$

This gives

$$\varepsilon \approx C_\mu k^2 / \nu_t \approx 10^{-4} U_\infty^4 \tag{4.12}$$

The turbulent length scale, which can be specified by the FLACS user, should then be set to

$$l_t = C_\mu k^{3/2}/\varepsilon \approx 10^{-3}/U_\infty \tag{4.13}$$

When the initial velocity is zero, a satisfactorily effective viscosity can be obtained with

$$k = \varepsilon = 10^{-4} \tag{4.14}$$

which is 10% of the present default initial values used in FLACS. The high values used in FLACS results in an effective viscosity which is an order of magnitude too large in laminar flows.

4.2.3 Turbulent length scales

Different turbulent length scales are used in this thesis. The definition of some of these scales and the relation between them are therefore given below. The integral length scale in homogeneous turbulence is approximately, Townsend (1974)

$$l_I = C_I \frac{k^{3/2}}{\varepsilon} \tag{4.15}$$

where $C_I = 1/3$. Bradley (1992) uses however $C_I = 0.2$ in his burning velocity correlations. In most flows the integral length scale is direction dependent.

The mixing length scale can, when k is in local equilibrium, be shown to be

$$l_m = C_\mu^{3/4} \frac{k^{3/2}}{\varepsilon} \tag{4.16}$$

The turbulent length scale used in presentation of results from FLACS simulations is

$$l_t = C_\mu \frac{k^{3/2}}{\varepsilon} \tag{4.17}$$

The relation between these three length scale can therefore roughly be expressed as

$$l_I \approx 2 l_m \approx 4 l_t \tag{4.18}$$

4.3 Turbulent shear flows

Turbulent shear flows can be divided into three groups according to the number of fixed boundaries, Fernholz (1978).

- Free turbulent shear flows bounded by no wall, such as jets, wakes, mixing layers and plumes
- Turbulent shear flows bounded by one free and one fixed boundary, such as boundary layers or wall jets.
- Turbulent shear flows bounded by two or more fixed boundaries such as pipe, dutch and channel flows.

The flow field in a gas explosion in an offshore geometry consists of a combination of flows from mainly the first two of these groups. It is essential that the code can handle these flows, whether they are created ongrid or subgrid. A presentation of free turbulent flows and boundary layer flows and how they are modelled is therefore presented.

4.3.1 Free turbulent shear flows

The most common flows in confined gas explosions are free turbulent shear flows. They are bounded on at least one side by an ambient non-turbulent fluid. In the region between the turbulent and non-turbulent region exists an intermittency region with roughly homogenous turbulence, Townsend (1974). In the literature two-dimensional free flows are evaluated. They can be either plane or axisymmetric.

The three most common types of free turbulence is:

- a mixing layer between two streams of different velocity (typically behind a corner)
- a jet issuing into a still (or moving) stream
- a wake behind a body

The self-similar forms of these flows, shown in Table 4.2, are obtained far down stream the origin of the flow and are widely discussed in literature, White (1991) and Tennekes and Lumley(1972). Of more interest in a gas explosion is the turbulence and flow fields close to the origin of the flows. These data exists rarely in literature and had therefore to be found in the EMERGE project, as presented by Arntzen (1996) and in the next section.

The flows around ongrid represented geometry should be handled by the k-ε turbulence model. Jets and wakes downstream subgrid geometry need however subgrid turbulence modelling to produce representative turbulence fields. Mixing layers can only be created subgrid if an obstruction is subgrid and located on the wall, it will then be treated as a wake flow in FLACS.

Table 4.2: Downstream variation of U_s and l_m

	Powers of x for		$\frac{l^*}{l_m}$
	U_s	l_m	
Plane wake	-1/2	1/2	4.5
Axisymmetric wake	-2/3	1/3	4.8
Mixing layer	0	1	6.6
Plane jet	-1/2	1	6.9
Axisymmetric jet	-1	1	7.9

4.4 Turbulent flow experiments

The turbulent flow experiments done by British Gas and CMR in the EMERGE project can be used directly to validate the turbulence field produced by FLACS and other CFD codes in simulation of the experiments. They may also give information about factors as production and dissipation of turbulence, which may be used in improvement of (subgrid) turbulence models.

4.4.1 Steady flows from CMR

The flow field, including turbulent velocities, have been measured downstream several geometries in the CMR test section, as shown in Figure 4.3.

These include:

- 1 and 5 cm cylinder
- 1 and 5 cm square cylinder
- 5 cm square cylinder mounted at wall
- 5*5*5 cm^3 cuboid mounted at wall
- two 5 cm cylinders
- five 1.67 cm cylinders
- 10 cm plate
- two 10 cm plates

Flow and turbulence velocities, as well as Reynolds stresses from these experiments are stored in data files. It is therefore easy to combine data in a figure, comparing flow and turbulence field for different positions, velocities, size and shape of geometry. The data can be represented dimensionless, by dividing the downstream positions with the obstacle dimension and dividing the velocities with the free stream velocity.

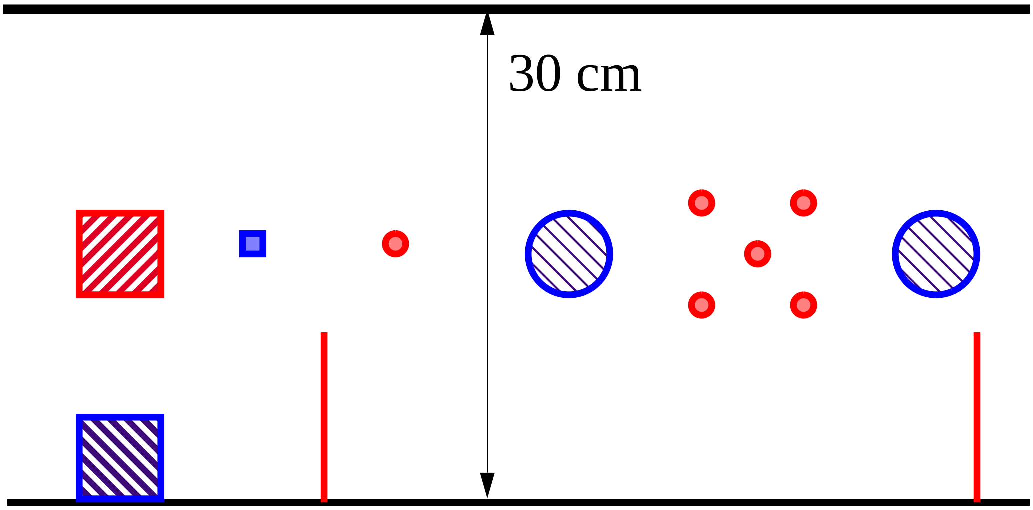

Figure 4.3 The different obstacle systems used by CMR in turbulent flow measurements

Figures 4.4 and 4.5 show dimensionless velocities and velocity fluctuations behind round cylinders and square cylinders, with diameters 1 and 5 cm (*B* is the diameter of square cylinders, *D* is the diameter of round cylinders). These figures show that for these Reynolds numbers the dimensionless velocity and turbulence field data are nearly independent of size. Experiments have also been done at other velocities, showing that the dimensionless data are independent of velocity. The influence of shape of the obstacle can also be seen. Square cylinders have a wake which is about 50% thicker than the wake from the round cylinders.

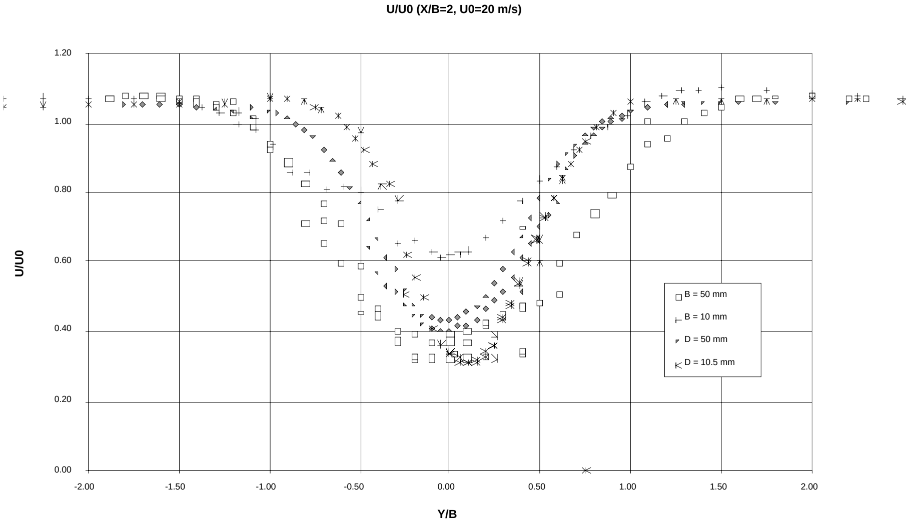

Figure 4.4 Velocity in flow direction behind cylinders in free stream

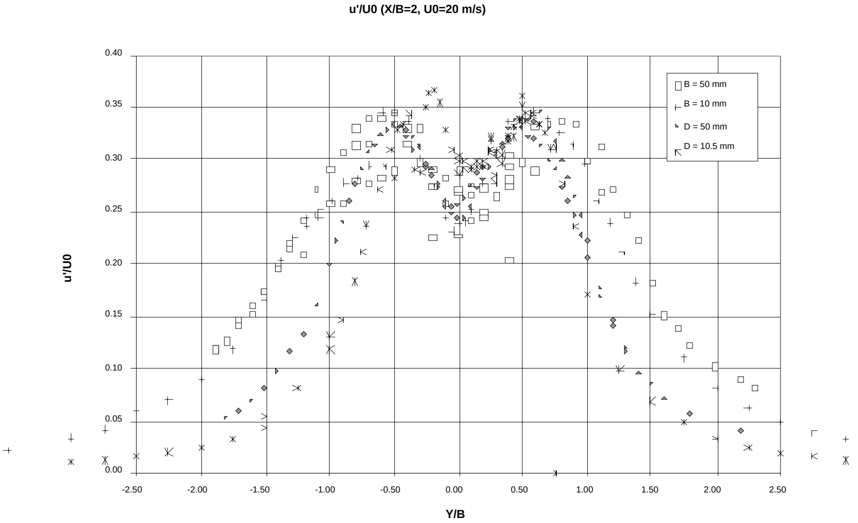

Figure 4.5 Velocity fluctuation in flow direction behind cylinders in free stream

The velocity and/or size of the experiments can therefore be scaled up, to give data for turbulence field around objects in full scale. An exception for this rule may be round cylinders at high Reynolds numbers ($Re > 3\times10^5 \Rightarrow UD > 5$) where the wake becomes much thinner and the drag drops to a quarter, due to turbulent instead of laminar separation. Obstacles with more rough surface need a lower *Re* number to have turbulent separation.

Objects other than ellipsoid and elliptical cylinders are known to have fixed separation points and drag, independent of *Re* number, White (1994). The turbulence field for these objects may therefore also be assumed independent of *Re* number. For Mach numbers, *Ma*, above 0.3 compressibillity becomes important and the local velocity near the obstacle surface may be sonic. The drag factor increase with a factor between 2 and 5, as *Ma* moves toward 1.

Flows downstream obstacles in a free stream, with steady velocity on the upstream flow, may be unsteady, with a periodic vortex shedding. The shedding occurs in the range $10^2<\mathrm{Re}<10^7$, with an average Strouhal number $fD/U \approx 0.21$. The velocity fluctuations measured in the vortex street behind cylinders therefore consist of a periodic and a turbulent compound. The periodic motion was filtered away from the flow behind the 5 cm cylinder by Kong (1995), to obtain data with turbulent velocity fluctuations.

A lot of objects like boxes and plates mounted at the wall (or floors) are also often present in geometries were explosions can occur. The measured velocity fluctuations behind such objects can be seen as turbulence, since they contain no periodic motion. The dimensionless velocity field behind obstacles mounted on the wall can be compared with those for obstacles in a free stream (where the symmetry line is similar to the wall). As can be seen in Figure 4.6, the flow is reverse in some parts of the wake, only for the obstacles mounted at the wall.

.

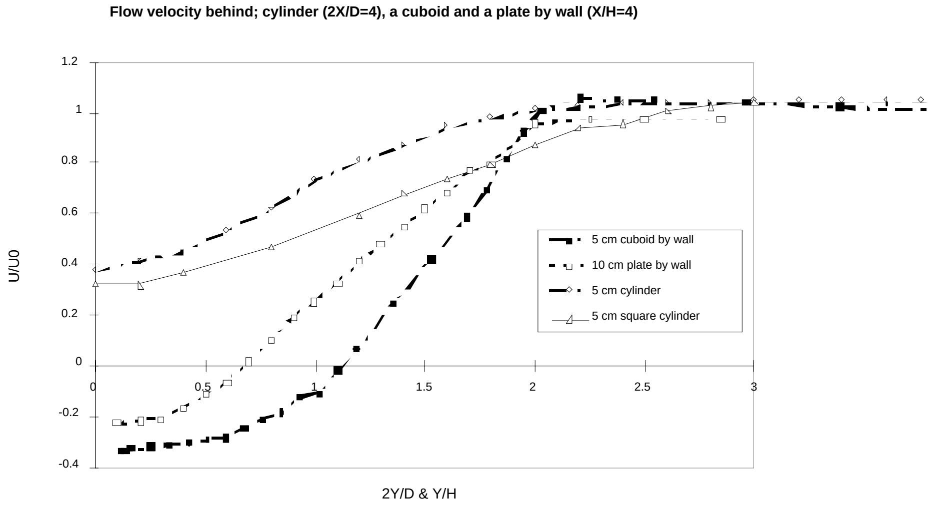

Figure 4.6 Velocity field downstream obstacles in free stream and mounted at the wall

Figure 4.7 shows that the turbulent intensity is not much different, but it is higher near the symmetry line for flows with vortex shedding. The vortex shedding causes both these differences due to transport of both momentum and turbulence to centre of the wake.

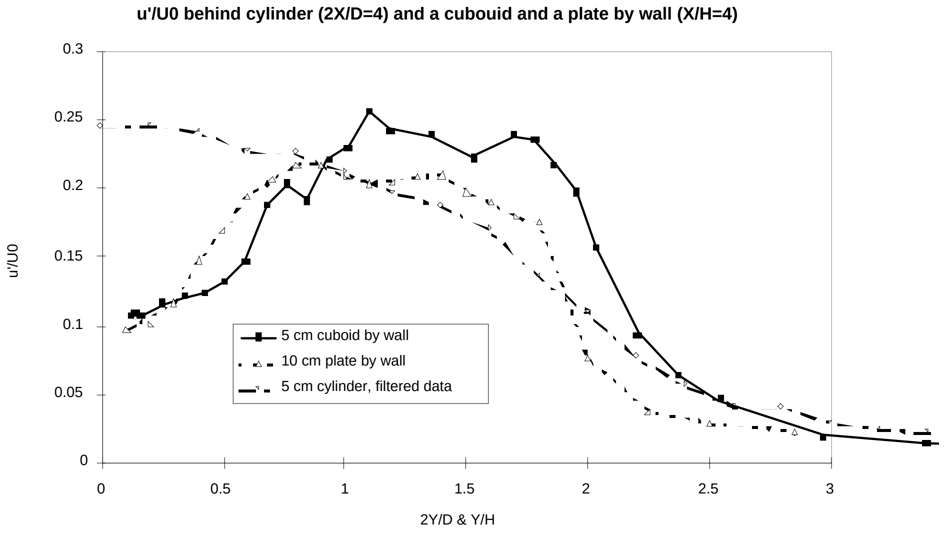

Figure 4.7 Turbulence velocity fluctuations in flow direction, behind a cylinder in free stream, and a cuboid and a plate mounted at the wall

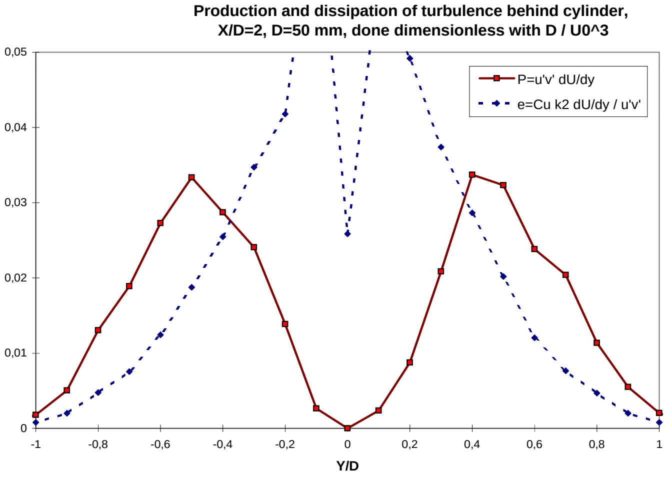

Figure 4.8 Turbulent production and dissipation 10 cm downstream a 5 cm cylinder

The production of turbulence downstream a cylinder, due to velocity gradients in flow direction may be estimated with (4.7) and the dissipation can be estimated by combining (4.3), (4.7) and (4.8), when the velocity, turbulence intensity and Reynolds stresses are known. This has been done, 10 cm downstream a 5 cm cylinder, as shown in Figure 4.8. The production, concentrated in the shear layers, seems here to be around 2/3 of the dissipation. The decay of *k*, to be used in the subgrid turbulence model, is therefore only a third of the dissipation. The turbulent integral length scale was calculated from the turbulent intensity and the dissipation with (4.14). It was found to be around 0.2D in the wake, 2D downstream the cylinder, and agree well with results from literature, as presented in subsection 4.4.4.

4.4.2 Steady flows from British Gas

British Gas (B.G.) measured velocity fluctuations behind one and two rows of cylinders and behind a MERGE geometry with 75 pipes, Rogers (1994) in the EMERGE project. As can be seen in Figure 4.9, the measured velocity fluctuations from B.G., behind two rows of cylinders, and CMR, behind two cylinders, are very similar.

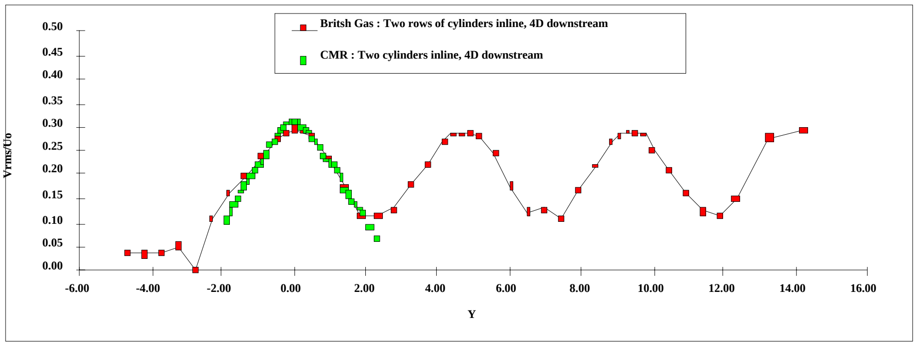

Figure 4.9 Transverse velocity fluctuation, v', 4D downstream of; 2 cylinder from CMR and 2 rows of cylinders from British Gas

From this, two conclusions can be drawn: The cylinders in a row have very little influence on each other when the pitch between them is as large as 4.65*D*, as used in these experiments (this is also the pitch of the MERGE geometries used in explosion experiments). The second conclusion is that the quality of the measurements from both institutions must be quite good since they agree well.

4.4.3 Turbulence data for subgrid modelling of turbulence

The turbulent kinetic energy, *k*, seems to have a maximum around two to three diameters downstream the cylinder. The simulated turbulent kinetic energy behind a subgrid represented obstruction must be largest in the grid cell containing the obstruction, since there is no production of turbulence farther downstream, due to lack of representation of the shear layers. The subgrid model should give similar turbulence fields as seen in experiments. A representative dissipation, which is equal to real dissipation minus the real production of turbulence is therefore needed.

4.4.4 Turbulence field data from literature

In addition to flow around a cylinder, flow over a backward facing step, is a very popular test case in turbulence modelling. Kwon and Hah (1995) include mean velocities, turbulent kinetic energy and Reynolds stresses at 10 lines downstream a backward facing step. These data can be used to estimate length scales and dissipation, as well as in validation of turbulent flow simulations.

White (1991) describes a range of complex flow test cases where experimental data exists. They were presented on the 1981 Stanford Conference on Complex turbulent flows where a range of CFD codes / turbulence models were tested. Some of these tests may also be used for validation of explosion codes like FLACS.

A far field solution (X>100D) exists for the wake behind a cylinder, as described by Tennekes and Lumley (1990).

$$k = k_0\left(1 + g\frac{X}{D}\right)^{-1} \tag{4.19}$$

$$l = l_0\left(1 + g\frac{X}{D}\right)^{1/2} \tag{4.20}$$

$$\varepsilon = \varepsilon_0\left(1 + g\frac{X}{D}\right)^{-2} \tag{4.21}$$

Closer to the cylinder this solution is less valid. However, with the filtered data from experiments with flow around the 50 mm round cylinder: g=0.2, k_0=0.18 and ε_0=0.038. These formulas and values may be used in evaluation and improvement of subgrid turbulence models.

Turbulence behind grids have been used in determination of the constants in the k-ε model, since both diffusion and production of k is zero downstream the grid. Roach (1987) describes the turbulence field downstream a grid by

$$\frac{u'}{U} = C\left(\frac{X}{D}\right)^{-5/7} \tag{4.22}$$

$$\frac{v'}{U} = \frac{w'}{U} = 0.89\frac{u'}{U} \tag{4.23}$$

with C=0.80 for round wires and C=1.13 for square bars

$$\frac{k}{U^2} = 1.3C^2\left(\frac{X}{D}\right)^{-10/7} \tag{4.24}$$

Streamwise and normal component measurements of integral length scales gives

$$l_t^X/D = 0.20(X/D)^{1/2} \text{ and } l_t^Y/D = 0.10(X/D)^{1/2} \tag{4.25}$$

showing a relatively high degree of isotropy.

The grating floor in an offshore module is a grid with D around 0.005 m. The turbulent energy downstream and close to the grid may be high, but 1 m downstream it is reduced to less than 1‰, according to (4.23). This high decrease should be included in sub grid turbulence models. In the new sub grid turbulence model the decrease will be included if the D is used in description of the obstacle diameter in the representation of the grated floor for the code.

4.5 Transient turbulent shear flows

The modelling of transient turbulence field should give turbulence fields which are representative for the transient turbulence buildup independent of grid resolution and initial values. The time it takes to develop a turbulence field behind an obstruction should typically be proportional with the obstruction flow time (flow velocity divided with flow size perpendicular to the flow direction).

4.5.1 The *k*-ε model in transient flows

The time it takes to develop a turbulence field behind obstructions in simulations with the standard *k*-ε model has however shown to be a function of the ratio of initial to final turbulent length scale, and the grid flow time (flow velocity divided with grid size). Another conclusion on the buildup time for turbulence in simulation was that the build-up time was nearly independent of initial turbulent velocity and time step length.

Simulations with an initial mixing length around 0.2 grid cell (l_m around 0.2Δ) give rapid turbulence buildup. Typical grid size used in offshore module explosion calculations is 0.4 to 1.0 m, but a representative initial mixing length, from (4.15) and (4.13), is only 1 mm. Improvement in the grid resolution to the mixing length level will increase the number of grid cells with a factor of 10^6. An increase in initial mixing length is therefore a better solution, but will lead to an initial viscosity 100 times larger than the laminar.

The use of a *k* model with a constant l_m around 0.2Δ in the hole calculation domain, or on all solid walls through wallfunctions (wf_2 in FLACS), also give the same rapid turbulence buildup. These two methods give less chance for divergence in solutions than the one above since the length is bounded. Behind subgrid geometry the length scale and viscosity will be overestimated and the dissipation of turbulence will be underestimated. Subgrid geometry in calculations represents a large part of the obstructions in an offshore module, so a better solution should be found for this use. In calculations with no subgrid geometry both methods are a good solution for securing rapid and stable turbulence build-up.

The reason for the slow build-up of the turbulence field can be found from the sources term linearizations of production and dissipation in the modelled turbulence equations. Due to numerical stability, Patankar (1980), positive sources are modelled with the constant part and negative sources (sinks) with the dependent part in $S_\phi = S_C + S_P\phi$ which is inserted into (2.15). The production is therefore modelled with viscosity (4.3) from previous time step

$$S_C = P_k^{n+1} \sim \frac{(k^n)^2}{\varepsilon^n} \tag{4.26}$$

The dissipation is however a sink which is modelled with *k* from the same time step

$$\varepsilon^{n+1} = k^{n+1}\frac{e^n}{k^n} = \phi S_P \tag{4.27}$$

This leads to an underestimation of the production and a overestimation of dissipation when the initial length scale is small compared with the final, and is the main reason for the corresponding slow turbulence build up. However it secure stable solutions.

Parts of the production term was in some test simulations moved from the constant part, S_C, to the dependent part S_P (which still was kept negative, as required). This led to a rapid turbulence buildup, but in some situations the solutions became unstable and led to divergence and non existing turbulence field. Another method, which secures more initial condition independent turbulence buildup, had therefore to be found.

Problems with too slow build-up of turbulence has also been seen in other CFD codes, e.g. by Pritchard et al. (1996) in their calculation of explosions in geometries which were resolved on the grid. With a standard k-ε model, they obtained pressures which were an order of magnitude lower than seen in experiments. They conclude that in some geometries, like their, there is not sufficient shear present to dominate the turbulence production. They have therefore tried to solve the problem by adding two extra turbulence generation terms, where one is due to Rayleigh-Taylor instability at the flame front, to obtain higher (faster buildup of) turbulence levels which results in higher pressures.

4.5.2 Transient turbulence in experiments

An indication on how the transient turbulence fields should develop may be fond from experimental results. As reported by Arntzen (1996) the turbulence intensity measured by CMR in explosion driven transient flows, were lower than expected from results in steady flows. In these transient flows behind a cylinder, Kong (1996) did not measure the mean velocity gradients. Lindstedt and Sakthitharan (1995) and Bjørkhaug (1986) have presented velocity and turbulence profiles, at several positions downstream a sharp obstacle with height, h in their explosion driven transient flows. A dimensionless thickness of the shear layer can then be found from the velocity gradients

$$l_* = \left(\frac{\Delta U}{h}\right) \Big/ \left(\frac{\partial U}{\partial y}\right)_{max} \tag{4.28}$$

where ΔU is the velocity difference over the shear layer. For these transient flows, the thickness is

$$l_* = \frac{x}{3h} \tag{4.29}$$

where x is the distance downstream the obstacle. This is the same as measured in steady flows behind a sharp obstacles by Kong (1996). Since the shear layer has the same thickness in the steady and transient situation, also the turbulent viscosity as well as the velocity gradients should be similar. The product of turbulent viscosity and the velocity gradient is modelled as the turbulence production, which also should be similar in transient and steady flows.

The maximum turbulent velocity measured by Lindstedt et al. (1995) was 10% of the flow velocity, calculated from velocity measurements in time windows of 0.5 ms. (Kong used 1.0 ms) The short time windows used for calculation of turbulence results in losing the high energy low frequency turbulence. The real turbulence is therefore probably significantly higher, as shown by Bjørkhaug (1986), who found that the maximum turbulent velocity was larger than 30% of the flow velocity.

In steady flows, turbulent velocities around 30% of the flow velocities were measured.

The dimensionless shear layer thickness behind a backward facing step is $l_* = \frac{1}{2}(x/h)^{0.6}$ and behind a quadratic box located by a wall $l_* = x/2h$

4.5.3 Modelling of the transient turbulence buildup

The best way found in securing a rapid enough build-up of the turbulence field in geometries which includes both ongrid and subgrid geometry, was to include a large enough minimum value for the turbulent production $P_{k,min}$. This method is nearly independent of initial conditions and grid resolution.

In the initial phase of an explosion, as the shear layers are built up, they may be much thinner than the numerical grid, also behind objects resolved on the grid. A model which represents this layer and secure a rapid buildup of the turbulent length scale, l_m is needed. The turbulence production in a shear layer located in a grid cell can be found through integration of (4.7)

$$P_k \approx \frac{1}{\Delta y}\int_{\Delta y} -\overline{u'v'}\frac{\partial U}{\partial y}\partial y \tag{4.30}$$

Pradtls mixing length concept gives the relation between the shear stresses and the mixing length

$$-\overline{u'v'} = l_m^2\left|\frac{\partial U}{\partial y}\right|\frac{\partial U}{\partial y} \tag{4.31}$$

which can be inserted to the production expression

$$P_k \approx \frac{1}{\Delta y}\int_{\Delta y} l_m^2\left|\frac{\partial U}{\partial y}\right|^3\partial y \tag{4.32}$$

From Schlichting (1968) the mixing length can be assumed proportional to the width of the mixing layer in wakes, jets and shear flows. Tennekes and Lumley (1972) give the relation for the thickness of the mixing layer

$$l_* = (\Delta U)/\left(\frac{\partial U}{\partial y}\right)_{max} \tag{4.33}$$

as function of maximum velocity gradient and difference in flow velocity through the shear

$$l_m/l_* = f' \tag{4.34}$$

where *f'* is 0.22 for a plane wake and 0.16 for a plane jet or a mixing layer (from Table 4.2).

$$P_k \approx \frac{1}{\Delta y}\int_{l_*} l_m^2\left(\frac{\partial U}{\partial y}\right)_{max}^3\partial y \approx \frac{1}{\Delta y}\int_{l_*} l_m^2\left(\frac{\Delta U}{l_*}\right)^3\partial y = \frac{\Delta U^3 f'^2}{\Delta y} \tag{4.35}$$

$$P_k \approx 0.04\frac{\Delta U^3}{\Delta y} \tag{4.36}$$

This term is independent of the initial turbulence field, but always smaller than the steady state production and independent of grid resolution of the shear layer. This term can therefore be used as a minimum value for shear generated turbulence.

To avoid generation of turbulence upstream objects (a weakness of the k-ε model) the modified production term (4.10) is used. In 3D this modified minimum turbulence production can be modelled as in FLACS by

$$P_{k,\,min} = \left|\Delta y^2\left(\frac{\partial U}{\partial y}\right)^3 - \Delta x^2\left(\frac{\partial V}{\partial x}\right)^3\right| + \left|\Delta z^2\left(\frac{\partial U}{\partial z}\right)^3 - \Delta x^2\left(\frac{\partial W}{\partial x}\right)^3\right| + \left|\Delta z^2\left(\frac{\partial V}{\partial z}\right)^3 - \Delta y^2\left(\frac{\partial W}{\partial y}\right)^3\right| \tag{4.37}$$

where the velocity gradients are modelled with the sum of absolute values of velocity gradients on both sides of the cell centre. This is done to secure representation of the velocity gradient (and turbulence production) in the wake of an obstruction represented with one grid cell. In the wake behind such obstructions the velocity gradients on both sides of the centre line will often be equal but with opposite sign so a pure summation gives no gradient and no turbulence production, as seen in simulations shown in subsection 4.10.1. The gradients are modelled as:

$$\left(\frac{\partial U}{\partial y}\right)^3 = \frac{1}{2}\left\{\left|\frac{\partial U}{\partial y}\right|_n^3 + \left|\frac{\partial U}{\partial y}\right|_s^3\right\} \tag{4.38}$$

$$\left|\frac{\partial U}{\partial y}\right|_n = \left|U_{Nw} + U_{Ne} - U_{Sw} - U_{Se}\right| / 2\Delta y \tag{4.39}$$

With porosities included the gradients are modelled by

$$\left(\frac{\partial U}{\partial y}\right)_n = ((\beta_{Nw}U_{Nw} + \beta_{Nw}U_{Ne})\beta_n - (\beta_{Nw}U_{Sw} - \beta_{Nw}U_{Se})\beta_s) / 2\Delta y \tag{4.40}$$

4.5.4 Simulation of transient build up in an ongrid turbulence field

In evaluation of the transient buildup of turbulence, a range of factors was evaluated. These were the effects of initial conditions, time step length, turbulence model, the numerical implementation and the discretization of the turbulent production source term. The results of this evaluation was reported previously in this section.

The transient turbulent flow experiment, reported earlier in this section, was done at a small scale which is not very representative for the scales in an offshore module. The experiment was simulated by inserting the measured transient upstream velocity as a boundary condition in the simulations. Due to influence of turbulence initial conditions (the initial and steady state scale were similar), the turbulence was built up representative on this small scale, but the time used to build up the turbulence field increased largely when the scale of the obstruction and grid was increased, as shown by Arntzen (1996).

Transient flows over a plate, as shown in Figure 4.10 have also been analysed. The simulated results shown in Figure 4.11 are all from a point located at x = 2.4 m and y = 1.25 m.

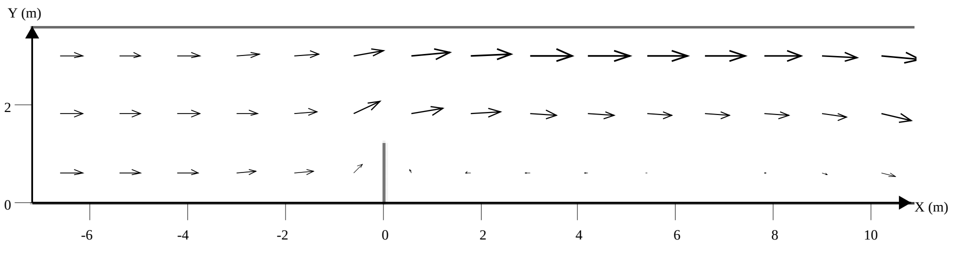

Figure 4.10 Flow over a 1.2 m high plate, location of coordinate system

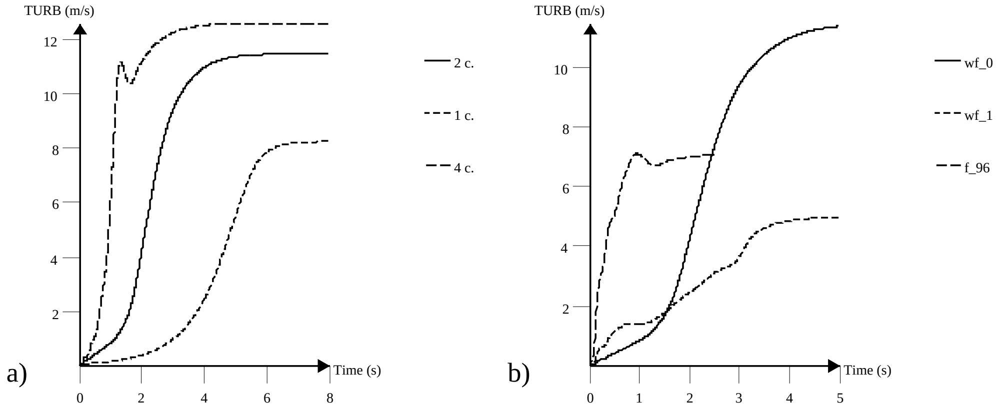

a: Plate resolved with 1, 2 and 4 cells, w.f. = 0

b: Plate resolved with 2 cells, w.f. = 0 and 1, and FLACS-96

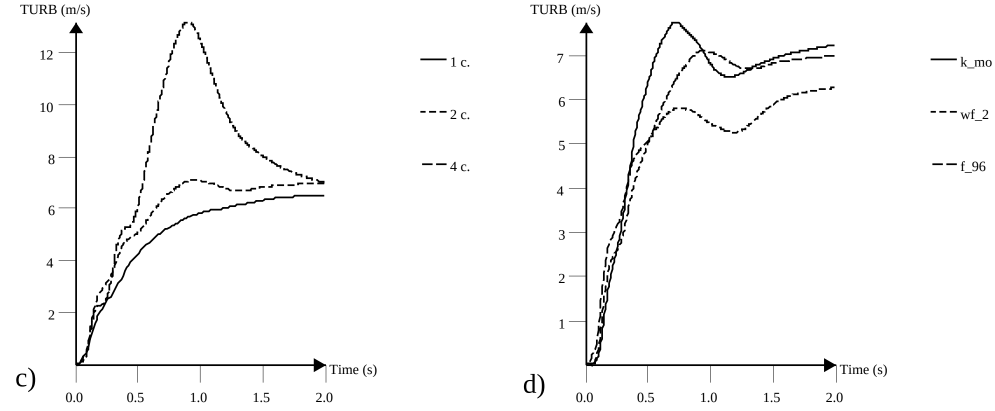

c: Plate resolved with 1, 2 and 4 cells, FLACS-96

d: Plate resolved with 2 cells, k model, w.f. 2 and FLACS-96

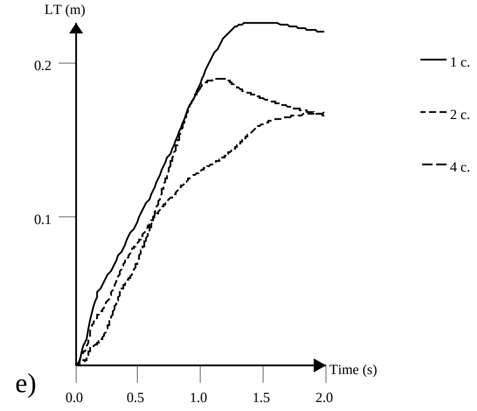

e: Plate resolved with 1, 2 and 4 cells, FLACS-96

Figure 4.11 Turbulence velocity fluctuation and length scale in a point 2.4 m downstream the plate, for different boundary conditions and resolutions of the plate

The transient build up of the turbulence field behind a 1.2 m high plate in a 3.6 m high 2D channel was investigated with different grid resolutions. The plate height was resolved with 1, 2 and 4 grid cells, with grid cell size 1.2, 0.6 and 0.3 m. Initial mixing length was 5 mm. Differences in turbulence modelling included use of wall functions. They give a fixed mixing length scale on solid walls, which is around 2% and 20% of the grid size for respectively “wf_1” and “wf_2”. “wf_0” is calculations without wallfunctions. The *k* model, “k_mo”, has a constant mixing length equal to 20% of the grid size and “f_96” use the minimum production term from last subsection.

The flow field which gave the turbulence field in Figure 4.11 was made by increasing the flow velocity at the left boundary from 0 to 20 m/s from time 0 to 0.1 s. Another way of measuring the turbulent build-up time is to have the turbulence model switched off in a steady flow, and turn the model on at a specified time.

Figure 4.11a shows the influence of grid resolution on the turbulent velocity. The time needed by the traditional *k*-ε model for the build up of the turbulence level is proportional to the ratio grid cell size to initial mixing length. It was also seen that this time is inverse proportional with the flow velocity. From these results it is shown that the time it takes to build up the turbulence field, when the ratio of obstruction size to initial mixing length is around 200, is similar to the time it takes for the flow to pass through about 60 grid cells.

Figure 4.11b shows the influence of wallfunctions. “wf_2” secures a rapid build-up, in contrast to the two other. “wf_1” has a more rapid initial build-up in the beginning than “wf_0” since it initially has a larger mixing length on walls, but later it develops slower, since the length on walls then are lower.

Figure 4.11c shows calculations done with the minimum production term $P_{k,min}$ (f_96) for different grid resolutions. The turbulence field develops rapidly for all three resolutions. The build up time is about the time it takes for the flow to pass through a distance equal to 5 plate heights.

.

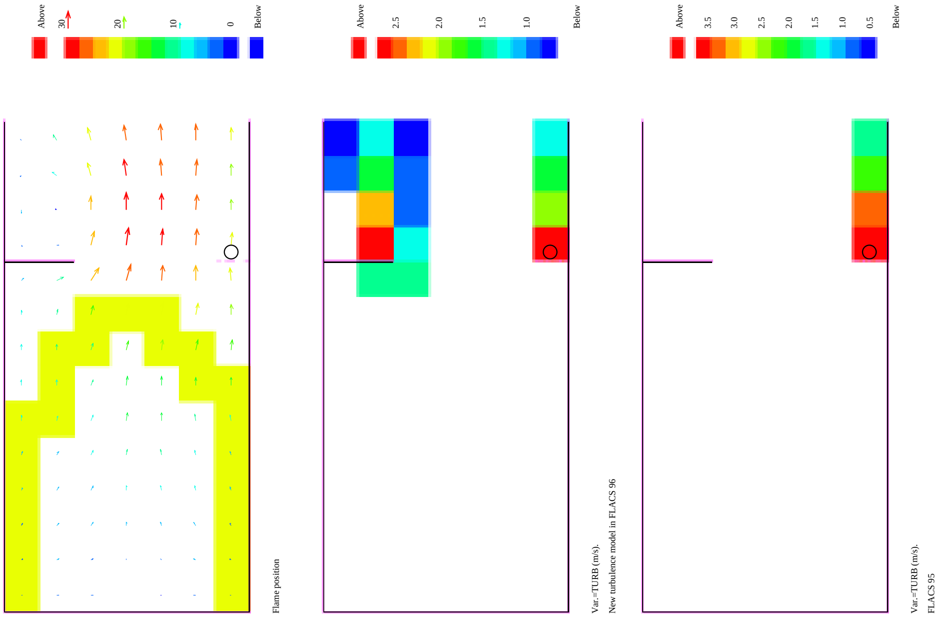

Figure 4.12 Flame position, turbulent fluctuation and length

Figure 4.11d shows three methods which all secure a rapid build up of the turbulence field; The k model (k_mo), wall functions (wf_2) and the minimum production term (f_96). All three models gave about the same buildup time. The first two methods are recommended when no subgrid geometry is present. The third method should be used when subgrid geometry (subgrid generated turbulence) is present. In calculations with only subgrid and no ongrid geometry no methods are required to secure a rapid turbulent build-up.

Figure 4.11 e shows the turbulent length scale $_{lt}$ for the same calculations as Figure 4.11c, with the minimum production term. It seems to take about 50% longer time to develop the turbulent length field, compared with the turbulent velocity field. The turbulent length scale in transient simulations can therefore be some what too small. This should be taken into account when the length scale is used for calculation of burning velocities in transient explosion calculations. The slowly build-up of the length scale is due to a too rapid build up of the dissipation, ε. Several attempts were done to secure a rapid length scale build up, like not including $P_{k,min}$ in (4.6). This gave a rapid buildup, but resulted sometimes in divergence of the solution. A more numerical stable method should therefore be found.

The turbulence build-up will be some what different in other points, for other resolutions, other obstruction sizes and behind other obstructions than shown in Figure 4.11. Several other points, resolutions, sizes and obstructions (cylinders) have, however, also been studied and this point, obstruction and scale, and these resolutions are believed to be representative.

The difference in transient behaviour for calculations done with and without the transient turbulence production term is shown in Figure 4.12. The left figure shows flame position and velocity vectors in a box, where the reactant was ignited at the bottom. The centre and right figures show the turbulent intensity at the same time as in the left figure, calculated with and without the transient term respectively. The subgrid turbulence production model created a turbulence field behind the subgrid resolved cylinder in both cases. The ongrid k-e model produced significant turbulence behind the ongrid resolved plate, only when the transient term was included in the turbulence model

4.6 Reactive flows

The k-ε turbulence model is not intended for reactive flows. It should therefore be used with caution and eventually include modifications in reactive flows like gas explosions. The effect of dilatation on the turbulence field has been discussed by Chomiak et al. (1995), Bray (1996) and Grimsmo (1991). Bray (1996) has multiplied the turbulent viscosity with the density ratio ρ/ρ_R to avoid negative k in his calculation with premixed flames in stagnation turbulence. For more general situations as those we have, this is however not helpful.

The turbulent kinetic energy should increase during compression and decrease during expansion. The numerical effect of expansion due to combustion in the k-ε turbulence model is, however, that the turbulence level increases, if the turbulent time scale is above a time scale based on the velocity gradient in the cell, and decreases opposite, as is shown below.

The fluid stresses in the turbulence production term consists of both shear and normal stresses, which is modelled by velocity gradients. If the flame is one dimensional and propagates in the x direction, the velocity gradients may be expressed as:

$$\frac{\partial U_i}{\partial x_j} = \begin{pmatrix} \frac{U}{\Delta}, i = j = 1 \\ 0, else \end{pmatrix} \tag{4.41}$$

where Δ is the grid cell size and U the velocity difference on the two cell faces, due to expansion caused by combustion. The production term for k, (4.7) and (4.8) is then

$$P_k = \frac{2}{3}\frac{U}{\Delta}\left(2\mu_t\frac{U}{\Delta} - \rho k\right) = \frac{2}{3}\frac{U}{\Delta}\rho k\left(2C_\mu\frac{k}{\varepsilon}\frac{U}{\Delta} - 1\right) = \frac{2}{3}\frac{U}{\Delta}\rho k\left(1.66\frac{l_t}{u'}\frac{U}{\Delta} - 1\right) \tag{4.42}$$

which is below zero when

$$\frac{l_t}{u'} < 0.6\frac{\Delta}{U} \tag{4.43}$$

and above zero opposite. The negative turbulence production can be up to twice the dissipation ε (when $\varepsilon\Delta = 2C_\mu kU$) and thereby reduce the turbulent energy considerably. The positive turbulent production due to dilatation and high turbulent time scale can in contrary, incorrectly increase the turbulent energy considerably.

For a flame propagation in a diagonal direction, the velocity gradients in cells containing the flame will be represented by

$$\frac{\partial U_i}{\partial x_j} = \frac{U}{2\Delta} \tag{4.44}$$

where U is the velocity difference between the two cell faces. The production term (4.7) calculated over the flame will in addition to the normal stresses also include shear stresses.

$$P_k = \frac{U}{\Delta}\left(\frac{3}{2}\mu_t\frac{U}{\Delta} - 2\rho k\right) = 2\frac{U}{\Delta}\rho k\left(0.41\frac{l_t}{u'}\frac{U}{\Delta} - 1\right) \tag{4.45}$$

Comparing (4.39) and (4.42) shows that the only difference between flames propagating in diagonal and x direction is that the change from negative to positive turbulence production occur for a higher turbulent time scale for the former.

The turbulent length scale l_t is typically 10% of obstacle dimension. If the obstacle is resolved ongrid, then $l_t > 0.1\Delta$. The velocity ratio may typically be $U \approx 10u'$. When the β flame model is used instead of SIF, the expansion in each cell, U, is smaller, typically a third compared to the velocity difference between reactants and products used for SIF, since the β flame is several grid cells thick. The large length scales which will give a positive turbulence production occur typically in the wake of large objects. The largest unphysical turbulent productions are however found in situations with a flow (e.g. a leakage) into the geometry before the explosion. A turbulent flow field will then be set up. When the flow field is stopped, the turbulent intensity will decrease and the length scale will increase with time. The turbulent time scale (and turbulence production) will therefore increase with delay time between stop of flow and ignition. This is seen in FLACS calculations in e.g. the M24 module, where peak pressure incorrectly increases with this delay time due to the increase in turbulence production.

The turbulent burning velocity has been found experimentally as a function of turbulent parameters in the reactant. The production of turbulence due to shear and normal stresses, calculated from velocity gradients over the flame, must be eliminated, since it is the turbulent parameters in unreacted gas which determine this burning velocity.

Several methods can be used. The simplest is to set the velocity gradients over the flame equal to zero. This results in no shear or normal stress generated production if the flame is present in the grid cell. The shear stresses calculated from neighbour cells containing the flame must also be annulated. This method results in some decay of turbulence in the flame cells. This decay can be avoided by freezing the turbulence field as long as the flame is present in the cell. In calculations of explosion experiments the two methods gave similar results, so the first method was chosen in FLACS.

When the flame is represented with SIF in FLACS, the shear is set to zero when the flame is present in the cell. When the flame has moved to the next cell due to combustion, the flame is not present, but there will still be an expansion. There will however be no combustion in this cell so the mistake will be small. When the β-flame model is used, the reaction rate of fuel can be used to decide if flame is present in a cell or not.

Figure 4.13a shows the product concentration for a SIF flame propagating with constant burning velocity in positive x direction, which results in an expansion and constant flow velocity, *U*, ahead of the flame. (PROD=0 is reactants and PROD=0.28 is products) Figure 4.13b shows the turbulent intensity, TURB, for the same flame location in a calculation with initial turbulence field represented by the ratio $(Ul_t)/(u'\Delta) = 2$. This gave a 3 times increase of turbulent intensity in the products.

When the ratio was 0.4, 0.8 and 4, the turbulent intensity increased 0, 0.8 and 6 times, about as expected. Lower values of the ratio gave a decrease in turbulent intensity. Figure 4.13c shows the turbulence intensity when the shear was set to zero in cells containing the flame as described above. This resulted successfully in nearly no change of turbulent intensity through the flame.

In FLACS calculations with the β model in the M24 geometry (*P*=0.08 barg) the peak pressures increased with 5% when the dilatation was switched off in the turbulence equation. However, in the highly densed SCI module, the peak pressures were higher in some points and lower in others, but the pressure top arrives 30% later. The impact of dilatation on calculated turbulence fields and peak pressures are therefore geometry dependent.

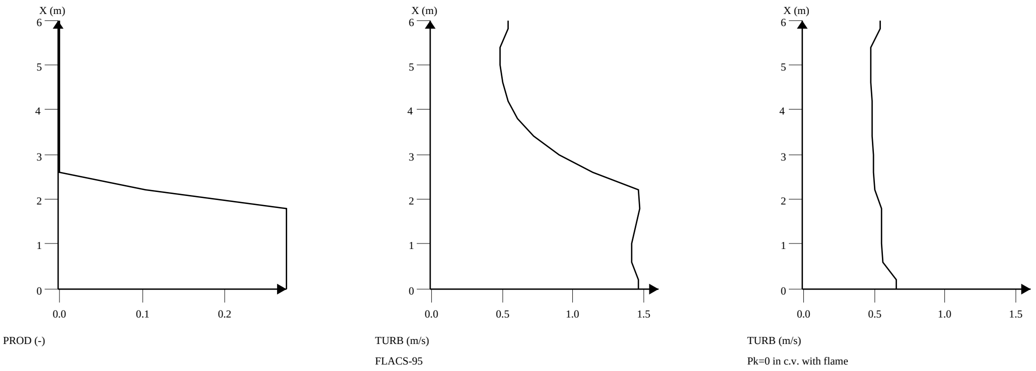

Figure 4.13 Flame propagating in 1D channel with burning velocity 1 m/s (give U=7 m/s)

4.6.1 Production of turbulence due to buoyancy

The generation of turbulence due to buoyancy, Rodi (1986), is

$$G_g = -\beta g_i \overline{u_i \varphi} \tag{4.46}$$

where β is a volumetric expansion coefficient and φ is a fluctuating scalar quantity. It is modelled in FLACS, through a Boussinesq assumption for buoyant flows, assuming small density changes in the flow as a function of turbulent viscosity, the gravity constant, g, and the density gradient

$$G_g = -\frac{\nu_T}{0.9} g \frac{\partial \rho}{\partial z} \tag{4.47}$$

This will lead to a positive production when hot gas is located below cold gas, and negative production when opposite. In a cell with reactants on top and products on bottom (4.47) gives

$$G_g \approx 6u' l_m / \Delta z \tag{4.48}$$

This model should not include velocity gradients over the reactant-product interface, similar to the situation for production due to normal stresses when the flame is present in the cell.

A quasi laminar flame is observed to burn faster upwards, due to instabilities, caused by a cold gas above a hot gas. This effect will not be included by (4.47), since the turbulent viscosity in the reactant around a quasi laminar flame is small.

4.7 Boundary layer flows

4.7.1 Representation with wall functions

Wall functions are used mainly because the numerical resolution of the thin near-wall layers with step gradient need large computer resources and the standard *k*-ε model is not applicable in this viscosity-affected region. Instead of resolving this region, the first grid point away from the wall is placed outside the viscous sub-layer. Basically, wall functions relate the velocity as well as the turbulence parameters *k* and ε at the first grid point to the friction velocity and lean heavily on the assumption of a logarithmic velocity distribution and validity of local equilibrium of turbulence (production = dissipation) at this point.

These assumptions are generally not valid for separated flows, Cordees et al. (1993). Wall functions involving the friction velocity are of course particularly unsuited for separation and reattachment regions where the friction velocity change sign. The law of the wall in the logarithmic overlap layer give the wall-friction velocity, u^*

$$u^* \equiv (\tau_w / \rho)^{1/2} \tag{4.49}$$

$$\frac{U_\infty}{u^*} = \frac{1}{\kappa} ln \frac{y u^*}{\nu} + 5 \tag{4.50}$$

With the viscosity and grid cell size normally used for gas explosion calculations inserted

$$\frac{U_\infty}{u^*} \approx 20 \tag{4.51}$$

The dimensionless wall distance can for gas explosion calculations be approximated by

$$y^+ \equiv \frac{yu^*}{\nu} \approx 3000 y U_\infty \tag{4.52}$$

With normal grid cells in FLACS, Δy>0.1, the cell centre is in the outer turbulent layer (outside the viscous wall and overlap layers) for velocities above 1 m/s and outside the viscous sublayer for velocities above 0.1 m/s. This shows that the boundary layer occupies only a small fraction of the wall grid cells. The effect of uniform wall roughness k_r was investigated in experiments by Nikuradse, which showed there is no viscous sublayer if

$$k_r / \nu > 1300 \Rightarrow U k_r > 0.02 \tag{4.53}$$

which is the normal situation in a gas explosion e. g. with U=20 m/s and k_r=1 mm. The turbulence field given by wall functions in the gas explosion calculations may therefore not be representative for the real turbulence field. The turbulence field made by the wallfunctions in the FLACS and MUSIC codes have therefore been analysed.

The wall shear expressions, used in FLACS as well as in MUSIC are two layer models

$$\tau_w = \left[\begin{array}{cc} \rho \nu U_P / y_P & y_P^+ \le y_\nu^+ \\ C_\mu^{1/4} \rho \kappa U_P k_P^{1/2} / ln(E y_P^+) & y_P^+ > y_\nu^+ \end{array}\right] \tag{4.54}$$

The generation of turbulence in the viscous sublayer is zero. The wall generation in a cell is then

$$P_k^w = -\rho \int_V \overline{u_i u_j} \frac{\partial U_i}{\partial x_j} dV = \frac{1}{y_e} \int_{y_\nu}^{y_P} \left(\tau_w \frac{\partial U}{\partial y} \right) dy \approx \frac{0.02}{y_e} \rho U_P^2 k_P^{1/2} \tag{4.55}$$

In the wall functions in FLACS, the dissipation is assumed to have the following distribution as function of distance from the wall, Chieng and Launder (1980), Sand and Bakke (1989).

$$\varepsilon(y) = \left[\begin{array}{cc} 2\nu k_\nu / y_\nu^2 & y \le y_\nu \\ \kappa k^{3/2} / y & y_\nu < y \le y_P \\ \varepsilon_P + y(\varepsilon_E - \varepsilon_P)/(y_E - y_P) & y_P < y \end{array}\right] \tag{4.56}$$

where k_ν is a function of k_P and k_E. The average dissipation in a typical grid cell, with y_P>y_ν, $k_P \approx k_E$ and $\varepsilon_P \approx \varepsilon_e$ is found from integration over the cell

$$\bar{\varepsilon}_k = \frac{1}{y_e} \int_0^{y_e} \varepsilon(y) dy = \frac{\kappa}{y_P} k_P^{3/2} ln(y_P^+ / E) \tag{4.57}$$

In MUSIC the average dissipation is assumed as in Melaaen (1990) and Hjertager (1986)

$$\bar{\varepsilon}_k = \frac{\kappa}{y_P} k_P^{3/2} ln(E y_P^+) \tag{4.58}$$

The small difference between these two approaches is located in the assumption for $\varepsilon(y)$ for $y < y_v$. These average dissipations correspond to a small mixing length scale, as also seen in simulations

$$l_m \approx 0.1\kappa y_P \tag{4.59}$$

A dissipation is also needed for calculation of a turbulent viscosity, which is used in calculation of both shear generated turbulence production and turbulent diffusion. The turbulent viscosity is calculated as

$$\overline{\mu_t} = \frac{C_\mu}{y_e}\int\frac{k^2}{\varepsilon}dy \approx \frac{C_\mu k_P{}^2}{y_e}\int\frac{dy}{\varepsilon} = \frac{C_\mu k_P{}^2}{y_e\overline{\varepsilon_\mu}} \tag{4.60}$$

The dissipation $\overline{\varepsilon_\mu}$ which will give a representative turbulent viscosity is then

$$\overline{\varepsilon_\mu} = y_e \Big/ \int_0^{y_e}\frac{dy}{\varepsilon} = y_e \Big/ \int_0^{y_e}\frac{y\,dy}{\kappa k_P^{3/2}} = \frac{2\kappa k_P^{3/2}}{y_e} \tag{4.61}$$

$$\overline{\varepsilon_\mu} = \frac{\kappa k_P^{3/2}}{y_P} \tag{4.62}$$

This dissipation is an order of magnitude smaller and corresponds to a mixing length scale which is an order of magnitude larger compared with $\overline{\varepsilon_k}$

$$l_m = \kappa y_P \tag{4.63}$$

The dissipation equation is not solved in the wall grid cells, instead it is given a value which should secure a representative turbulent viscosity. Hjertager (1986) and Melaaen (1990) and thereby MUSIC use $\overline{\varepsilon_k}$ in the k equation and give $\overline{\varepsilon_\mu}$ as the fixed value in the dissipation equation, for calculation of the turbulent viscosity. This seems to be the best solution, as indicated above. Both White (1991) and Cordes (1993) use $\overline{\varepsilon_\mu}$, in both cases.

In FLACS $\overline{\varepsilon_k}$ is used both places. This results in a too low turbulent viscosity and thereby too low turbulent diffusion and shear generated turbulent production. In FLACS 96 it is therefore also possible to use the same model as in MUSIC, by changing the value of WALLF from “1” to “22” in the cs-file or in CASD.

Wall functions may be a good alternative for flow over a flat plate, and when the purpose of the turbulence field is to estimate e. g. the heat transfer through the wall. In complex flow, where turbulence is generated behind both subgrid and ongrid geometry, turbulence with length scales different of those from wall functions would be created.

The wall functions, with a fixed length scale will therefore typically give too high dissipation of ongrid generated turbulence and too low dissipation of subgrid generated turbulence.

Two alternatives to wall functions are possible near solid walls.

- Implementation of a low Reynolds number extension, where the coefficients in the original k-ε model are modified to take into account the near-wall damping effects. This is easy to implement, but require a very fine mesh near the walls in order to resolve the strong gradients.
- Development of a new subgrid model for boundary layer flows which fulfils the needs for wall modelling in complex geometries, as presented in the next section

Table 4.3: Values for the constants in the wall functions for smooth impermeable walls

κ	E	y_v^+
0.4187	9.0	11.63

4.7.2 Subgrid modelling of boundary layer flows

Wall functions are mostly used in situations where heat transfer between the wall and flow is important. The turbulent parameters obtained from wall functions will therefore support a representative heat transfer. In a gas explosion, a representative burning velocity is much more important than the heat transfer near walls. The wall model for gas explosions must therefore give turbulence field which result in representative burning velocities near walls.

The boundary layer thickness is also small compared with the grid cells present in gas explosion calculations. Wall functions give a representative turbulence field only when grid cells are located in the boundary layer. They should therefore be replaced by a subgrid model which represents the average turbulence field in the boundary layer and outside. The turbulent displacement thickness is given by Blasius, Olson (1980), as

$$\delta^* = 0.048 x Re_x^{-1/5} \approx 0.005 x^{4/5} U^{-1/5} \tag{4.64}$$

which is less than 10% of the grid cell size Δx in practical gas explosion modelling (x<40Δx, U>1 m/s). The boundary layer $\delta = 8\delta^*$ is turbulent for $Re_x > 4\times10^5 \Rightarrow Ux > 3$, which is normal in practical gas explosion situations. In small scale explosion experiments the boundary layer can however be laminar. The turbulent kinetic energy in the boundary layer over a wall (flat plate) have been measured in experiments for $Re_x \approx 10^7$, where

$$\delta = 0.16 x Re_x^{-1/7} \approx 0.016 x \tag{4.65}$$

In FLACS calculations, the flow distance, x, will not be known, but may be estimated as $x \approx 10\Delta x$, then $Re_x \approx 10^6 \Delta x U$ and the boundary layer thickness is

$$\delta \approx 0.02 x (U\Delta x)^{-1/7} \tag{4.66}$$

around 2% of the flow distance. On a smooth wall, (White, 1991), the turbulent energy in the boundary layer decreases with the distance, y, from the wall

$$k = 0.006(1 - y/\delta)U^2 \tag{4.67}$$

The turbulent energy in the boundary layer is therefore proportional with the boundary layer thickness, where it has the average value

$${}_{\delta} = \alpha_{\delta} U^2 \tag{4.68}$$

where the constant α_δ is around 0.003 for a smooth and 0.007 for a rough wall, Rodi (1993). The mixing length is proportional to the distance to the wall near the wall

$$l_m = \kappa y \tag{4.69}$$

and proportional to the boundary layer thickness farther from the wall

$$l_m = 0.09\delta \tag{4.70}$$

The model for the turbulent energy production in boundary layer grid cells, should give representative values which secure a representative turbulent burning velocity. The turbulent energy may be proportional to the ratio boundary layer thickness to grid cell size

$$k = \frac{\delta}{\Delta y} k_\delta \approx 0.02 \frac{x}{\Delta y} (U \Delta x)^{-1/7} k_\delta \tag{4.71}$$

The turbulent energy (and burning velocity) will then be too low in the boundary layer and too high outside. The increase of k with distance (from the increase in boundary layer thickness) is

$$\frac{\partial k}{\partial x} \approx \frac{0.02}{\Delta y} (U \Delta x)^{-1/7} k_\delta \tag{4.72}$$

The dissipation of k, (4.2) and (4.6), has a maximum value when the production of ε is equal to the dissipation of ε

$$c_{\varepsilon 1} P_k = c_{\varepsilon 2} \varepsilon \Rightarrow \varepsilon = 0.75 P_k \tag{4.73}$$

This can be used to find P_k from the gradient of k in the 1D steady k equation

$$U \frac{\partial k}{\partial x} = P_k - \varepsilon \approx 0.25 P_k \tag{4.74}$$

$$P_k \approx 4U \frac{\partial k}{\partial x} \approx \alpha_\delta \frac{0.08}{\Delta y} U^3 (U \Delta x)^{-1/7} \tag{4.75}$$

These values for production and dissipation agree with those reported by Rodi (1993) for the turbulent energy balance in the boundary layer. The turbulent energy in boundary layers are only 10% of the energy in free shear flows for the same free stream velocity. The boundary layers are also normally much thinner than e. g. wakes behind obstruction. The turbulence generated in boundary layers are therefore only important in geometries with a large wall area and few obstructions.

Figure 4.14 shows the turbulence field calculated on a flat plate with 0.5 m grid cells and flow velocity 20 m/s, calculated with wall functions and new subgrid model on walls. The new subgrid model on walls gives correctly turbulent energy and length scale which is proportional with flow distance (boundary layer thickness) as seen in experiments, White (1991). The wall function gives a fixed length scale and a high turbulent energy, which is only valid inside the boundary layer, and not representative for the hole grid cell.

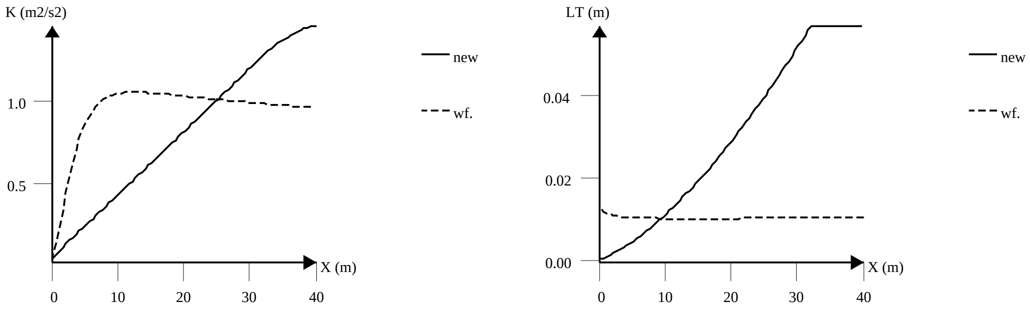

Figure 4.14 Turbulence field from wall function (wf.) and new wall subgrid model (new)

4.7.3 Maximum turbulent length scale close to walls

The mixing length scale has a maximum value near walls, proportional to the distance between the wall and the grid cells centre

$$l_m < \kappa \Delta y \tag{4.76}$$

A corresponding minimum dissipation, ε^*, can then be found, with $\kappa \approx C_\mu^{3/8} \approx 0.4$ and (4.15)

$$\varepsilon^* \geq \frac{\kappa k^{3/2}}{\Delta y} \tag{4.77}$$

The following production term in the ε equation secures this minimum value on wall boundaries

$$\frac{k}{\varepsilon} P_\varepsilon = max\left(c_{\varepsilon 1} P_k, Fk\left(2\frac{\varepsilon^*}{\varepsilon} - 1\right) + c_{\varepsilon 2}\varepsilon^*\right) \tag{4.78}$$

This leads to the following steady ε equation near walls when the diffusion is small

$$F(\varepsilon_2 - \varepsilon_1) = P_\varepsilon - c_{\varepsilon 2}\varepsilon_2{}^2 / k_2 \tag{4.79}$$

$$(c_{\varepsilon 2}\varepsilon_2 + 2Fk_2)(\varepsilon_2 - \varepsilon^*) = \varepsilon_1 F k_2 \tag{4.80}$$

$$F = \sum \beta_{i,\,in} U_{i,\,in} / \Delta x_i \tag{4.81}$$

Four special cases can be investigated, the first with no flow, the others with different values on the upstream dissipation

$$F = 0 \Rightarrow \varepsilon_2 = \varepsilon^* \tag{4.82}$$

$$\varepsilon_1 = 0 \Rightarrow \varepsilon_2 = \varepsilon^* \tag{4.83}$$

$$\varepsilon_1 < \varepsilon^* \Rightarrow 1 < \varepsilon_2 / \varepsilon^* < 1.5 \tag{4.84}$$

$$\varepsilon_1 > \varepsilon^* \Rightarrow \varepsilon_2 > \varepsilon^* \tag{4.85}$$

In all four situations the dissipation will as shown be larger than the minimum value, ε^*. This new source is to some degree similar to Yap's correction to the ε equation, Leschziner (1991)

4.8 Subgrid modelling of turbulence

Subgrid turbulence models are used to generate turbulence from subgrid objects. When the obstacles in a geometry are smaller than the grid, the velocity gradients in the wakes behind them are not resolved, so the shear generated production term in the k-ε model will not give turbulence production.

Subgrid turbulence models generate normally turbulence in the grid cell where the obstacle is located. Downstream the obstacle there is no production, since the velocity gradients are not resolved. The dissipation at a position downstream an obstacle, should therefore ideally be equal to real dissipation minus real production in the position. The dissipation is inverse proportional to the turbulent integral length scale (4.16). The length scale behind an obstacle represented subgrid must therefore be larger than the length scale behind the same obstruction represented ongrid, with production of turbulence in the wake due to velocity gradients.

4.8.1 Turbulence field behind subgrid objects

The experiments presented in section 4.4 show that the turbulent energy in a plane downstream an obstruction is proportional with the obstruction area in the flow direction and the flow velocity squared. The turbulent energy also depends on the shape of the obstruction and is therefore similar to the relation for drag loss due to an obstruction.

The turbulence kinetic energy in the first grid cell downstream subgrid obstructions, if no turbulence is present upstream, may be set equal to the maximum k in a plane downstream the obstructions, which is about 2D downstream a cylinder. For a grid cell, with transverse dimension Δy, this k^* may be expressed as

$$k^* = \frac{a}{2} C_D n \frac{d}{\Delta y} U_\infty^2 \tag{4.86}$$

where C_D is the drag factor, d is the diameter and n is the number of obstructions. In a 3D flow

$$k^* = a\left(\sum (T_i U_i^2)^2\right)^{1/2} \tag{4.87}$$

with T_i given by (2.2) and the constant a is in the range 0.15 - 0.45, depending on factors as whether vortex shedding and the value of the turbulence fluctuation in the third direction, should be included or not. If the subgrid model should give representative turbulent energy at the measured positions 2D and 4D downstream the obstructions, a is typical 0.5. The energy will then be too high closer to the cylinder since the subgrid model gives the highest energy around the cylinder. It is therefore recommended to use the lower a which results in a representative k closer to the cylinder.

The dissipation at this position, ε^*, can be specified in two ways. Which of them to choose depends on whether one wants to give priority to the turbulent length scale or the decay of turbulence. With the first alternative, the turbulent length scale can be set to a fraction (e.g. 10%) of the obstacle dimension, d. The dissipation will with (4.16) be

$$\varepsilon^* = \frac{C_\mu}{0.1d} k^{*1.5} \approx \frac{1}{d} U^3 (aT_x)^{1.5} \tag{4.88}$$

The dissipation can also be estimated from the decay of turbulence found in the experiments described in subsection 4.4.1

$$\varepsilon^* = \frac{b}{d}T_x U^3 \tag{4.89}$$

For a 3D flow

$$\varepsilon^* = b\left(\sum (T_i U_i^3 / d_i)^2\right)^{1/2} \tag{4.90}$$

where the constant *b* was found in the experiments to be around 30% of the constant *a*. This dissipation is the sum of real dissipation and production, and should be representative since the production downstream a subgrid object is zero, since the velocity field behind the subgrid object is not resolved.

Instead of the turbulence, *k** and ε*, the turbulent flow per volume, *Fk** and *F*ε*, behind an obstruction will often represent the turbulence production better, especially when the subgrid object is large with corresponding low area porosity and flow rate. For 3D flows they can be specified as

$$Fk^* = a\left(\sum\left(\frac{T_i U_i^3}{\Delta x_i}\right)^2\right)^{1/2} \tag{4.91}$$

$$F\varepsilon^* = b\left(\sum\left(\frac{T_i U_i^4}{\Delta x_i d_i}\right)^2\right)^{1/2} \tag{4.92}$$

This method of combining the compounds from the three directions secures that the turbulence production is a function of absolute value of the velocity and independent of directions for flows past a cylinder. This is true also for square cylinders, where a 45 degree flow has a $\sqrt{2}$ greater area, but a drag factor equal to $2^{-1/2}$ compared with a 0 degree flow.

When turbulence is present in the upstream flow, the downstream turbulence will also be influenced by the upstream turbulence values, in addition to what is produced in the cell.

4.8.2 Influence of *Re* and *Ma* numbers on turbulence production

The turbulence production and the drag from an obstruction are both functions of flow velocity and the width of the wake behind the obstruction. For circular cylinders the drag factor drops from 1.2 to 0.3 for $Re > 3\times10^5$ (or $UD > 5$ in air) due to movement of the separation points, which results in a much thinner wake. This drag drop occurs for lower Reynolds numbers if the flow is turbulent. The turbulence production would probably have the same drop as the drag, since the wake becomes thinner.

The drag is also influenced of Mach number, *Ma*, as shown by White (1994), and increase for *Ma*>0.4, partly due to formation of shock waves. For *Ma*=1, a circular cylinder has drag factor 2.0, independent of *Re.*

These effects have not been included in the subgrid turbulence model, so the turbulence production will probably be overestimated for high Reynolds numbers, and underestimated for high Mach numbers. However these two numbers increase together so the total effect is normally not known.

4.8.3 Analytical analysis

The performance of a subgrid turbulence production model may be evaluated based on an analytical solution of the turbulence model with the subgrid production terms. The equations for k and ε for a constant density flow are

$$\frac{\partial k}{\partial t} + \frac{\partial}{\partial x_i} u_i k_i = \mu_t \frac{\partial^2}{\partial x_i^2}(k_i) + P_k - \varepsilon \tag{4.93}$$

$$\frac{\partial \varepsilon}{\partial t} + \frac{\partial}{\partial x_i} u_i \varepsilon_i = \mu_t \frac{\partial^2}{\partial x_i^2}(\varepsilon_i) + P_\varepsilon - c_{\varepsilon 2}\frac{\varepsilon^2}{k} \tag{4.94}$$

A simple analysis of the subgrid turbulence generation model has been done, as presented below. In a steady situation the first term in both equations are zero. The ratio of convective to diffusive terms, the Peclet number, *Pe*, is normally much larger than one since $l_m < \Delta x_i$ in a grid cell with subgrid geometry.

$$Pe \equiv \frac{u_i \Delta x_i}{\mu_t} \approx 9\frac{u_i \Delta x_i}{u' l_m} \gg 1 \tag{4.95}$$

The steady state turbulence transport equations can then be reduced and discretized to

$$F\Delta k = P_k - \varepsilon \tag{4.96}$$

$$F\Delta\varepsilon = P_e - c_{\varepsilon 2}\varepsilon^2 / k \tag{4.97}$$

where F is the volume flow rate per volume entering and leaving the grid cell

$$F = \frac{1}{\beta_V}\sum_{in}\frac{\beta_i u_i}{\Delta x_i} = \frac{1}{\beta_V}\sum_{out}\frac{\beta_i u_i}{\Delta x_i} \tag{4.98}$$

The subgrid turbulence model, with upstream turbulence values on the flows through the cell faces, can then be reduced to and analysed from the following two discretizated equations

$$F(k_2 - k_1) = P_k - \varepsilon_2 \tag{4.99}$$

$$F(\varepsilon_2 - \varepsilon_1) = P_\varepsilon - c_{\varepsilon 2}\varepsilon_2^2 / k_2 \tag{4.100}$$

where *1* indicates the value upstream and on the inflow face, and *2* indicates the value in the cell and on the outflow face.

4.8.4 Subgrid turbulence energy generation model

In FLACS the subgrid turbulence production has been related to the drag formulation, assuming that a fraction a of the drag loss is converted to turbulence (a=0.5 has been used).

$$P_k = \frac{a}{2} C_D n \frac{d}{\Delta x} U^2 F \approx \frac{1}{2} T_x U^2 F \tag{4.101}$$

where the flow is given by (4.98), $F = U / \Delta x$.

In the k-ε model the relation between the turbulent energy and dissipation production is

$$P_\varepsilon = c_{\varepsilon 1}\frac{\varepsilon}{k}P_k \tag{4.102}$$

(4.102) was also used for the subgrid turbulence production model in FLACS and gave, when inserted into the ε equation

$$Fk_2(1-\varepsilon_2/\varepsilon_1) = c_{\varepsilon 1}P_k - c_{\varepsilon 2}\varepsilon_2 \tag{4.103}$$

Combining these two, gives a second order expression for ε_2

$$(C_{\varepsilon 2}-1)\varepsilon_2^2 + (P - C_{\varepsilon 1}P + Fk_1 + \varepsilon_1)\varepsilon_2 - (Fk_1 + P)\varepsilon_1 = 0 \tag{4.104}$$

After inserting $C_{\varepsilon 1} = 1.44$ and $C_{\varepsilon 2} = 1.92$ from Table 4.1, the model can be analysed as shown by Arntzen (1996), where the equation system was analysed by looking at some special cases. If both k_1 and ε_1 are small, as with the initial values of 10^{-3} for k and ε, they can be neglected and (4.104) reduced to

$$(C_{\varepsilon 2}-1)\varepsilon_2 + (1 - C_{\varepsilon 1})P_k = 0 \tag{4.105}$$

It follows then that 48% of the generated turbulent energy dissipates in the first cell. (4.106). The rest, 52% is transported downstream to the next cell (4.107).

$$\frac{\varepsilon_2}{P_k} = \frac{(C_{\varepsilon 1}-1)}{(C_{\varepsilon 2}-1)} = \frac{11}{23} = 0.48 \tag{4.106}$$

$$\frac{Fk_2}{P_k} = 1 - \frac{\varepsilon_2}{P_k} = \frac{13}{23} = 0.52 \tag{4.107}$$

Inserting P_k from (4.101) into (4.107) gives the turbulence energy as function of grid cell size,

$$k_2 = 0.26U^2T_x \tag{4.108}$$

which is in agreement with the experiments, represented by (4.87). The dissipation rate from (4.107) is however inverse proportional with the grid size in flow direction

$$\varepsilon_2 = 0.24U^3T_x/\Delta x \tag{4.109}$$

instead of with the obstacle diameter as found in (4.88) and (4.89). The dissipation rate will only be representative for $\Delta x \approx 10d$. For larger objects the dissipation will be too large. The turbulent length scale given by (4.17) will due to the dissipation dependence also be grid dependent

$$l_t = C_\mu\frac{k_2^{3/2}}{\varepsilon_2} = 0.09\frac{(0.26U^2T_x)^{3/2}}{0.24U^3T_x/\Delta x} = 0.05\Delta x T_x^{1/2} \tag{4.110}$$

This subgrid turbulence model gives therefore a turbulent length scale which is proportional to cell size in the flow direction and the square root of the blockage, instead of on obstacle diameter. This length scale will therefore be underpredicted for small T_x.

The left part of Figure 4.15 shows the turbulence fields generated behind a single cylinder at two grid resolutions, with the subgrid energy model. These simulations verify the results found theoretically above, that the turbulent dissipation and length are very grid dependent, and the turbulent energy is not. Since no representative length scale is obtained with this model, the length scale obtained must not be used in the turbulent burning velocity model.

Since no length scale information is included in this model, a single object and a row of ten objects, both with the same area blockage, will give the same turbulence field. They should produce the same turbulent energy, but the turbulent length scale downstream them should be proportional with the smallest object dimension perpendicular on the flow direction.

Another test is to investigate the turbulence field obtained if subgrid geometry (subgrid turbulence production) is present in a range of cells located after each other in the flow direction. The dissipation of turbulence reaches after a short distance a maximum value, $\varepsilon_2 = \varepsilon_1$. From (4.103) this maximum value is given by (4.111) and is expressed by (4.112).

$$c_{\varepsilon 1} P_k - c_{\varepsilon 2} \varepsilon = 0 \tag{4.111}$$

$$\varepsilon_{max} = \frac{c_{\varepsilon 1}}{c_{\varepsilon 2}} P_k = \frac{3}{4} P_k \tag{4.112}$$

Since this dissipation is less than the turbulence generation in each cell, the turbulent length scale and energy will increase for each cell. The minimum turbulent energy increase per cell is

$$F \Delta k_{min} = P_k - \varepsilon_{max} = P_k / 4 \tag{4.113}$$

and the turbulent length is proportional with $k^{3/2}$ since ε is constant, ε_{max}. This development is also seen in simulations. In Figure 4.16 this turbulent velocity and length is labelled *f95.*

This is totally wrong. Turbulence does not add up in this way. When a flow is passing several grids, the turbulence field will soon reach a maximum value and be similar downstream each grid, since turbulence is produced in the shear layers downstream the obstructions.

This model will typically lead to too high turbulent intensity and length scale fields when the geometry includes subgrid geometry in a range of grid cells. The main problem with this model is that the production of dissipation is a function of the turbulence field. It must be independent of this field, like the production of turbulent energy, if a satisfactory turbulence field should be obtained.

A very simple solution to the last problem is to set a maximum value for the turbulent length scale. In FLACS 96, $l_{t,\,max} = 0.16 \Delta x$, has been implemented as a preliminary solution. This is however not a good solution since the length scale behind objects larger than a grid cell may be much larger.

4.8.5 Subgrid turbulence production with fixed length scale

An alternative to subgrid modelling of both turbulence equations is to solve only the k equation in cells with subgrid obstructions. The value on ε may be given through (4.15), with l_m , taken as a function of obstacle dimension (typically 10%). This method was used by Sha and Launder (1979) in modelling of flows in large rod bundles.

In a geometry with homogeneous distribution and size of obstructions this model is a good concept, which e.g. was used in several codes for calculation of explosions in MERGE geometries, Popat et al. (1996). In a 1D flow with obstruction and turbulence production in every cell, the turbulent energy will reach a maximum when $\Delta k = 0$ and $P_k = \varepsilon$, since the length scale is given. With (4.16) inserted for ε

$$k_{max}^{3/2} = P_k l_t / C_\mu \tag{4.114}$$

This fixed length scale is however not a good solution when large scale turbulence passes a grid cell with only one very small obstacle. The turbulence will then wrongly be converted to small scale turbulence, with high dissipation. Too little turbulence will then be present downstream this cell.

4.8.6 Subgrid turbulence energy and length generation model

A subgrid turbulence model, which gives a representative turbulence field behind one as well as several subgrid obstacles is needed.

A better production of turbulence which will give a more representative and more grid independent turbulence field can be achieved by using a P_ε which is independent of the turbulence field and give a dissipation and length scale which is a function of obstacle dimension instead of grid size in flow direction. Since the model shall give representative turbulent length scales, it is called a subgrid turbulence energy and length generation model.

The two equations for k and ε, (4.100) and (4.101), can be combined to the following second order equation for ε_2

$$(C_{\varepsilon 2} - 1)\varepsilon_2^2 + (k_1 F + P_k + \varepsilon_1 + P_\varepsilon / F)\varepsilon_2 - (k_1 F + P_k)(\varepsilon_1 + P_\varepsilon / F) = 0 \tag{4.115}$$

P_k and P_ε can be found from a situation with low upstream k_1 and ε_1, $k_1 \approx \varepsilon_1 \approx 0$. The resulting turbulence field should then be $k_2 = k^*$ and $\varepsilon_2 = \varepsilon^*$. The value for P_k is found with these data inserted into (4.100)

$$P_k = F k^* + \varepsilon^* \tag{4.116}$$

The second order equation for ε_2 (4.115) with low (zero) ε_1 and k_1 is reduced to

$$(C_{\varepsilon 2} - 1)\varepsilon_2^2 + (P_k + P_\varepsilon / F)\varepsilon_2 - P_k P_\varepsilon / F = 0 \tag{4.117}$$

with the expression for P_k (4.116) inserted, this equation is reduced to

$$P_\varepsilon = F\varepsilon^* + \varepsilon^* \frac{\varepsilon^*}{k^*} C_{\varepsilon 2} \tag{4.118}$$

The production terms (4.116) and (4.118) secure the specified values k^* and ε^* when there is low turbulence upstream. The second term in both productions are compensations for the dissipations in the cell, since the values in the cell is wanted to be the one upstream the cell, instead of downstream.

The turbulent length scale will be proportional with the obstruction diameter if the dissipation is given by (4.88). With k^* and ε^* from (4.87) and (4.89), both are proportional with the ratio obstacle blockage to grid size, T_i. Since the length scale is proportional to $k^{1.5}/\varepsilon$, they give together a length scale proportional to both the obstruction diameter and the square root of T_i.

$$l_t = C_\mu \frac{k^{1.5}}{\varepsilon} = d\frac{a}{b} C_\mu (aT)^{1./2} \approx 0.2 d T^{1/2} \tag{4.119}$$

In experiments the integral length scale was found to be around 0.2d, then $l_t = 0.05d$, from (4.17). The length (4.119) will therefore be overestimated for T above 0.1.

The right part of Figure 4.15 shows that this energy and length generation model gives representative turbulence energy, *K*, dissipation, *EPS*, and length, *LT*, in the field downstream a single object, independent of grid resolution.

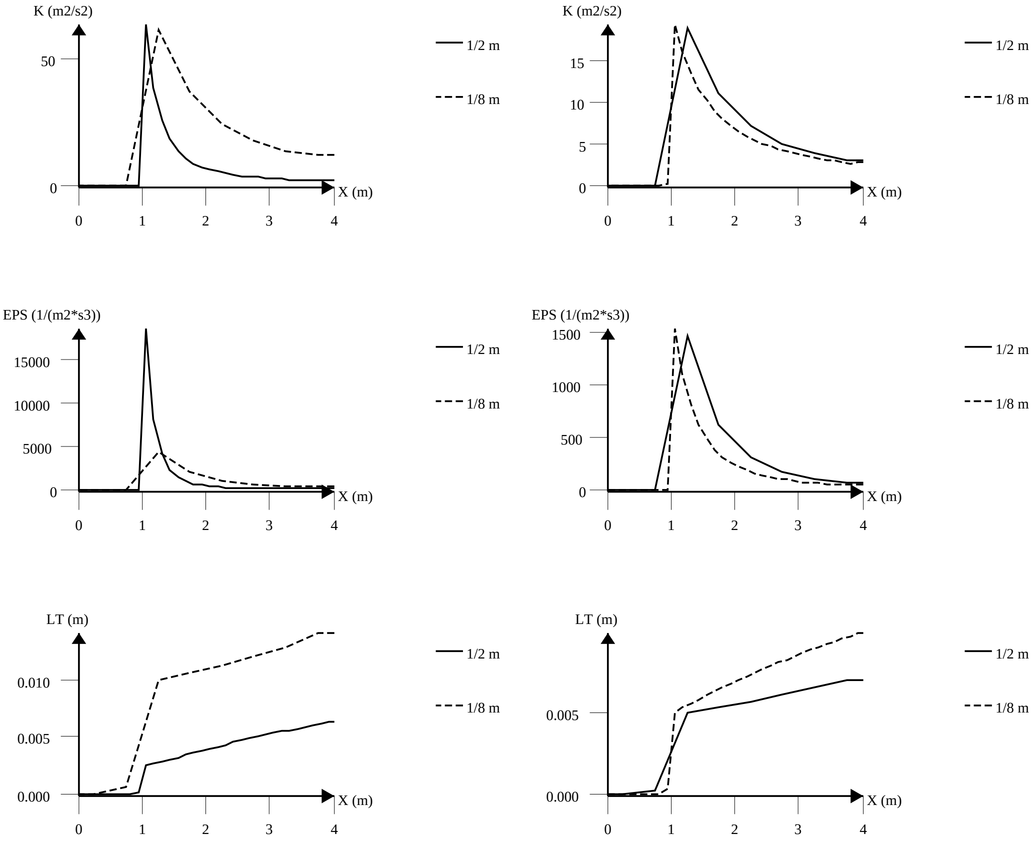

Figure 4.15 Turbulence field downstream subgrid geometry for two different grid sizes in the flow direction. Left: subgrid energy model. Right: subgrid energy and length model

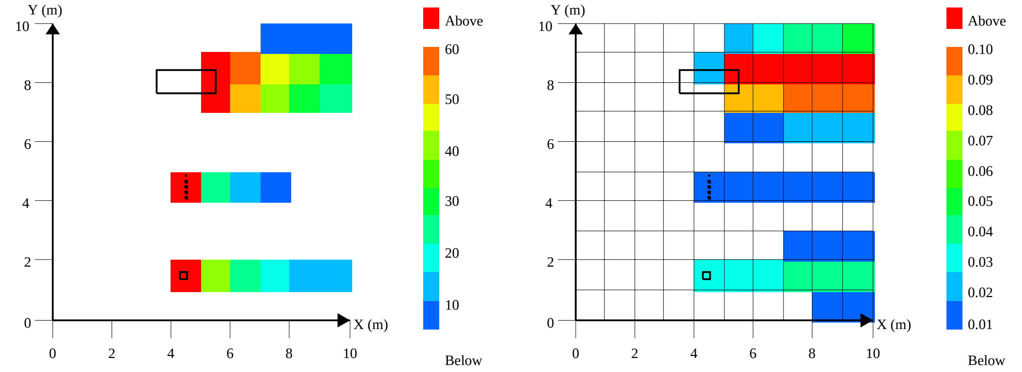

Job=800700. Var.=K (m2/s2).

Time=3.0044 (s). IJ plane, K=1

Job=800700. Var.=LT (m).

Time=3.0044 (s). IJ plane, K=1

Figure 4.16 Turbulent energy and length from objects with equal subgrid blockage

In a 1D flow with obstruction and turbulence production in every cell, the turbulent dissipation and energy will reach a maximum where $\Delta k=0$ and $\varepsilon_{max}=P_k$. Then from (4.118)

$$P_\varepsilon = c_{\varepsilon 2}\frac{\varepsilon_{max}^2}{k_{max}} \Rightarrow k_{max} = c_{\varepsilon 2}\frac{P_k^2}{P_\varepsilon} \tag{4.120}$$

The turbulent intensity and length scale in such an obstruction field in simulations are shown in Figure 4.17, labelled *f96*. Both reach a maximum within 5 grid cells (5 m). Also after the obstructions (10 m) the turbulence field has a correct development, with decrease in intensity and increase in length scale.

In flows where high length scale turbulence is passing a cell with a single small obstruction, only the turbulence generated in this cell will have a small length scale. The turbulence field downstream should therefore be representative. The turbulence field, including length scale, obtained with this model is representative and should therefore be used as input for the turbulent burning velocity model.

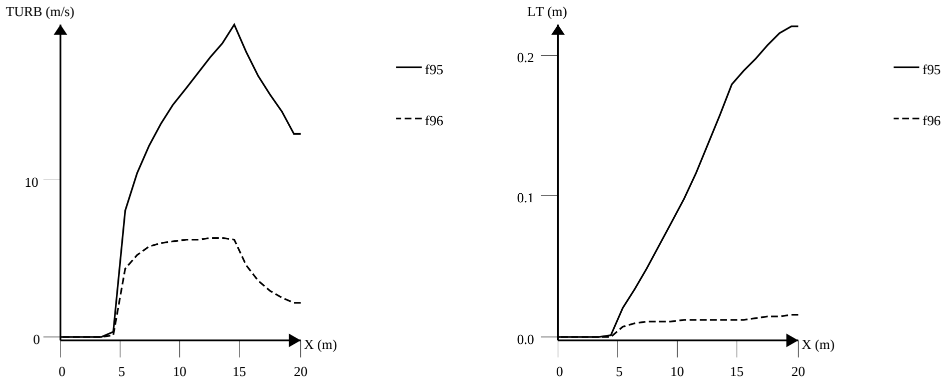

Figure 4.17 Turbulence field behind 10 subgrid objects with diameter 0.1 m (10% area blockage in the flow direction) located between x = 5 and 15 m. Flow velocity is 50 m/s

Figure 4.16 shows the turbulent energy and length fields for flows past three objects with similar subgrid blockage, 40%, in the flow direction. From top a 0.8 m object (located in two cells), five 0.08 m objects and a 0.4 m object. They should all give similar turbulent energy just downstream the objects, as they do in the left figure. They should also have a turbulent length scale proportional to the object dimension in the flow direction, as they do in the right figure. The small scale turbulence (from small objects) should decay much faster than the large scale turbulence, and it does, as shown in the left figure. These results were obtained with the subgrid turbulent energy and length generation model. However the turbulent energy generation model used in FLACS gave no difference in the turbulence fields from these three objects. It should therefore be replaced with the subgrid turbulent energy and length generation model, which is influenced by the size of the objects in the flow direction, instead of by the size of the grid cell.

4.8.7 Transient subgrid turbulence build up

The time it takes to build up the turbulence field with the subgrid turbulence models is an important parameter in evaluation of the ability of the models to represent the turbulence field in transient flows like those in gas explosions. This time has been found to be proportional to the time it takes for the flow to pass through the grid cell, $\Delta t = \Delta x / U$. The build up time is independent of initial turbulence conditions, since the production term in the model is independent of the turbulence field. The build up time is also independent of the time step length, as shown in Fig 3.X, for a test with the turbulence model switched on at time=1 s in a steady flow. The flow velocity was 20 m/s, the grid size 0.5 m and the cell passage time $\Delta t = \Delta x / U = 0.5 / 20 = 25 ms$. As can be seen in Figure 4.18 the turbulent intensity has reached around 80% of the steady state value after one cell passage time. Figure 4.12 showed also that a subgrid turbulence field was set up in a flame propagation simulation. The subgrid turbulence generation model can therefore be assumed to handle well the transient build up of turbulence fields, as has also been seen in explosion calculations with FLACS.

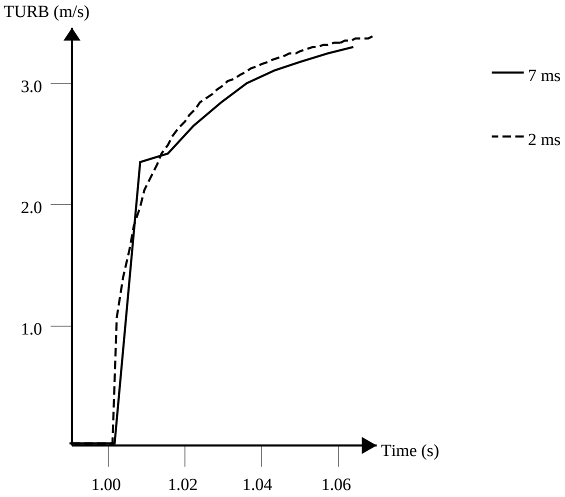

Figure 4.18 Turbulence build up with time step length 2 and 7 ms

4.8.8 Turbulence production from subgrid jets

The turbulence field generated by the shear layers in a jet is to some degree similar to the turbulence field generated by the shear layer in the wake behind a cylinder.

In FLACS all subgrid porosities and blockages are treated as subgrid obstructions, even if they in reality are jets. Therefore, in FLACS a small subgrid jet will give turbulence production as a large subgrid obstruction, and a large subgrid jet will be represented as a small subgrid obstruction.

It is however easy, based on the porosity on the surrounding cell faces, to distinguish whether a subgrid flow is a jet or a wake flow.

4.8.9 Flow velocity for subgrid turbulence generation

The flow velocity, used for subgrid turbulence generation in a cell, must be based on the flow velocity through the upstream cell face. This must be done to avoid a positive feedback when the flame is present in the cell. Increased turbulence gives increased burning velocity, which gives increased flow velocity downstream the cell, which eventually gives an unphysical increase of the turbulence in the cell.

In FLACS-96 the turbulence generation from obstructions was represented by the variable T_i, which was located in the cell. A better solution for representation of subgrid geometry seems to be to locate them on the nearest cell face in each direction, and generate turbulence in the cell downstream the face, as was done in FLACS 93-95.

The drag force caused by a subgrid object, is used in the momentum equations

$$R_j = \frac{1}{2}C_D(1-\beta_j)U_{\infty,j}|U_{\infty,j}| \tag{4.121}$$

where j is the three directions x, y and z. In FLACS the free stream velocity, used in subgrid drag and turbulence equations, has been taken directly as the flow velocity on the cell face.

$$U_{\infty,j} = U_j \tag{4.122}$$

This flow velocity may however be reduced due to large drag when the blockage is typically larger than 50%. This results in a lower velocity than in the surrounding grid cells. The turbulence production, which is a function of this velocity will therefore be too low. If the subgrid drag force is neglected, the velocity will be too large for large blockages, since the available flow area in the cell is reduced and no drag is present. A free stream velocity, which also includes the velocity on the six neighbour cells faces, U_{nb}, has therefore been introduced.

$$U_\infty = U_P(0.3 + 0.7 max(1, \beta_{nb}U_{nb}/U_P)) \tag{4.123}$$

This expression resulted in relatively blockage independent free stream velocity and turbulence production in tests performed with obstructions giving porosities on the cell faces ranging between 0 and 1.

4.9 Modelling of transient, reactive sub- and ongrid flows

Based on the analysis in the previous sections, the following modelling is recommended, and have been implemented in FLACS, for modelling of transient reactive turbulent flows around geometry represented ongrid and subgrid.

The turbulence production downstream an obstruction is modelled either ongrid or subgrid. The total turbulence production when no subgrid obstructions is present in the grid cell are modelled as produced from shear layers, P_{kS} (4.7), from buoyancy, $P_{k,B}$ (4.47), and boundary layers beside walls, $P_{k,W}$ (4.75), with a maximum turbulent length scale from (4.78).

$$G_k = P_{k,S} + P_{k,B} + P_{k,W} \tag{4.124}$$

$$G_\varepsilon = C_{\varepsilon 1}\frac{\varepsilon}{k}G_k \tag{4.125}$$

To secure a rapid buildup of the transient turbulence field, an extra term has been added

$$G_S = max(G_S, G_T) \tag{4.126}$$

$$G_T \approx C_T\left(\frac{\partial u_i}{\partial x_j}\Delta x_j^{2/3}\right)^3 , \tag{4.127}$$

where C_t is a non-dimensional constant.

When subgrid obstructions are present, and the subgrid turbulence production is larger than the shear generated, the shear generated production term is replaced by the turbulent energy and length generation due to subgrid obstructions, (4.116 and 4.118), represented by

$$G_k = P_{k,R} + P_{k,B} + P_{k,W} \tag{4.128}$$

$$G_\varepsilon = P_{\varepsilon,R} + C_{\varepsilon 1}\frac{\varepsilon}{k}(P_{k,B} + P_{k,W}) \tag{4.129}$$

$$P_{k,R} = \sqrt{\sum_{i=1}^{3}\left(u_i^3 T_i\left(\frac{a}{\Delta x_i} + \frac{b}{d_i}\beta_v\right)\right)^2} \tag{4.130}$$

$$P_{\varepsilon,R} = \sqrt{\sum_{i=1}^{3}\left(\frac{b u_i^4 T_i}{\Delta x_i d_i}\left(1 + \frac{\beta_v}{a}\right)\right)^2} \tag{4.131}$$

where T_i is a non-dimensional constant depending on type, blockage and orientation of the obstruction, d_i is the smallest of the two obstacle dimensions perpendicular to the flow direction, and a and b are constants. This model secures turbulence field with representative velocity fluctuations and length scales.

The k-ε model is not intended for reacting flow with expansion due to heat release, such as in gas explosions. A modification of the turbulence production for such flows is needed, to avoid non-physical turbulence production. The ongrid turbulence production due to shear stresses and buoyancy, is a function of velocity and density gradients. Velocity and density gradients through the flame have therefore been excluded in the present turbulence model.

In FLACS, the walls in a geometry are moved to the nearest cell face. To avoid non existing vent openings in the geometry, objects larger than 1.5 grid cells in one direction are therefore expanded to include the whole cell face if they block more than half of it. On average 50% of the larger objects in a geometry will therefore be expanded and represented only ongrid. The other half is represented partly ongrid and partly subgrid, with subgrid blockage, but without subgrid drag and turbulence generation, since these effects are handled by the ongrid representation.

4.10 Simulation of turbulent flow experiments

The simulations shown in this section were done with two versions of the FLACS code, FLACS- 94 and FLACS-96*. The FLACS-96* code includes the improvements in turbulence modelling described in the previous section. With respect to simulation of turbulence in steady unreactive flows, the difference between the codes is as follows: Both use the k-ε turbulence model, but FLACS-96* uses a better description of velocity gradients, to include turbulence production behind obstructions with diameter resolved with one grid cell. FLACS-94 use the subgrid turbulent energy production model, but FLACS-96* uses the subgrid turbulent energy and length production model. Wall boundaries are treated with the subgrid model for walls in FLACS-96* and eventually by wall functions in FLACS-94.

The experiments with turbulent flows past obstructions, from the EMERGE project, have been simulated with different grid resolutions. The comparison of simulated and experimental results are shown in this section. The simulation results from FLACS-94 were presented earlier by Arntzen (1996). Flow past obstructions should generate the same turbulence field, independent of grid resolution, whether they are represented subgrid, ongrid or partly subgrid, as the cylinders in Figure 4.19. A range of simulations have been done to secure that a representative turbulence field is produced, independent of obstruction form, localization and size. Flows past a range of obstruction configurations have been represented both subgrid and ongrid, where the ratio of obstruction diameter to grid cell size were in the range 0.1 to 12, typically 0.1, 0.2, 0.4, 0.9, 1, 1.3, 1.9, 2, 3, 4 and 5.

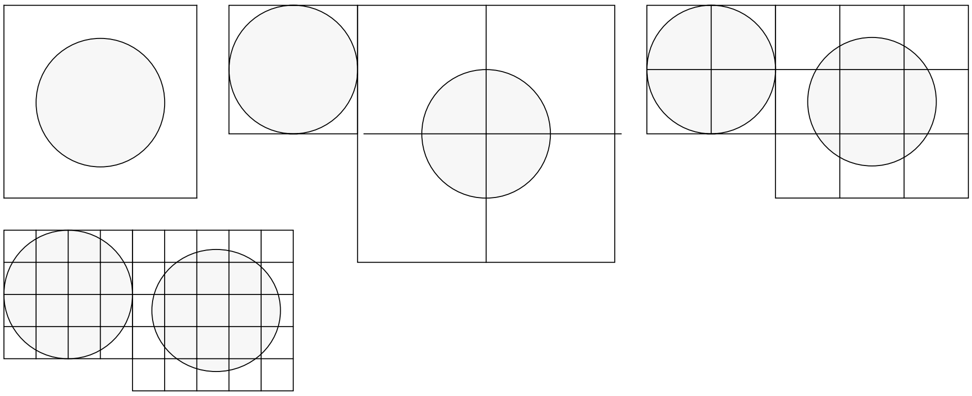

Figure 4.19 Cylinder, represented subgrid, ongrid, and partly subgrid

4.10.1 One single cylinder

Simulations of a single cylinder, represented ongrid, in a steady flow, with variation of grid resolution of the cylinder diameter, were done with the four explosion codes COBRA (British Gas), EXSIM (Tel-tek), REAGAS (TNO) as well as FLACS-94 (CMR) as a part of the EMERGE project, presented by Mercx (1996), Arntzen (1996) and Arntzen (1997b).

Figure 4.20 show the drag force on the cylinder as function of grid resolution, from calculations done by Tel-tek and British Gas. The drag force can be calculated as the sum of pressures around the cylinder. The pressure on the cylinder wall is however not known, only the pressure in the grid cell outside the wall is known.

The drag loads from CMR was therefore calculated as the momentum difference between two planes, located upstream and downstream the cylinder. This gives a some what higher, but probably more correct value than the first method. Round and square cylinders had the same representation on the coarse grid, with the diameter represented with one or two grid cells. The drag load was therefore too small if the cylinder was square, and too large if the cylinder was round. The drag loads were however relatively acceptable for all codes and grid resolutions.

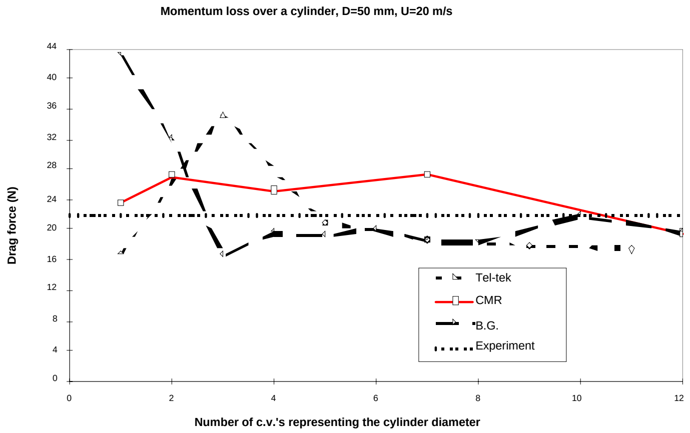

Figure 4.20 Drag force on a 5 cm cylinder as a function of grid resolution, calculations done by Tel Tek, British Gas and CMR

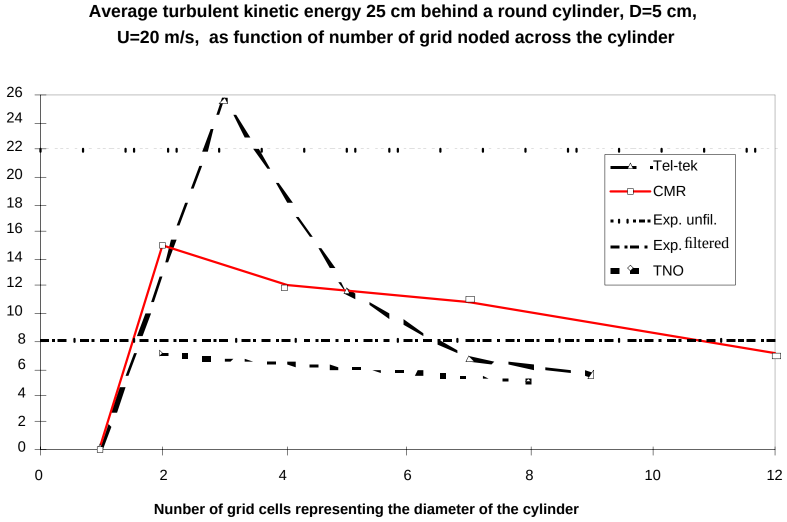

Figure 4.21 Total turbulent kinetic energy in a plane 5D downstream a cylinder, as a function of grid resolution, calculated by Tel-tek, TNO and CMR

Figure 4.21 shows the total turbulent kinetic energy, 5 diameters downstream the cylinder, as function of grid cells used to resolve the cylinder diameter. Several simulations of steady flows, 20 m/s, around a single cylinder, resolved on the grid, have been done. When the cylinder diameter was represented with two or more grid cells, the velocity gradient in the shear layers was resolved and turbulence was produced.

As can be seen in Figure 4.21 both Tel-Tek and CMR found that nearly no turbulence was produced when the cylinder was represented with only one grid cell. The model for turbulence generation due to free stream fluid stress, had therefore to be improved with a better velocity gradient expression for the velocities, as described in subsection 4.5.3 and by Arntzen (1996).

The experimental fluctuating velocities consist of filtered values, which is equivalent to turbulent fluctuations, and the unfiltered values, the velocity fluctuations, which is the sum of turbulence intensity and periodic velocity fluctuations (due to vortex shedding). In Figure 4.21 EXSIM and FLACS show turbulent kinetic energy, whereas REAGAS shows an energy based on the velocity fluctuations. The simulated results of EXSIM and FLACS agree well with the experiments, since the periodic fluctuations normally are included in the simulated flow field for fine resolutions, but not for coarse. The REAGAS results, which is based on velocity fluctuations, has however only a third of the experimental values. Something must be incorrect in their simulations since all three codes used the same turbulence model. At CMR, Salvesen and Sand (1993) achieved periodic fluctuations which agreed well with experiments. Detailed calculation of flows around cylinders are also known from literature, Franke and Rodi (1991), Begue et al. (1990) and Kato and Launder (1993).

The turbulence flow field for different grid resolutions with FLACS-94 with wall functions is presented by Arntzen (1996). The simulated flow velocity in the wake behind the cylinders, was here too low. The reason for this was that the main momentum transport behind the cylinder is mainly caused by the vortex shedding (which was present only for the finest resolution). The difference in flow velocity was caused by the difference in turbulent viscosity, which is proportional to the turbulent length scale which decreased with grid cell size. Therefore, the better the resolution the larger difference between simulations and experiments, until vortex shedding was included. This velocity difference in the wake has also been reported by Franke (1991) and the other EMERGE modellers except Tel-tek. The vortex shedding was clearly included in the simulations with 12 grid cells resolution and partly for 7 grid cell resolution. The calculation results from these resolutions were therefore periodic fluctuating, while the results from the other resolutions can be seen as steady. FLACS simulations without wall functions gave no vortex shedding. For the resolutions without vortex shedding, there was nearly no difference between simulations with or without wall functions. Simulations performed in the EMERGE project showed that the grid resolution needed to obtain vortex shedding differed between the codes, probably due to different wall functions and different ways of representing the cylinder on the numerical grid.

The turbulence intensity upstream the cylinder was acceptable for all resolutions except the finest, where turbulence was wrongly produced since the turbulence model did not distinguish between stress and strain. Downstream the cylinder the turbulence intensity was best described by the coarsest resolution. Close to the cylinder the intensity was nearly proportional with the grid cell size, but farther downstream it become more equal.

FLACS 94 simulations with the cylinder represented subgrid gave representative turbulence kinetic energy downstream the cylinder, independent of grid resolution. The turbulent length scale (and dissipation) was however dependent on the grid cell size in the flow direction, as found theoretically in subsection 4.8.4.

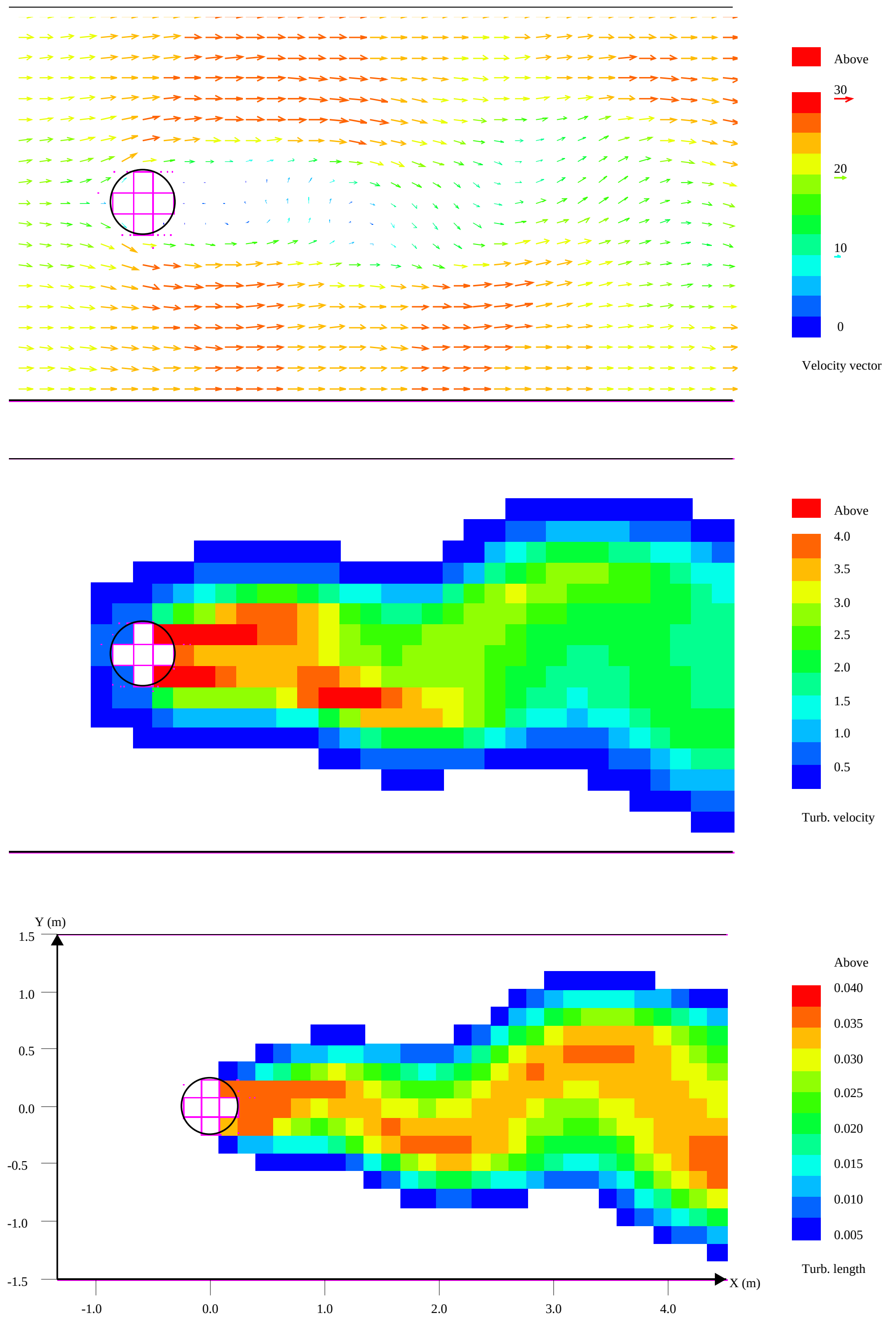

Figure 4.22 Velocity, turbulent velocity and length fields, vortex street behind a round cylinder with diameter 0.5 m resolved with 3 grid cells

Simulations with FLACS-96*, with a new subgrid model for walls, give vortex shedding for cylinder diameters resolved with only three grid cells. This is shown in Figure 4.22 for flow around a cylinder with diameter 50 cm. The Strouhal number is here correctly around 0.2.

Figure 4.23 and 4.24 shows the flow velocity, turbulent intensity and length, at lines located 2D (1 m) and 4D (2m) downstream the centre of the cylinder. FLACS 96* simulations with different grid resolution are compared with experimental data. The raw data with velocity fluctuations from experiments have been filtered and the turbulent and periodic fluctuations have been separated. Assuming the experimental data from section 4.4 can be scaled, the flows around a 50 cm cylinder are compared with experimental data. (For this high Reynolds number the wake behind a round cylinder would be thinner in reality) This scaling of these and other experimental data has been done for validation of simulations with similar obstruction and grid cell sizes as in explosion simulations.

In Figure 4.23 simulation results with the cylinder diameter resolved with 1, 2, 3 and 4 grid cells are compared with filtered experimental data. In contrast to simulations with the previous presented codes, grid resolution one grid cell gives representative turbulence field and resolution 3 and 4 grid cells gives vortex shedding. The turbulent intensity, TURB in the figure ($1.5\ TURB^2 = k$), is some what higher for grid resolution two cells than for the three other resolutions. The turbulent length scale for grid resolution three grid cells is smaller than for the other resolutions. This may be due to that the cylinder here is represented as a cross with smaller geometrical details, as seen in Fig. 4.22.

Figure 4.24 shows the same flow situation, with the cylinder represented subgrid. The simulations are compared with both turbulence (uf and vf) and total (u, v an w) fluctuations. One may argue that turbulent intensity from the resolution which is too coarse to include the vortex shedding, should be compared with total fluctuations instead of turbulent fluctuations. The periodic fluctuations will stretch the flame and increase the flame area, and this effect has to be included. The periodic fluctuations may however not affect the local turbulent burning velocity due to turbulent diffusion. The simulated intensities showed the right tendency with values between the turbulent and periodic fluctuations. With the chosen value of the constant a, in the subgrid model, the turbulent intensity and velocity field agree well with the experimental values for all grid resolutions. The obtained turbulent length are also representative, where FLACS 94 gave a grid dependent length. The 3m wide channel was resolved with 3, 5 and 8 cells, resulting in a subgrid blockage of 50%, 83% and 2x37.5%.

A square cylinder may have the same representation as a round cylinder, when the diameter is resolved ongrid with 1 or 2 grid cells, but the wake of a square cylinder should be about 60% wider. The simulated fields were very similar to those from the round cylinder. The wake and the width of the turbulent intensity are therefore too narrow. The turbulent flow field from a square cylinder represented subgrid gives, however, larger turbulence production than round cylinders, due to a higher T_i value.

The flow field around a 5 cm round cylinder was also represented on a curve linear grid with the MUSIC code, as presented in section 2.7. The turbulence field from this simulation is shown in Figure 4.25. The flow follows the cylinder wall nearly to the backside of the cylinder, instead of separating at the side of the cylinder, as seen in experiments and in flow simulations on cartesian grid. The result is therefore a thin wake and lower turbulence intensity downstream the cylinder, compared with experiments and cartesian grid simulations. Unless this problem is solved, round cylinders will be better represented on a cartesian grid, than on a curve linear grid.

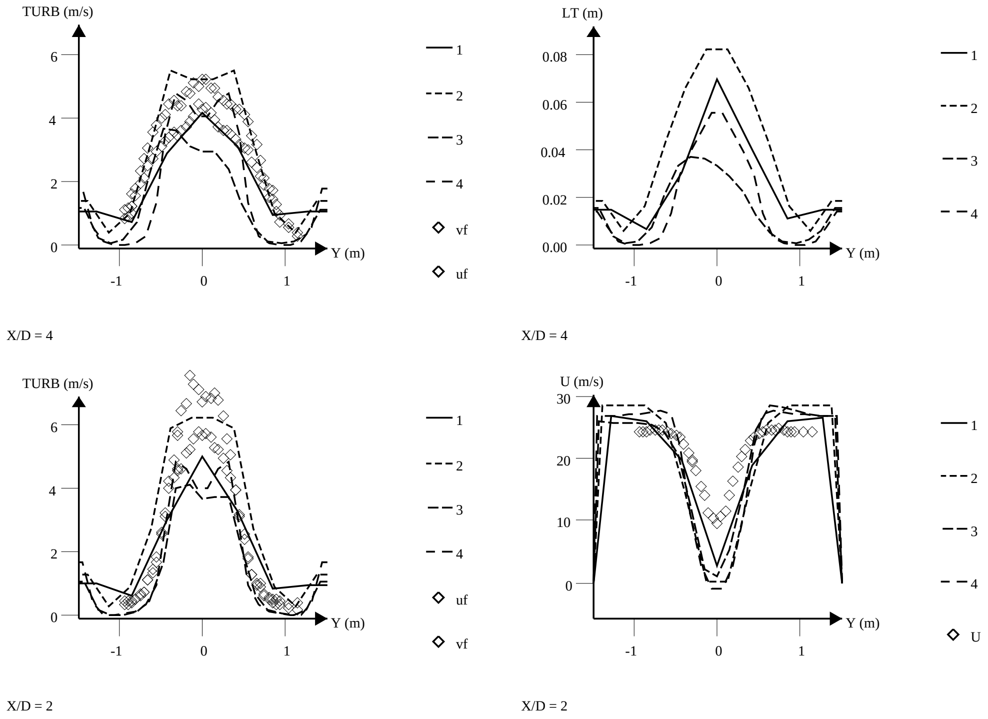

Figure 4.23 Turbulent flow field behind 0.5 m round ongrid cylinder in a 3 m channel

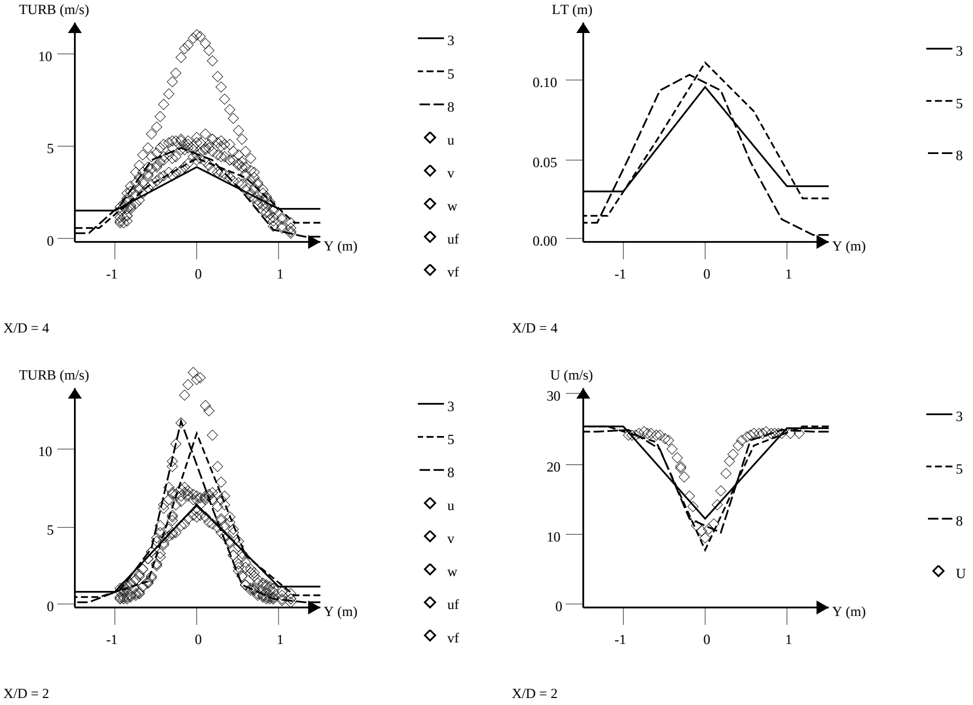

Figure 4.24 Turbulent flow field behind 0.5 m round subgrid cylinder in 3 m channel

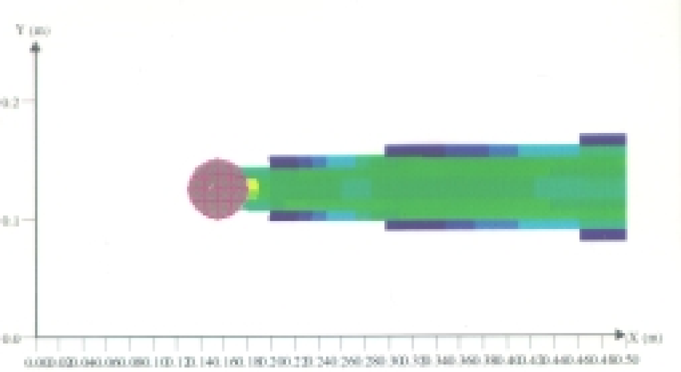

Figure 4.25 Turbulent kinetic energy, k_{max}=15 m^2/s^2, U=20 m/s, from the MUSIC code

4.10.2 Obstructions used in the EMERGE experiments

In addition to flows past a cylinder, the flows past a range of other obstruction configurations were studied both experimentally and numerically in the EMERGE project, as presented in section 4.4. The next pages show comparisons between simulated and experimental data for some of these flows.

Figure 4.26 shows the turbulent velocity fluctuation and flow velocity at lines located at x=2.0m and y=0.5m, downstream a 0.5m square cylinder (box) mounted at the wall. FLACS-96* calculations, with the cylinder resolved with 1, 2 and 4 grid cells and five subgrid resolutions, are compared with experimental data. The figure legend gives the ratio of cylinder size to grid cell size. The setup is shown on the top of the figure and the original EMERGE experiment is scaled up with a factor of 10 to obtain representative grid cell sizes. The three ongrid simulations underpredicted the recirculating flow and (thereby) the turbulent intensity. The subgrid simulations gave, however, a turbulent intensity which agreed well with experimental data for all resolutions, as seen in the figure.

Figure 4.27 shows the turbulent velocity fluctuation, flow velocity and turbulent length scales at lines located 2.4 and 6.6 m (2 and 5.5 h) downstream a 1.2 m high plate. FLACS-96* calculations with the plate resolved with 1, 2 and 4 grid cells are compared with experimental data. The setup is shown in Figure 4.10 and the original EMERGE experiment is scaled up with a factor of 12 to obtain representative grid cell sizes. The simulated flow and turbulence fields agree well with experimental data for all three grid resolutions. Even the plate resolved with only one grid cell resulted in a recirculating zone behind the cylinder. Subgrid simulations give also good agreement with the experimental data.

Figure 4.28 shows the turbulent velocity fluctuation and flow velocity at lines located at x=0.66m and y=0.0 m, downstream five round cylinders with diameter 17 cm. The setup is shown on the top of the figure and the figure legends are the ratios of cylinder diameters to grid cell sizes. In the FLACS-96* calculations the cylinders are represented ongrid (1), subgrid with each cylinder alone in a cell (2) and subgrid with all cylinders in the same grid cell (6). The simulated flow and turbulence fields agree well with experimental data for all three grid resolutions. Since the turbulence intensity on the line in the flow direction (y=0) agree, the turbulent length also agree well.

Simulations of steady turbulent flow fields past rows of cylinders are shown in Figure 4.29 - 4.31. The results are compared with measured data from British Gas (subsection 4.4.2) at positions two and four diameters downstream the centre of the last cylinder row. The experimental flow velocity in the wake is much lower than behind a single cylinder, indicating that transverse momentum transport and vortex shedding is less important here than behind a single cylinder. The flow velocity in the wake is therefore represented well in the ongrid simulations.

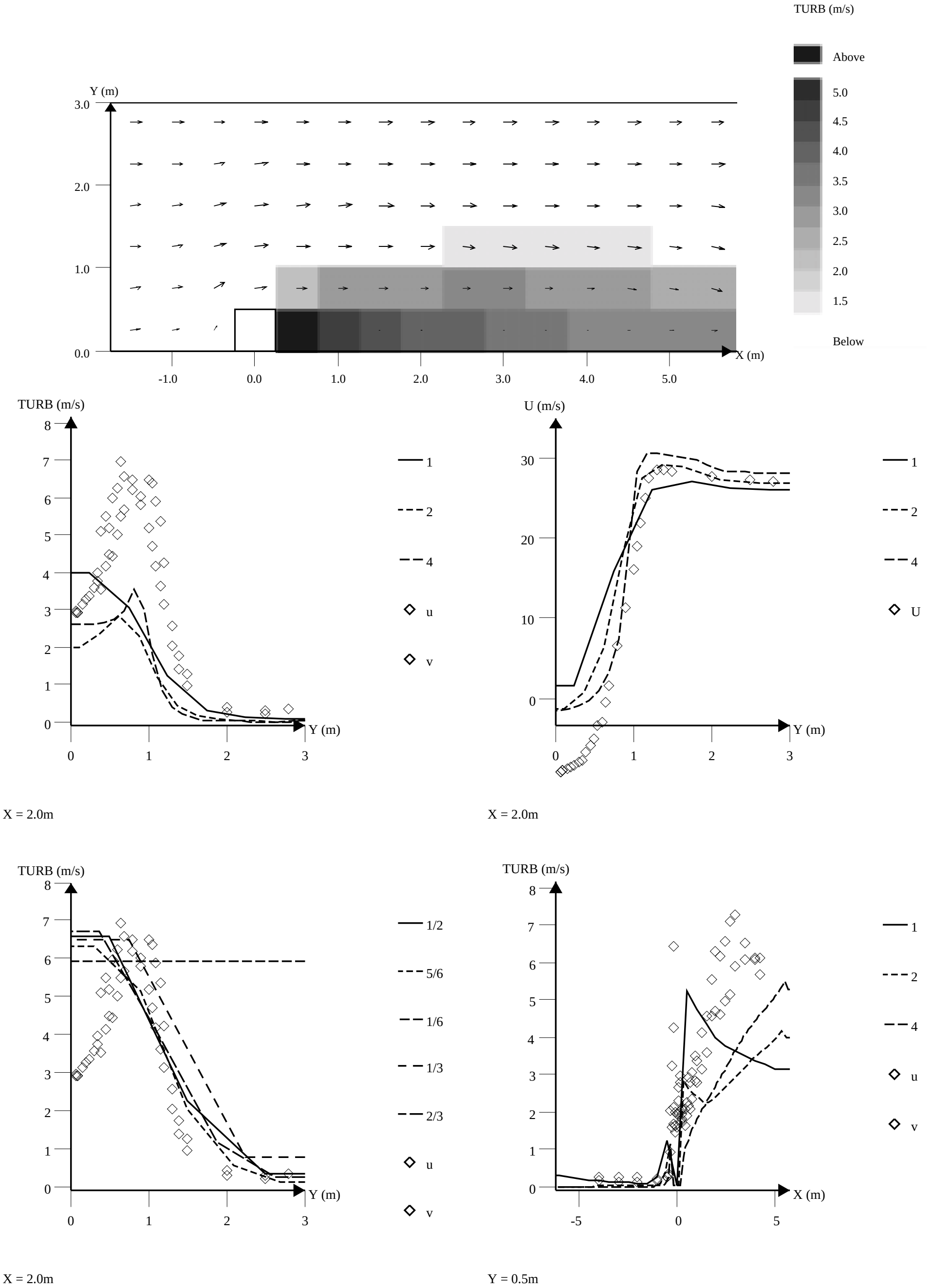

X = 2.0m X = 2.0m

X = 2.0m Y = 0.5m

Figure 4.26 Turbulence fields behind a 0.5 m square cylinder mounted at a wall

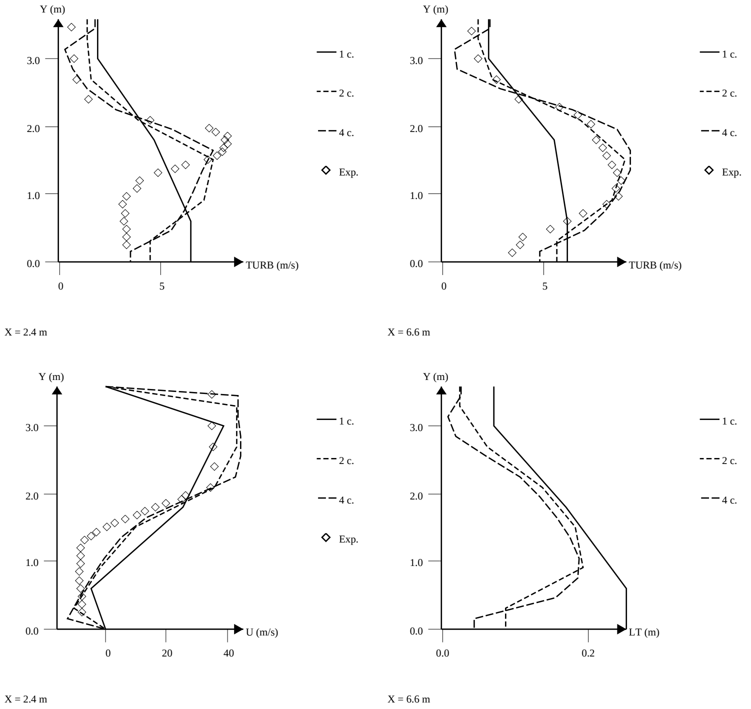

Figure 4.27 Turbulence fields behind a 1.2 m plate located by a wall

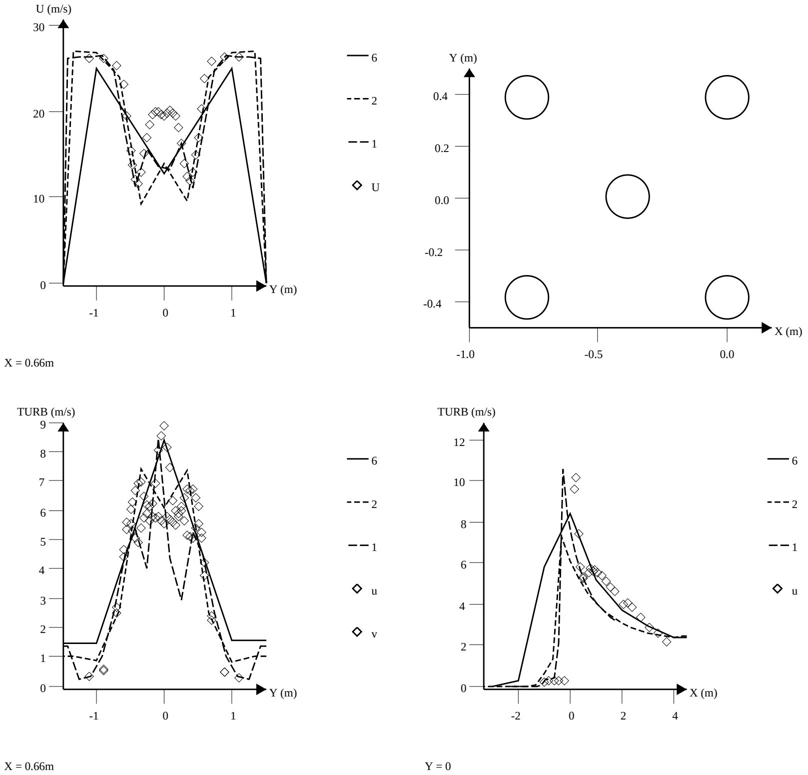

Figure 4.28 Turbulent flow field downstream five cylinders

Figure 4.29 shows the flow velocity and turbulent intensity downstream two in line rows of cylinders. This simulation was performed with FLACS-94. The diameter is resolved ongrid with 1 and 2 grid cells, and subgrid with 0.6 and 0.3 grid cells. The ongrid simulations with the diameter resolved with one grid cell gave nearly no turbulence, since the velocity gradient is poorly resolved, as discussed in subsection 4.5.3. When the diameter was resolved with two cells the turbulent intensity becomes too high, probably due to too high turbulent length (and viscosity) behind the second row. When the length scale around the cylinders is restricted with wall functions, the turbulent intensity becomes lower.

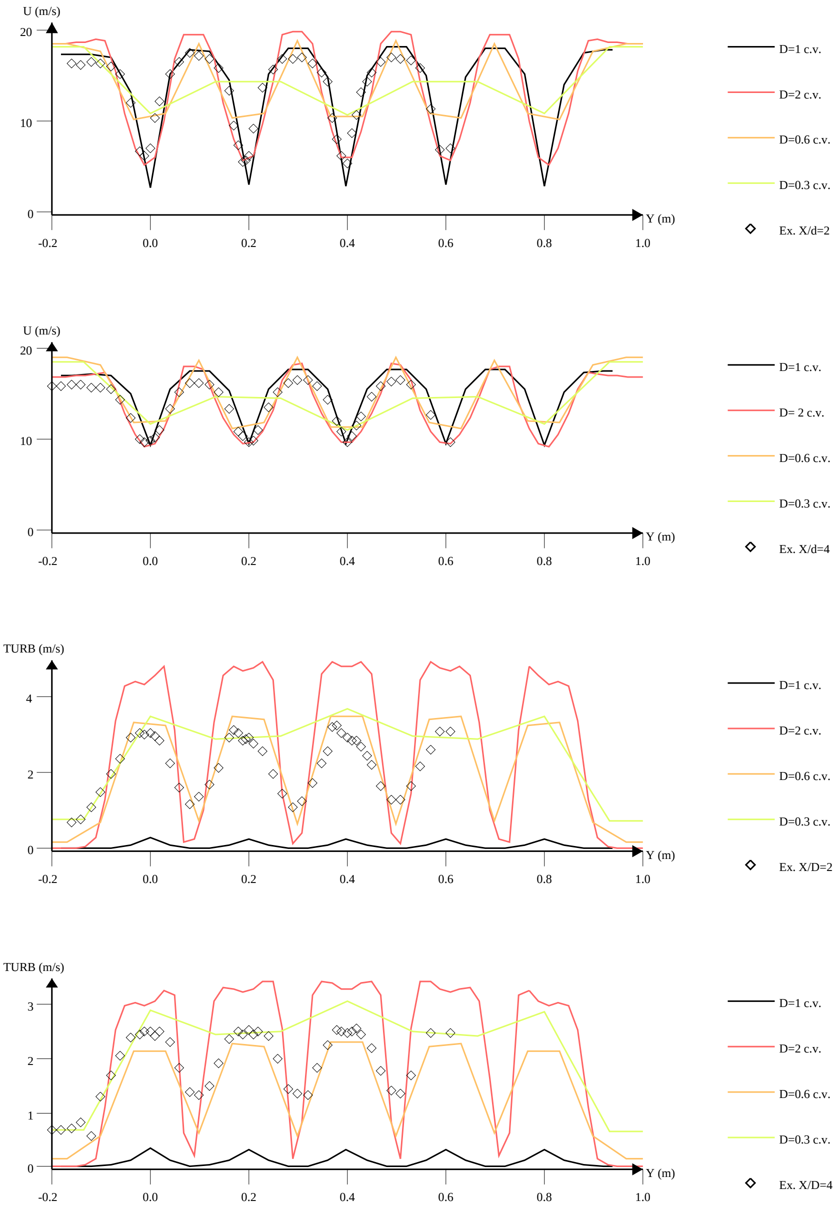

Figure 4.29 Turbulent flow field behind two in line rows of cylinders, from FLACS 94

The two subgrid simulations show a decay in turbulence fluctuations which is inverse proportional to grid size, since the turbulent length scale from the subgrid turbulence energy production model wrongly becomes proportional to the grid size. FLACS-96* simulations agreed well with these experiments for all four resolutions.

Figure 4.30 shows the simulated turbulent flow field behind two staggered rows of cylinders from FLACS-96*. The cylinders were resolved with one and two grid cells. Due to the improvements in representation of velocity gradients, turbulence is produced also in the wake behind cylinders resolved with one grid cell. The simulated velocities agree well with the experiments, but the turbulence fluctuations are somewhat underpredicted. The same underprediction was also seen with FLACS-94 for resolution two grid cells. However, the turbulence fields from subgrid simulations agreed well with the experimental data.

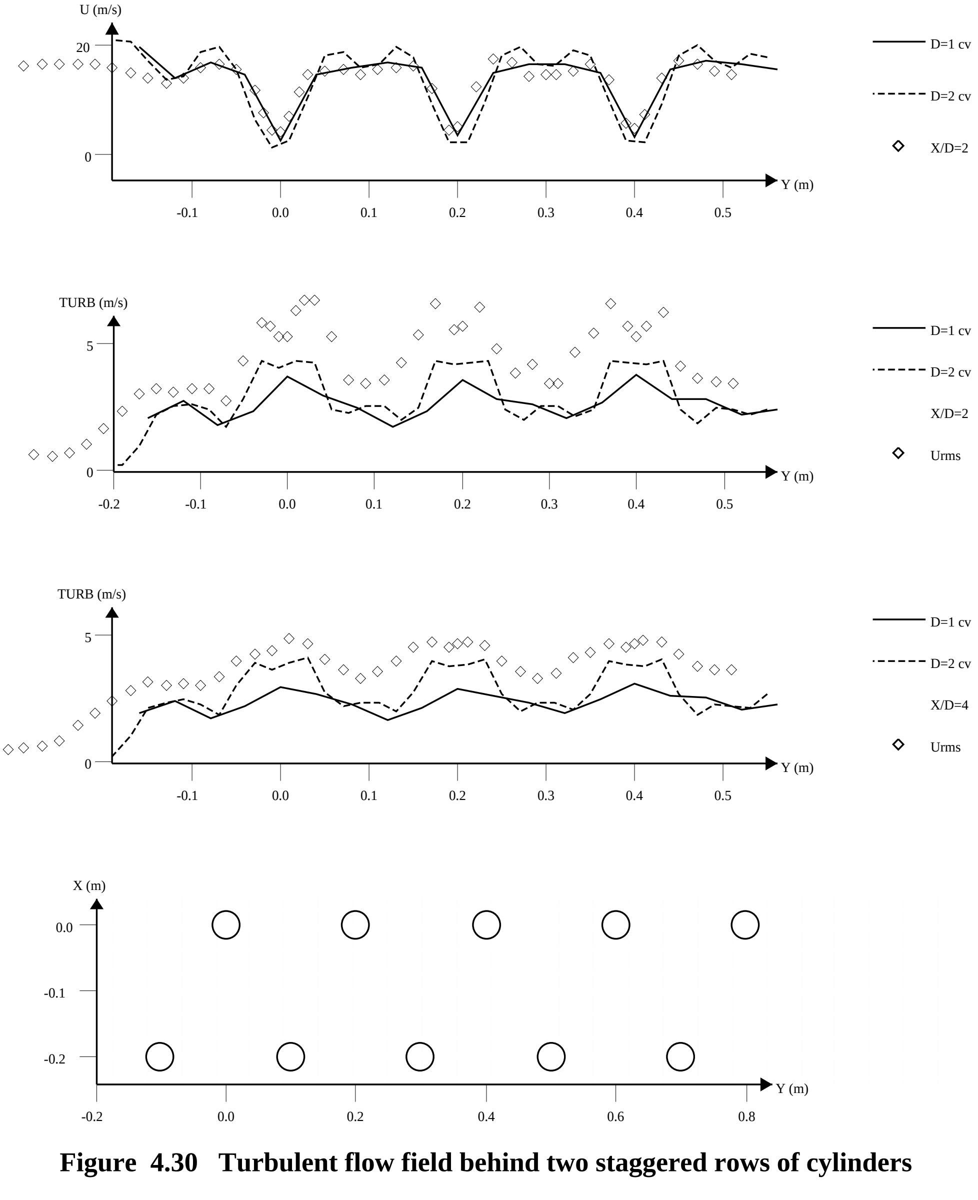

Figure 4.30 Turbulent flow field behind two staggered rows of cylinders

Figure 4.32 shows the British Gas array of 5 * 5 * 3 pipes, which was located in a flow field in positive x direction. A range of subgrid resolutions was tested. The turbulent intensity and flow velocity from simulations were compared with experimental data on lines downstream the obstruction. In Fig 4.32 comparison is done at a line 4D downstream the centre of the last cylinder row. The turbulent intensity is represented with the velocity fluctuation in the x and y direction. FLACS-96* gave similar and representative turbulent intensity for all resolutions since it uses the subgrid turbulent energy and length generation model, and thereby had a representative turbulent length. The subgrid turbulent energy generation model in FLACS-94 gives an overprediction of the turbulent length when the flow has past some obstacles. This results in a too low dissipation and thereby a too large turbulent intensity, as shown in the figure and discussed in subsection 4.8.4.

The flow through this 75 pipes geometry was also simulated ongrid, with the cylinder resolved with one and two grid cells. The FLACS-96* simulations underpredicted the turbulent intensity with 20% at the “4D line”. FLACS-94 simulations, with the cylinder resolved with two grid cells gave three times too large turbulent intensity, unless the length scale at walls (around the cylinders) was restricted.

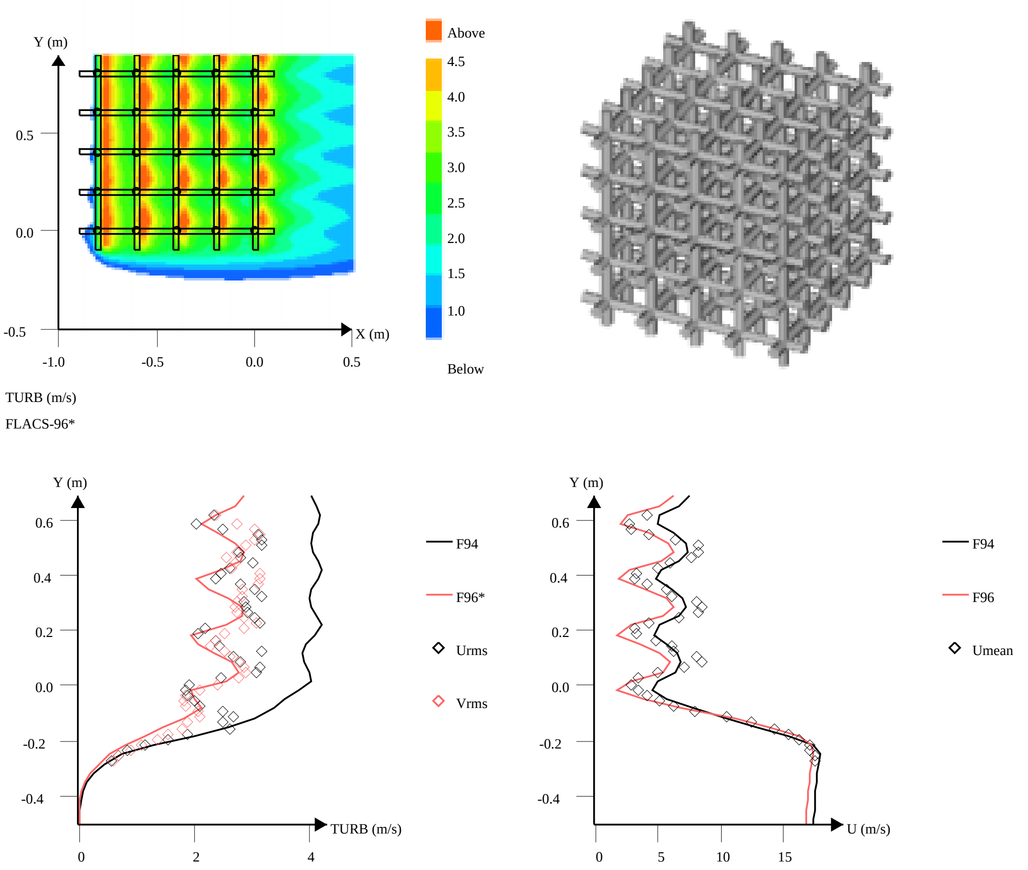

Figure 4.31 Turbulent intensity, length and flow velocity around a 5 x 5 x 3 array of pipes

The turbulent intensity level downstream complex ongrid obstructions depends on the restrictions in turbulent length scale in grid cells beside walls. A some larger maximum length scale in (4.78) would therefore give a larger and in some situations a more representative turbulent intensity downstream complex ongrid obstructions.

The turbulent flow field around other obstruction configurations has also been simulated, for a range of grid resolutions, and compared with experimental data. These includes flows past a backward facing step, past two plates located at a wall and a 3D cuboid located at a wall, as presented in subsection 4.4.1.

4.11 Summary

The turbulence models ability to give representative turbulence field in complex, transient and reactive flows, where the geometry were represented both ongrid and subgrid, have been evaluated.

The k-ε turbulence model is not intended for transient or reactive flows. Simulations of transient flow fields gave turbulence buildup times which depend strongly on initial conditions as well as grid resolution. Inclusion of a minimum turbulence production from velocity gradients now secure an independent and rapid buildup of the turbulence field. This also secure representative turbulence production for objects resolved with only one grid cell.

Reactive flows, as in explosion simulations, had a similar initial and grid dependency, since at flame arrival, the expansion caused by the flame was treated as normal stresses by the turbulence model and resulted in a decrease in k if the turbulent time scale was of order less then the flow to grid time scale, and an increase in k if opposite. Velocity and density gradients through the flame were excluded to avoid non-physical turbulence production.

Wall functions give a turbulence field with a fixed length scale in grid cell located by walls. This turbulence field may be representative for calculation of problems like heat transfer to walls, but not for calculation of gas explosions in complex geometries, where the turbulence field is used as input for the burning velocity model. A better representation of the effects of upstream geometry is needed, and has been achieved through a new subgrid model for walls.

The subgrid turbulent energy generation model gave representative turbulent energy production, but the turbulent length depended on grid size instead of obstruction size. A subgrid turbulent energy and length generation model, which was developed, solved this problem.

Simulations of turbulent flow experiments past a range of complex obstacle configurations were done. The simulations showed that with the improvements in turbulence modelling included, the turbulence fields were well represented, independent of grid resolution of the obstructions.

5 Combustion models, the β flame model

The purpose of a combustion model for premixed combustion, like gas explosions, is to localize the reaction zone and convert reactants to products at a rate similar to that a real flame does in an explosion. Turbulent combustion processes are often handled by mixing controlled combustion models of eddy break-up type. The combustion process may however be described better by dividing the combustion model into two parts, a flame model and a burning velocity model.

This chapter consists of two parts. The first part is an analysis and evaluation of mixing controlled combustion models. The analysis shows the burning velocities which are obtained analytically with the models, and the grid resolution needed to obtain these grid independent analytical solutions. The last part is a presentation of the β flame model, which was developed by the author, based on the analysis in the first part of the chapter. Two other flame models are presented at the end of the chapter and the Simple Interface Flame model, SIF, is presented in next chapter. Burning velocity models are presented in Chapter 7.

5.1 Analysis of mixing controlled combustion models

In a premixed mixing controlled combustion model, the reaction zone, reactants and products are described by a transport equation for the progress variable c, where c is mass fraction of products, taking values ranging from zero in the unburned reactants to unity in the fully burned products

$$\frac{D\rho c}{Dt} = \nabla\bullet\rho D\nabla c + w \tag{5.1}$$

D is the diffusion coefficient and w is the reaction rate (mass of reactants converted to products per time and volume). When c is replaced by (3.28) and (3.24), $c = 1 - Y_f / Y_{f0}$, (5.1) is replaced by (5.2), the conservation equation for mass fraction of fuel, Y_f, as used in FLACS. Y_{f0} is the initial mass fraction of fuel in the gas mixture.

$$\frac{D\rho Y_f}{Dt} = \nabla\bullet\rho D\nabla Y_f - Y_{f0}w \tag{5.2}$$

Four mixing controlled combustion models are analysed. These are the H-M model, which have been used in FLACS and the eddy dissipation concept, EDC, both based on Magnussen and Hjertager (1976). In adjoin to the so-called Bray model, Bray (1990) and a version of the Eddy Break-up, EBU, model, shown e.g. in Catlin et al. (1991).

All four models use similar models for the diffusion, D. The difference between the models is therefore related to the differences in reaction rate, shown in Table 5.1. The reaction rate, w, is proportional to the density and the turbulent frequency in all four models

$$w \propto \rho\frac{u'}{l_t} = 9\rho\frac{\varepsilon}{k} \tag{5.3}$$

The difference in the reaction rate models is related to reaction rate, w, as proportion of *max w*, and may be seen as difference in probability density functions, *pdf*, and cold quench criteria as seen in Table 5.1.

The *pdf* makes the reaction rate a function of mass fraction of products, c, as seen in Figure 5.1. The H-M and EDC have similar *pdf*, so only the H-M model is shown in the first part of the analysis. The cold front quench criteria is a boundary condition which shall secure a unique burning rate and is typically a criteria which gives zero reaction rate for values of c below a specified c, c_q. In numerical simulations of combustion in a 1-D fixed turbulence field we have observed that the burning velocity accelerates because the flame becomes wider with time, unless a cold front quench criterion is used. The cold front quench results in a finite flame thickness and therefore a unique burning velocity.

In a steadily propagating 1D planar flame, the flame burns with burning velocity S into the reactant. Since mass is conserved it follows that

$$\rho U = \rho_R S = const \tag{5.4}$$

Multiplication of (5.4) with $\frac{\partial c}{\partial x}$ gives

$$\frac{D\rho c}{Dt} = \rho_R S \frac{\partial c}{\partial x} \tag{5.5}$$

Inserting (5.5) into (5.1) replaces U with the burning velocity S.

$$\rho_R S \frac{\partial c}{\partial x} = \frac{\partial}{\partial x}\left[\rho D \frac{\partial c}{\partial x}\right] + w \tag{5.6}$$

5.1.1 Analysis with cold front quench criteria

The burning velocities for a such 1D flame, obtained from premixed mixing controlled models, may be determined analytically, by solving the Favre averaged 1D steady equation for the progress variable, c (5.6), as presented by Catlin and Lindstedt (1991) for analysis of the Bray, Moss and Libby (BML) version of the Eddy Break-up (EBU) model. The reaction rate w can be replaced by the dimensionless reaction rate W and the function $A(c)$

$$w = W \rho_R \frac{\rho_R}{\rho} A(c) \tag{5.7}$$

$$A(c) = \frac{\rho}{\rho_R^2} \frac{w}{W} = \frac{1}{(1+\tau c)^2} \frac{w}{\rho W} \tag{5.8}$$

(5.6) can then be replaced by (5.9)

$$\rho_R S \frac{\partial c}{\partial x} = \frac{\partial}{\partial x}\left[\rho D \frac{\partial}{\partial x}(c)\right] + W \rho_R \frac{\rho_R}{\rho} A(c) \tag{5.9}$$

The order of the differential equation, (5.9), may be lowered by introducing a coordinate transformation through the independent variable P.

$$P = \frac{\rho D}{\rho_R S} \frac{dc}{dx} \tag{5.10}$$

Introducing P into (5.9) and multiplication with $P\frac{dx}{dc}$ gives:

$$\rho_R S\frac{dc}{dx}P\frac{dx}{dc} = \frac{d}{dx}(\rho_R SP)P\frac{dx}{dc} + \frac{1}{\rho_R S}\rho DW\rho_R\frac{\rho_R}{\rho}A(c) \tag{5.11}$$

Division by $\rho_R S$ in (5.11) gives:

$$P = P\frac{dP}{dc} + \frac{DW}{S^2}A(c) \tag{5.12}$$

Introduction of Λ as given by (5.13), where $\Lambda^{-1/2}$ is a dimensionless burning velocity, replace (5.12) with (5.14).

$$\Lambda = \frac{DW}{S^2} \tag{5.13}$$

$$P\frac{dP}{dc} - P + \Lambda A(c) = 0 \tag{5.14}$$

An approximation to an analytical solution of (5.13) may be found by using truncated Taylor series for *P(c)* and *A(c)*. Since the reaction rate is zero, $A(c) = 0$, when $c < c_q$, (5.14) has the trivial solution $P = c$ in the range $c < c_q$. *P(c)* must vary continuously across c_q, $P(c_q) = c_q$ and

$$P(c) = c_q + \frac{dP_q}{dc}(c - c_q) + \frac{1}{2}\frac{d^2}{dc^2}P_q(c - c_q)^2 + \frac{1}{6}\frac{d^3}{dc^3}P_q(c - c_q)^3 + O((c - c_q)^4) \tag{5.15}$$

Similarly the reaction rate can be expanded

$$A(c) = A_q + \frac{dA_q}{dc}(c - c_q) + \frac{1}{2}\frac{d^2}{dc}A_q(c - c_q)^2 + O((c - c_q)^3) \tag{5.16}$$

Substituting the two Taylor series into (5.14) and equating powers of $c - c_q$ yields the three algebraic equations, (5.17) -(5.19)

$$c_q\left(\frac{dP_q}{dc} - 1\right) + \Lambda A_q = 0 \text{ to } O(1) \tag{5.17}$$

$$\frac{dP_q}{dc}\left(\frac{dP_q}{dc} - 1\right) + c_q\frac{d^2P_q}{dc^2} + \Lambda\frac{dA_q}{dc} = 0 \text{ to } O((c - c_q)) \tag{5.18}$$

$$c_q\frac{d^3P_q}{dc^3} + \frac{d^2P_q}{dc^2}\left(3\frac{dP_q}{dc} - 1\right) + \Lambda\frac{d^2A_q}{dc^2} = 0 \text{ to } O((c - c_q)^2) \tag{5.19}$$

Four equations are needed for eliminating P and its three derivatives. Catlin and Lindstedt argue that the last equation is given by

$$\frac{d}{d\Lambda}\left(\frac{d^3P_q}{dc^3}\right) = 0 \tag{5.20}$$

Inserting $\frac{d^2P_q}{dc^2}$ from (5.18) into (5.19) gives

$$\left\{\left[\Lambda\frac{dA_q}{dc} + \frac{dP_q}{dc}\left(\frac{dP_q}{dc} - 1\right)\right]\right\}\left(3\frac{dP_q}{dc} - 1\right) - \Lambda c_q\frac{d^2A_q}{dc} = c_q^2\frac{d^3P_q}{dc^3} \tag{5.21}$$

With $\frac{dP_q}{dc}$ from (5.17)

$$\left\{\Lambda\frac{dA_q}{dc} - \left(1 - \frac{\Lambda}{c_q}A_q\right)\frac{\Lambda}{c_q}A_q\right\}\left(3 - 3\frac{\Lambda}{c_q}A_q - 1\right) - \Lambda c_q\frac{d^2A_q}{dc} = c_q^2\frac{d^3P_q}{dc^3} \tag{5.22}$$

$$-3\Lambda^3\left(\frac{A_q}{c_q}\right)^3 + \Lambda^2\frac{A_q}{c_q}\left(5\frac{A_q}{c_q} - 3\frac{dA_q}{dc}\right) + 2\Lambda\left(\frac{dA_q}{dc} - \frac{A_q}{c_q}\right) - \Lambda c_q\frac{d^2A_q}{dc} = c_q^2\frac{d^3P_q}{dc^3} \tag{5.23}$$

Differentiating (5.23) with respect to Λ and remembering (5.20), yields the following quadratic equation in Λ

$$9\left(\frac{A_q}{c_q}\right)^3\Lambda^2 - 2\frac{A_q}{c_q}\left(5\frac{A_q}{c_q} - 3\frac{dA_q}{dc}\right)\Lambda + 2\left(\frac{A_q}{c_q} - \frac{dA_q}{dc}\right) + c_q\frac{d^2A_q}{dc_q^2} = 0 \tag{5.24}$$

The burning velocity is found when the larger of the two roots is inserted into (5.13).

When w from the H-M, EBU and Bray combustion models are inserted into (5.8), *A(c)* and it's derivatives, which are needed in (5.24), are as shown in the Table 5.1

where $\delta(c - c_q) = \begin{bmatrix} 0,\ c < c_q \\ 1,\ c > c_q \end{bmatrix}$

It should be noted that the eigenvalue for the H-M model is function of the product τc_q whereas the other two models are functions of both c_q and τ.The equation for the eigenvalue, (5.24), with *A(c)* and it's derivatives for the H-M model inserted from Table 5.1, gives the equation for the eigenvalue for the H-M model (5.25).

$$9\Lambda^2 - 4(1 + \tau c_q)(1 + 4\tau c_q)\Lambda + 2\tau c_q(\tau c_q - 2)(1 + \tau c_q) = 0 \tag{5.25}$$

The eigenvalue of the H-M model is the larger root of the second order equation (5.25)

$$\Lambda = [1 + 4\tau c_q + \sqrt{1 + 9\tau c_q + 15.5\tau^2c_q^2}](1 + \tau c_q)/4.5 \tag{5.26}$$

With the eigenvalue for a specified c_q and τ, the burning velocity can be calculated from (5.13), as shown below for the H-M model with τ=6.5 and c_q=0.3 and 0.05.

$$\tau c_q = 2 \Rightarrow \frac{DW}{S_T^2} = \Lambda = 12 \Rightarrow S_T = 0.29\sqrt{DW} \tag{5.27}$$

$$\tau c_q = 0.325 \Rightarrow \Lambda = 1.37 \Rightarrow S_T = 0.85\sqrt{DW} \tag{5.28}$$

The diffusion, *D*, can be either laminar or turbulent. The laminar diffusion coefficient should be used for laminar flames and is often modelled as

$$D_L = \mu/0.7 \approx (1.4 \cdot 10^{-5})/0.7 \approx 2 \cdot 10^{-5} \tag{5.29}$$

The turbulent diffusion coefficient, D_T, can be described by a gradient transport expression. In the H-M model in FLACS, as well as in other eddy break-up, turbulent combustion, models, D_T is described by the gradient transport expression:

$$D_T = \frac{\mu_T}{0.7} = \frac{C_\mu k^2}{0.7\,\varepsilon} = \frac{k^{1/2}}{0.7} l_t = 1.75 u' l_t \tag{5.30}$$

The dimensionless reaction rate, W, in all eddy break-up type combustion models is proportional to the turbulent frequency

$$W \propto \frac{u'}{l_t} = 9\frac{\varepsilon}{k} \tag{5.31}$$

Together with D_T from (5.30), inserted into (5.27) or (5.28), the turbulent burning velocity is a function only of the turbulent velocity fluctuation

$$S_T \propto \sqrt{D_T W} \propto u' \tag{5.32}$$

as seen in simple correlations for turbulent burning velocities from experiments (see Chapter 7). The thickness of the turbulent flame can also be calculated and is found to be of same order as the turbulent length scale.

Table 5.1: A(c) and it’s derivatives for some mixing controlled combustion models

	FLACS (H-M)	Eddy Break-Up	Bray (1990) model
w	$2.2\rho\frac{u'}{l_t}min(c, 1-c)\delta$	$w \propto \rho\frac{u'}{l_t}c(1-c)$	$w \propto \rho\frac{u'}{l_t}\frac{c(1-c)}{(1+\tau c)}$
$\frac{w}{\rho W}$	$\delta(c-c_q)min(c, 1-c)$	$\delta(c-c_q)c(1-c)$	$\delta(c-c_q)\frac{c(1-c)}{(1+\tau c)}$
$A(c)$	$\delta(c-c_q)\frac{min(c, 1-c)}{(1+\tau c)^2}$	$\delta(c-c_q)\frac{c(1-c)}{(1+\tau c)^2}$	$\delta(c-c_q)\frac{c(1-c)}{(1+\tau c)^3}$
$\frac{A_q}{c_q}$	$\frac{1}{(1+\tau c_q)^2}$	$\frac{1-c_q}{(1+\tau c_q)^2}$	$\frac{1-c_q}{(1+\tau c_q)^3}$
$\frac{dA_q}{dc_q}$	$\frac{1-\tau c_q}{(1+\tau c_q)^3}$	$\frac{1-2c_q-\tau c_q}{(1+\tau c_q)^3}$	$\frac{1-2c_q-\tau c_q+\tau c_q^2}{(1+\tau c_q)^4}$
$\frac{d^2A_q}{dc_q^2}$	$2\tau\frac{\tau c_q-2}{(1+\tau c_q)^4}$	$2\frac{\tau^2 c_q+2\tau c_q-2\tau-1}{(1+\tau c_q)^4}$	$\frac{-2\tau^2 c_q^2+3\tau^2 c_q+8\tau c_q-5\tau-2}{(1+\tau c_q)^5}$

$$\delta \propto \frac{S}{W} \propto \frac{D}{S} \propto \sqrt{D_T/W} \propto l_t \tag{5.33}$$

which also corresponds with results from experiments.The results from this analysis have been tested numerically in simulations of a flame, propagating in a 1D geometry. The results from the simulations and the analysis were about the same.

Since the flame has a thickness of the same order as the integral length scale, the grid cell size in simulations was (and must be) less than the integral length scale. If the grid cell is larger, the flame can not be resolved on the grid. The burning velocity obtained will then depend on the flame thickness obtained due to numerical diffusion. For a flame propagating from the closed end in a 1D channel, towards the open end, minimum flame thickness will be around 2 grid cells and the resulting minimum burning velocity will be proportional to the grid cell size, as shown in (5.34) for the H-M model.

$$S_{min} = \frac{1}{\rho_R}\int_{-\infty}^{\infty} w dx \approx \frac{1}{\rho_R}\int_{2\Delta x} 2.2\rho\frac{u'}{l_t} min(c, 1-c)\rho dx \approx 0.3u'\frac{\Delta x}{l_t} \tag{5.34}$$

For a flame propagating towards the closed end of a 1D channel, the burning velocity will however be zero if the flame is not resolved, because the diffusion of products toward the closed end then will be around zero.

Due to calculation time restrictions $\Delta x > 0.1m$ and due to turbulence theory $l_t < 0.03m$ for 3D calculations of explosions in offshore geometries. These laminar flamelet and eddy break-up models should therefore not be used for calculations in offshore or other geometries unless the turbulent length scale is resolved on the grid.

5.1.2 The KPP burning velocity analysis

Bray (1990) argues with background in a KPP analysis (determination of burning velocity done by Kolmogorov, Petrovski and Piskonov) of (5.6), done by Hakberg (1982) and others that a spectrum of possible burning velocities exists, limited from below by:

$$S_T = 2(D_T w^{\circ})^{1/2} \tag{5.35}$$

where the turbulent diffusion coefficient D_T is described by the gradient transport expression (5.30). The reaction rate at the leading end of the flame, w°, may be written as

$$w^{\circ} = \left(\rho^{-1}\frac{\partial}{\partial\tilde{c}}w\right)_{c \to 0} \tag{5.36}$$

For all four models evaluated $w^{\circ} = W$. Comparing (5.35) with (5.13) shows that $\Lambda = 0.25$ would give the same burning velocity for both analyses. The cold front quench analysis gives, however, a larger minimum value, $\Lambda \to 0.44$ when $c_q \to 0$, and will therefore always give a lower burning velocity than the KPP analysis.

The KPP analysis, which has been used by Bray to incorporate turbulent burning velocities from experiments into his model, gives only a minimum, not necessarily unique, burning velocity. The use of his model without a quench criteria will therefore give burning velocities greater than (or equal to) those from experiments. When a quench criteria is used the burning velocities will be to low.

5.2 Analytical determined burning velocities

5.2.1 The H-M model in FLACS

The reaction rate for turbulent combustion used in FLACS, before the FLACS 93 version, was the Hjertager-Magnussen (H-M) model, Hjertager (1982). This model was first presented as the eddy dissipation concept by Magnussen and Hjertager (1976). Versions of the model is still used in the EXSIM code and was used in the REAGAS code until 1995.

In an equation for Y_f as in FLACS, the reaction rate can be written as:

$$w_f = N_a \rho \frac{e}{k} min(Y_f, Y_{f0} - Y_f) \text{ when } \tau_e > \tau_{id} \tag{5.37}$$

where N_a is a constant, with the value 20 used in FLACS. The ignition delay time, τ_{id}, for the fuel is compared with the turbulent time τ_{e}, to establish whether there can be combustion or not. This is equivalent to a cold front quench criterion which depends on τ_{id}. The turbulent time scale is

$$\tau_e = 1000(k/\varepsilon) \tag{5.38}$$

The chemical time scale used is from shock tube experiments, with τ_{id} given from

$$\tau_n = P_n e^{E_n/(RT)} C_{fu_n}^{a_n} C_{ox}^{b_n} \tag{5.39}$$

where P_n, E_n, a_n and b_n are constants for fuel n., found from experiment and calculations of a shock tube with CHEMKIN, Arntzen (1992), Kee et al. (1980). T is the temperature of the gas and C_{fu} and C_{ox} are the concentrations of fuel and oxygen. When $\tau_e < \tau_{id}$ the reaction rate is equal to zero. The model is therefore mixing controlled with a cold front quenching criteria. This model for quenching of the flame is an attempt to include both strain effects and chemical effects on the flame.

The source term in the fuel equation, (5.38), can be transformed to a transport equation for c (5.40) as (5.1) and (5.2). The corresponding dimensionless reaction rate is then (5.41)

$$w = N_a \rho \frac{\varepsilon}{k} min(c, 1-c) = 0.11 N_a \rho \frac{u'}{l_t} min(c, 1-c) \text{ when } c > c_q \tag{5.40}$$

$$W = 0.11 Na \frac{u'}{l_t} \tag{5.41}$$

With the τ_{id} used in FLACS, c_q for methane and propane is between 0.19 and 0.36. c_q is here a function of the ignition delay time of the gas mixture (5.39) and the turbulent time (5.38). After replacement of temperature in (5.39) with $T = 293(1 + \tau c)$ and the turbulent time with $\tau_t = 9100(l/u')$, c_q can be found. For a stoichiometric mixture of fuel and air at atmospheric pressure, c_q can be represented approximately by

$$c_q \approx a(u'/l_t)^{0.06} \tag{5.42}$$

where the constant a differ with the fuel as seen in Table 5.2. Propylene has a longer ignition delay time and hence a larger c_q than propane. This results in lower a and lower calculated burning velocities and explosion pressures for propylene than for propane in FLACS simulations, in contrast to experiments where propane gives lower pressures than propylene.

The turbulent burning velocity is given by (5.13), with $D{=}D_T$ from (5.30) and W from (5.41).

$$S_T = \left(\frac{DW}{\Lambda}\right)^{1/2} = 0.44u'N_a^{1/2}\Lambda^{-1/2} \tag{5.43}$$

The burning velocity eigenvalue of the H-M model (5.26) can be approximated by (5.45), which when inserted to (5.44) give (5.46).

$$\Lambda^{-1/2} \approx 0.46(\tau c_q)^{-0.6} \tag{5.44}$$

$$S_T/u' = 0.2N_a^{1/2}(\tau c_q)^{-0.6} \tag{5.45}$$

With c_q from (5.43) and τ=6.5 inserted into (5.46), the turbulent burning velocity for different fuels with the H-M model is a functions of the constants a or b from Table 5.2, as seen in (5.47) and (5.48)

$$S_T/u' = 0.14a^{-0.6}(u'/l_t)^{-0.036} \approx 0.15a^{-0.6} \tag{5.46}$$

$$S_T/u' = b \tag{5.47}$$

Simulations with this model with different c_q gives about the same S_T as the theoretical predicted value from (5.48) when the grid resolution in terms of turbulent length scale was good enough. This strongly indicates that the eigenvalue analysis is correct.

The H-M model calculates a difference between different gases, but is not very influenced by strain. The burning velocity obtained with this model is however far too low. From experiments with propane and methane the ratio of turbulent burning velocity to velocity fluctuation, *b*, is known to be around 2 as shown with (7.20). If the model shall give a more representative burning velocity, the constant N_a must be increased with an order of magnitude to $N_a \sim 200$. The reason that the $N_a = 20$ used in FLACS-89 worked well for several explosion calculations is that the grid size used was too coarse to resolve the flame numerically. This resulted in a much thicker reaction zone and burning velocity than the model theoretically should give, as will be discussed for the β flame model in Section 5.3.

Table 5.2: Ratio of turbulent burning velocity to intensity from (5.45) - (5.47)

Gas	Acetylene	Hydrogen	Ethylene	Ethane	Propane	Propylene	Methane
a	0.025	0.035	0.10	0.145	0.191	0.195	0.235
b	1.37	1.12	0.60	.0.48	0.41	0.40	0.35

5.2.2 The eddy dissipation concept

This model is developed and used at the institute at NTNU where the author is registered with this thesis. The eddy dissipation concept, EDC, has also background in the H-M model. For a flame propagating isobaric in a stoichiometric premixed fuel-air mixture, the reaction rate for the eddy dissipation concept, Gran (1994), may be written as:

$$w \approx 11.2\rho\frac{\varepsilon}{k}min(c, 1-c) \tag{5.48}$$

The reaction rate in this concept depends on the residence time τ^* in a perfectly stirred reactor. A cold front quench criteria is then obtained for the product concentration, c_q, which corresponds to a temperature which gives $\tau^* \rightarrow \infty$ in a stirred reactor. In simulations the EDC is reported to give

$$S_T = 2.0u' \tag{5.49}$$

when the chemistry is fast compared with the turbulent time. The burning velocity is reported to be reduced through c_q when the chemistry becomes slower. The burning velocity from the cold front quench analysis is found by inserting (5.48) into (5.13).

$$S_T \approx 1.5u'\Lambda^{-1/2} \tag{5.50}$$

with Λ given by (5.26). The Λ needed to obtain the reported simulated results is $\Lambda \approx 0.6$. From (5.26) this Λ is obtained with c_q=0.01 and τ=6.5. The minimum c which corresponds to a temperature which gives a finite residence time in a stirred reactor is however likely to be much higher,

$$c_q \approx 0.2 \Rightarrow \Lambda \approx 6.4 \Rightarrow S_T \approx 0.6u' \tag{5.51}$$

This burning velocity is much lower than seen in experiments, so the reaction rate should be raised with an order of magnitude if such quench criteria are used. The EDC will of course give higher burning velocities if a too coarse grid is used, as discussed at the end of subsection 5.1.1.

5.2.3 EBU model

The Bray, Moss and Libby (BML) version of the Eddy Breakup (EBU) model has no quench criteria, makes no difference between different fuels and has the following reaction rate, with C_f=3.0

$$w = C_f\rho\frac{\varepsilon}{k}c(1-c) = 0.33\rho\frac{u'}{l_t}c(1-c) \tag{5.52}$$

The KPP analysis (5.35) used on the EBU reaction rate above gives

$$w^\circ = W = C_f\frac{\varepsilon}{k} \tag{5.53}$$

$$S_T = 0.88C_f^{0.5}u' = 1.52u' \tag{5.54}$$

which agree well with burning velocities from experiments. Velocities from KPP analysis, like (5.54), are however only minimum values. A fixed value is however needed and will be obtained with a cold front quench criterion. From the cold front quench analysis (5.24) for the EBU model, c_q=0.1 and τ=6.5 give $\Lambda = 2.58$ and

$$S_T = 0.27C_f^{0.5}u' \tag{5.55}$$

Comparing (5.54) and (5.5) shows that C_f has to be increased from 3 to around 30 to give a S_T similar to the one obtained in the KPP analysis for c_q=0.1. Other values for c_q and τ will of course require another value on C_f.

5.2.4 Bray´s model (1990)

Bray (1990) argues that the reaction rate is proportional to

$$w = \rho_R S_L I(K)\Sigma \tag{5.56}$$

where Σ is the flame surface to volume ratio and the factor I reduces the reactions due to strain, K. He propose Σ is proportional to $(u'/S_L)^n$. With n=1 from a fractal analysis he suggests:

$$\Sigma = \frac{3}{S_L}\frac{u'}{l_I}f(1-f) \tag{5.57}$$

Introducing (5.57) and ρ_R through (6.1) into (5.56), where the volume fraction of products, f, is given by (6.3), the reaction rate in the laminar flamelet model (5.56) becomes

$$w = 3\rho\frac{u'}{l_I}c(1-c)\frac{(1+\tau)}{(1+\tau c)}I(K) \tag{5.58}$$

$$w° = W = 3\frac{u'}{l_I}(1+\tau)I(K) \tag{5.59}$$

Bray (1990) has evaluated the burning velocity from the reaction rate in (5.59) with the coefficient D_T defined in (5.30) replaced by $D_T = \mu_T = 0.547u'l_I$, and argues with background in the KPP analysis (5.35) that his model will give

$$S_T = 2.56(1+\tau)^{1/2}I(K)^{1/2}u' \tag{5.60}$$

In an evaluation of turbulent burning velocities as function of strain rate in experiments Bray found that $S_T \sim u'$ at constant Karlovitz number and made the following relation (see Chapter 7), which now is used in FLACS and other explosion codes

$$S_T = 0.875uK^{-0.392} \tag{5.61}$$

By combining (5.61) and (5.62) a flamelet library for $I(K)$, (5.63), was made by Bray.

$$I(K) = 0.12(1+\tau)^{-1}K^{0.784} \tag{5.62}$$

Because Bray´s model does not have a cold front quench criterion it will give a burning velocity increasing with time, instead of following (5.62). A better approach is to introduce a cold front quench and combine (5.62) with (5.64) to obtain (5.65). The analytical burning velocity with a cold front quench criteria, with $c_q=0.05$,and τ=6.5 gives for this model Λ =1.85, which inserted into (5.13) gives

$$S_T \approx 0.94(1+\tau)^{1/2}I(K)^{1/2}u' \tag{5.63}$$

$$I(K) = 0.9(1+\tau)^{-1}K^{0.784} \tag{5.64}$$

This model will have the same problem with grid resolution of the turbulent length scale, as the three previous models, and are therefore like them useful for calculation of explosions in offshore geometries.

5.3 The β flame model

The β flame model was developed by the author, Arntzen (1993), as a solution to the problems with the combustion models analysed in the previous section. The combustion modelling was divided into two parts, flame and burning velocity modelling. The burning velocity eigenvalue analysis in section 5.1 is used in the β model to implement a flame with specified burning velocity into the CFD code. The β model avoids the grid requirement $\Delta x < l_t$ by introducing a new coordinate system through a β transformation for the combustion model (Butler et al.). Since we would like a flame as thin as possible, but still larger than the grid cell size Δ the turbulent flame is made thicker of order Δ / l_t through a β transformation where D_T is multiplied with Δ / l_t and W is divided with Δ / l_t (Thereby the name β model)

$$D_\beta \propto S\Delta \text{ and } W_\beta \propto S/\Delta \tag{5.65}$$

The product of the constants in D and W depends on the burning eigenvalue which again depends on τc_q, as shown in (5.26), and the larger D, the thicker flame. From (5.33), $\delta \propto D/S \propto \Delta$, e.g. the flame will have a thickness proportional to the grid cell size. The β model has been tested for a range of c_q , *pdf* of w through the flame ($A(c)$), W and D, with purpose of producing the thinnest possible flame.

The H-M model as used earlier in FLACS had c_q around 0.3 for methane, according to (5.42). From (5.27) $WD = 12S^2$ for $\tau c_q = 2$. In simulations W=4 S/Δ and D=3 $S\Delta$ were used and they resulted in the specified burning velocity, S. In the left part of Figure 5.1 the variation of mass fraction of products, c, mass of products, ρc, and reaction rate, w, through this flame is shown, as function of grid lines. A thin reaction zone (3 grid cell) is obtained, but the diffusion zone in front of the flame is about 9 grid cells, resulting in a flame 4 times thicker than the reaction zone. A flame zone of 12 grid cells from reactants to products is too wide to be practically useful for calculations on the coarse grid used in representation of 3D offshore geometries.

$\tau c_q = 0.325$ gives a thin reaction zone and a diffusion zone less than 1 grid cell thick. However a higher order numerical scheme, the van Leer scheme, presented by van Leer (1974), had to be implemented in the CFD code FLACS to keep the flame numerically thin. Numerical diffusion from the former scheme in FLACS, the Hybrid scheme, Patankar (1980), gave a minimum flame thickness which was twice as thick.

After testing a range of *pdf* of w through the flame, a modification of the *pdf* used in the H-M model (but with same $A(c)$) were chosen, resulting in the following reaction rate.

$$w_\beta = W\rho min(\delta(c - c_q), c, 9 - 9c) \tag{5.66}$$

where c_q and W correspond with the burning eigenvalue of (5.28) and therefore must satisfy

$$\tau c_q = 0.325 \tag{5.67}$$

$$WD = 1.37S^2 \tag{5.68}$$

The right part of Figure 5.1 shows the variation of mass fraction of products, c, dimensionless mass of products, $\rho c / \rho_R = c/(\tau c + 1)$, and reaction rate, w, through a flame as function of grid lines, with the values on W and D chosen as W=2.75S/Δ and D=0.5$S\Delta$. These values give, as seen in the figure, or from (5.70) a flame thickness around 4Δ. In FLACS values on W and D which decreases the flame thickness to around 3Δ has later been chosen.

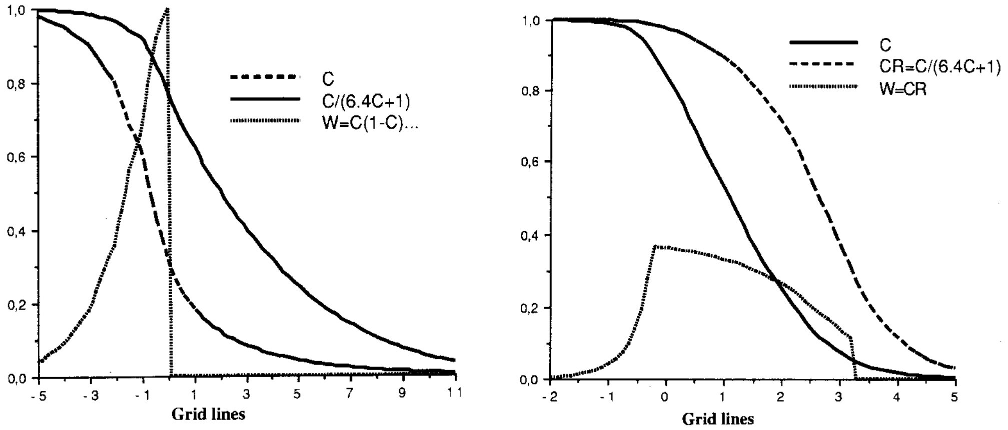

Figure 5.1 w, c **and** $\rho c/\rho_R$ **through the flame, for** c_q**=2.0 (left) and** c_q**=0.325 (right)**

Figure 5.2 shows the ratio between input and simulated burning velocities from simulations as function of input flame thickness, estimated as

$$\delta = 10\sqrt{D/W} \qquad (5.69)$$

for a range of D/W. c_q was 0.05 and the flame was propagating from the closed end in a 1D channel, towards the open end. The simulated burning velocity was calculated as described in next subsection. The minimum value of the reaction zone was around 2 Δ (seen by setting the diffusion equal to zero, D=0). When the input flame thickness is smaller than the minimum reaction zone, the burning velocities from simulations will be overestimated since the burning velocity is proportional with the reaction zone thickness. For flame thickness less than about 3Δ the flame is not properly resolved and the burning velocity increases, since the flame is thicker than assumed by the resolved β model. Values on W and D, giving a flame with thickness around 3Δ have therefore been chosen to be used in FLACS. A too thin flame also gives a too coarse resolution of the product gradient which results in numerical diffusion in the flow direction, which gives a wider flame and thereby increased flame thickness.

Tests of a flame propagating towards the closed end of a 1D channel gave opposite a decrease in the burning velocity as the flame thickness decreased. Since the flame here propagates in the opposite direction of the flame, the numerical diffusion makes the diffusion smaller and it approached zero for $\delta < 0.25$ and gave then no burning velocity. For a thin flame, as in FLACS, propagating towards the closed end, the burning velocity seems to be around 10% too low, compared with 10% too high for a flame propagating from the closed end. This may be explained by numerical diffusion which transports products in the flow direction. The burning velocity which is a function of diffusion of product in the burning direction will therefore be decreased for a flame propagating inwards and increased for a flame propagating outwards.

The ability of the β flame to propagate with any given burning velocity was investigated and showed that the flame performed well, unless the time steps were too long, compared with the ratio flow velocity to grid size. The β flame needs a resolution in both time and space to have the numerical diffusion under control and keep the flame thickness constant. A function which compensates the numerical diffusion, as function of time step, grid size, flame direction and velocity field has been made for the FLACS code to obtain more accurate burning velocities. It is, however, probably better to introduce a numerical scheme with more accuracy in space and time, to avoid the numerical diffusion.

The β flame responds also well to transient burning velocities in a transient turbulence field, as shown in Popat et al. (1996). For very high burning velocities compressibility effects become important and it is difficult to define a simulated burning velocity.

Another advantage with a flame model, like the β model, compared with the combustion models presented, is that both laminar and turbulent burning can be modelled within the same model, when the burning velocity, *S*, is a function of known variables. Representation of a laminar flame without a β transformation would have required a very fine grid since the laminar flame thickness is typically a tenth of a millimetre.

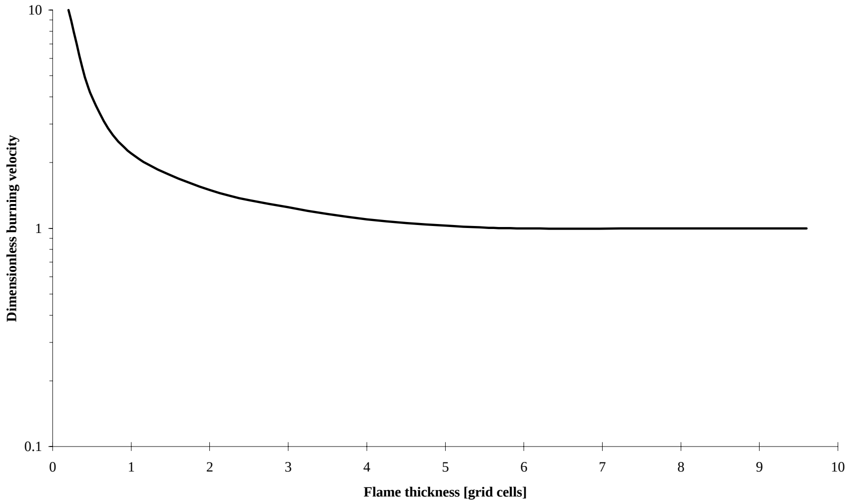

Figure 5.2 Burning velocities from simulations as function of flame thickness

5.3.1 Estimation of burning velocities from simulations

The burning velocity of a flame is the velocity with which the flame propagates into the unburned reactants. The flame velocity of a flame is the absolute velocity the flame moves with. The burning and flame velocity are similar only when the reactant is quiescent.

The burning velocity from simulations is therefore calculated from the increase per time in mass of products, divided by density of reactant and flame area. In 1D simulations the flame area is constant and equal to the grid cell area.

In 2D and 3D simulations the flame area varies with flame radius.

The flame area is best estimated from the volume of products assuming the flame propagates spherically (circularly) outwards from a point. Estimation of flame position based on mass fraction of product, *c*, was earlier used in FLACS. This give wrong estimates since the density is not constant, but around 7 times larger in reactants than in products.

5.3.2 β flame model in 2D and 3D

The β model was developed in 1D. In 2D and 3D this 1D model burns too slowly when the flame radius is of the same order as the flame thickness, as shown in Figure 5.3. This is due to the fact that the radius of the reaction zone is more than one grid cell smaller than the radius of the "products". This can be seen in Figure 5.1b, where the reaction zone, *W*, has the centre around grid line = 1, and the mass of products ρ*c* has it's centre around grid line = 2.5. For small flame radii the reaction zone area is much smaller than the flame area based on volume of products.

A correction function, f_r, depending on the ratio, reaction zone thickness divided with flame radius, is necessary for the model to give the specified burning velocity in 3D. The function depends on the flame thickness and quench criteria chosen, and may for the chosen variables be described by

$$f_r = max\left(1, 2\left(\frac{\Delta}{r}\right)^{1/4}\right) \tag{5.70}$$

A thinner flame will decrease the needed correction for a given flame radius, since the ratio of flame radius to flame thickness then will be larger. The flame should therefore be made as thin as possible, to minimize the needed correction due to flame curvature.

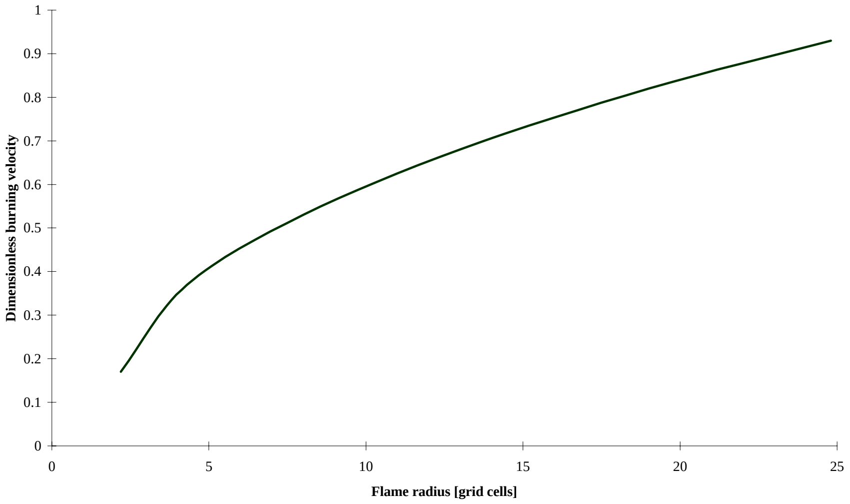

Figure 5.3 Dimensionless burning velocities from simulations as function of flame radius

In the experimental geometries, with a flame propagating spherically outwards, the flame radius is normally known, but in more realistic geometries this ratio may be more difficult to define. Some work has been done to find the inverse radius, the curvature of the flame, as a function of the product concentration field (field of *c*), but in complex geometries this seems about impossible. The distance between the burning grid cell and the ignition grid cell are therefore used to estimate the flame curvature in any geometry. If the flame has a large curvature far away from ignition, due to obstructions in the geometry or that the flame has entered new compartments, the burning velocity in simulations will be too low.

Figure 5.4 shows the reaction rate in each cell, for a flame propagating freely outwards from a point, and demonstrates that the model has a spherical flame propagation. A better and more accurate way of implementing a flame to a grid thicker than the flame, where problems like flame curvature is avoided, is SIF, the Simple Interface Flame model, which is presented in the next chapter.

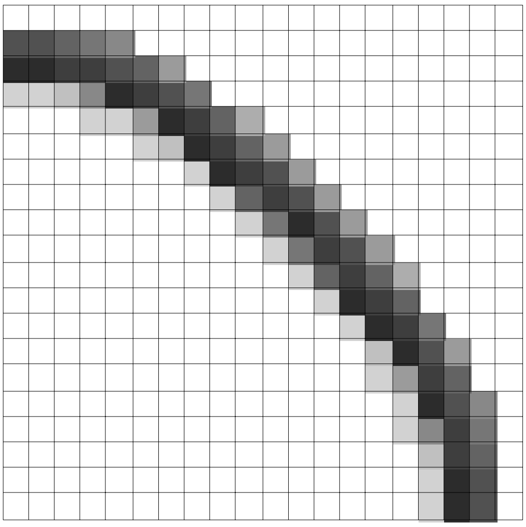

Figure 5.4 Reaction zone for the β flame propagating from a point

5.3.3 Compensation for burning towards walls

In flame propagation towards walls, the reaction zone becomes thinner until it is only one grid cell thick. Some of the reaction rate is then lost. The total reaction rate over the flame must satisfy the burning velocity

$$\int w \partial x = S \rho_R \tag{5.71}$$

A compensation model in cells located by walls must add a reaction rate, $w+$ to w, to satisfy (5.72). This w+ can be found as function of c, by summation of the reaction rates in all cells on the reactant side, for different values of c, in ordinary 1D flame propagation.

$$w+(\mathrm{c}) = \int_{x(c)+\Delta x/2}^{\infty} w \partial x \tag{5.72}$$

The function found is only valid with values for c_q, τ, W and D it was made from. τ will vary with fuel type, and decreases for rich and lean fuel-air mixtures, so the function should include a τ dependence. From Figure 5.1b, $w+$ for this β model can be estimated as

$$w+ \approx 6c^2 S\rho / \Delta \tag{5.73}$$

Flames propagating parallel with the wall shall have no compensation. The degree of adjustment is found as the product of normal vectors for the wall and for the flame $\vec{F} = -\nabla c$

It should be noted that this correction and the corrections due to numerical diffusion or small flame radius should not be added together since this may lead to a reaction rate corresponding to a much too high burning velocity. Like the other correction models, it is only valid for the specified values on flame thickness and quench criteria it was made for. For other values new correction models are needed.

5.4 Ignition modelling

Ignition in the H-M model, Bakke(1986) was modelled by assuming that at time zero half of the flammable mixture in the ignition cell is converted to products. This high c was needed due to the high quench criteria (5.42) used. With this concept, the time between ignition and peak explosion pressure will depend largely on the grid size chosen and will normally not agree with the experimental results.

The ignition model implemented with the β model, converts reactants to products at rate given by flame area and burning velocity in the ignition cell. The corresponding flame area for a given volume of a sphere is given by

$$A = \pi^{1/3}(6V)^{2/3} \tag{5.74}$$

where the flame volume is proportional to the volume fraction of products, f, which again is a function of mass fraction of products given by (6.3). The burning velocity is modelled with a dependence on gas mixture and flame radius, as described in Chapter 7.

As product gradient has been made and products have been transported to the surrounding cells, products are also made here. The reaction in the ignition cell is then adjusted so the total conversion corresponds with total volume of products. This model secures the same conversion as for the real flame and gives a good agreement between simulated and experimental time to peak pressure, independent of grid size chosen.

5.5 Combustion and β flame model in FLACS

The presented source term combustion models may represent the combustion in situations like an internal combustion engine where the grid cell size can be of the same order or smaller than l_t. In gas explosion simulations done with FLACS, the grid cell may be an order or two of magnitude greater than l_t. If they should be of the same order, the number of grid cells may typically be increased from 10^5 to 10^{11} and the time it takes to do the simulation will increase with a factor of 10^8, since the time step length is proportional with the grid size.

The β model has therefore been used instead of the H-M combustion model, in every version of the FLACS code from 1993 to 1997.

The β model is developed for, and should preferable be represented through the equation for mass fraction of products (5.1). In FLACS it is represented through the equation for fuel (5.2). The product fraction is changed only due to combustion, but the fuel fraction may also be changed due to a change in the mixture fraction. The relation between mass fraction of products, mass fraction of fuel and mixture fraction is described by (3.24) and (3.28). To avoid a change in fuel fraction far away from the flame zone, due to the implemented β diffusion, which will be in conflict with the mixture fraction, the β diffusion shall only be used near the flame, typically for $0.001<c<0.999$. Outside the flame area the effective (normally turbulent) diffusion should be used.

In simulations of combustion in areas where the fuel is not mixed with the oxidant, the flame will be a diffusion flame instead of a premixed flame where the reactant is mixed before combustion. In diffusion flame the reaction rate is controlled by the mixing of reactants given by the diffusion, instead of the burning velocity as in premixed flames. The β diffusion should therefore only be used in premixed areas, which may be characterized by the equivalence ratio, E, e.g. by $0.5 < E < 1.5$, and near the flame $0.001<c<0.999$. Outside these areas the effective diffusion must be used to avoid a too large diffusion and thereby a too fast reaction rate.

The β model has some drawbacks, and most of them were described by Arntzen (1993). The flame in the model has been chosen to be around 3 grid cells thick. If the flame becomes thicker the burning velocity will be too large and if it becomes thinner it will be too small.

In flame propagation towards walls, the flame becomes thinner until it is one grid cell thick. A compensation model near walls is needed to keep the burning velocity high enough. The flame propagation is also affected by the curvature of the flame. The reaction zone is located around one grid cell behind the centre of the flame. For small flame radii the reaction zone area is much smaller than the flame area. This can be compensated when the flame radius is known, as in a free flame propagation from a point. However when the flame burns from one room to another the flame radius is not known and a correction is not possible.

In simple 1D calculations the flame becomes too thin and burns too slowly when the flame burns towards a closed end. In calculations toward an open end the flame becomes too thick and burns too fast. The reason for this is that this flame model needs a resolution in both space and time. The burning velocity error is around 10% for low flame velocities, below 10 m/s. For higher flame velocities the error becomes larger since the flame can be moved longer in each time step. Shorter time steps can be introduced in connection with high flame velocities, or, as in FLACS 96, another compensation model can be introduced.

Turbulence production is crucial in the reaction zone and should be avoided. If this production is excluded in the reaction zone, with the three grid cell thick β model, some of the turbulent buildup will be neglected, but if it is included unphysical turbulence may be generated.

Despite the drawbacks, the β model is however an uncomplicated flame model which has been used for several years in explosion simulations, where it has given acceptable results in most situations.

5.6 Other flame models

The combustion model in the COBRA code from British Gas, Catlin et al. (1995) also consists of a burning velocity model and a flame model based on the burning velocity analysis of Catlin and Lindstedt (1991). This flame model does not include a β transformation, as the β model, so the flame thickness therefore becomes equal to the turbulent mixing length. The mixing length must therefore be resolved by the numerical grid. COBRA includes an adaptive grid algorithm but in real offshore geometries it is not possible to resolve the mixing length. The mixing length must therefore be given a value equal to, or larger than, the grid cell size. This length scale will typically be much larger than the real length scale, so the decay of turbulence will be too small and the turbulence intensity will be overestimated farther downstream obstructions. This high length scale will however secure a rapid buildup of the transient turbulence field, as shown in Chapter 4.

Flame models where the flame is represented as an interface as the SIF model, which are presented in next chapter.

The G flame model, where the flame front is represented as a level set of a scalar field $G(\vec{x}, t)$,

$$\frac{\partial G}{\partial t} + U \cdot \nabla G = S|\nabla G| \tag{5.75}$$

where U is the velocity field of the unburned mixture and S is the burning velocity. G takes the values 1 in reactant, 0 at the flame front and -1 in products. The model is presented by Aldredge (1992) and is implemented in commercially available CFD codes like FLUENT. The G model has not been tested in FLACS since there already exists two flame models here.

5.7 Summary

Combustion models have been analysed analytically. With good enough grid resolutions, with respect to turbulent length scale, the burning velocities obtained in simulations were grid independent and similar to the analytical results. On coarser grids the flame thickness increases and results in an increase in the burning velocity, since the reaction rate is unchanged.

The analytical solution of combustion models have been used together with a β transformation to make the β flame model, which propagates with a specified burning velocity and has a specified constant flame thickness, e.g. three grid cells. This flame model uses correction functions, depending on flame thickness, due to numerical diffusion, flame curvature and burning toward walls

The van Leer scheme had to be implemented in the CFD code to keep the flame thin. Numerical diffusion from the former scheme in FLACS, the Hybrid scheme, Patankar (1980), gave a minimum flame thickness which was twice as thick.

6 SIF, Simple Interface Flame model

The combustion model in FLACS consists of a flame model and a burning velocity model. The flame model shall give the localization and area of the flame.

The FLACS versions since 93 use the β flame model, described in the last chapter and developed by Arntzen (1993a). This flame model has some drawbacks, like a several grid cells thick flame. An alternative flame model, SLIC, the Simple Line Interface Calculation, was implemented and tested in a 2D simplified version of FLACS, Arntzen (1993a). The tests showed that SLIC could be a better flame model and it was therefore decided to develop this concept for the general 3D version of FLACS. In 3D the flame is not a line (as in 2D) but a surface. The name of the model is therefore modified to SIF, the Simple Interface Flame model.

The idea behind SIF is very simple, the gas consists of reactants and products. The interface between reactants and products is the flame. The flame is then represented with a reaction front of zero thickness which separates the zones with reactants and products, and converts reactants to products at a rate depending on burning velocity and flame area. Premixed flames are less than a millimetre thick for laminar flames and order of integral length scale (which is around 10% of obstruction dimension) thick for turbulent flames. These thicknesses are normally much smaller than the dimension of the grid cells, 0.4 to 1.0 m, used to represent a geometry numerically in the FLACS code.

The technique of replacing the flame structure with a discontinuity has been used by Noh et al. (1976), Chorin (1980), Ghoniem et al. (1982), Barr et al. (1982) and Sethian (1984). More recently, Bielert et al. (1996) presented different front tracking methods and concluded that the Volume of Fluid (VOF) gave a better representation of the flame than SLIC. The methods presented in literature have however a lot of limitations compared with requirements for a flame model in 3D FLACS. They are only developed for 2D, the pressure is mostly constant and the volume expansion is small. The SIF model which should be used in FLACS must be developed for 3D compressible flows with large volume expansion. The model must also handle grid cells with different sizes in each dimension and wall faces with porosity between zero and one, due to representation of the geometry.

6.1 Description of SIF

The information needed for tracking of the flame is the status of the cells and the faces between them. Both the cell and the faces can be either reactants, *R*, products, *P*, or a mixture, *M*. If a cell face is totally blocked (has zero porosity), it can have different status on each side, e.g. *R* and *P*. The SIF flame is always located crossing cell and cell faces, it never crosses the corners between cells.

The flame is moved from one cell into a neighbour cell with products, by convection, and to a neighbour cell with reactants by combustion or convection. The flame is located in cells with status *M*.

The mass of product is represented by the density and mass fraction of products in each cell. The relation between the density in reactant, ρ_R, the density, ρ, expansion ratio, τ, and mass fraction products, c, is defined as

$$\rho_R \equiv \rho(1 + \tau c) \tag{6.1}$$

where the expansion ratio is defined from the density in reactant and product as

$$\tau \equiv \frac{\rho_R}{\rho_P} - 1 \tag{6.2}$$

.

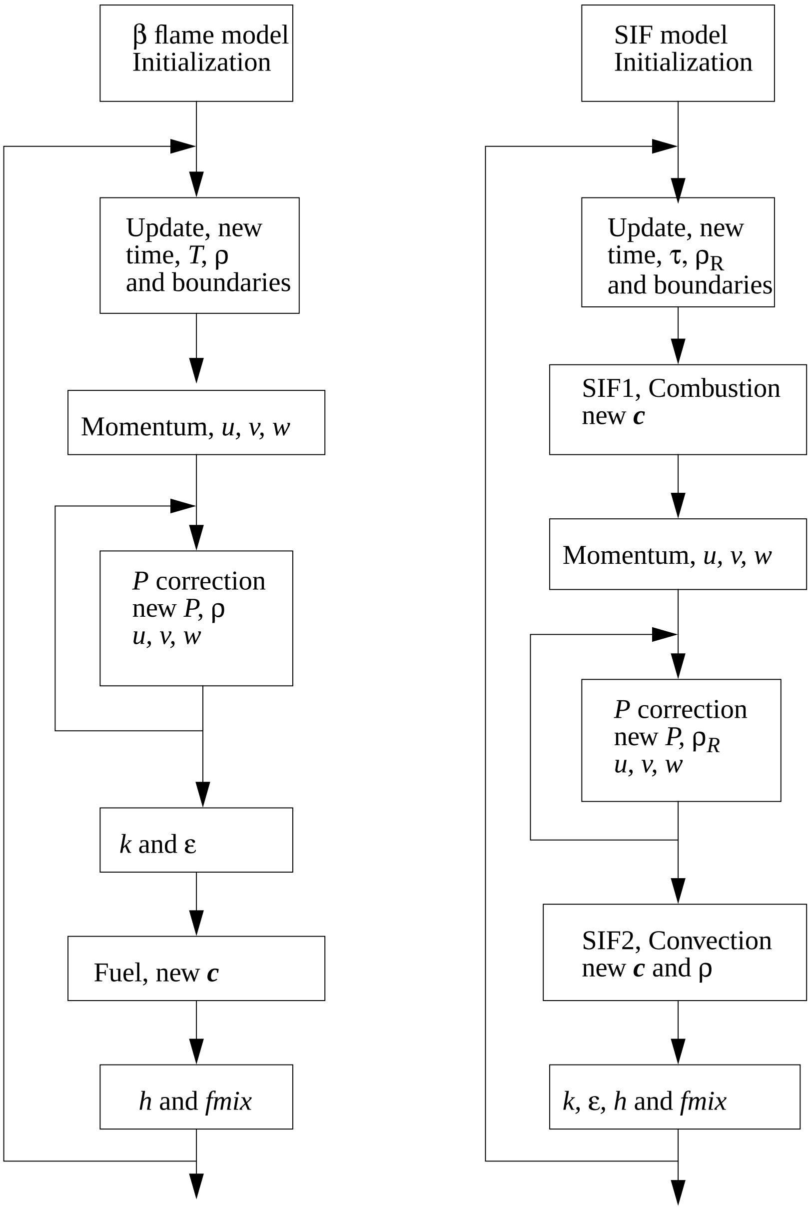

Figure 6.1 FLACS algorithms for the β flame model (left) and SIF model (right)

The mass fraction of products is a global variable in FLACS. The volume fraction of products, f, is a local variable used in estimation of flame areas and convection of the flame. The relation between them is

$$f \equiv c\frac{1+\tau}{1+\tau c} \tag{6.3}$$

6.1.1 The SIF algorithm

The main differences between SIF and the β flame model on an algorithm basis in FLACS are shown in Fig. 6.1. For each time step, both start with the update routine and calculation of values on the boundaries.

In the combustion routine, SIF1, reactants are converted to products at a rate as function of flame area and burning velocity. This results in an increase in the mass fraction of products, c.

The momentum equation gives a velocity field based on pressures from previous time step. The pressure correction routine for compressible flows, used with the β model, corrects the pressure, density and velocity field and secures that the continuity equation is satisfied. The equation of state is however normally not satisfied in a reactive flow. A modified pressure correction routine, which also satisfies the equation of state and gives the density in reactant, has been developed and implemented with SIF.

In the convection routine, SIF2, reactants and products are convected from one cell to another at a rate given by the velocity field. From this convection new mass fraction of products, c, and density, ρ, are calculated.

The β flame model uses the same burning velocity as SIF to calculate the amount of reactants converted to products in the fuel equation. This partial differential equation also handles the convection of reactants and products. The equations for turbulence enthalpy and mixture fraction are solved equally in the two algorithms.

6.1.2 Connection between cells

In FLACS porosity is used to represent the geometry on the grid. The grid cells have a volume porosity and the cell faces have an area porosity. An ongrid object will typically give zero area porosity on the cell faces where it is located. Subgrid objects are smaller than the grid cells and will give an area porosity between zero and one in the cell walls they influence. Cell faces located away from objects have area porosity one.

An algorithm is needed, to decide whether the flame can move from a cell to all or some of the 26 neighbour cells. This is done by evaluation of each of the eight corners separately. The flame can move to one of the 7 neighbours located around a corner if there is a passage (porosity greater than zero) at all faces on a route, limited into the eight cells, between two cells.

Figure 6.2 shows a 2D example with an obstruction located below cell *P*. The flame can move from cell *P* to all the surrounding cells except cell *SW*. It has a direct passage to *W* and *E*, and an indirect to *SE* and *S*. Cell *P* has therefore a connection with all surrounding cells except cell *SW*. From the figure one may argue that the flame should not be moved to cell *S* and *SE*, but the algorithm above is needed to obtain a consistent flame representation.

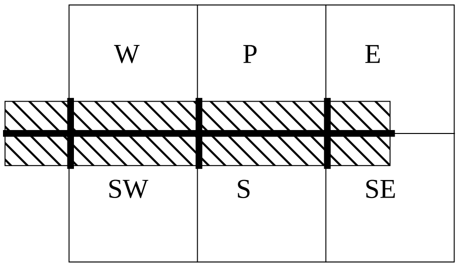

Figure 6.2 Representation of an obstruction on the numerical grid

6.1.3 Combustion

In the combustion part of SIF, mass fraction of products, *c*, is increased due to combustion. *c* is the only variable which is changed. How much *c* is increased depends on the burning velocity, *S*, and the relative flame area in the cell, *A*. The change of mass of product in a cell through combustion in a time step Δt is

$$\rho(c_1 - c_0) = S\rho_R A \Delta t \tag{6.4}$$

where both densities are known from last time step. The burning velocity is found with the burning velocity model, Arntzen (1993b), as with the β flame model. The flame area is found with a model which is outlined below.

If $c_1 \geq 1$ all reactants in the cell have been burned during the time step. The flame is then moved to all of the 26 neighbour cells with which it has connection and which contains reactants. *c* becomes one after a fraction of the time step $\Delta t - \Delta t^*$. Burning takes place in the remaining part of the time step.

$$\Delta t^* = (c_1 - 1)\frac{\rho}{S\rho_R A} \tag{6.5}$$

in those of the six closest neighbour cells which the flame was moved to, which contained only reactants.

When products from rich and lean gas air mixtures is mixed, the remaining reactions occur immediately, “mixed is burnt” in SIF, whereas the β model has an unphysical reaction rate which is inverse proportional to the grid cell size.

6.1.4 Flame area

The flame area in a cell depends on the orientation of the flame. Based on the status at each of the six cell faces (*P*roduct, *R*eactant or *M*ixture, at the faces *w, e, s, n, b, t*), 20 different types of flame orientations can be identified. The status on the two faces in each of the three directions have been grouped together to identify these types.

Since the flame is an interface crossing cells and cell faces (never the corners between cells), there is only one possibility that the six faces contain both an *R* and a *P*. That is for the 1D flame, with face status *RP* in one direction and *MM* in the two other directions, which have been named type 1.

For all other situations, the six faces will be a combination of either *R* and *M*, or *P* and *M*. This has restricted the possible combination of faces considerably. Based on the status of the faces in each direction, 20 different types can be identified. If the status is *MM* in one of the directions the flame may be seen as a 2D flame where the flame type can be found from Table 6.1, depending on the face status in the two other directions.

Table 6.1: Flame type for cells with face status MM in one direction

	RR	*RM*	*MM*	*PM*	*PP*
RR	6	7	2	X	X
RM	7	4	8	X	X
MM	2	8	12	10	3
PM	X	X	10	5	11
PP	X	X	3	11	9

Face status *RM, RM, RM* is named type 13, and *PM, PM, PM* is named type 14. The remaining six types are shown in Table 6.2, where the status is *RR* and *PP* in at least one direction. No other types of flame orientation can exist.

Table 6.2: Flame type for cells as function of face status in all three directions

RR	*RR*	*RM*
RR	15	16
RM	16	17

PP	*PP*	*PM*
PP	16	15
PM	17	16

The flame area is for most flame types a function of volume fraction of products, *f*, and for some also of flame direction in the cell, represented by the flame vector $\vec{F}$ as shown by Gjesdal (1996).

$$\vec{F} = \frac{\nabla F}{|\nabla F|} = \left[F_x \; F_y \; F_z\right] \tag{6.6}$$

$$\nabla F = \left[f_e - f_w,\; f_n - f_s,\; f_t - f_b\right] \tag{6.7}$$

The values of *f* at the cell faces are determined by the state of each face; the value is given by interpolation if the flame bisects the face, otherwise a value of zero or unity is chosen depending on whether the face has only reactants or products.

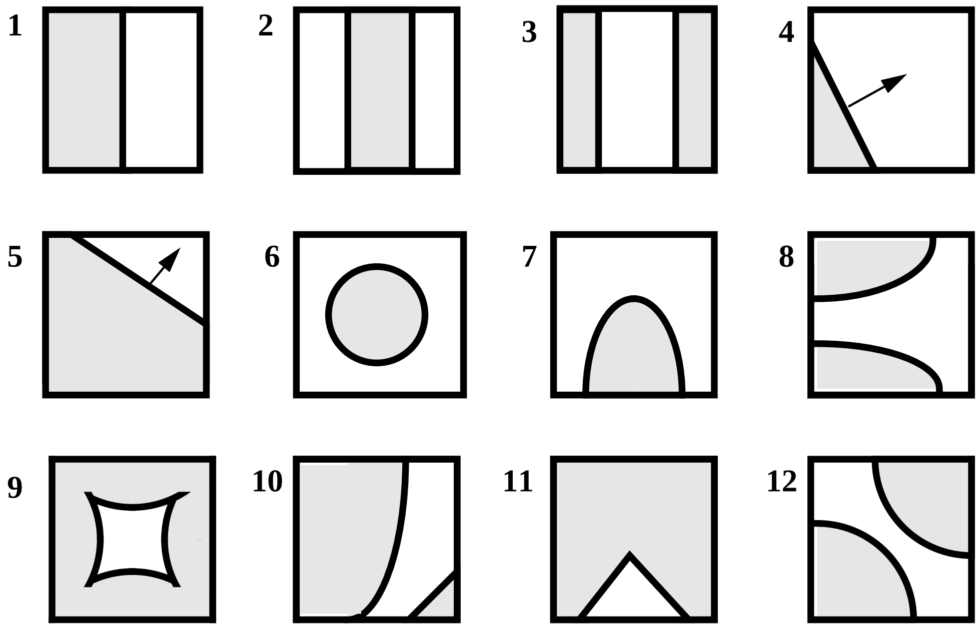

Figure 6.3 2D flame orientation, type 1 to 12

The flame orientation developed is more similar to the 2D Volume Of Fluid, Bielert et al. (1996), flames than those of SLIC, since the VOF gives a better representation of the flame.

2D flame orientations are shown in Figure 6.3. The flame orientation type 1 is the most common type. Type 2 is most likely in an area ignition cell and type 3 is found when two flames meet. The relative area (per volume) in cells of type 1, 2 and 3 can from Fig. 6.3 easily be seen to be

$$A_1 = 1/\Delta x \tag{6.8}$$

$$A_2 = A_3 = 2/\Delta x. \tag{6.9}$$

Type 4 and 5 are 2D corners and the second most common types. The area of type 4 is given by

$$A_4 = \left(2f\left(\frac{F_x}{F_y(\Delta y)^2} + \frac{F_y}{F_x(\Delta x)^2}\right)\right)^{1/2} \tag{6.10}$$

when the flame sector is represented by a straight line. For *f>1/2* or if *f* in the cells around is low compared with *f* in the cell, the area A_4 is reduced since it is too much products in the cell that it can be part of a cylindrical flame shell. The area of type 5 is given by

$$A_5 = \left(2(1-f)\left(\frac{F_x}{F_y(\Delta y)^2} + \frac{F_y}{F_x(\Delta x)^2}\right)\right)^{1/2} \tag{6.11}$$

Type 6 and 7 is most likely in 2D ignition cells, with respectively line and area ignition.

$$A_6 = 2\sqrt{\pi f} \approx 3.5\sqrt{f} \tag{6.12}$$

$$A_7 = 1.5\sqrt{\pi f} \approx 2.7\sqrt{f} \tag{6.13}$$

Type 8, 10 and 12 are more likely 3D types, a part of a sphere shell, rather than a 2D type. The faces with M are then as follows. For type 8, two faces look like type 1, two look like type 4 and the last look like type 5. For type 10, two faces look like type 1, two look like the cut planes through type 5, and the last look like the cut plane through type 4. For type 12, the six faces could be any combination of type 4 and 5, where 3 of each is most likely. The flame areas in 3D type 8 and 10 can have values between $\sqrt{2}/2$ and $(\sqrt{2}+1)/2$

$$A_8 \approx min(1.2, 0.5 + 0.75f)/\Delta x \tag{6.14}$$

$$A_{10} \approx min(1.2, 0.5 + 0.75(1-f))/\Delta x \tag{6.15}$$

Since the flame in type 12 crosses all six faces, the area is estimated independent of f

$$A_{12} \approx 2/\sqrt{\Delta x^2 + \Delta y^2 + \Delta z^2} \tag{6.16}$$

Type 9 and 11 are cells where flames from different directions meet.

$$A_9 \approx 6\sqrt{1-f} \tag{6.17}$$

$$A_{11} \approx 4\sqrt{1-f} \tag{6.18}$$

The rest of the flame orientation types are definitively 3D types. Type 13 and 14 are 3D corners, and they are the most common 3D types. Type 13 cells have R and M faces in all three directions. The 3 cell faces with M will lock like type 4. Type 14 cells have P and M faces in all three directions, where the 3 cell faces with M will lock like type 5. The flame area of type 13 is

$$A_{13} = \frac{1}{2}\left(\frac{6f}{F_x F_y F_z}\right)^{2/3}\left(\left(\frac{F_x F_y}{\Delta z}\right)^2 + \left(\frac{F_x F_z}{\Delta y}\right)^2 + \left(\frac{F_y F_z}{\Delta x}\right)^2\right)^{1/2} \tag{6.19}$$

For $f>1/5$ or if f in the cells around are low compared with f in the cell, the area A_{13} is reduced since the cell contains too much products that it can be part of a sphere. If this is an ignition cell, the area is better described by

$$A_{13ignition} = 2.4\left(\frac{f^2}{\Delta x \Delta y \Delta z}\right)^{1/3} \tag{6.20}$$

The flame area in type 14 cell is

$$A_{14} = \frac{1}{2}\left(\frac{6(1-f)}{F_x F_y F_z}\right)^{2/3}\left(\left(\frac{F_x F_y}{\Delta z}\right)^2 + \left(\frac{F_x F_z}{\Delta y}\right)^2 + \left(\frac{F_y F_z}{\Delta x}\right)^2\right)^{1/2} \tag{6.21}$$

Type 15 to 17 have reactants, R, on both walls in at least one direction. They are therefore typical only in cells where ignition takes place, in a point or on a line. If they exist outside the ignition area, their area is more unclear, and have therefore been set to a much lower value.

Type 15 is a typical point ignition cell, with reactants on all six walls. Inside it looks like type 6

$$A_{15} = \pi^{1/3}(6f)^{2/3} \approx 4.8 f^{2/3} \tag{6.22}$$

Type 16 is typical after ignition in two neighbour cells. It has reactants on five of the walls. Inside it looks like type 7.

$$A_{16} = \frac{1}{2}\pi^{1/3}(12f)^{2/3} \approx 3.8 f^{2/3} \tag{6.23}$$

Type 17 is typical after ignition in four neighbour cells. Inside it looks like type 4.

$$A_{17} = \pi^{1/3}(3f)^{2/3} \approx 3.0 f^{2/3} \tag{6.24}$$

Type 18 to 20 have products on both walls in at least one direction. They are typical cells where flame from different directions meets. Inside, type 18 looks like type 9, type 19 looks like type 11 and type 20 looks like type 5.

$$A_{18} = 6(1-f)^{2/3} \tag{6.25}$$

$$A_{19} = 5(1-f)^{2/3} \tag{6.26}$$

$$A_{20} = 4(1-f)^{2/3} \tag{6.27}$$

6.1.5 New pressure correction equation for reactive flows

The so-called pressure equation shall give a new pressure field, with corresponding change of velocity and density field, which satisfies the continuity equation and the equation of state, as well as the momentum equation. The correct pressure is the sum of a guessed pressure *p** and a pressure correction *p'*.

$$p = p^* + p' \tag{6.28}$$

Also the correct density in reactant and velocity can be expressed by guessed and corrected values, where the corrected values can be expressed as functions of the pressure correction

$$\rho_R = \rho_R^* + \rho_R' = \rho_R^*\left(1 + \frac{p'}{\kappa p^*}\right) \tag{6.29}$$

$$u_w = u_w^* + u'_w = u_w^* + d_w(p'_W - p'_P) \tag{6.30}$$

In FLACS, the momentum equation gives a first guess of the velocity field based on the pressure field from last time step. The correction of the guessed pressure and velocity field, to obtain fields which satisfy the continuity equation is done with the traditional SIMPLE algorithm, Patankar (1980).

The pressure correction equation in FLACS, supplemented with a modification for compressible flows, needs the density (as function of pressure) after the convection.

In FLACS it is assumed that the fraction of products in the control volume is the same after convection as before. This is normally true only if the grid cell contains only reactants or only products.

If products are entering and reactants leaving a control volume, the density should decrease if the pressure is constant. The numerical consequence of this is that when a flame is burning with constant velocity, the outflow will be too low if the outflow is reactants and too high if it is products. The average flow velocity is more accurate, resulting in a jump in flow velocity as the flame moves from one control volume to another. This effect gives relatively large velocity oscillations in SIF calculation. With the β flame model the problem is smaller than with SIF, since the flame is several grid cells thick.

In a simplified situation where the pressure is constant, also the density in reactant and products will be constant. The flow rates can then be found from a volume of fluid method, as shown by Sethian (1984) for 2D SLIC calculations with constant pressure. In a gas explosion the pressure will vary with time so this method is not possible to use in FLACS.

The pressure correction equation is based on conservation of mass. As shown above a problem arises when the density after convection is a function of density of in- and out-flows in addition to pressure. This problem has been avoided by introducing a pressure correction equation based on conservation of both mass and mass of products as shown below.

Mass conservation (velocities are done dimensionless, $U_i = U_i \Delta t / \Delta x_i$) gives:

$$\rho_2 = \rho_1 + \sum \rho_x U_x \tag{6.31}$$

Product conservation:

$$c_2 \rho_2 = c_1 \rho_1 + \sum c_x \rho_x U_x \tag{6.32}$$

The relations between density in the cell and in the reactant are

$$\rho_2 + \tau \rho_2 c_2 = \rho_{2,R} = \rho_R{}^* + \rho_R{}' \tag{6.33}$$

$$\rho_{1,R} = \rho_1 (1 + \tau c_0) \tag{6.34}$$

The equations for conservation of product and mass can be added together when we assume that τ has the same value at the cell walls as in the cell. This assumption is valid except when there is variation in enthalpy or mixture fraction, typically around the boarders of a gas cloud. If τ is larger at the out-flowing cell face than in the grid cell, or lower at the in-flowing face, then the density in the grid cell will be lower than it should, with background in the equation of state.

$$\rho_1 + \sum \rho_x U_x + \tau c_1 \rho_1 + \tau \sum c_x \rho_x U_x = \rho_R{}^* + \rho_R{}' \tag{6.35}$$

$$\sum (1 + \tau c_x) \rho_x U_x = \rho_R{}^* + \rho_R{}' - \rho_1 (1 + \tau c_1) \tag{6.36}$$

In 1D the equation is reduced to

$$\rho_{Rw} U_w - \rho_{Re} U_e = \rho_R{}^* + \rho_R{}' - \rho_1 (1 + \tau c_1) \tag{6.37}$$

where the fluxes can be expressed by guesses and corrections of densities and velocities

$$\rho_{Rw} U_w = \rho_{Rw}{}^* U_w{}^* + \rho'_{Rw} U_w{}^* + \rho_{Rw}{}^* U_w{}' \tag{6.38}$$

The density and velocity corrections have been expressed by pressure corrections

$$\rho_{Rw}U_w = \rho_{Rw}^*\left(U_w^* + U_w^*\frac{p'_w}{\kappa p^*} + d_w(p'_W - p'_P)\right) \tag{6.39}$$

where the pressure corrections between two cells is modelled with upstream values

$$U_w^*\frac{p'_w}{\kappa p_w} = \|U_w^*, 0\|\frac{p'_W}{\kappa p_W} - \|-U_w^*, 0\|\frac{p'_P}{\kappa p_P} \tag{6.40}$$

where the operator $\|a, b\|$ gives the largest value of a and b.

The equation for conservation of mass and products can then be expressed with a discretizated equation where the only unknowns are the pressure corrections. In 3D and 1D they are

$$a_P p'_P = a_E p'_E + a_W p'_W + a_N p'_N + a_S p'_S + a_T p'_T + a_B p'_B + b \tag{6.41}$$

$$a_P p'_P = a_E p'_E + a_W p'_W + b \tag{6.42}$$

where

$$a_E = \rho_{R,e}^*\left(d_e + \frac{\|-U_e^*, 0\|}{\kappa p_W^*}\right) \tag{6.43}$$

$$a_W = \rho_{R,w}^*\left(d_w + \frac{\|U_w^*, 0\|}{\kappa p_W^*}\right) \tag{6.44}$$

$$a_P = \frac{\rho_R^*}{\kappa p^*}\frac{\Delta x}{\Delta t} + \rho_{R,e}^*\left(d_e + \frac{\|U_e^*, 0\|}{\kappa p_P^*}\right) + \rho_{R,w}^*\left(d_w + \frac{\|-U_w^*, 0\|}{\kappa p_P^*}\right) \tag{6.45}$$

$$b = (\rho^1(1 + \tau c^1) - \rho_R^*)\frac{\Delta x}{\Delta t} + \rho_{R,w}^* U_w^* - \rho_{R,e}^* U_e^* \tag{6.46}$$

After the pressure correction equations have been solved, new pressures, densities in reactant and velocities are calculated. They are used as new guessed values and the equations are solved again until b is below a given small limit. This assures that both the momentum equation, the continuity equation and the equation of state are satisfied.

For a non-reactive flow, and in the non-reacted part of a reactive flow, the new pressure correction algorithm for reactive flows will be identical to the SIMPLE algorithm for compressible flows used in FLACS, since the density in reactant and the density in the cell is identical. All tests done with the FLACS code for non-reactive flows (e.g. shock tube, turbulent flows) are therefore still valid and need no new validation.

6.1.6 Convection of reactants and products

The volume flow rate through all the grid cell faces were found with the pressure correction equation. The mass flow through the same faces is the sum and product of volume flow rates of reactants and products and their densities.

On faces which contain only reactants or only products, the mass flows can be calculated directly as the product of the volume flow and the average of density in reactant or product in the two surrounding grid cells.

When the flame is crossing a cell face, as illustrated in Figure 6.4, the mass flows through the face is not known directly and the mass flow rate must therefore be estimated. The background for these estimates can be the velocity on cell faces around which contains only reactants or only products.

In a situation where the flame propagates freely from a point, the velocity of products is typically zero, but when the flame propagates towards a wall, the velocity of reactants towards and near the wall is typically zero.

Based on the velocity in the six closest cell faces in the same direction (upstream, downstream and on the four neighbour faces, later noted as *W, E, S, N, B* and *T*) an estimate for the velocity of reactant, U_R (or products, U_P) can be found if some of these cell faces consists only of reactants (or products). There must also be a connection between the faces and the cell, and the faces are given different weight depending on location and porosity between them. An estimate for the fraction of the cell wall used for flow of products, *f*, can be found from the volume fraction of products in the two cells around the cell wall. The mass flow is then

$$\dot{m} = \rho_R F_R + \rho_P F_P \tag{6.47}$$

where ρ and F are the density and volume flow rates of reactants and products. The volume flow rate of reactants and products, F_R and F_R, can then be described from the following three equations

$$F_R + F_P = U \tag{6.48}$$

$$F_R = (1 - f)U_R \tag{6.49}$$

$$F_P = fU_P \tag{6.50}$$

where U represents the volume flow. Four situations can be identified: U_R and U_P are unknown, only U_R is known, only U_P is known, or both U_R and U_P are known.

If U_R and U_P are unknown, the reason for this is typically that the flame is nearby a corner. It is therefore most likely that only products are flowing and that the velocity of reactant is zero

$$F_P = U \text{ and } F_R = 0 \tag{6.51}$$

.

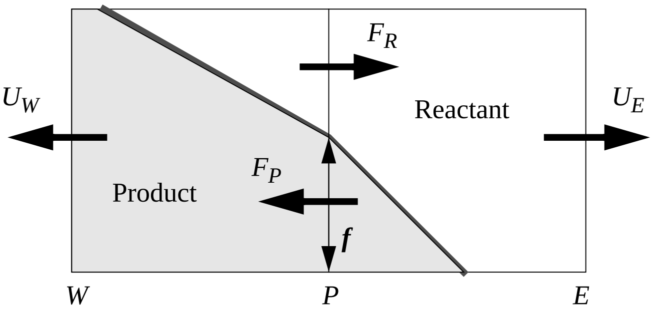

Figure 6.4 Two grid cells, the flows of reactants and products on the face between them

When only U_R, or only U_P, are known, one of the three equations vanishes and the two flow rates can be found from the remaining two equations.

When both U_R and U_P are known, the equation set is over-determinated, with three equations and only two unknown flows. The equation set must be reduced by giving the three equations different weights.

When U is between U_R and U_P the flow rates can be found in the following way. The difference in real and estimated volume flow rates is

$$U_x = U - fU_P - (1-f)U_R \tag{6.52}$$

The flow rate can be changed to the real value by changing the volume fraction of products flowing through the wall, f, (γ=1) or by changing the flow rates F_R and F_P equally (γ=0) or by a combination of these two.

$$f_2 = f + \gamma U_x / (U_P - U_R) \tag{6.53}$$

The resulting flow rate of product

$$F_P = f_2(U_P + (1-\gamma)U_x) \tag{6.54}$$

where γ=0.7, seems to give the most realistic convection of the flame.

When U is larger (or smaller) than both U_R and U_P , it is impossible to get the real flow rate by only changing f. The flow rate of products is then well expressed by

$$F_P = U \Big/ \left(1 + \left(\frac{1}{f} - 1\right)\left(\frac{U_P - U}{U_R - U}\right)\right) \tag{6.55}$$

When pockets of reactants are left in the products, or opposite, it is necessary to identify and secure a high flow rate of reactants (products) from these cells too avoid to high wrinkling of the flame.

The calculation of mass flow rates when both reactants and products are present at the cell face is the only part of SIF which can be critical and where improvements may be necessary. It may typically lead to unphysical wrinkling and then too large flame areas. The model for flow of reactant and product may therefore be improved further.

6.1.7 Convection of the flame

The densities and mass fraction of products after convection are found from the conservation equations for mass and products. Volume and mass flows are used for

$$\rho_2 = \rho_1 - \sum F_1 \tag{6.56}$$

$$\rho_2 c_2 = \rho_1 c_1 - \sum F_1 c_{x1} \tag{6.57}$$

where the mass flows are positive as outflows and negative as inflows. The mass flows are calculated from the volume flows of reactant and product, and their densities, estimated above. Calculation of mass fraction of products, c_x in the flows includes also (2.1).

6.1.8 Convection of the flame from one cell to another

The flame can be convected from one cell to a cell which contains reactants or to a cell which contains products. In a fraction of the time step, products will then flow between the cells, instead of reactant, or opposite. The needed adjustment of mass fluxes in these two situations are described below. The volume flux is constant, but the mass flux is adjusted (the density and product fraction on the flows between the cells are adjusted).

When the flame crosses a cell wall since all reactants have been convected from the cell, the calculated mass fraction of product will be greater than one, $c_2 \geq 1$ (eventually the calculated density will be less than zero, $\rho_2 < 0$ and $c_2 < 0$).

The flow rates through the cell walls with reactants and mixture must then be adjusted to have outflow of products during a fraction, α, of the time step, which results in $c_{2'} = 1$ or

$$\rho_{2'} = \rho_{2'} c_{2'} \tag{6.58}$$

The fraction α of the time step, where only products are leaving the cell can be found from the densities, ρ_2 , and mass fractions of products, c_2 , before and after adjustment

$$\rho_{2'} = \rho_2 + \alpha \sum (F_1 - F_P) \tag{6.59}$$

$$\rho_{2'} c_{2'} = \rho_2 c_2 + \alpha \sum (F_1 c_F - F_P) \tag{6.60}$$

$$\alpha = \frac{\rho_2 (c_2 - 1)}{\sum F_1 (1 - c_F)} \tag{6.61}$$

where the flows are summarized for all faces which contain reactant. The flow of products, F_P, can be expressed with F_1 and the face values c_F and τ_F from (6.1) and (6.2). Inserted into (6.59) give the new density (6.62), with α from (6.61)

$$\rho_{2'} = \rho_2 + \alpha \sum \left(F_1 \frac{1 - c_F}{1 + \tau_x} \tau_F \right) \tag{6.62}$$

In grid cells with common faces with this grid cell, densities and c are changed, due to new mass flows, from ρ_2^{nb} and c_2^{nb} to adjusted values

$$\rho_{2'}^{nb} = \rho_2^{nb} - \alpha (F_1 - F_P) = \rho_2^{nb} - \alpha F_1 \frac{1 - c_F}{1 + \tau_F} \tau_F \tag{6.63}$$

$$\rho_2^{nb} c_2^{nb} = \rho_1^{nb} c_1^{nb} - \alpha (F_1 c_F - F_P) = \rho_2^{nb} c_2^{nb} + \alpha F_1 \frac{1 - c_F}{1 + \tau_F} \tag{6.64}$$

The mass flow fluxes into the surrounding cells are adjusted from F_1 to F_2.

$$F_2 = F_1 - \alpha (F_1 - F_P) = F_1 \left(1 - \alpha \frac{1 - c_F}{1 + \tau_F} \tau_F \right) \tag{6.65}$$

If the flame crosses a cell wall since all products have been convected from the cell, the calculated mass fraction of product will be less than zero, $c_2 \leq 0$, and the density too large, $\rho_2 \geq \rho_R$.

The flow rates through the cell walls with product and mixture must then be adjusted to have outflow of reactants during a fraction, α, of the time step, which results in no mass of products in the cell.

$$\rho_{2'}c_{2'} = \rho_2 c_2 + \alpha \sum F_1 c_F = 0 \tag{6.66}$$

$$\alpha = \frac{-c_2 \rho_2}{\sum F_1 c_F} \tag{6.67}$$

The density in the cell will then be

$$\rho_2 = \rho_1 - \alpha \sum (F_R - F_1) = \rho_1 - \alpha \sum \tau_F c_F F_1 \tag{6.68}$$

where the flows are summarized for all faces which contain product. The flow of reactants, F_R, was expressed with F_1, c_F and τ_F from (6.1).

In grid cells with common faces with this grid cell, densities and c are changed, due to new mass flows, from ρ_2^{nb} and c_2^{nb} to adjusted values

$$\rho_{2'}^{nb} = \rho_2^{nb} + \alpha(F_R - F_1) = \rho_2^{nb} + \alpha \tau_F c_F F_1 \tag{6.69}$$

$$\rho_{2'}^{nb} c_{2'}^{nb} = \rho_2^{nb} c_2^{nb} - \alpha F_1 c_F \tag{6.70}$$

The mass flow fluxes are adjusted from F_1 to F_2.

$${}_2 = F_1 + \alpha(F_R - F_x) = F_1(1 + \alpha \tau_F c_F) \tag{6.71}$$

The new mass flow fluxes and densities are needed in the calculation of turbulence, enthalpy and mixture fraction.

6.1.9 Update and boundary conditions

In the update routine the temperature in reactant and products are calculated from enthalpy and gas composition in reactant and product. The temperatures are used to calculate the density ratio, as shown above. The density in reactant at the present pressure is calculated from the equation of state, temperature and the gas constant in reactant

$$\rho_R = \frac{P}{T_R R_R} \tag{6.72}$$

No changes have been done with the boundary conditions in FLACS in connection to the introduction of SIF, and it seems not necessary to do any changes either. The mostly used boundary conditions in FLACS are EULER and NOZZLE. Both of them seem to do well together with SIF, except for the combination of EULER and ignition in a grid cell located at the boundary of the calculation domain. This combination results in an unphysical increase in density and decrease in velocity at the boundary. This can be fixed by moving the density of the grid cell out to the boundary. However ignition at the (open) boundary of the calculation domain is normally not used in FLACS.

6.1.10 Evaluation of the momentum equation

The ability of the momentum (2.7) and pressure correction equations to handle transient compressible flows was verified by Bakke (1986). He simulated a shock tube problem, which has an analytical solution. An analysis of the momentum equation's ability to represent reactive flow, particularly with respect to SIF has been done and is presented below.

The momentum equation for an 1D flow without viscous forces is

$$-\frac{\partial P}{\partial x} = \frac{\partial}{\partial x}(\rho U^2) + \frac{\partial}{\partial t}(\rho U) \tag{6.73}$$

In a steady situation where the flame is burning with constant velocity *S*, reactants are flowing with constant velocity U_R on the left side and products with U_P on the right side of the flame, the change of momentum with space and time can be written as

$$\int \frac{\partial}{\partial x}(\rho U^2)\partial x = \rho_P U_P^2 - \rho_R U_R^2 \tag{6.74}$$

$$\int \frac{\partial}{\partial t}(\rho U) = (S + U_R)(\rho_R U_R - \rho_P U_P) \tag{6.75}$$

The change of momentum with time is due to the movement of the flame. If the flame and reactants have the same velocity, but in opposite directions, the flame will have a fixed position. The pressure drop over the flame is found by inserting (6.74) and (6.75) into (6.73).

$$P_R - P_P = \rho_P U_P^2 - \rho_R U_R^2 + (S + U_R)(\rho_R U_R - \rho_P U_P) \tag{6.76}$$

Due to continuity and density ratio, the following two relations exist

$$U_R - U_P = \tau S \tag{6.77}$$

$$\rho_R = \rho_P(\tau + 1) \tag{6.78}$$

The momentum equation (6.76) can therefore be reduced to

$$P_R - P_P = \tau S^2 \rho_R \tag{6.79}$$

In a deflagration, the pressure is therefore higher in the reactant than in the product. This should therefore also be the situation for the numerical flame. This relation between pressure and densities is often referred to as the Rayleigh-line relation.

In FLACS, the transient term is represented as

$$\frac{\partial}{\partial t}(\rho U) = \rho \frac{\partial U}{\partial t} \tag{6.80}$$

This term will only contribute when the flame has moved from one cell to another, when the velocity is changed from U_R to U_P. An unphysical jump in the pressure gradient each time the SIF flame passes a grid cell face is then the result. This unphysical pressure jump can be avoided in several ways. A simple method is to increase the constant *d* in (6.30) with a factor of around 100, when the flame is located in one of the two grid cells around the cell face. Then only a small pressure gradient will be needed to change the velocity and the unphysical pressure jumps are avoided. This will however normally not give the pressure drop of (6.79).

6.2 SIF calculations

A range of calculations has been done to test the submodels in SIF.

The total mass in a closed system must be conserved (unchanged) through the tests. The total mass of products in a closed system shall only be changed in the combustion routine, SIF1, and then it shall increase with an amount equivalent to the product of flame area, burning velocity and density in reactant. The critical part here is when the flame is moved from one grid cell to another, by combustion or convection. The mass fraction of products, *c*, and density are then adjusted to represent the movement. The tests gave a relative difference in total mass and products between two time steps of order 10^{-12}, due to the numerical accuracy of FLACS. The model for movement of the flame between cells therefore has a correct mass and product conservation.

6.2.1 Testing of the sub models in SIF

In a 1D test, the flame shall propagate towards a closed end with the specified burning velocity. Towards an open end the propagation velocity shall be the product of burning velocity and density ratio between reactant and product, due to continuity. The SIF model fulfilled these two tests, for different grids and burning velocities.

Testing of the flame area model is best done when the flame burns with no density change from reactants to products, and consequently no velocity field. In a pure air mixture the heat release (and density change) will be zero (as well as the burning velocity). A fixed burning velocity can be used in these tests, named as constant *T* (temperature) combustion. Figure 6.5 shows that the flame has a splendid shape and location in a 2D test. The figure also shows that the flame area model handles cells with different sizes in each direction. Figure 6.7 shows a part of the flame surface of a 3D flame propagating outwards from a point and that the constant *T* combustion flame is spherical. The grid cells used had dimension 0.4 m.

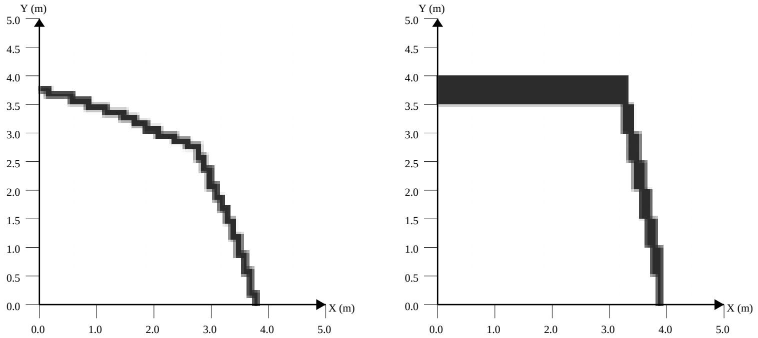

Figure 6.5 Flame positions after 3.8 s, burning velocity 1 m/s, constant T combustion, grid cell size 0.1 x 0.1 (left) and 0.1 x 0.5 (left)

A hydrocarbon-air flame expands around seven times. The movement of the flame is therefore mainly due to convection. In tests where the flame can move freely outwards with low velocity the pressure is nearly constant. Figures 6.6 and 6.7 show the 2D and 3D flame positions from such constant *P* combustion tests. The wrinkling of the flame area for relatively large flame radii shows the limitation in the model for convection of reactants and products.

A flame propagating outwards from a point should ideally have the same relation between flame area and volume of products as the surface area and volume of a sphere (cylinder in 2D).

$$A_{sphere} = \pi^{1/3}(6V_P)^{2/3} \tag{7.1}$$

Figure 6.9 shows the relative flame area, the ratio of the flame area from SIF and the area of a sphere (a cylinder in 2D) with similar volume of products, as function of flame radius in a number of grid cells (relative flame radius). This ratio has a top of 1.24 (1.13 in 2D) when the flame has left the first grid cell, since the flame area in SIF then will be represented by flame area and product volume of a cube instead of a sphere.

The constant *T* combustion gives a flame area ratio close to one, independent of flame radius. The flame area model is therefore evaluated to be fine.

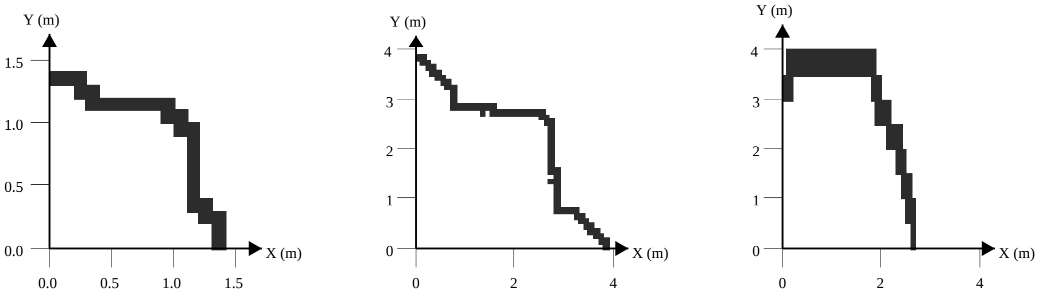

Figure 6.6 Flame positions, burning velocity 1 m/s, constant *P* combustion

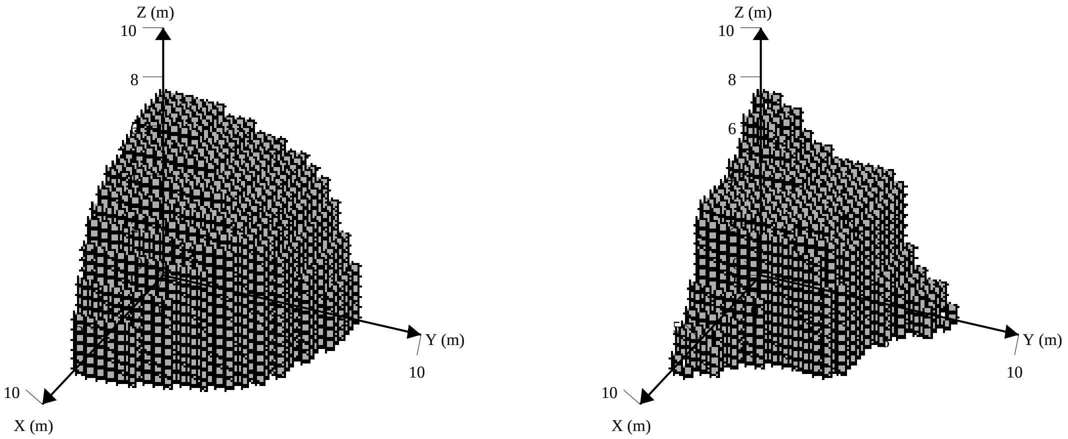

Figure 6.7 3D flame positions for combustion with constant *T* (left) and constant *P* (right)

However the constant *P* calculations show an increase in flame area with relative flame radius. The flow field seems to transport the flame more in the direction of the axis and the diagonals between the axis than in the other directions. There may be several reasons for this instability, e.g. an improper convection model or that the viscosity is not switched off in flame cells. The reactants and products shall normally flow in opposite directions, due to the expansion in the flame. This will give a shear and the viscosity will limit some of this difference in reactant and product velocity. This may make the flame surface more unstable and increase the flame area.

The 3-D constant volume, *V*, calculations gave about the same relative flame area as the constant *P* calculations. In addition they showed that the flame burns relatively stable towards the walls, which is important in the often enclosed geometries where gas explosions are calculated.

Removal of the flame instability may not be essential in the modelling of flames connected to explosions since flames exhibit many kinds of physical instabilities. Thus, flame fronts do not remain smooth, but acquire wrinkles. But it may be more desirable to model these instabilities directly in terms of their physical parameters rather than let this mathematical instability mimic them.

In FLACS the increased flame area caused by hydrodynamic instabilities is taken into account in the burning model through the quasi laminar burning velocity model, Arntzen (1993b), which typically increase the laminar burning velocity with a factor of two over a distance of around one meter. The numerical instabilities will therefore give a smaller area increase than the real flame instabilities as long as the grid cell size is larger than around 1 cm.

As shown by Gjesdal (1996) the wrinkling of the flame is only a function of grid cell radius. A change in scale from 1 to 10 m calculation domain, had no influence when the same number of grid cells was used.

6.2.2 Simple burning tests

SIF and the β flame model have been compared in several tests. Figure 6.10 shows flames burning outwards from a point with burning velocity 1 m/s in a wind field of 22 m/s. As the flame propagates outwards from its centre, it is also transported with the wind field since the flow velocity is larger than the burning velocity. The test shows the flame models ability to move the flame with the flow and convert cells with products to cells with reactants. SIF handles this test well.

Figure 6.8 shows a moment of flame propagation for three grid resolutions in a simulation of an explosion in a SOLVEX experiment. In these simulations SIF gives a larger and more representative flame area than the β flame model for the same resolution.The flame area from the SIF model is in most situations larger than the flame area from β flame model, since the SIF flame is thinner and thereby more easily can follow the flow field. An adjustment of submodels such as flamefolding models is therefore necessary in the validation, to obtain similar explosion simulation results with the two flame models.

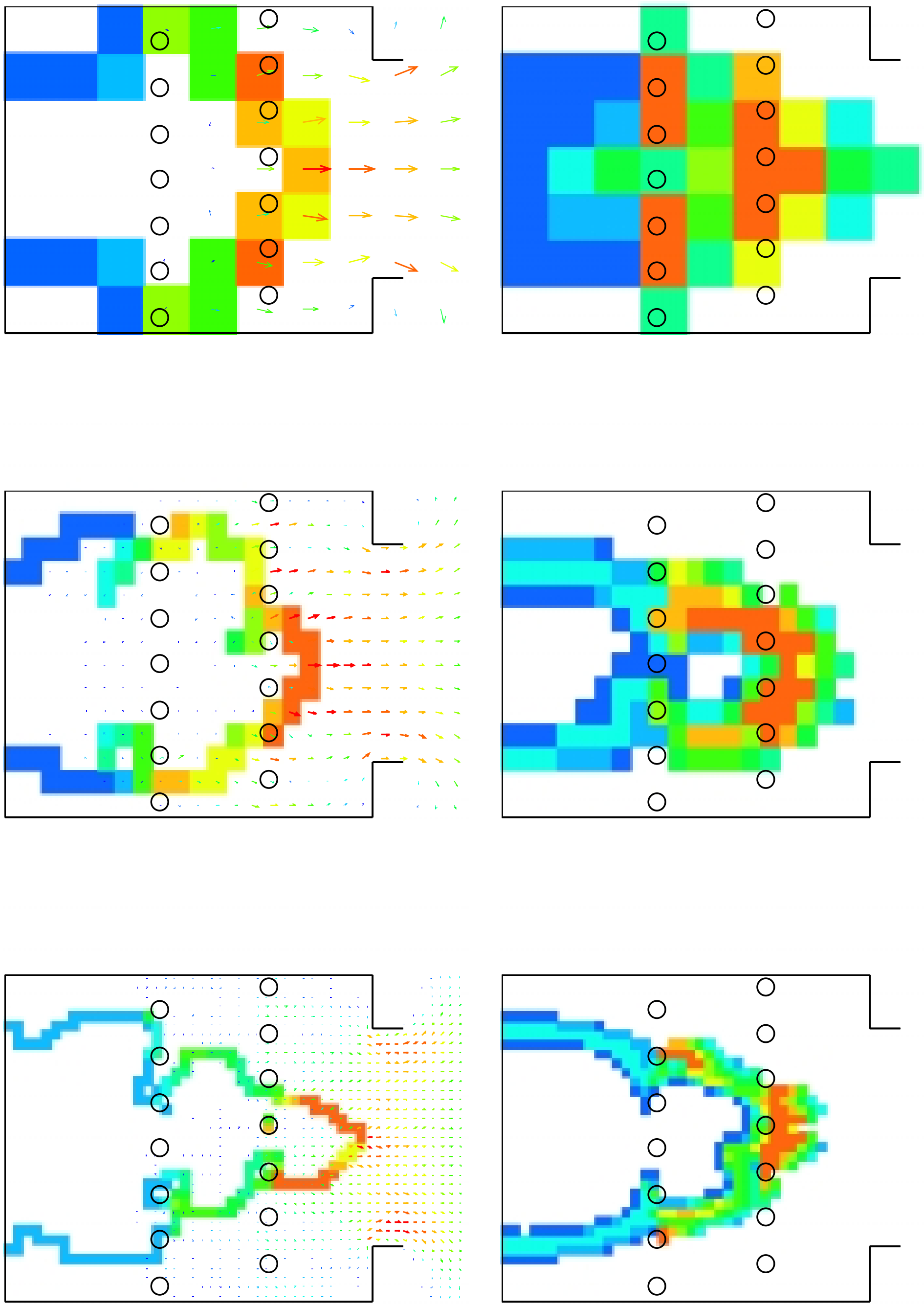

Figure 6.8 Representation of the flame with SIF (left) and the β flame (right) model at three grid resolutions. The colour shows the burning velocity (SIF) and reaction rate (β), (blue is low and orange is high) which depends on the turbulent intensity.

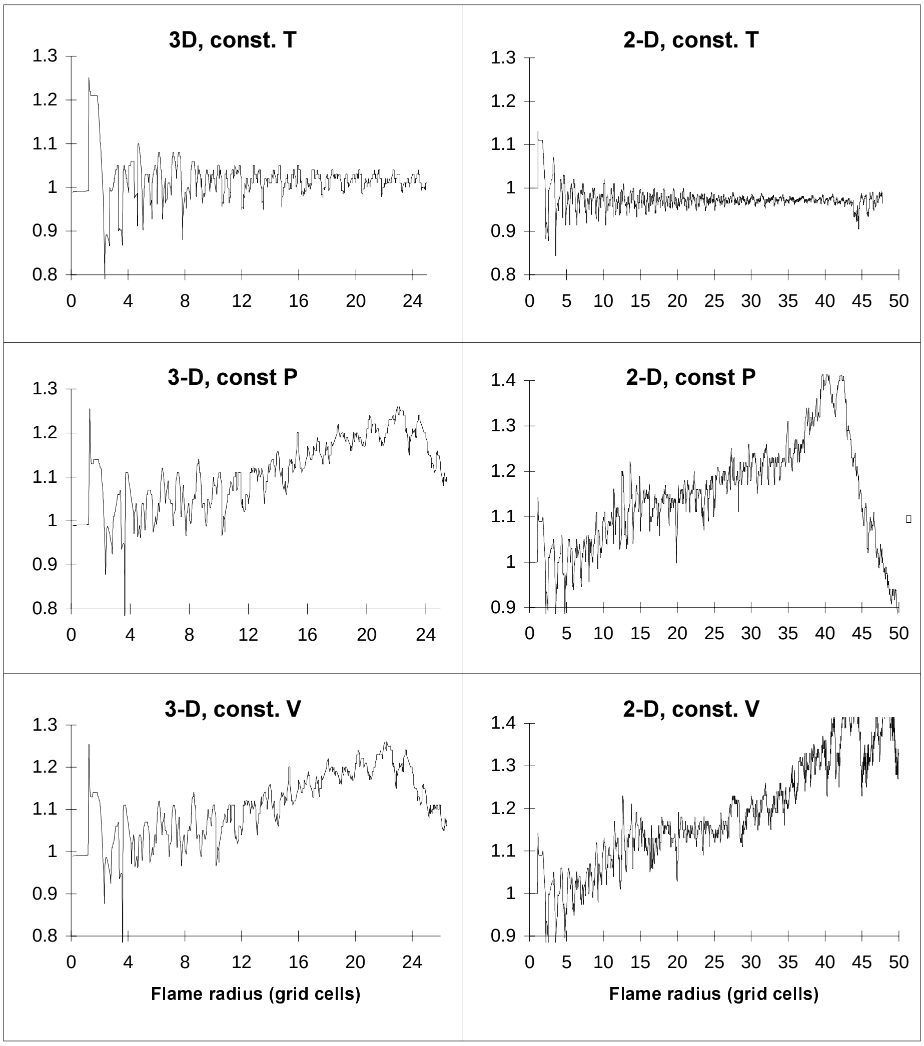

Figure 6.9 Flame area from SIF calculations versus area of a sphere / cylinder

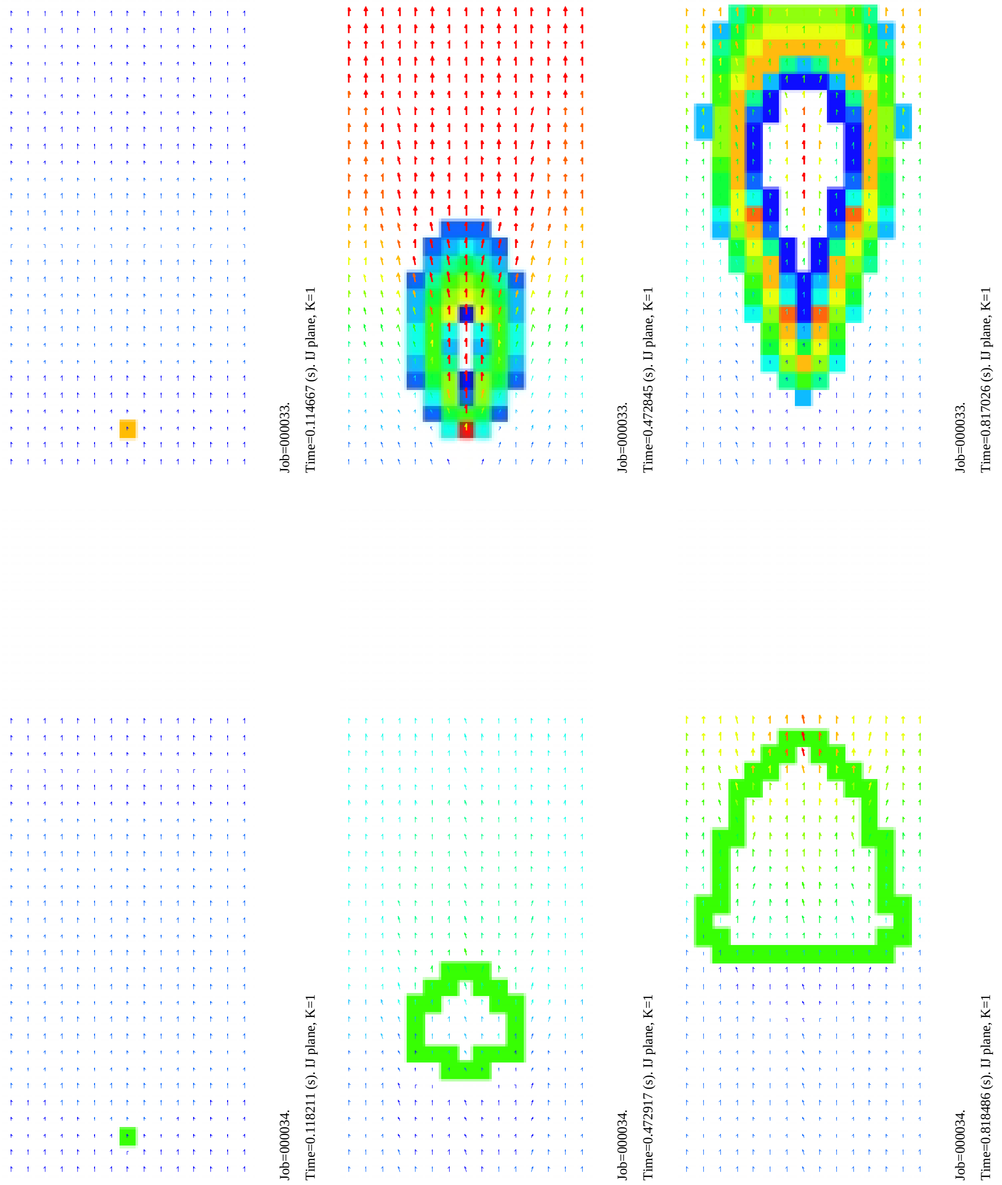

Figure 6.10 Calculations with SIF (below) and the β flame model (above), with burning velocity 1 m/s in a wind field of 22 m/s. Grid cell size is 1 m.

6.3 Summary

A new flame model, SIF, the Simple Interface Flame model has been developed, implemented and tested in the FLACS code. SIF is a two fluid model where the flame is represented as an interface between the two fluids, reactants and products. The model consists of two parts. A combustion part, including a flame area model, and a convection part, for modelling the flows of reactant and products. A model for movement of the flame between obstructed grid cells was also needed. The pressure correction equation in FLACS was only for compressible flows. An equation for reactive compressible flows had to be developed to secure that the equation of state was satisfied.

SIF has been compared with the β flame model, the other flame model in FLACS. SIF burns with specified burning velocity, independent of walls, flame radius and flame velocity. SIF also gives a better representation of the flame area on a coarse grid and the unphysical turbulence generation connected to expansion in the flame is easier to avoid with SIF than with the β model.

7 Burning velocity modelling

The SIF and β flame models, presented in the two previous chapters, need burning velocities as input for the speed with which the flame propagates into the premixed reactants, Arntzen (1993b). In an explosion the flame normally begins as quasi laminar and when it reaches obstructed areas it becomes turbulent. Both the quasi laminar and turbulent burning velocities have been modelled in FLACS as functions of the laminar burning velocity of the fuel mixture. Models for laminar burning velocity are therefore presented before the models for quasi laminar and turbulent burning velocities. The burning velocity used by FLACS in each cell where the flame is present, is modelled as the largest of the quasi laminar and turbulent burning velocities.

The actual flame area is mostly larger than the flame area on the numerical grid. The ratio of these flame areas must be included to give a representative flame propagation. This area ratio is estimated with so-called flamefolding models, presented in Section 7.6.

7.1 Laminar burning velocity models

The laminar burning velocity is an experimentally determined property characterizing the propagation velocity of the flame normal to the flame front into the premixed reactants under laminar flow conditions.

There is a large scatter on observed laminar burning velocity, S_L, for most hydrocarbon gases in the literature, as described by Arntzen and Bakke (1990). The variation with temperature, pressure and gas mixture is not very well known either. Different methods for measurements of laminar burning velocities are used. These techniques include experiments in a tube, in a spherical bomb, in a soap bubble and on a bunsen burner, as presented by Kuo (1986). The scatter in the burning velocity data is due to differences in measurement methods, dimension of experiments and reactant temperatures.

The laminar burning velocity depends on a range of factors as fuel mixture, equivalence ratio, pressure and temperature. All these factors are important for description of combustion in a gas explosion. Models for this dependencies are therefore described in this section. However it starts with a presentation of flame propagation theories to explain some of the dependencies

7.1.1 Laminar flame theories

There are three main groups of theories used for description of laminar flame propagation, the thermal theory, the comprehensive theory and the diffusion theory. In the diffusion theory the burning velocity is determined by the diffusion of active radicals into the unburnt reactants. From both the thermal and comprehensive theory, presented by Kuo (1986), Willams et al. (1993) and Strehlow (1979), it is generally accepted that the burning velocity can be represented as proportional to the square root of thermal diffusivity and the reaction rate

$$S_L = \sqrt{\alpha w / \rho} \tag{7.1}$$

or the chemical timescale

$$S_L = \sqrt{\alpha / \tau_c} \tag{7.2}$$

where the thermal diffusivity is inverse proportional with the density and can be estimated, Welty (1984), as

$$\alpha = \frac{\lambda}{\rho c_p} \propto \frac{1}{P^{5/4} C_p} \left(\frac{T}{M}\right)^{7/4} \tag{7.3}$$

The laminar burning velocity models (7.1) and (7.2) were for a gas with Lewis number equal to one. The Lewis number is the ratio of thermal to molecular diffusivity.

$$Le = \alpha / D \tag{7.4}$$

Williams et al. (1993) argue that the effect of decreasing the Lewis number is to decrease the burning velocity since increasing the molecular diffusion coefficient decreases the reaction rate by increasing the diffusion loss of reactants from the reaction zone, thereby decreasing the reactant concentration in the reaction zone. Based on the comprehensive theory, Glassman (1977) and Kuo(1986) show the same effect, expressed by (7.5).

$$S_L = \sqrt{\alpha Le / \tau_c} \tag{7.5}$$

The flame consists of a diffusion zone and a reaction zone. From the energy balance in the diffusion zone the flame thickness can be expressed as

$$\delta = \alpha / S_L \tag{7.6}$$

The reaction zone thickness is δ/β where β is the Zel'dovivch number which is of order 10. Since the reaction zone is thin, the chemical reactions must take place at a temperature close to the product temperature T_P. This temperature is therefore used in the one-step Arrhenius approximation for the reaction rate (mass per unit volume per unit time)

$$w = AP^{m+n} Y_F^m Y_{O_2}^n e^{-T_A/T_P} \tag{7.7}$$

where the mass fractions Y_i, the activation temperature T_A and the prefactor A are constants characteristic of the combustible mixture. m and n are overall reaction orders with respect to fuel and oxidizer. m is mostly small and the oxygen fraction varies little in fuel-air mixtures. (In oxygen enriched mixtures Y_O must be included.) Inserting (7.7) into (7.1) therefore shows that the laminar burning velocity of a mixture can be represented mainly as function of the product temperature, T_P, as long as the pressure and thermal diffusivity are unchanged.

7.1.2 Dependency on product temperature

Also Kuo (1986) concludes that the burning velocity for hydrocarbons is essentially determined by the flame temperature. The temperature in products for some stoichiometric hydrocarbon air mixtures have been plotted against burning velocities from experiments in Figure 7.1 to illustrate this dependency.

In Figure 7.2 the burning velocity and the product temperature as function of equivalence ratio have been plotted together. This figure, with experimental data for propane, methane and propylene from Gibbs et al. (1959), shows that the laminar burning velocity at normal pressure and reactant temperature may be estimated by

$$S_L \approx T_P / 1550 - 1 \tag{7.8}$$

This burning velocity dependency can also be represented by the exponential relation

$$S_L \approx 16e^{\frac{-8000}{T_P}} \tag{7.9}$$

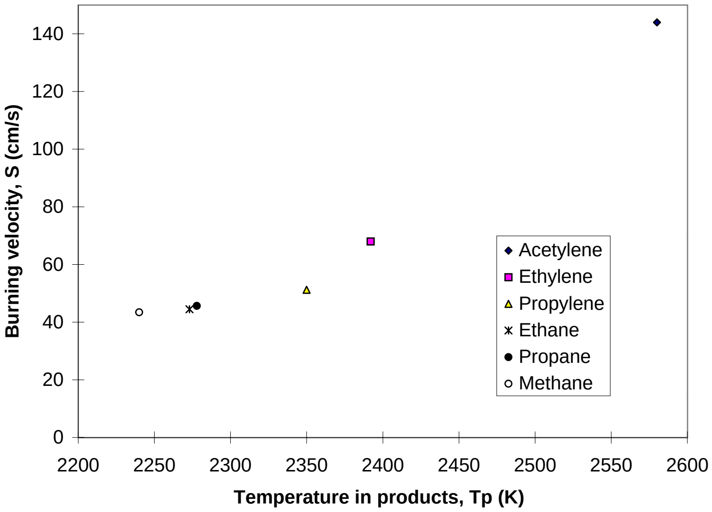

Figure 7.1 Burning velocity of hydrocarbons as function of temperature

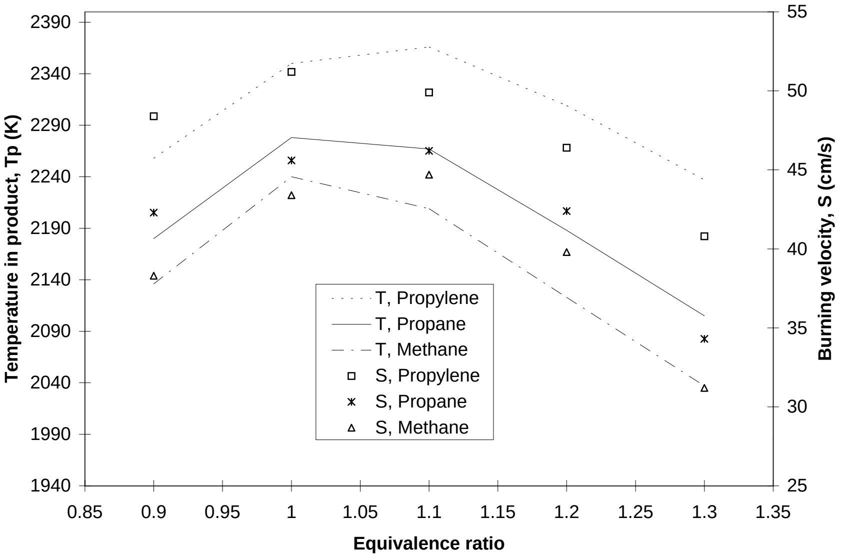

Figure 7.2 Burning velocity and temperature in products, equivalence ratio dependence

Combining (7.2) and (7.9) give an expression for the chemical timescale

$$\tau_c = Ae^{T_A / T_P} \tag{7.10}$$

The constant $A = 8.6\ 10^{-8}$ and the activation temperature $T_A = 16\,000$, can be used in (7.10) for propylene and alkanes (paraffins) as methane, ethane, propane and butane. The activation temperature for other fuels can typically be represented with 15 100 for ethylene, 12 400 for acetylene and around 12 000 for hydrogen.

An expanded version of (7.9) with $S_L \sim Y_O^{0.8}$ gives burning velocities that also consist with experimental results for fuel-air mixtures with different oxygen concentrations and equivalence ratios, reported by Lewis and von Elbe (1961). Oxygen enrichment and dilution with nitrogen or other inert gases give respectively higher and lower product temperature due to the variation in fraction of inert gas to be heated. Mixtures containing CO_2 have however, a larger decrease in burning velocity than the reduction in product temperature (7.9) should give, since CO_2 is not a inert gas but affects the chemical reactions. This effect of CO_2 can however be included by using a high activation temperature for CO_2. At elevated reactant temperatures the burning velocity of alkanes is well expressed by a version of (7.9) which is expanded with $S_L \sim T_R^{1.3}$.(The exponent is here smaller than α in (7.14) since (7.9) includes the product temperature.)

Hydrogen air mixtures will burn faster than the hydrocarbons since the slow reaction from CO is not present, and due to an eight times higher thermal diffusivity. Hydrogen also has a maximum burning velocity for a rather rich mixture, where the thermal diffusivity is large.

Remembering that the experimental burning data may differ with 15- 30% on the value for the burning velocity, depending on the measurement method, Gaydon (1979), the temperature in the product model gives a good prediction of laminar burning velocities. Such a temperature dependent model handles most hydrocarbon mixtures and includes the burning velocity variations independent of equivalence ratio, temperature rise due to compression, fuel mixture and oxygen enrichment, through the temperature in products. A burning velocity or chemical time scale model based on pressure and product temperature (and eventually concentrations of fuel and oxygen) is therefore recommended to be used in a later version of FLACS. This model is especially useful if the burning velocity is not well known, as for several hydrocarbon mixture and at elevated reactant temperatures (e.g. due to the compression in explosions). With temperatures calculated in reactant and product separately, the product temperature is known in FLACS and can be used in calculation of laminar burning velocities or chemical times.

In FLACS the temperature in reactant and product was not calculated separately before the 96 version, as described in Chapter 3. In the reaction zone both reactants and products are present and only the average temperature in this mixture was known. Laminar burning velocities could therefore not be estimated from the temperature in products. Submodels for laminar burning velocity as function of fuel mixture, equivalence ratio, pressure and temperature in reactant were therefore implemented, as presented in the next subsections.

The influence of extra O_2, N_2 or CO_2 in the gas are also handled by simple correction models for the burning velocity. As shown by Arntzen and Hansen (1997), these models secure the same laminar burning velocity dependence as seen in the experimental data reported by Lewis and von Elbe (1961). It is however not clear how well this submodel perform together with the other burning velocity submodels, e.g. for other fuels and at elevated temperatures.

7.1.3 Fuel and equivalence ratio dependency

The laminar burning velocity used in FLACS is modelled through a range of submodels, which take into account the variation in burning velocity as function of parameters like equivalence ratio, mixture of different fuels, pressure and temperature in reactant.

The laminar burning velocities, S_{L0}, of hydrogen and a range of hydrocarbons as function of equivalence ratio, as implemented in FLACS-94, are shown in Fig. 7.3.

The burning velocity as function of equivalence ratio for each fuel, is here described by two second order polynomials, given from the equivalence ratio for maximum burning velocity and the minimum and maximum equivalence ratios for which the mixture is flammable. Gibbs et al. (1959) give the burning velocity as function of equivalence ratio for a range of fuels. Such data sets have been tabulated in later FLACS versions. Laminar burning velocities have also been calculated with the chemical kinetics code CHEMKIN from Kee et al. (1989).

In later versions of FLACS the fuels H_2S and CO have also been included. The burning velocity of air mixtures with CO are very low unless some hydrogen containing species is present. A raise in H_2O content from 0 to 2% in the CO, increase the burning velocity of CO with two orders of magnitude, to values close to those of methane (which was implemented in FLACS). The reason for this is that CO reacts fast with H and slowly with O_2.

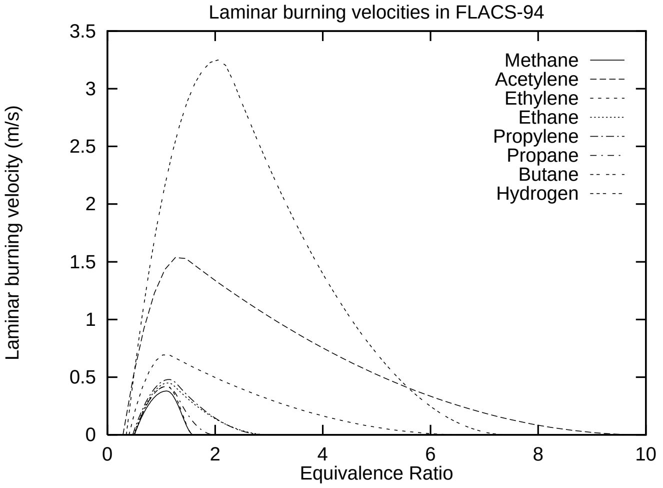

Figure 7.3 Laminar burning velocity as function of equivalence ratio for some fuels

7.1.4 Mixing rule for mixtures of fuels

A mixture of fuels can be represented by the maximum burning velocity, *S*, and the three equivalence ratios for maximum burning velocity, and minimum and maximum equivalence ratios, for which the mixture is flammable. These values were in FLACS 93, and earlier versions, found from average values for the mixture based on volume fraction V_i of each of the possible fuels.

$$S_{mix} = \sum_{i=1}^{n} S_i V_i \tag{7.11}$$

Calculation of the three equivalence ratios is done by replacing S with these ratios. This mixing rule gave low molecular weight fuels, like methane and hydrogen, too much importance.

Based on the difference in heat of formation (Table 3.2) between reactants and the products (CO_2 and H_2O formed from oxygen and the fuel) the energy release per mole (and volume) of a fuel can be represented approximately with $1.3C_i+H_i$, where the mole fraction ratios C_i and H_i of fuel i is taken from Table 3.2.

A mixing rule based on the energy released for each of the fuels can then be expressed as

$$S_{mix} = \sum_{i=1}^{n} S_i V_i (1.3C_i + H_i) / \sum_{i=1}^{n} V_i (1.3C_i + H_i) \tag{7.12}$$

This mixing rule may also be used to calculate other reaction rate dependent properties of fuel mixtures, like activation temperature, by replacing S with T_A.

Burning velocity experiments with mixtures of butane and hydrogen, is reported by Sher and Ozdor (1992). With 5% hydrogen on mass basis, (on volume basis 59% hydrogen and 41% butane), the burning velocity of butane increases 35% (hydrogen’s burning velocity is about 4 times butane’s for stoichiometric mixtures). With (7.11), as used in FLACS-93 and earlier, the burning velocity becomes 2.7 times as high as for pure butane, 2 times the value seen in the experiment. Explosion simulations with a mixture like this will of course give far too high pressures. With (7.12) hydrogen counts only 12% and the burning velocity increase 37%, which is about the same as seen in the experiment. In a mixture of methane and other hydrocarbons the burning velocity calculated with (7.11) will be lower than with (7.12) since methane has a low burning velocity. FLACS-93 gave therefore a too low burning velocity for such mixtures.

7.1.5 Pressure dependency

There has been little published data on burning velocities at elevated pressures. What has been available was, usually, obtained from pressure records, and the influence of flame stretch and/or cellular instability was not recorded. Since flames usually become cellular at higher pressure and in rich mixtures, there may be a cellularity boost on the measured laminar burning velocity. This cellular flame area effect increases with pressure, but methane is less affected than other gases. This may explain why methane has a “large” decrease in burning velocity due to reduced thermal diffusivity, whereas the other gases have a smaller decrease with pressure.

For a pressure range below atmospheric, Strelow (1979) and Kuo (1986) reports experiments which correlates the laminar burning velocity with pressure.

$$S_L = S_{L0}\left(\frac{P}{P_0}\right)^{\beta} \tag{7.13}$$

The pressure exponent β was observed to be around zero for hydrocarbons with burning velocity between 0.5 and 1.0 m/s.

For lower and higher burning velocities β was respectively lower and higher than zero. β were respectively -0.05 and -0.18 for stoichiometric propane and methane air mixtures.

Laminar burning velocity, S_L, at elevated pressures and temperatures, as function of laminar burning velocity, S_{L0}, pressure, P, and temperature in reactant, T_R, is in literature often described by

$$S_L = S_{L0}\left(\frac{T_R}{T_0}\right)^{\alpha}\left(\frac{P}{P_0}\right)^{\beta} \tag{7.14}$$

since T_P is often not known and a change in T_R also will change T_P. Metghalchi and Keck (1980) reported $\alpha = 2.0$ and $\beta = -0.5$ as exponents for methane and $\alpha = 2.13$ and $\beta = -0.17$ for ethylene and propane. Milton and Keck (1984) also gave exponents for hydrogen and acetylene. The reported exponents are average values which are more negative than those reported above, for pressures below one atmosphere. The exponents vary with pressure and temperature and β is closer to zero for lower elevated pressures.

In FLACS-96 the temperature in reactant is a known variable. In earlier versions of FLACS, and in most other codes T_R is unknown but may be expressed as a function of pressure. Assuming isentropic compression with $\kappa = 1.4$, the temperature can be replaced by

$$\frac{T_R}{T_0} = \left(\frac{P}{P_0}\right)^{(\kappa-1)/\kappa} = \left(\frac{P}{P_0}\right)^{2/7} \tag{7.15}$$

Inserting (7.15) into (7.14) gives the laminar burning velocity dependency as function only of pressure when the gas is compressed

$$S_L = S_{L0}\left(\frac{P}{P_0}\right)^{\beta+\alpha 2/7} \tag{7.16}$$

The laminar burning velocity dependency for compressed gas, used in FLACS, was therefore

$$S_{LP} = S_{L0}(P/P_0)^k \tag{7.17}$$

where k=0.07 for methane and k=0.44 for other fuels as ethylene and propane.

A general pressure dependence for the chemical time (7.10) of hydrocarbons can be estimated by assuming a pressure dependence as $S_L \propto P^{-0.1}$ and combining it with (7.2) and (7.3).

$$\tau_c = \frac{A}{P}e^{16000/T_P} \tag{7.18}$$

The constant A in (7.10) is changed to 6.6 10^{-3} in (7.18). This chemical time may be a better timescale for turbulent burning velocity models than a timescale based on laminar burning velocities. The reasons for this are discussed in Section 7.3.

Laminar burning velocity data at a range of pressures can be estimated from 1D laminar flame simulations with the chemical kinetic code CHEMKIN. These data are not likely to be similar with experimental data since effects as cellular instabilities are not included in 1D simulations. CHEMKIN can also be used to obtain chemical time data, from simulation of stirred reactors or shock tubes, as done by Arntzen (1992). The chemical time to be used in the turbulent burning velocity model should be calculated for stirred reactors (as the eddy dissipation concept in subsection 5.2.2) at product temperature. The chemical time in shock tubes may be used in a model for shock or pressure induced ignition.

7.2 Quasi laminar burning velocity

In the flame propagation from a point, the burning velocity of the flame increases with the distance from the point and is typically doubled when the flame radius has reached two meter. This is due to flame instabilities, as Rayleigh Taylor instability (when a hot gas is accelerated into a cold gas), body force, gas dynamic and diffusive-thermal instabilities. Since the modelled numerical flame in FLACS is much thicker than the real flame, such instabilities have nearly no effect on the numerical flame.

This effect has therefore been included in FLACS with a quasi laminar burning velocity enhancement factor, which is a function of flame radius and gas mixture. In this model heavy gases like propane have a larger enhancement than light gasses as methane. The quasi laminar burning velocity is modelled as the product of the enhancement factor, which is radius and fuel dependent, and the laminar burning velocity from the previous section. After ignition in a point, the ratio of flame radius to flame thickness is small, then the flame is strained. This strained laminar burning velocity is often smaller than the unstrained laminar burning velocity from the previous section. The enhancement factor should then start with a value below one.

Linnan and Williams (1994) divide the physical mechanisms that may be involved in flame instabilities into groups. Intrinsic instabilities are caused by chemical-kinetic, diffusive-thermal, hydrodynamic and buoyancy/acceleration mechanisms and these effects are included in the quasi laminar burning velocity model described above. Chamber instabilities are caused by acoustic, shock-wave and vortex-shedding. The acoustics is difficult to include but the vortex shedding seems to be included downstream obstructions represented with minimum 3 grid cells, as shown in Chapter 4.

The quasi laminar enhancement models are based on data from experiments where the flame radius was measured as function of time. Such experiment have been done by Lind et al. (1977) who explain the flame acceleration with Landau hydrodynamical instability, and at CMR, Arntzen et al. (1995). The vertical flame velocity accelerates for a larger flame radius than the horizontal. The buoyancy is probably the cause of this difference, so the burning velocity in vertical and horizontal directions may be similar in all directions, unless Rayleigh Taylor instabilities make the vertical burning velocity faster upwards and slower downwards.

The quasi-laminar burning velocity model as function of flame radius in FLACS-86 and 89, were implemented by Bakke (1986) and were taken from experiments in a 3D corner. It was found that the burning velocity increased linearly, due to flame instabilities and flame wrinkling, with a factor of 2.5 over the distance 0.05 to 0.5 m from the ignition point. After 0.5 m the laminar burning velocity was assumed to be constant. Since three walls were present for this flame one may wonder how much the flames were influenced by instabilities generated from the walls. Experiments measuring the flame velocity, as a function of flame radius for a flame not influenced by walls, were performed, by CMR in GSP 90 - 92, for methane, propane and ethane. From these experiments the burning velocity was calculated and found to increase over a distance of two meter, with a factor around 2.25 for methane and 2.6 for the other gases. Nearly no experimental data exist for flame radii above 3m, but the burning velocity, of a flame not influenced by walls, seems to increase at least until this limit.

The enhancement factor model should ideally take into account the number of walls surrounding the ignition point. This have not been done in FLACS, and in the later versions, enhancement factors corresponding to no walls have been used, since they resulted in the most representative time difference between ignition and peak pressure, in simulation of explosion experiments. The factors used give a maximum enhancement for radius 3m. Above the same enhancement as for 3 m is used, assuming no increase in flame area or effective burning velocity. Numerical studies, as done by Rahibe et al. (1995) indicates however that the wrinkling of the flame due to instabilities increases the flame area with flame radius in a fractal manner. The upper cutoff scale is here typically proportional with the flame radius. The enhancement factor should then increase with radius, independent on how large the radius is. The relation between the quasi laminar and laminar burning velocity may then be described by enhancement models as

$$S_{QL} = S_L(1 + aR)^{1/2} \tag{7.19}$$

where R is the flame radius and a is a constant, typically between 2 and 8, depending on factors related to the gas mixture and the number of walls located by the ignition point.

Parameters like whether the flame is propagating horizontally or vertically, upwards or downwards, whether the mixture is rich or lean, and the Lewis number, can also be important for the effective flame velocity. Rich propane- and lean methane air mixtures forms cells and give a larger increase in flame area than mixtures with higher *Le* number. These parameters are not included in FLACS yet, but should also be included to give a more representative flame propagation in the initial phase. The SIF flame model is influenced by flame instabilities when the flame radius in terms of number of grid cells is in the order of ten or higher, as shown in Chapter 6. The enhancement must therefore be reduced when SIF is used to avoid taking the instabilities into account twice. (The β flame model does not seem likely to be influenced by instabilities for flame radii below 30 grid cells.) A representative quasi laminar model is essential to get the correct time history of the explosion, as time between ignition and peak pressure. It may also have a large influence on peak pressures in closed, non-obstructed geometries, but has less influence on pressures in open obstructed geometries.

7.3 Turbulent burning velocity

For laminar flames it is possible to define a burning velocity that, within reasonable limits, is independent of the experimental technique. It would be very desirable to do the same for turbulent flames. Turbulent burning velocities are however more dependent on the experimental technique, as well as the concept of turbulent flames assumed by the investigator. These points should be kept in mind for evaluation and use of turbulent burning velocities from the experimental literature.

The increased burning rate of a fuel-air mixture in a turbulent flame, compared with a laminar flame may be due to any of, or a combination of three processes.

- The turbulent flow may distort the flame so that the surface area is markedly increased.
- Turbulence may increase the rate of transport of heat and active species.
- Turbulence may rapidly mix reactants and products, as in a stirred reactor.

7.3.1 Combustion regimes

The flamelet concept, modelling turbulent combustion as a flamelet propagating into unburnt reactants with a specified turbulent burning velocity requires that such flamelet is representative for the turbulent combustion. The relationship between the turbulent premixed flame velocity and the turbulent parameters (intensity and scale) has been the subject of continues interest. Despite the continuing progress in the understanding of turbulence and turbulent combustion mechanisms, there is still a lack of a universal relationship or model, even for the wrinkled flamelet regime, that would satisfactory explain the turbulent premixed flame data available in literature.

In the literature it has been popular to divide turbulent combustion into different regimes based on the ratio of turbulent to chemical length scale and velocity scale, as presented e.g. by Ballal (1979), Peters (1986) and Gulder (1990), and more recently by Bray (1996). The location of gas explosion combustion in these regimes was discussed by Sand and Arntzen (1991). The reaction sheets regime, where flames exhibit a wrinkled laminar flame structure is obtained when the laminar flame thickness, δ, (7.6), is smaller than the Kolmogorov length scale, η. When the turbulent mixing is rapid compared to the chemistry, the combustion occurs in a distributed zone. In between the two regimes, there is an intermediate region, the corrugated flame regime, about which little is known certainly.

The upper limit of the flamelet regime is often given by $K<1$, where K is the ratio of chemical to turbulent time scales given by (7.23). Numerical simulations by Poinsat et al. (1991) indicate that this limit should be increased by an order of magnitude, to $K<7$, since small scale turbulence rapidly decays within a flamelet before local quenching can occur. Bradley et al. (1992) argues that the reaction zone thickness, δ/β, may give a better chemical timescale for K than the thermal thickness δ. The expression for K will then be reduced with an order of magnitude.

7.3.2 Experimental data

A comparison between turbulent burning velocity prediction and experiment requires care because the experiments are difficult to carry out and to interpret. Unlike the laminar case, the turbulent burning velocity is not simply a function of the chemical reaction rates and molecular transport properties. It is not entirely clare that a steadily propagating flame can exist, independently of the nature of the stabilization device or the ignition period, even in steady homogeneous turbulence. Turbulent flame propagation is a poorly understood function of many properties relating both to the turbulent flow field and to the reacting medium. Turbulent flame brushes tend to be relatively thick, and the rate at which the leading edge of a propagating flame entrains reactants may be significantly greater than the rate at which reactants are converted into products inside the flame. This leads to a difference between the burning velocity and the mass burning velocity, as discussed by Abdel-Gayed et al.(1986b). The burning velocity is normally reported from experiments. The mass burning velocity is however the input needed for the burning velocity model.

A range of simple formulas for turbulent burning velocities exist in the literature. Their validity are however restricted by factors as scale, gas mixture and combustion regime, as discussed by Gulder (1990). An example on such simple formulas are shown (7.20) and (7.21).

$$S_T = 2u' \tag{7.20}$$

$$S_T^2 = S_L^2 + u'^2 \tag{7.21}$$

The main problem is to make a general turbulent burning velocity model, which give representative velocities for any turbulence field (distribution of turbulence and length scale) gas mixture (fuel type, Lewis number, equivalence ratio), pressure and temperature.

Abdel-Gayed et al. (1987) presents sources for turbulent burning velocity data, with a total of 1650 experimental values. These data were evaluated and made dimensionless by dividing the turbulent burning velocity and intensity with the laminar burning velocity. The data are presented in Figure 7.4 from Bradley et al. (1992). Abdel-Gayed et al. (1987) presented the data in a older version of Figure 7.4, where the turbulent burning velocities were correlated against K (for Le<1.3 and Le>1.3) instead of $K\ Le$. Most experiments were performed in a fan-stirred bomb. The burning velocities were here measured with the double kernel technique, in which the closing velocity of two propagating flame fronts of separate kernels was measured. Other experiments were performed in burners, ductes and tubes. The experimental data cover many fuels and equivalence ratios, but the turbulence is restricted to integral length scales below 4 cm and intensities below 18 m/s. None of the experiments were performed at elevated pressures. There is typical a factor of two in difference between

The turbulence fields were measured in the cold reactants, with varying degree of accuracy, and were in some cases only estimated. The effects of the spectrum of turbulence were evaluated by Abdel-Gayed et al. (1986b). As the flame propagates from a spark in a turbulence field, the flame is affected first by the higher frequencies and then progressively by the lower ones. In several of the experiments an effective turbulent intensity, which takes into account the frequency spectrum affecting the flame, is therefore reported.

Interpolation of the turbulent burning data into a turbulent burning velocity have been done, as presented in next subsection. It is however not obvious how these data should be extrapolated for elevated pressures, turbulence length scales larger than 4 cm and turbulence velocity fluctuations larger than 10 m/s where nearly no experimental data exist.

The experimental data shown in Figure 7.4 shows that the maximum burning velocity and the quench occur for the same turbulence intensity, when the length scale is constant (R_L / u' is constant). However experiments where the length scale is kept constant, as Abdel Gayed et al. (1984) and Sokolik et. al. (1967) shows that the maximum burning velocity is achieved for one intensity, whereas quenching is obtained for a higher intensity with a much lower burning velocity. Figure 7.4 is therefore not too representative close to quenching, since it does not include this parabolic dependency.

Transient explosion experiments were done at CMI by Bjørkhaug (1986) in a 1 m radial vessel, (a similar vessel is shown in Figure 8.1). Turbulence, *u*', and flow velocity, *U*, were measured, in addition to a 1D flame velocity, $F=\Delta x/\Delta t$, based on differences in time of flame arrivals at different monitor points. Assuming that the flame and the flow propagate horizontally, as a 1D flame, the experimental burning velocities were calculated as

$$S_T(u') = F - U \tag{7.22}$$

Figure 7.5 shows these experimental velocities, compared with (7.30) which give velocities based on data from Figure 7.4. Both the flame and flow directions may, however, have an angle α with the horizontal plane, then the burning velocity will be lower, and can be calculated as

$$S_T(u') = F\cos(\alpha) - U/\sin(\alpha) \tag{7.23}$$

The scatter in the burning velocity data in Figure 7.5 may be explained with a range of different angles, α, in the different CMI experiments.

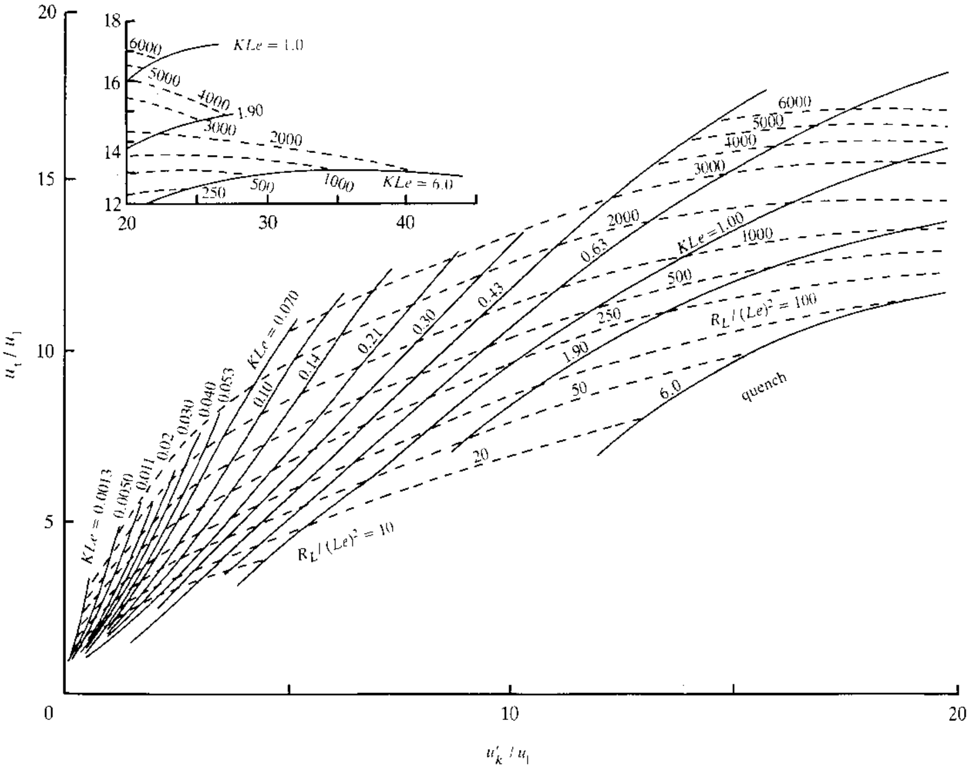

Figure 7.4 Correlation of turbulent burning velocities, from Bradley et al. (1992)

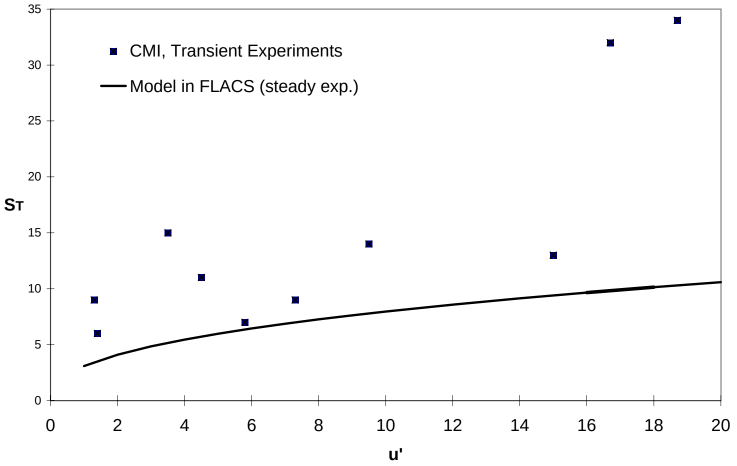

Figure 7.5 Turbulent burning velocity as function of turbulent intensity

7.3.3 Model in FLACS

The turbulent burning velocity in most burning velocity based explosion codes, like FLACS and Cobra, is based on the simple correlation from Bray (1990)

$$S_T = 0.875 u' K^{-0.392} \tag{7.24}$$

which is derived from the figure with experimental data presented by Abdel-Gayed et al. (1987). The Karlovitz stretch factor, K, is the ratio of flow strain rate to flame gradient, which is expressed by Abdel-Gayed et al. (1987) as the ratio of burning velocity timescale, δ/S_L, to Taylor timescale, u'/λ. With the flame thickness expressed by (7.6) the strain rate is

$$K = \frac{\alpha}{S_L^2}\frac{u'}{\lambda} \tag{7.25}$$

The Taylor microscale, λ, is in isotropic turbulence related to the turbulent dissipation by

$$\frac{\varepsilon}{\nu} = 15\left(\frac{u'}{\lambda}\right)^2 \tag{7.26}$$

Inserting (7.26) into (7.25) and assuming the Prandtl number, $Pr=\nu/\alpha$, is equal to one gives this strain rate as function of turbulent dissipation (for hydrocarbon-air mixtures $Pr=0.7$).

$$K = 15^{-1/2} S_L^{-2} \sqrt{\nu\varepsilon} \approx \frac{1}{200}\sqrt{\varepsilon} \tag{7.27}$$

This strain rate is often expressed in terms of the integral length scale through the turbulent Reynolds number R_T, which is obtained by inserting the Bradley version of (4.15) into (7.27)

$$K = 0.157 (u'/S_L)^2 R_T^{-1/2} \tag{7.28}$$

$$R_T = u' l_I / \nu \tag{7.29}$$

With K and R_T inserted into (7.), the turbulent burning velocity is

$$S_{T1} = 1.8 S_L^{0.784} u'^{0.412} l_I^{0.196} \nu^{-0.196} \tag{7.30}$$

S_{T1} was reported to be valid for $Le<1.3$, but it is not valid for large values of K or for low turbulent fluctuations. In the limit $u' \to 0$, (7.16) gives $S_T \to 0$, but should instead give $S_T \to S_L$. From the experiments presented by Abdel-Gayed and Bradley simple correlations can be made for low u' that satisfies this limit, as done by Gulder (1990)

$$S_T = 0.6 S_L^{1/2} u'^{3/4} l_I^{1/4} \nu^{-1/4} + S_L \tag{7.31}$$

The author have made his low intensity correlation by adding the product of (7.30) and the square root of u'/S_L to the laminar burning velocity

$$S_{T2} = 0.96 S_L^{0.284} u'^{0.912} l_I^{0.196} \nu^{-0.196} + S_L \tag{7.32}$$

Both (7.31) and (7.32) give representative results, but they include a too large influence of l_I. (7.32) is more similar to (7.30) and is therefore used in FLACS. The turbulent burning velocity in FLACS is therefore, as reported by Arntzen (1993) and Popat et al. (1996):

$$S_T = min(S_{T1}, S_{T2}) \tag{7.33}$$

In measurements of burning velocities in experiments, it was seen that turbulent strain reduced the turbulent burning velocity, and when the turbulent strain was large enough, the flame was totally quenched. Since the bomb experiments were done in connection to internal combustion engines, a total quench of the flame was defined for the strain rate where ignition did not occur in the bomb in minimum 10% of the tests. This occurred typically for $K \approx 1$. For flame propagation in an explosion the whole flame will be totally quenched at a much higher strain rate, only parts of the flame will be quenched at this strain rate.

The effect of strain on the maximum turbulent burning velocity has been incorporated in the FLACS code with a conservative approach. The turbulent burning velocity, at constant turbulent length scale, follows (7.30) but is set constant for strain rates above a limiting value. Figure 7.6 shows the burning velocities with K=1 as the limiting value.

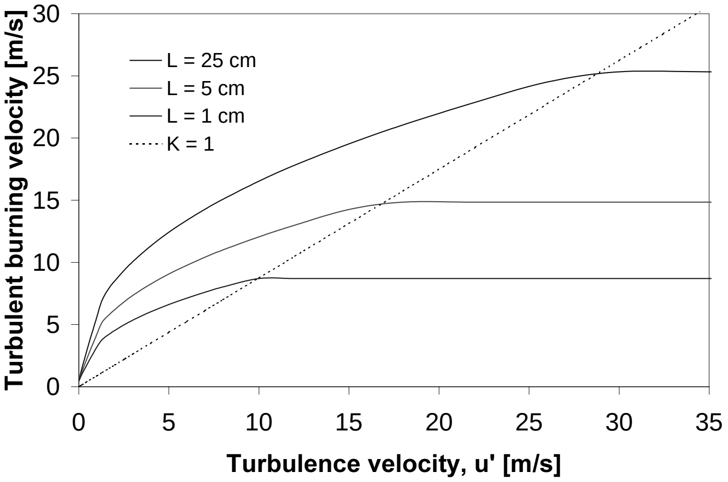

Figure 7.6 Turbulent burning velocity as function of turbulence field, for S_L=0.45 m/s

This burning model leads to an increase in the importance on length scale for high *u*'. At *u*' = 9, the burning velocity for l_I = 25 cm is twice of that for l_I = 1 cm, but for *u*' = 30, the burning velocity is three times larger. In FLACS a some what higher limiting *K* value was later chosen, since Figure 7.4 gives a maximum burning velocity under constant length scale for a *K* value somewhat above 1. This neglection of total as well as partly quenching of the burning rate was done to avoid that an over-prediction of turbulent strain and/or under-prediction of turbulent length should lead to underestimation of explosion pressures. Quenching is, however, most important at small scale where the code is validated. The neglection of quenching may therefore lead to under-prediction in real scales, as discussed in Subsection 7.3.6.

Several gas mixtures, like those including ethylene, do not fit into the turbulent burning velocity model, (7.30) and Figure 7.4. Experiments with hydrogen-air mixtures seems to give higher values than (7.30). The experimental data for these fuels should be evaluated in an attempt of expanding the model to also include these fuels. The effect of different volume expansions, τ, on the turbulent burning velocity has not been included. The larger the expansion, the more the flame front will be disturbed and the flame area be increased, with a corresponding increase in burning velocity. The expansion is likely to disturb the flame front most, when the flame and flow field is in the same direction, and least when they are in opposite directions. Bray (1990) argues that the turbulent burning velocity should be proportional with $(1+\tau)^{1/2}$. The burning velocity model should rather have been represented by a parabolic dependence on *u*' for constant length scale. This however require a representative and less grid dependent length scale from the turbulence model, since a parabolic burning velocity model will typically, for the same turbulent intensity, give a high burning velocity for one length scale and zero velocity for a smaller length scale. Better experimental burning velocity data will also be needed.

The turbulent burning velocity model presented above is only valid at atmospheric pressures, it does not take into account the effects of Lewis number or include a parabolic dependency for constant length scale. These three deficiencies are therefore evaluated and solutions are suggested in the next three subsections.

7.3.4 Turbulent burning velocity as function of pressure

The turbulent burning velocity in FLACS is based on a formula where the chemical reactivity is included through the laminar burning velocity. However this formula is valid only at atmospheric pressure.

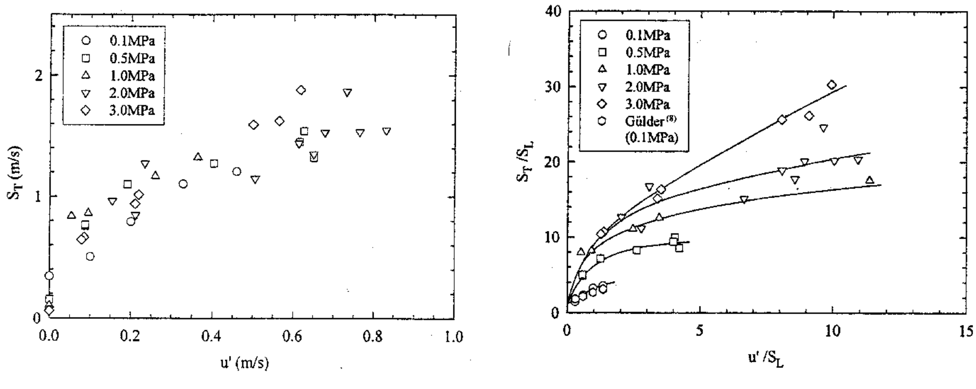

Figure 7.7 Pressure dependence of turbulent burning velocity, Kobayashi et al. (1996)

The laminar burning velocity for most hydrocarbons decreases with pressure, due to decrease in thermal diffusivity, as can be seen from (7.1) and (7.3). Experiments done by Sokolik et. al. (1967) show that the turbulent burning velocity is independent of thermal diffusivity, except for low turbulence intensities where the laminar burning velocity is dominant. Experiments done by Kobayashi et al. (1997) indicate an increase with pressure for the turbulent burning velocity. They also shows that the area of the flame increases with pressure. Kobayashi et al. (1996) have measured the turbulent burning velocity as function of pressure and turbulent intensity for a lean methane air mixture. The measured data are shown in Figure 7.7.

At constant reactant temperature, the increase in turbulent burning velocity from one to five bar absolute pressure was observed to be on average around 30% in Figure 7.7. This may roughly be described by

$$S_T \propto P^{\beta} \tag{7.34}$$

where β is around 0.17. In FLACS the implemented pressure dependency can be found by inserting (7.14) into (7.30). Since the kinematic viscosity, ν, has been given a constant value in FLACS, β is here as low as -0.39. Incorporation of a pressure dependent ν, increases β to -0.2, which is still too low. The burning velocity shall therefore be 47% higher at a pressure of one barg and 84% higher at two barg compared with the turbulent burning velocity in FLACS, for methane. The pressure dependence can mainly be explained by the increase in density (and kinematic viscosity), which results in a thinner flame and increased flame area. The simplest way of implementing this dependency in the present burning velocity model in FLACS is to neglect the pressure dependency of the laminar burning velocity, and only include the temperature dependency. The pressure dependency of the turbulent burning velocity model (7.30) will then only be a function of the kinematic viscosity.

$$S_T \propto \nu^{-0.19} = \mu^{-0.19}\rho^{0.19} \sim P^{0.19} \tag{7.35}$$

This dependency is close to the experimental for methane, but ethane and propane have a larger β ιν (7.34), as shown by Kobayashi et al. (1998). A better way of including the pressure dependency may be to make a turbulent burning velocity which is based on a chemical timescale, instead of laminar burning velocities, as presented in the next subsection. The pressure dependency for mixtures with other equivalence ratios, fuels and length scales is not known, due to lack of experimental data. Such experiments must be performed before a general pressure dependence model for turbulent burning velocities can be verified.

FLACS-93 to 96 have done well in calculation of explosion experiments, including those with high peak pressures, despite the under estimating of turbulent burning velocities at elevated pressures. The code may calculate the high pressures as follows: High pressures occur mainly in highly obstructed geometries, where the unmodified subgrid turbulence model in FLACS produce too high turbulence intensity and length scale (see section 4.8). When the flame arrives in a cell with a high length scale, the unmodified turbulence model gives a high unphysical turbulence generation. A too high turbulence results in a too high burning velocity, which compensates the incorrect burning velocity model at high pressures. The neglection of quenching will also help in overestimation of burning rates, as discussed in Subsection 7.3.6.

Simulation of explosion experiments with FLACS-96*, which should have a better representation of both the flame and turbulence production, resulted in underprediction of peak pressures above one barg, when the turbulent burning velocity model of FLACS-96 was used. The validation of FLACS-96* continued with the improved pressure dependence of (7.35) on the turbulent burning velocity. The simulations were repeated and agreed then well with the experiments, independent of peak pressures.

7.3.5 Lewis number dependence

Abdel-Gayed et al. (1984) show that mixtures with similar laminar burning velocity, but different Lewis number can have very different turbulent burning velocities for the same turbulence field. The background for this is that turbulent flames in mixtures with low Lewis number is less quenched than those with high *Le*, for the same strain rate. This shows the importance of including the effect of *Le* in turbulent burning velocity models. The Lewis number is typically around one for stoichiometric fuel air mixtures but may deviate with a factor of five for rich and lean mixtures. Bradley et al. (1992) argue that the turbulent burning velocity data correlate better with *K Ma* than *K*. Since the Markstein number in many situations changes linearly with *Le,* he claims the turbulent burning velocity can be approximated with

$$S_T = 0.88u'(KLe)^{-0.3} \tag{7.36}$$

for $0.01<KLe<0.63$ where *Le* is given by (7.4). He shows that (7.36) where *Le* is taken into account, correlates much better with experimental data than (7.30). It should here be noted that the laminar burning velocity can be described as a function, (7.2), of thermal diffusivity and the chemical time scale (which is mainly a function of product temperature). From (7.25) *KLe* can be expressed as

$$KLe = \frac{\alpha}{S_L^2}\frac{u'}{\lambda}Le \tag{7.37}$$

Subsection 7.1.1 and (7.5) showed that the velocity squared can be seen as proportional with $\alpha Le/\tau_c$. Inserting of (7.5) into (7.37) give (7.38), which illustrates that the turbulent burning velocities are likely to correlate better with a strain rate based on the chemical timescale, τ_c, than a timescale based on the laminar burning velocity. The *Le* dependence is also avoided.

$$KLe \approx \tau_c\frac{u'}{\lambda} \tag{7.38}$$

KLe in (7.36) may therefore be replaced by a new strain rate based on the chemical timescale τ_c.

$$S_T = 0.88u'K^{*-0.3} \tag{7.39}$$

$$K^* = 0.157\tau_c\left(\frac{u'^3}{l_I\nu}\right)^{1/2} \tag{7.40}$$

Incorporation of τ_c from (7.10) into (7.40) converts (7.39) to a representative general turbulent burning velocities model for hydrocarbons at atmospheric pressures. The effect of pressure are included by using pressure dependent ν and τ_c. The kinematic viscosity, ν, which is a function of pressure and temperature, can be expressed through the dynamic viscosity, μ, which is essential dependent on temperature only. With small changes in the product temperature ν can be seen as only proportional with the pressure

$$\nu = \mu/\rho \sim 1.5/P \tag{7.41}$$

The only way of including the observed pressure dependence of turbulent burning velocities, from Figure 7.7, through the strain rate, (7.40), is to assume that the chemical timescale is inverse proportional with pressure, as (7.18). A chemical time calculated with a chemical kinetic code, as CHEMKIN, is likely to give a lower pressure dependence than (7.18), but then an extra model, e.g. for increase in flame area with pressure, must be included in the turbulent burning velocity model, (7.39). With the chemical timescale, (7.18), and ν, (7.41), inserted into the improved strain rate, (7.40), it can be expressed by turbulence parameters, pressure and temperature in products

$$K^* = \frac{1}{1180}\left(\frac{u'^3}{l_I P}\right)^{1/2} e^{16000/T_P} \tag{7.42}$$

A pressure dependent turbulent burning velocity model, where (7.42) is inserted into (7.39), should be representative for most hydrocarbon-air mixtures. The activation temperature as well as the pressure exponent may, however, differ for some fuel mixtures.

7.3.6 Parabolic dependency

The turbulent burning velocity data have been fitted with power functions of the arguments, as (7.39). However the experiments show a parabolic dependence with turbulent fluctuations, e.g.

$$S_T = S_L + 2u' - 0.3u'^2 \tag{7.43}$$

for a specific gas mixture, Solik (1967), Abdel-Gayed et al. (1984). A turbulent burning velocity model should therefore be specified with a parabolic dependency. A requirement of such a model can be to have maximum burning velocity for one specified strain rate and zero burning velocity for another strain rate. The simplest model which fulfils this is

$$S_T = S_L + u'(a - bK^{*d}) \tag{7.44}$$

where *a*, *b* and *d* are constants which must be determined so the model fits experimental results. Values below zero from (7.44) is equal to no burning velocity. Since *K* is proportional with $u'^{3/2}$, this model gives a maximum for

$$K^{*d} = \frac{a}{b(1 + 1.5d)} \tag{7.45}$$

and is zero for

$$K^{*d} = \frac{1}{b}\left(a + \frac{S_L}{u'}\right) \approx \frac{a}{b} \tag{7.46}$$

With the coefficients *a*, *b* and *d* chosen to be 2.15, 1.3 and 1/5, the turbulent burning velocity model with parabolic dependency roughly fits experimental results and is expressed as

$$S_T = S_L + u'(2.15 - 1.3K^{*1/5}) \tag{7.47}$$

This model gives the burning velocity a maximum for *K**=3.33 and a zero value just around *K**=13. As the strain rates increases toward this maximum value, the probability that some parts of the flame is quenched increases. The turbulent burning velocity from the model in this limit may therefore be seen as the product of the unquenched burning velocity and the probability that the flame is not quenched.

The burning velocity for a hydrocarbon air mixture may be expressed as a function only of turbulence parameters, pressure and temperature in products, as (7.48), by inserting *K** through (7.42) into (7.47).

$$S_T = S_L + 2.15u' - 0.32\frac{u'^{1.3}}{(l_I P)^{0.1}}e^{T_A/5T_P} \tag{7.48}$$

With T_A inserted from (7.10) and l_I replaced by a dependence on ε, (4.15)

$$S_T = S_L + 2.15u' - 0.35u'\left(\frac{\varepsilon}{P}\right)^{0.1}e^{3200/T_P} \tag{7.49}$$

For a gas mixture around atmospheric pressure (P=10^5)and laminar burning velocity equal to 0.4 m/s (T_P=2170) this turbulent burning velocity model can be expressed as

$$S_T = 0.4 + 2.15u' - 0.43u'^{1.3}l_I^{-0.1} \tag{7.50}$$

The dependency from of formula (7.50) is shown in Figure 7.8, for three values of the turbulent integral length scale, l_I, 1, 10 and 100 mm. Experimental values from Figure 7.4 for the two smaller length scales are also shown. Turbulent intensities are not likely to be much higher than 50 m/s, since the flow velocity is restricted by the velocity of sound. As can be seen from (7.48) an increase in pressure from 1 to 10 bar will in this model have the same effect on the turbulent burning velocity as increasing the length scale with a factor of ten.

This parabolic representation can be a much better representation of the turbulent burning velocities, since it includes the quenching process more representative, with a slow decrease towards zero for the burning velocity as the turbulent strain increases. The modelled burning velocities in Figure 7.8 agree well with the experimental data from Figure 7.4, for u’ < 10 m/s and l_I = 1 cm and 1 mm. For larger u’ and l_I above 3 cm, experimental data are very rare so a comparison is difficult. The parabolic model (7.49) gives a lower burning rate for high turbulent strain rates than the model used presently in FLACS. For high strains the flame is no longer a flame sheet, but a reaction zone which is partly quenched.

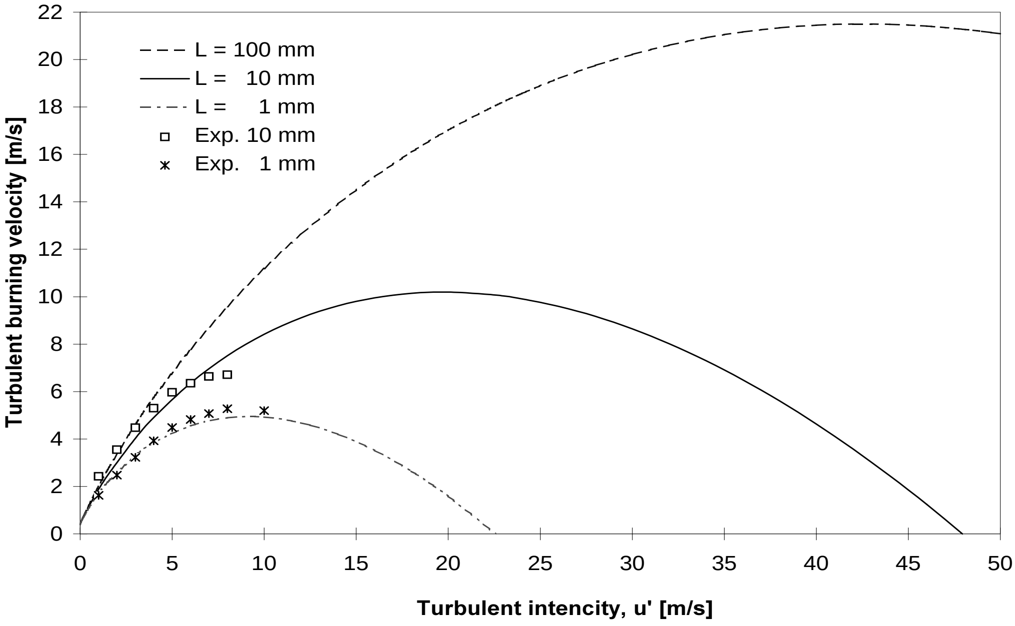

Figure 7.8 Turbulent burning velocity with parabolic dependency

It is therefore difficult to measure a burning velocity in experiments. In Figure 7.4, quench is defined as when ignition failed in minimum 10% of the tests in the bomb. In reality the flame will burn at much higher strain rates than shown in Figure 7.4, but the burning rate will decrease with strain rate as more and more of the flame is quenched. The decrease in turbulent burning velocity with intensity may be seen as the product of the burning velocity of an unquenched flame and the probability that the flame is not quenched, as illustrated by Bradley et al. (1992).

(7.49) gives nearly no length scale dependency for smaller strain rates. This is also seen in experiments, but is not included by the formulas from Bray (7.30) or Bradley (7.36). Other functions than (7.49) may, however, describe the turbulent burning velocity even better. It is not certain that the strain rates for maximum burning velocity and total quench are the same for all turbulent length scales. Even if they are the question is then how representative the strain rate expression used is. The higher turbulent burning velocities of fuels as hydrogen, acetylene and ethylene, are not likely to be explained by lower strain and be expressed by (7.49) or (7.30). They may be better represented by e.g. giving the constant a in (7.44) a reaction rate dependency. Simulation of explosion experiments with the burning velocity based on (7.30), give, therefore, a significant underprediction of explosion pressures for these three gasses, as shown in subsection 8.2.2.

This parabolic model requires that the turbulent length scale is well represented. This can be illustrated from Figure 7.8, where u'=23 gives respectively 0 and 9 m/s in burning velocity for the two smaller length scales. Turbulence modelling which gives representative turbulent length scales, as presented in Chapter 4, is therefore a requirement before a parabolic turbulent burning velocity model like this can be implemented. As shown in Chapter 4, the turbulent length scale is typically 10% of the obstruction diameter. If Figure 7.8 is representative, the turbulence generated from larger objects in an offshore module will not lead to a decrease in burning rate for high turbulent intensities. Turbulence generated behind smaller pipes, or in down scaled experiments will lead to quenching for relatively low intensities.

The consequence of not including the parabolic decrease in burning velocity due to quenching into an explosion code, is that if all other models are correct, too high burning velocities, and thereby too high peak pressures will be calculated. The defect increases as the length scale becomes smaller. The explosion experiments which the explosion codes are validated against, are mostly done in smaller scales with corresponding small length scales. When the burning velocity model does not include quenching other sub models must be adjusted to give lower values at high strain rates, to avoid overprediction of peak pressures. These submodels can typically be the pressure dependence of burning velocity (which was underestimated in FLACS) and the flamefolding model. When these tuned explosion codes are used in larger scale, where quenching is less important, they will underpredict peak pressures. This is also seen in prediction of large scale experiments. At high turbulent intensities, the burning rate around small objects will be to large compared to the burning rate around larger objects.

Simulation of gas explosion experiments may be used in the extrapolation of the turbulent burning velocity models under the assumption that other submodels in the explosion model, like the flame and turbulence model, are representative. Experiments with a few large cubic obstructions which result in high flow velocities, should be ideal to extrapolate the burning model with respect to both turbulent length and intensity

Turbulent burning velocity expressions, like (7.49) should be compared with all the experimental data from the Leeds database, for validation and to obtain improvement in their coefficients. The mean deviation between experimental data and the expressions should be minimized by adjusting the coefficients in the expressions.

7.3.7 Turbulent burning velocity as function of turbulent length scale

The turbulent length scale, to be used in the turbulent burning velocity models as (7.30) or (7.48), should ideally be taken from the turbulence model. This was done for FLACS-96*, where the subgrid turbulent energy and length model, presented in Chapter 4, is used. In the other versions of FLACS, the length scale from the turbulence model was too grid dependent to be used. More representative length scales were, therefore, instead estimated as function of distance from ignition, and dimension of geometry (distance between walls) as presented by Hansen (1994). This gives a length scale which is independent of grid resolution, but it is a function of location and not very representative. The real turbulent length scale is normally a function of the width of the shear layer where the turbulence was created (as behind obstructions), and not the distance between walls. The length scale is also transported with the flow.

7.4 Dust-air clouds

Explosions in dust-air clouds may be modelled in a similar way as gas explosions, as described in Section 3.5. Bradley et al. (1988) measured turbulent burning velocities for fine cornflour dust. They found that the values obtained correlate with the laminar burning velocity and turbulent parameters in the same way as for purely gaseous fuel-air mixtures.

The laminar burning velocity in dust-air is, as in gas-air, dependent on fuel type and concentration. For dust-air the velocity may also depend on the particle size distribution. The dust flames are also thicker than gaseous flames, due to the time lag in the heating of the particles.

7.5 Waterspray

A water spray system can be an effective device in the case of a gas explosion, reducing the pressures significantly. This mitigating effect has been seen in many experiments. When the droplets are small enough, from the nozzle or due to break-up, they evaporate. The product temperature is then reduced, as discussed in Section 3.4. This results in a lower burning rate and a reduced volume expansion for products. However, large droplets tend to increase the turbulence level and thereby the burning rate. This effect is most important when other turbulence production is low. All three effects should be included in waterspray models.

The model included in FLACS for water spray is very simple, but performs well in simulation of explosion experiments. It is described by Storvik et al. (1996). The droplets are assumed to break-up and evaporate (the mitigation is effective) when the gas flow exceeds a so-called critical break-up velocity (depending on droplet diameter). The effective burning velocity can then be expressed as:

$$S_{waterspray} \approx min\left[\frac{8}{Q}S_T + 2S_L, S_T + \frac{Q}{4}S_L\right] \tag{7.51}$$

where Q is the mass flow of water per area (kg/m^2/min.). The S_L terms in (7.51) gives the increase in burning velocity due to the turbulence generation from the spray. The S_T terms includes the mitigating effect. According to (7.51), waterspray have no mitigating effect for flow rates, Q, below 8. This limit is doubtful. It is more likely that also smaller Q will have a mitigating effect. Furthermore this model does not include the reduction in volume expansion. It will normally be reduced with more than 10%, as described in Section 3.4.

In FLACS the water spray turbulence generation is included only by an increase in the burning velocity through (7.51). It should instead be modelled as generation of turbulence. The generation of turbulent energy is typically proportional with the mass flow of water, Q. From these relations and (4.17), the turbulent intensity, u', achieves a representative dependency on both l_t and Q.

$$u'^3 \propto l_t\varepsilon = l_tP_k \propto l_tQ \tag{7.52}$$

With the turbulent length scale modelled as a fraction of the droplet diameters, the length scale will be very small, the dissipation large and the resulting turbulent intensity small. A larger length scale, given by the larger scale flow field caused by the nozzle flow, may be more representative.

Also the mitigating effect, modelled in FLACS by (7.51), should be replaced. In the previous section it was recommended to use a turbulent burning velocity model which depends on a chemical time, given by the product temperature. The cooling effect caused by water spray on the flame temperature and the burning velocity, will here be included and there may be no need for further adjustment of the burning velocity due to the presence of water spray. The only remaining problem is then to estimate the evaporation rate, so the product temperature and the volume expansion of products can be calculated as described in Section 3.4. This will give a reduction of burning velocity in water sprays, which has larger validity than (7.51), and it will be independent of fuel mixture. In addition the effect of reduced volume expansion will be included.

7.6 Flamefolding

The flamefolding models shall give an increase in flame area, to compensate for the difference in flame area on the numerical grid and the actual flame area. The coarser grid is used, the smaller is the flame area on the grid, compared with the real flame area. This can be seen in Fig. 6.10 were the flame locations are shown at three grid resolutions in a simulation of a SOLVEX experiment. Also when the geometry is resolved on the grid, some of the flame area is missing since the flame is not able to follow all details of the flow field. The subgrid flamefolding model shall represent the extra flame area around subgrid objects.

7.6.1 Ongrid

The ongrid flamefolding models should give no increase in the flame area as long as the burning velocity is quasi-laminar, since this model should secure a correct flame area independent of grid resolution. As the flow becomes more turbulent and the burning velocity is turbulent, some parts of the flame are no longer resolved on the grid, and an ongrid flame folding model is needed.

One may assume that to obtain a representative burning rate, both the flame area and the burning velocity must be representative. The flame area of a turbulent flame, can typically be seen as the area the flame has if it is measured with resolution of the turbulent integral length scale, l_t. If the grid cell size is larger than l_t, the ratio between the real flame area and the area in the grid cell may be expressed as

$$\frac{A}{A_0} = \left(\frac{n\Delta}{l_t}\right)^{\alpha_t} \tag{7.53}$$

where n is the number of grid cells needed to resolve l_t. n may typically be 0.4 with the SIF model and 1.0 with the β flame model.

α_t is a function of the fractal dimension of the flame, if l_t is larger than the grid cell size. If l_t is smaller, it may be a function of the fractal dimension of the flow. Lower and higher cutoff values should also exist, due to the fractal theory. For the flame, these are typically the laminar flame thickness and a turbulent integral length scale. In FLACS-96* a value of 0.1 on α_t was chosen and it resulted in relatively grid independent explosion simulation results. If explosion simulations give lower pressures on a coarse grid than on a fine grid, α_t should be increased since this will result in larger flame areas (and peak pressures) on coarse grids and thereby result in a more grid independent code.

Standard FLACS-96 (with β flame model) does not use the ongrid flamefolding model, but uses an indirect concept to take ongrid flame folding into account and reduce the grid dependency of the code. The turbulence production from flows past an obstruction is proportional to the obstruction area, D, in flow direction. In FLACS-96, the subgrid turbulence production (4.101) has been replaced by

$$P_k \propto D(2 - D/\Delta) \tag{7.54}$$

where Δ is the grid cell area. Smaller subgrid objects are, incorrectly, given nearly double turbulence production per area compared with larger subgrid obstructions.

Since a higher turbulence level often gives higher burning velocity, this model in many situations gives a similar effect as a ongrid flame folding model. This increase in turbulence production may however give wrong trends, since the flame is more quenched for high intensity and small length scale turbulence.

7.6.2 Subgrid

The subgrid flamefolding model presented here is phenomenalogically based, and should give the eventual increase of flame area due to subgrid geometry. This model was developed by the author and was first implemented in FLACS 93, together with the β flame model. The need for a subgrid flamefolding model was recognized by the author through the MERGE project, Arntzen (1993a). The need for a subgrid flamefolding model in explosion codes is now generally accepted, Vasey (1995).

In the model it is assumed that the flame area will increase with the size of the obstruction and the distance the flame fronts are transported downstream before the wake behind the obstruction is burned out. The model for extra flame area is therefore proportional to the area fraction of subgrid obstructions (with an end wall in the flow direction) T_{i+} and the ratio of flow velocity to burning velocity.

Figure 7.9 illustrates the flame propagation in a box, which is closed on the left side and open on the right side. The flow velocity is zero, left of the flame, and U_e, right of the flame. It is assumed that there is no flame area increase for the flame propagating inwards, since there is no flow field ahead of the flame which could increase the flame area. As may be seen from Fig 7.9, the area increase should be based on the velocity downstream the object. This velocity must be in downstream direction and the flow must consist of reactants only, else the area increase is zero.

The ratio of outflow velocity to burning velocity, can be expressed as a function of flow velocity, by inserting values for the turbulent burning velocity, and turbulent fluctuations:

$$\frac{U_e}{S_T} \approx \frac{U_e}{6(S_L u')^{1/2}} \approx \frac{U_e}{3(S_L U)^{1/2}} \approx \frac{1}{3}\left(\frac{U_e}{S_L}\right)^{1/2} \qquad (7.55)$$

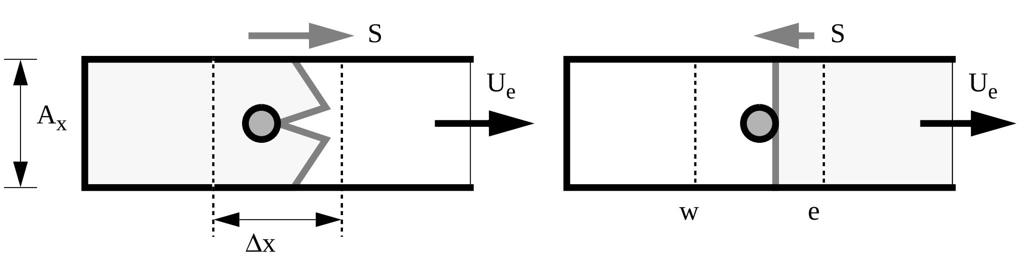

Figure 7.9 Flame area increase due to subgrid object for a flame propagating outwards of a box, (left) and inwards (right)

The extra area due to the flow in positive x direction can be expressed as

$$\Delta A = \alpha U_e^{1/2} \phi T_{x+} A_x^{3/2} / \Delta x_x \tag{7.56}$$

where α is a constant with values found from FLACS validation, This value depends on values chosen for other submodels. For FLACS-96* (with SIF) an α was found, which was only 40% of the α used in FLACS-96 (with the β flame model). This gives an area increase of 40% for SIF and 100% for the β flame, in a situation with an obstruction blocking 50% of the area, T_x=0.5, and U=40 m/s. The extra area will typically have a maximum if the flame and the flow propagates in the same directions and decrease as the directions differ. This is represented with the factor ϕ.

In the SIF model, the direction factor, ϕ, was set to 1, if the cell face has outflow and consists of reactants, and 0 else. This ϕ factor may need an adjustment, since simulation of explosion experiments with ignition at an open end (which tends to have ϕ=0) seems to under predict explosion pressures. In the β flame model, ϕ can be calculated from the vector product of velocity and the normal vector of the flame, defined from the gradient of the product concentration

$$\phi = max\left(\frac{\vec{U} \bullet \vec{F}}{|\vec{U}||\vec{F}|}, 0\right) \text{ and } \vec{F} = -\nabla c \tag{7.57}$$

The possibility of making a subgrid flame area model from the results of fine grid simulations was evaluated, but there are too many parameters involved which could be varied, like 3D flow fields, turbulence parameters, flame orientation and number and dimension of obstructions. The flame location from such a simulation is shown in Fig 7.10 with the flame located upstream and later around a cylinder. Dark cells indicate a higher burning velocity which is found in the shear layer behind the cylinder.

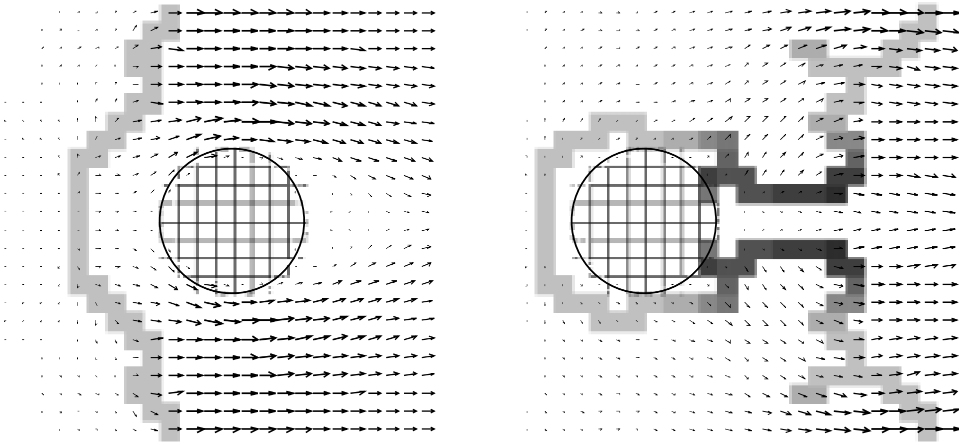

Figure 7.10 SIF simulation of flame propagation outward of a box, past a cylinder

7.7 Summary

Burning velocities is an input to the flame models in explosion codes. In an explosion the flame normally starts with a nearly laminar flame, which becomes turbulent when it reaches obstructed areas.

The turbulent burning velocity is modelled in the FLACS code as a function of turbulent parameters and a chemical time based on laminar burning velocities. This function is based on a correlation of data from turbulent burning experiments. The effects of fuel mixture, equivalence ratio, pressure and temperature on the turbulent burning velocity have all been modelled through correction models for these effects on the laminar burning velocity. This model gives the turbulent burning velocity a wrong pressure dependency and the effect of flame quenching is not included.

It has been shown that the turbulent burning data may correlate better against a chemical timescale calculated from pressure and temperature in the product. With this correlation the pressure dependency is more representative and the requirement for submodelling the effects of different gas compositions, as well as water spray and the increase in temperature due to compression, is reduced or even avoided. A turbulent burning velocity model with parabolic dependency on the turbulent intensity is described to include the effect of flame quenching. More experimental turbulent burning data is, however, needed to secure a representative model at elevated pressures, at higher turbulent intensities and scales, and for a broader range of gas mixtures.

Ongrid and subgrid flamefolding models are included to take into account that some of the flame area is not represented by the numerical grid.

8 Simulation of gas explosions

This chapter presents methods for validation of explosion codes and their submodels. A range of explosion experiments is presented, and experimental results are compared with FLACS simulations. Finally, the potential in prediction of gas explosions is demonstrated.

8.1 Validation of explosion codes

Simulation of explosion experiments is needed to assure that the models in the explosion code are representative and correct implemented. They should also give input to extend submodels for areas where no or few data exists for them.

This chapter will summarize/evaluate the FLACS code’s ability to simulate a real explosion. A range of data from explosion experiments, as pressure-time data and time of flame arrival in a range of monitor points are used in the validation of explosion codes.

The pressure - time data from experiments and simulation could be compared directly, but these data are easier presented by three figures:

- peak pressure
- duration of pressure pulse (defined normally from pressures above 10% of peak pressure)
- time from ignition to peak pressure

Except for explosions with two, or more peaks, these three figures give a good description of the time - pressure history in a point.

In several experiments the peak pressures exceed the maximum value the pressure transducers can measure. The maximum pressure is then not known. The pressures from simulations are static pressures. In experiments the total pressure is measured. Depending on the location of the pressure transducers used in the experiments, they may also include the dynamic part of the pressure.

The peak pressures from many explosion experiments have an uncertainty of at least 20%. This uncertainty has been observed when experiments has been repeated. Experiments in large scale offshore modules have normally not been repeated, but when they have, a large scatter in the results have been seen. The background for this difference is that it is not possible to have two of these large scale experiments 100% identical. The gas clouds can be inhomogenous or there can be scatter in the stoichiometric ratio, which may make the flame more instable. Wind may influence and give turbulence or the ignition source may give different initial results (if e.g. a chemical igniter is used instead of an electric spark).

The sub models included in the explosion code FLACS do not include models which describe shock/compression ignition, transition to detonation or flame acoustics interactions. The code’s ability to give a representative simulation of gas explosions where one or more of these phenomena are important is therefore limited. The flame acoustics interactions can be important for combustion in nearly empty boxes, like the empty SOLVEX experiments. Shock/compression ignition can typically occur for pressures above three barg for methane-air mixtures and above one barg for mixtures containing other hydrocarbons. Explosion experiments have been performed in simple test geometries as well as in more realistic geometries. The most simple geometries are presented first, later the more realistic geometries.

8.1.1 Validation of submodels

The explosion code consist of a range of submodels as presented in the previous chapters, like the turbulence models (ongrid and subgrid), the flame model, the burning velocity models and the flame folding models. Most of these models include some uncertain factors which must be determined.

Turbulence and flame models should first be tested with some basic tests, as shown in Chapters 4, 5 and 6. In the evaluation of flame models, the flame's ability to move according to the specified burning velocity in 1D, 2D and 3D was tested. The ability of the turbulence models to give representative turbulence fields was shown in the presentation of turbulence modelling.

All validation and adjustment of explosion models and submodels should be done with variation of grid resolution to secure a code with little grid dependency. Different fuel mixtures should be tested to ensure that the code also can handle different fuels. The validation may include the explosion experiments presented in the next sections, and may typically be divided into six steps as shown below:

- The validation/adjustment of explosion models against explosion experiments should start with free flame propagation from a point. The flame location as function of time should be compared with experimental values, to secure that the ignition and quasi laminar burning velocity models are satisfactory.
- Next step is calculation of explosion experiments done in empty boxes (with one open wall and no obstacles inside) like the Sotra pipe, the empty SOLVEX box (two scales) and the B.G./Mobil box. These tests will verify e.g. that the flame has a representative burning towards wall.
- Simulation of experiments where all obstructions/geometry can be resolved ongrid, like the Sotra radial vessel, some of the MERGE geometries, the TNO experiments and the SOLVEX and B.G./Mobil boxes with obstructions inside. These tests will secure that the generated ongrid turbulence field and the turbulent burning velocity models are representative. Eventually a better extrapolation of the burning velocity model, with respect to higher pressures, turbulent intensity and length scales, can be made. Simulation with different grid resolutions will validate the ongrid flame folding model.
- Simulation of experiments were the obstructions are represented subgrid. The experiments to be simulated can be the same as in the previous step (but on a coarser grid) and the rest of the MERGE geometries. The constants in the subgrid turbulence generation and subgrid flamefolding models will be adjusted in these simulations.
- Simulation of experiments in scaled down versions of real offshore modules, like the M24 on Sotra. This validation secures that real obstructions/geometry are represented well. Simulation with ignition at the end of modules should secure that boundary conditions, as well as the flame is represented satisfactorily.
- The validation should finish with simulation of the experiments in full scale offshore modules, as the SCI module. This simulations will show that the sub models handle the effect of scale (like the extrapolated turbulent burning velocity model) and the inclusion of considerably smaller detailed geometry.

8.1.2 Effect of scale in the experiments

A range of experiments have been done in small scale and the experimental data are tried extrapolated up to full scale. Some parameters are similar, and some are different for different scales.

The turbulent fluctuating field is likely to depend only on the velocity field, but the turbulent length field is proportional with scale. Since the turbulent burning velocity increases with the turbulent length, due to less strain, it will also increase with scale. Based on (7.30), increasing the laminar burning velocity gives the same effect as increasing the scale. Several experimental programs have included this for scaling of experiments. Through oxygen enrichment, the product temperature and burning velocity were increased. A drawback with this method is that also the volume expansion increases. A better solution can be to replace the gas with another gas mixture with higher burning velocity but equivalent volume expansion.

The temperature drop in the burned gas due to heat loss from the gas to the surrounding geometry will decrease with scale, since the heat loss is proportional with the area and the energy content is proportional with the volume. The turbulence production behind round cylinders may however decrease with scale for $Re>10^5$, since the wake becomes thinner.

The explosion codes were previously, before the SCI experiments, validated against experiments done at medium scale, as the M24 module, with grid size around 0.2 m in simulations. Real offshore modules has a scale four to five times larger. In simulations of them, should the grid size or the number of grid cell needed to represent the module be kept constant if the results of a code is grid dependent? This question shows that the code results must have minimal grid dependency to avoid the problem of scaling

8.2 Simple geometry experiments

In this section explosion experiments in simple idealized geometries are described. Results from the experiment are presented, together with some results from FLACS simulations. Further description of explosion experiments and results in a range of the geometries can be found in Bjerketvedt et al. (1997). These results should typically be used in validation of explosion codes. Results from FLACS simulations of the experiments.presentd in this and next section, are presented by Hansen et al. (1985). The comparison between peak pressures from experiments and FLACS simulations are shown in Figures 8.15 and 8.16.

8.2.1 Free flame propagation

In experiments where no obstacles are present, there will be nearly no shear generated turbulence. The flame propagation started by a spark ignition will start burning with a velocity which is somewhat lower than the laminar burning velocity due to straining of the flame. After a few centimetres the straining becomes unimportant. As the flame radius increases, so does the burning velocity, it becomes quasi laminar, due to hydrodynamic instabilities and reaches a burning velocity higher than twice the laminar, after about 2 m, depending on factors as gas mixture and flame direction. The higher flame velocities measured in vertical direction upwards compared to horizontally may be due to buoyancy. The burning velocity may then be similar in all directions.

The development of the flame radius for larger flame radii is not well known, due to lack of good experimental data, but numerical analyses support a further increase with radius, as discussed in Section 7.2.

In the EMERGE project (Arntzen et al. 1995) the effect of initial turbulence (around the ignition point) on flame propagation, were investigated. In the turbulent region the burning velocity was up to ten times higher compared with a non turbulent situation, but as the flame propagated outside the turbulent region, there was nearly no difference in burning velocity compared with the no turbulent situation. The burning velocity was again a function of flame radius.

8.2.2 2D radial vessel at Sotra

A range of explosion experiments has been performed by CMR in the 10 m radial wedge-shaped explosion vessel, shown in Figure 8.1. The volume of the 10 m radial vessel is 18.5 m^3 and the height is 1.25 m. In the explosion experiments, the type, size and number of obstacles were varied, in addition to the confinement on the top of the vessel. A range of fuels and stoichiometric ratios were also tested. The effect of scale was tested in a 1/10 scale version of the vessel. Pressure as function of time and time of flame arrival was measured in several monitor points. The results from a range of these experiments, were presented by Bjørkhaug (1986), who also showed that these experiments can be seen as two dimensional axis symmetrical.

These experiments will be poorly represented in simulations with the standard 3-dimensional cartesian FLACS code, and were therefore calculated with the 2-dimensional radial versions of FLACS-86, 89 and 93. The 2D radial version of FLACS-93 was used to validate the burning velocity model against a range of different fuels. The geometry was fully resolved on the grid. As reported in Section 4.2, simulations with the k-ε turbulence model are very sensitive to the ratio of initial turbulent length to grid size, and may have problems with a rapid turbulence buildup, when the geometry is resolved on the grid. Unphyscical turbulence is also generated in the flame zone if the turbulent length is too large compared to the grid size (discussed in Section 4.6) and led in some situations to breakdown of the code due to too high turbulence.

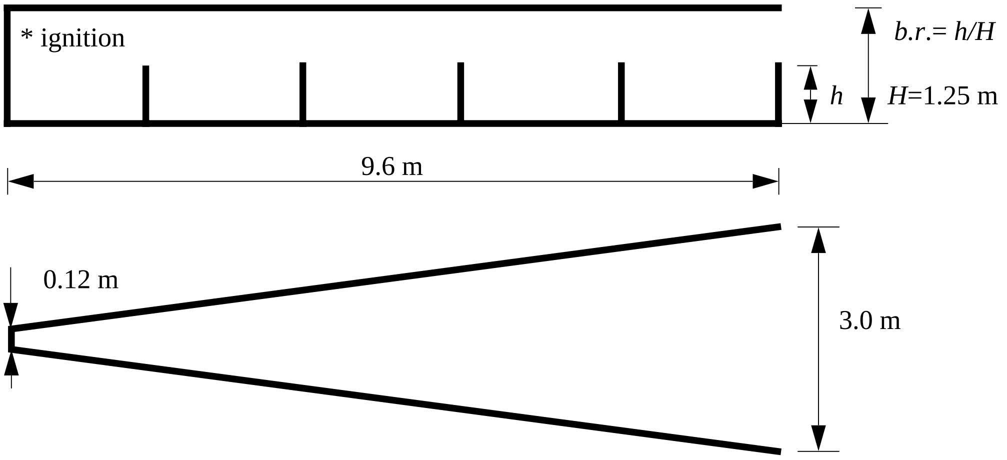

Figure 8.1 The 10 m radial vessel, used in gas explosion experiments at CMI

The simulations were therefore done with a k model with $l_t = 0.2\Delta$. This turbulent length scale was also used in the combustion model. The simulation results were then nearly grid independent.

Simulations with FLACS-89, which uses the k-ε turbulence model, and the *H-M* combustion model described in Subsection 5.2.1, were nearly independent of the initial value on l_t. The reason for this is that it uses a reaction rate proportional to the turbulence frequency, u'/l_t , which reaches its steady state value very quickly, nearly independently of the initial value on l_t, as observed by Bakke (1986). The results from FLACS-89 has, however a large grid dependency and is due to the weakness of the combustion model, not recommended for explosion predictions.

The peak pressures near the exit of the 10 m radial vessel can be seen in Figure 8.2, from 14 experiments, where gas type and blockage ratio (*b.r.*, see Figure 8.1) have been varied. The fuels ethylene, propylene, ethane, propane and methane were stoichiometric mixed with air. The blockage ratios were 1/2, 1/3 and 1/6. The peak pressures obtained from simulation of these experiments were within 7% for all fuels except ethylene. As discussed in Chapter 7.3.3, turbulent burning velocities for ethylene were known not to fit equation (7.30), which resulted in a simulated pressure around only 70% of the experimental. These results were presented by Arntzen (1993b), who also investigated the ability of models to handle different scales, by simulation of experiments in the 1 m radial vessel.

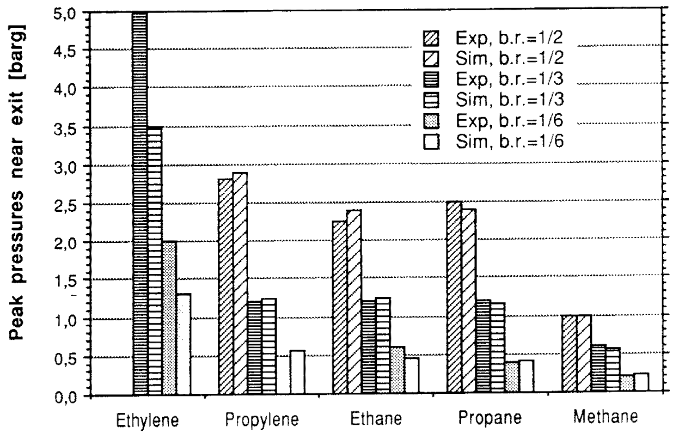

Figure 8.2 Peak explosion pressures in the 10 m radial vessel [barg]

The simulations in the 1m radial vessel were compared with experiments for 7 different stoichiometric fuel-air mixtures and blockage ratio 0.5. The extra fuels compared with the 10m vessel were acetylene and hydrogen. As shown in Table 8.3, the peak pressures obtained from simulation of these experiments were 30% too low for hydrogen and 20% too low for ethylene and acetylene. For the other fuels the difference between simulations and experiments were less than 12%. The turbulent burning velocity at elevated pressures was however underpredicted in FLACS-93, due to incorrect pressure dependency as discussed in Section 2.3.4. A more proper pressure dependency on the burning velocity will give simulations with acetylene, hydrogen and ethylene, better agreement with the experimental results.

It should also be noted that hydrogen has a higher laminar burning velocity than acetylene, but acetylene gives higher peak pressures. The reason for this is that the expansion ratio, for hydrogen is lower.

2D radial versions of FLACS have not been developed after 1993. The improvements in FLACS done later than 1993 are therefore difficult to validate against these radial vessel experiments or the tube experiments presented in the next subsection. The MUSIC code is a 3D CFD code in general coordinates, which can represent both the radial vessel and the tube. MUSIC was supposed to succeed FLACS (and remove the need of having a 2D radial code in addition to the 3D code) but was not able to do that, due to deficiencies, as discussed in Section 2.8.

Table 8.1: Peak explosion pressures in the 1 m radial vessel [barg]

Fuel	Acetylene	Hydrogen	Ethylene	Propylene	Ethane	Propane	Methane
Experiments	4.1	3.1	1.60	0.70	0.41	0.50	0.24
Simulations	3.6	2.2	1.25	0.62	0.48	0.44	0.24

8.2.3 Explosion tube at Sotra

The 50 m^3 explosion tube at Sotra is closed in one end and open in the other. It has dimensions as shown in Figure 8.3. Inside the tube, orifice plates can be mounted. The number of rings and the inner diameter of the rings are variables. The tube was filled with stoichiometric propane-air in most experiments. Explosion experiments with an inner diameter of 1.74 m and plane ignition resulted in peak pressures above 7 and 14 barg for respectively one and five rings. Experiment with no rings showed that jet ignition gave peak pressure of 0.5 to 2.0 barg, compared with 0.03 barg for point ignition. The flame propagation in the jet tube results in turbulence, and thereby larger burning velocity in the larger tube. Simulations with the 2D radial version of FLACS-93, as used for the radial vessel, gave about the same peak pressures as seen in experiments, both with jet and point ignition, and with rings.

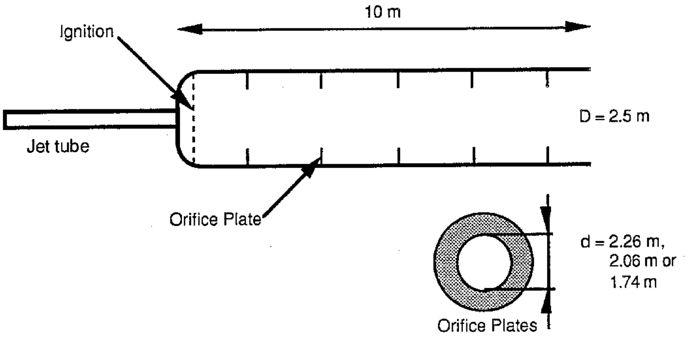

Figure 8.3 The Sotra explosion tube

8.2.4 3D-corner experiments at Sotra

The 27 m^3, 3D-corner consisted of pipes (and bars), where the number and sizes were varied, as shown in Figure 8.4. The pipe diameters were 164, 410, and 820 mm, and the number of pipes were varied from 2x2 to 15x15. In the explosion experiments, the fuel (stoichiometric methane or propane) was ignited in the corner to obtain the worst case scenario. The peak pressure ranged from 0.01 to above 1 barg, and showed the importance of the number of pipes, which results in the positive feedback loop, described in Figure 2.3. Most of the simulations in this 3D corner overpredict the experiments. The overprediction may have been caused by neglection of the quenching in the burning rate, as discussed in Subsection 7.3.6.

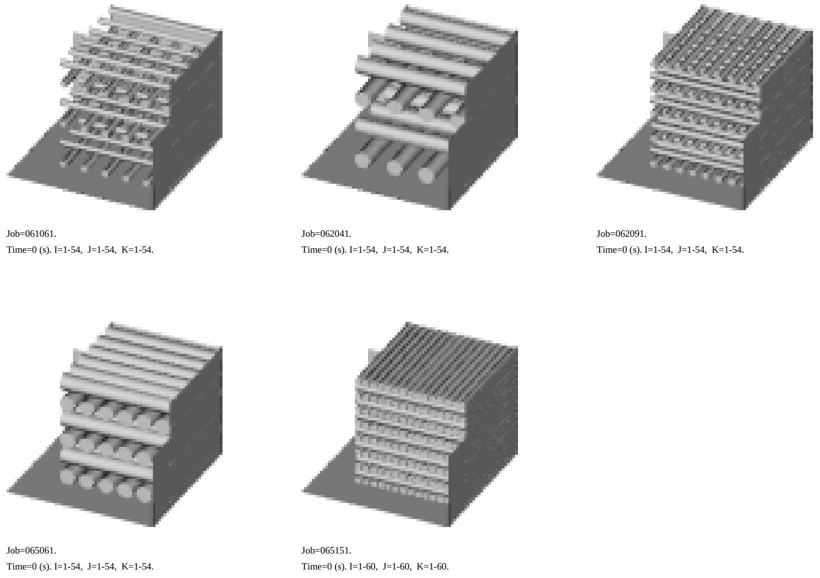

Figure 8.4 Different geometries in the 3D corner

8.2.5 TNO geometry

A range of gas explosion experiments have been done at TNO in Netherlands. Several of these experiments are reported by Wingerden (1995). One of the experimental sites contained cylinders with diameter 1/2 m, in a 12.5 m wide, 25 m long and 1 m high geometry, located as shown in Figure 8.7 as used in a SIF simulation with FLACS-96*. The experiments were also done on a smaller scale, with scaling factor 6.25. Obstacle pitch, height and blockage were varied, as well as type of fuel, methane, propane and ethylene.

Simulations with any version of FLACS overpredicts these experiments. The reason for this may, as for the 3D-corner, be that quenching is not included in the burning velocity model. In simulation of these experiments the flow velocity becomes sonic and the turbulent intensity reaches values around 50 m/s. With a turbulent length scale around 1 cm, Figure 7.7 shows that the burning velocity may be zero for intensities above 18 m/s. The burning model in FLACS does not yet include this quenching, so the burning rate and pressures will therefore be overestimated in situations with high intensities and small length scales.

8.2.6 MERGE

The geometries used in the MERGE explosion experiments consisted of rows of pipes with similar diameter and pitch in all three directions. The horizontal dimensions were twice the vertical. In simulation of the explosion experiment, two symmetry planes were inserted, then only a quarter of the geometry needed to be represented in the calculations. These experiments may also be seen as one or two dimensional, since the pipes are uniformly distributed in all three directions. Simulations with a 2D radial version of FLACS gave about the same good agreement as the 3D simulations. The peak pressures obtained in theses experiments were functions of size of geometry, pitch between pipes, number of pipes and fuel mixture. Large and medium scale experiments were performed by British Gas, and the small scale by TNO. Pressures and time of flame arrival were measured in a range of monitor points. The experiments, and results from them and simulations, are presented by Arntzen (1993a) and Popat et al. (1996). Some of the geometry configurations simulated are shown in Figure 8.5.

When results from experiments done in MERGE are presented in figures, some lines may be drawn, as presented by Arntzen (1993a). The effect of scale, fuel and pitch on peak pressures from experiments may be seen in Figure 8.6. All geometries presented here have the same volume and area blockage.When two of the three parameters are kept constant, the following may be seen:

On average a switch from methane to propane gives double peak pressures. Half pitch (double number of pipes) gives around 7 times higher peak pressures. An increase in horizontal dimension (scale) from 2 to 4 m increases the peak pressure with around 100%. From 4 to 8 m (medium to large scale), peak pressures increases with around 60%. The large increase with scale at small scale is due to the importance of quenching in small scale. At larger scale the quenching of the flame is less important.

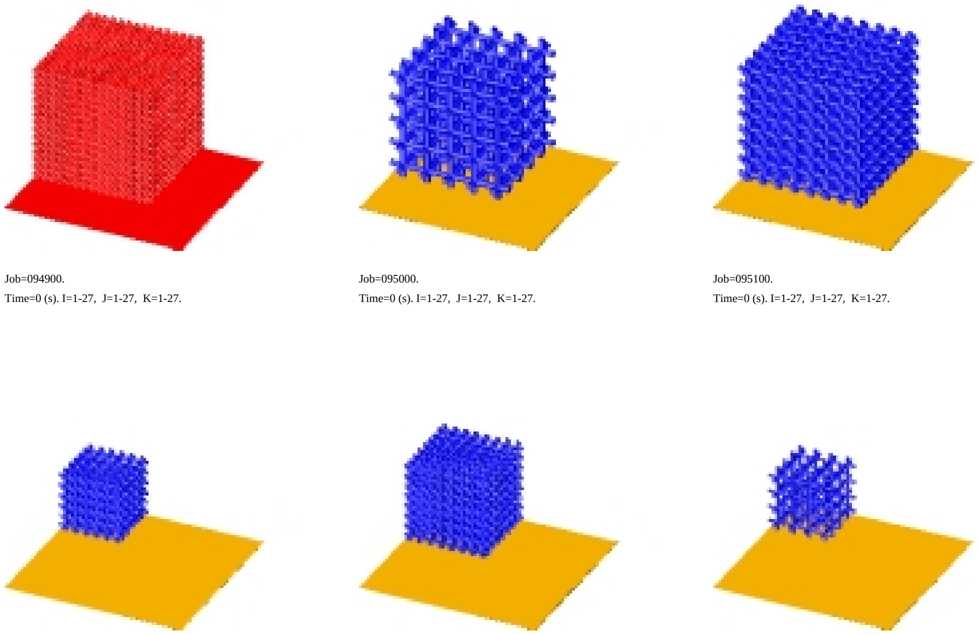

Figure 8.5 Some of the simulated MERGE-geometries

In the MERGE project, some of the explosion experiments were simulated before the experiments were performed. Figure 8.8 shows predictions of pressure in MERGE C* geometry compared with the pressure time curves from experiments which were performed later. The predictions agree well with the experiments in all manners, with respect to peak pressure, time and duration of pressure pulse for both methane and propane as fuels

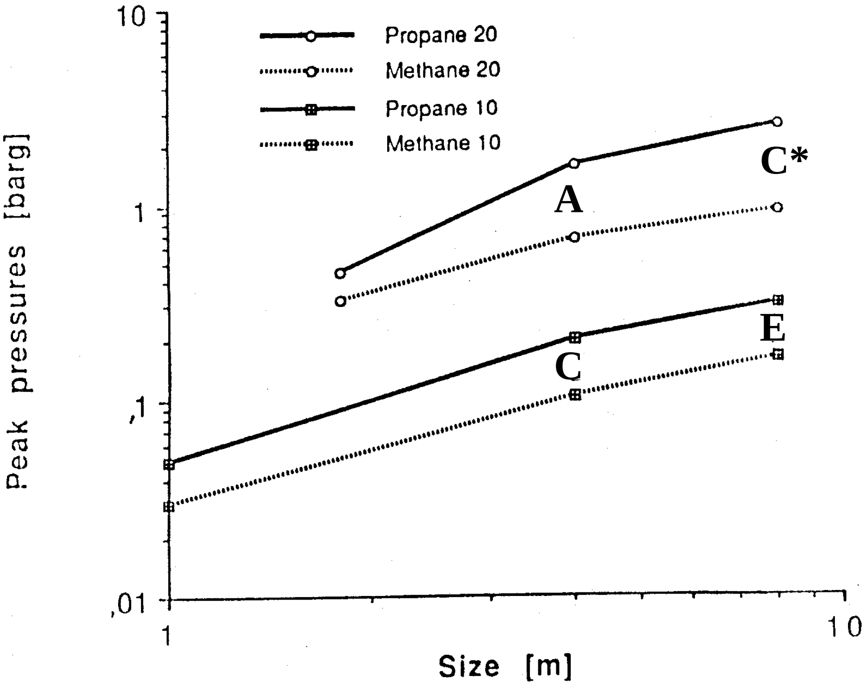

Figure 8.6 Peak pressures in MERGE geometries as function of size, fuel type and number of pipes

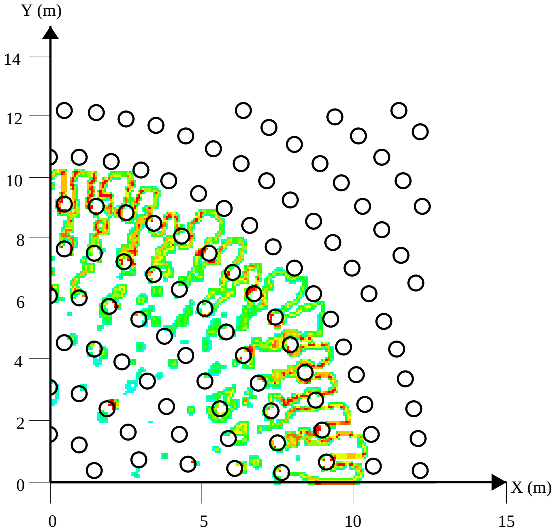

Figure 8.7 SIF simulation, showing the flame in the right half of a TNO geometry

In the EMERGE project, initial turbulence around the ignition point was introduced by four jets in the MERGE geometries, Mercx (1996). Also here the large scale experiments were simulated, as described by Arntzen et al. (1995), before they were carried out. The main difference between similar experiments with and without initial turbulence was the time to reach the peak pressure, which was much shorter with initial turbulence. The peak pressures and pressure pulse durations increased only slightly. Also here the FLACS predictions agreed well with the experiments, as regards peak pressures, time and duration of pressure pulses.

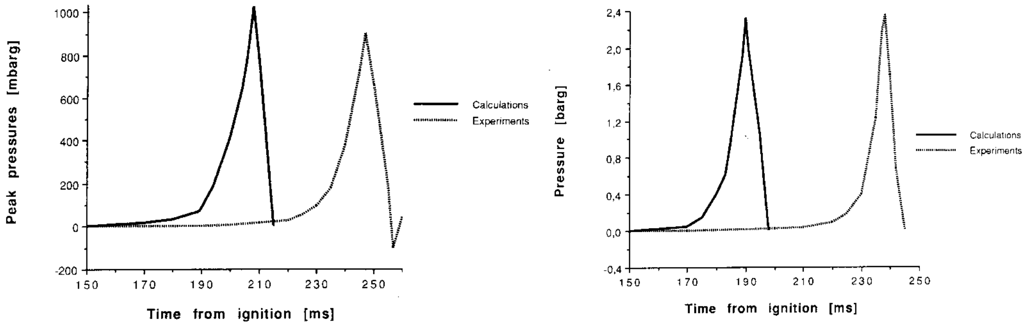

Figure 8.8 Predicted pressure in Merge C* geometry, methane (left) and propane (right)

8.2.7 Mobil/British Gas geometry

The experiments in the water spray module shown in Fig. 8.9, were performed by British Gas on behalf of Mobil. They were performed to investigate the effects of different water spray system on explosions, compared with situations where no water spray is used. The 180 m^3 explosion chamber is a 9 m long vessel with cross section 4.5 and 4.5 m, which has an opening at one of the ends. The gas in the experiments was stoichiometric mixtures of natural gas and air, which was ignited by a single spark located at the centre of the wall opposite of the vent opening.

Experiments were performed in five different geometries. These were in the box with 20, 40, 56 and 80 horizontal 18 cm diameter pipes inside, in addition to the empty box. For the two most obstructed cases there was a vent covering the entire wall of the box, in the other three cases the vent covered a ninth of the wall, 2.25m^3. The maximum pressures, times and durations are shown in Table 8.2. These experiment have a relatively simple geometry which makes it possible to represent it ongrid. The experiments done without waterspray have been, and are, a good basis for validation of explosion codes. The experiments with water spray were used as a basis in the development, as well as for validation of the waterspray sub model in FLACS

Table 8.2: Experimental results in the British Gas 180m^3 explosion chamber

Number of pipes	0	20	40	56	80
Max pressure (barg)	0.4	2.3	3.1	1.4	3.4
Time of max.pres. (s)	0.9	0.7	0.7	0.6	0.5

Simulation of these explosion experiments with FLACS-94 and FLACS-96 gave good agreement with the experimental results, as shown in Figures 8.15 and 8.16. FLACS-96* gave both low grid dependency and good agreement with experiments. Simulations in the empty Mobil box, with FLACS-96*, were performed with a range of grid resolutions, with the width/ height of the box resolved with 3, 6, 12 and 24 cells. The simulations gave grid independent pressure time curves with resolution 6 cells and higher. This give an indication of the grid resolution needed to represent explosions in enclosed geometries with the flame model SIF.

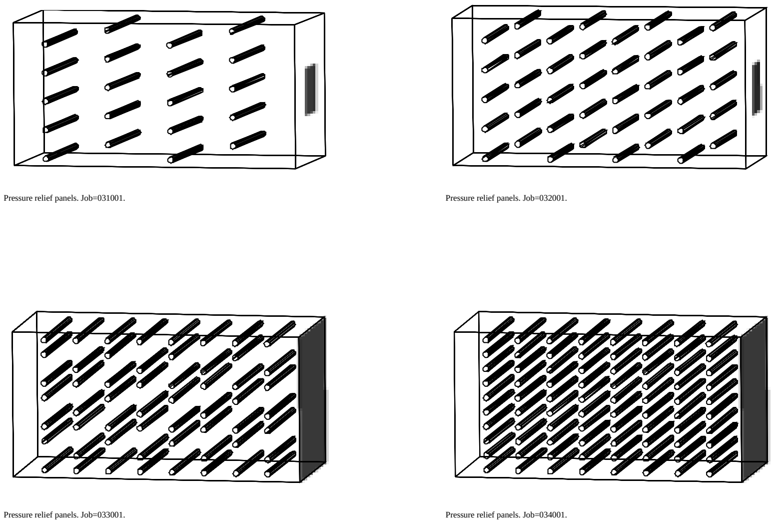

Figure 8.9 Geometries in the B.G. explosion chamber. Vent openings and pipes are black

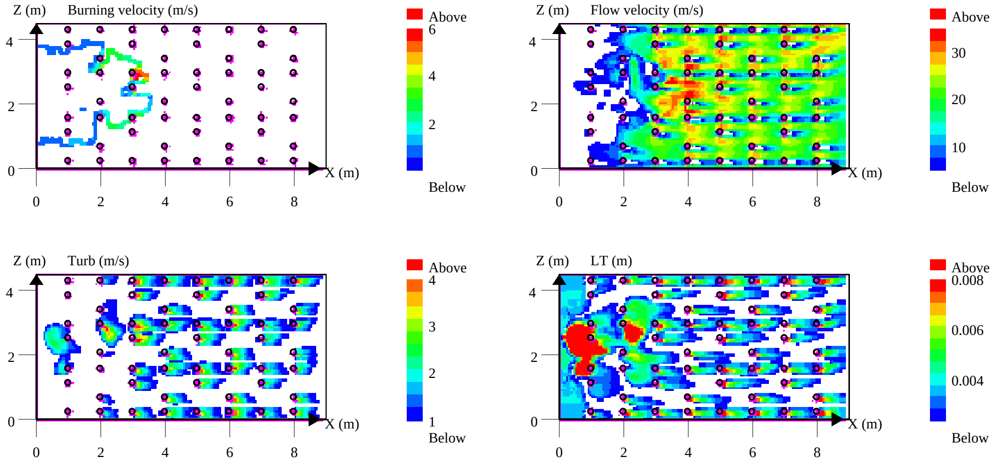

Figure 8.10 Simulated flame and turbulent flow field

Figure 8.10 shows field plots of the flame and the turbulent flow field, in the chamber with 56 pipes, from a fine grid simulation with FLACS-96*, where all the geometry is represented ongrid. The figure shows that the ongrid generated turbulence field is well built up in the wake of the cylinders, the turbulent fluctuation is 15% of the velocity and the length scale, l_t, is 5% of the cylinder diameter, and still raising.

8.2.8 Shell SOLVEX experiments

The SOLVEX (Shell Offshore Large Vented EXplosion) experiments were performed in vented vessels in two different scales, as shown in Figure 8.11. The series of experiments are reported by Bimson et al. (1993). The experiments were performed in four versions of the geometry, with either none, one front mounted, one rear mounted or two rows of cylinders, with seven cylinders in each row. The dimensions of the vented vessels were 10.0 x 8.75 x 6.25 m^3 and 1.67 x 1.50 x 1.00 m^3, with cylinder diameters of respectively 50 and 9 cm. Experiments were performed with stoichiometric methane- and propane-air mixtures, which were all ignited in the centre of the rear wall of the vessel. The vent on the front wall covers 50% of the area on the face. The experimental results, with respect to peak pressures and time is shown in Tables 8.3 and 8.4.

Figure 6.10 shows the flame representation for a range of grid resolutions, from both FLACS-96* and FLACS-96 simulations in the most obstructed SOLVEX box. Simulation of the SOLVEX experiments with FLACS-96 resulted in acceptable peak pressures for the obstructed versions of the geometry. The large scale empty box geometry with propane was, however, underpredicted with a factor of three, as shown in Figure 8.16. Pressures from FLACS-96* simulations give, however, good agreement with all experiments. The reason for this difference is probably that FLACS-96* have sub models which give a better representation of both the flame area and the turbulence production at the exit of the vessel. The better turbulence production may result in higher turbulence and burning velocity outside the vessel exit, and thereby higher peak pressures inside the vessel.

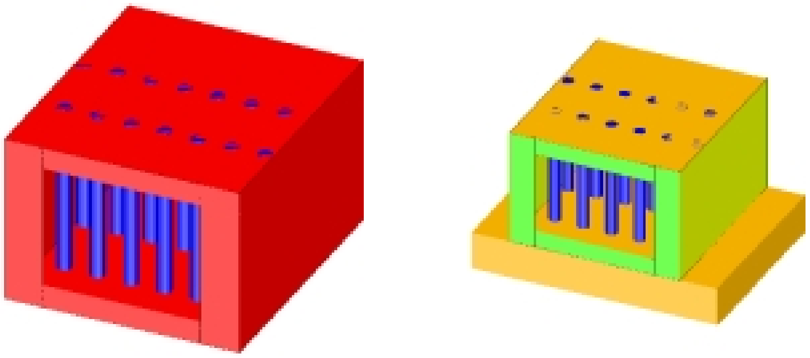

Figure 8.11 The Shell SOLVEX geometries, large scale (left) and small scale (right)

Figure 8.12 Comparison of flame propagation in experiment and simulation in M24

In explosion experiments which contain a range of round cylinders (as this and the previous geometry) the pressures can easily be overpredicted since the turbulence model in FLACS does not take into account that the turbulence production is reduced to less than a third from round cylinders, when the Reynolds number is around 10^6. When other submodels in the explosion code is adjusted “down”, so the code calculates pressures in these geometries better, the prediction in other geometries, where round cylinders are less dominant, will give too low pressures.

Calculation of explosions in the SOLVEX box have also been done with commercially available CFD codes, like PHOENICS, Heritage (1996), as part of a CEC project in the ESPRIT program. The eddy break-up combustion model (see Subsection 5.2.3) and k-ε turbulence model were used. A proper choice of initial (turbulence) conditions gave peak pressure in agreement with experiments. The duration of the pulse was however only 5%, and the time to peak pressure only 1% (0.01s) of the experimental values. This code is therefore not able to model the physics of an explosion. This is partly due to lack of models for ignition and laminar combustion. The PHOENICS calculations also used over 100 times longer calculation time than a FLACS calculation for the same grid resolution.

.

Table 8.3: Experimental results from large scale SOLVEX

Gas	Methane				Propane			
Pipe location	none	front	rear	both	none	front	rear	both
Max. pressure (mbar)	48	104	130	180	111	150	189	290
Time of max.pres. (ms)	1060	970	960	907	870	820	973	751

Table 8.4: Experimental results from small scale SOLVEX

Gas	Methane				Propane				Ethylene			
Pipe location	none	front	rear	both	none	front	rear	both	none	front	rear	both
Pres. (mbar)	17	43	34	74	30	64	78	115	139	222	222	322

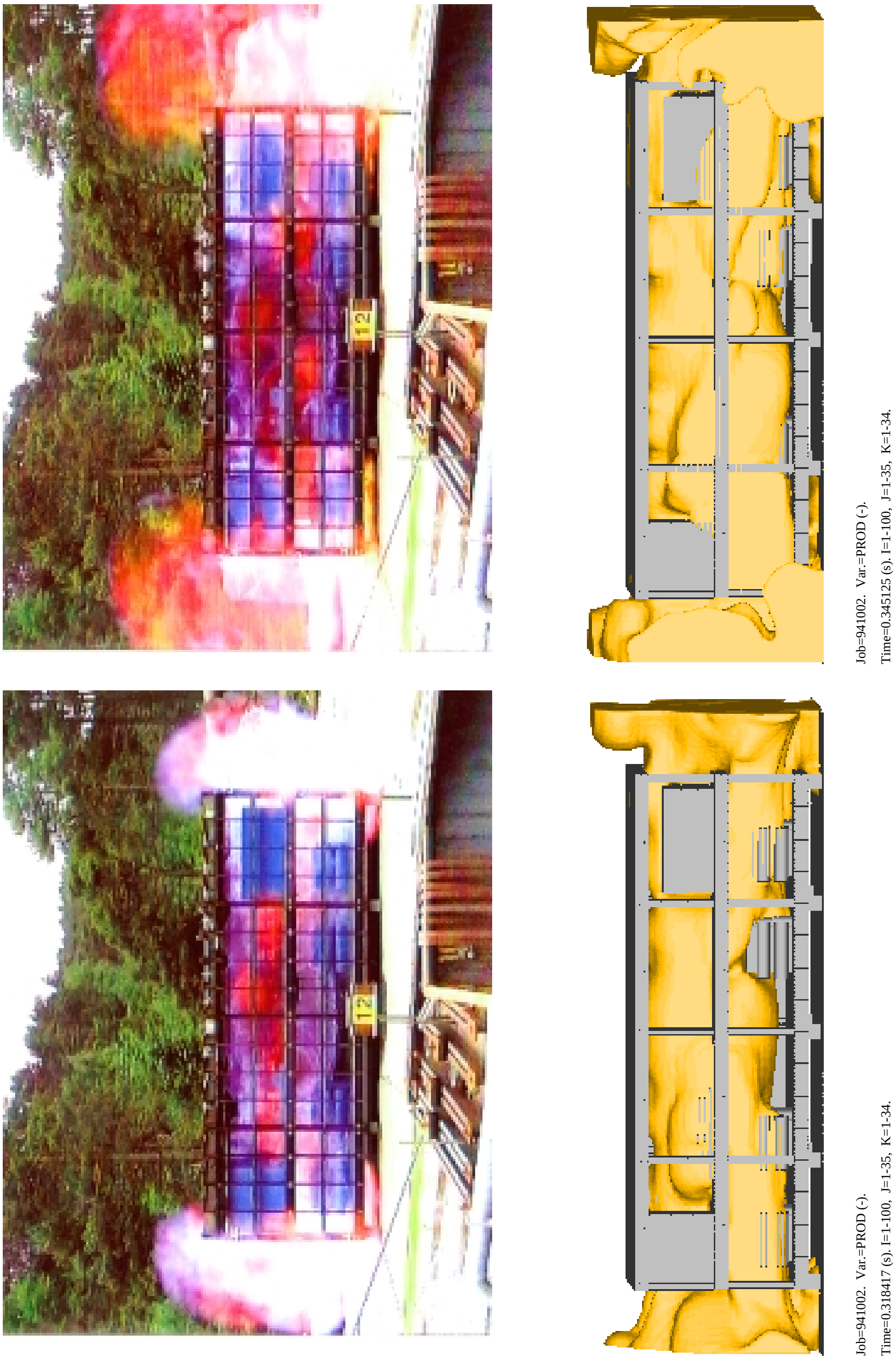

Figure 8.13 Comparison of flame propagation in experiment and simulation in M24

8.3 Realistic geometry experiments

The explosion experiments presented in this section are more representative for explosions in a real offshore module then the simple geometries presented in the last section. In the simple geometries presented in the previous section, the pressure-time histories, including the peak pressures, were mostly the same in the hole geometry, independent of location inside.

In the geometries presented below, the highest peak pressures occur often very locally, and the pressure load on different walls and objects inside the module may therefore differ a lot. Simpler explosion models, which give only one pressure in the calculated module, can therefore not be used to give e.g. representative pressure loads on the different walls.

8.3.1 CMR Compressor Module (M24)

The majority of the experiments in this 50 m^3 module, located at CMR's site at Sotra, have been performed with the compressor module equipment, M24, inside. The most recent experimental results are slightly different from the results reported by Hjertager et al. (1988). The latest experiments show a better repeatability than the earlier and it is supposed that the reason for the changed results is improved test facilities (more accurate gas analyser, better pressure measurements, improved gas mixing and spark ignition instead of chemical igniters).

The dimensions of the M24 module is 8 m x 2.5m x 2.5m, and it contains two decks, a lower and a upper, separated by a floor. The geometry is shown in Figures 8.12 and 8.13, where a series of pictures showing the flame propagation as function of time, are compared with the flame locations from simulations with FLACS.

A range of parameters were varied in the M24 experiments:

- Fuel, mostly methane and propane.
- Ignition location, at the centre or at an end, and at the lower or upper deck. Tests with ignition in initial turbulence fields from jets or wind.
- Gas concentration, different equivalence ratios and inhomogenous clouds.
- Several degrees of congestion in the module. Low, medium and high density levels of equipment.
- Variation in the degree of confinement through the different side walls venting, as open and solid walls, and walls with louvres or explosion panels.
- Solid or grated floor, between the two decks.
- With and without water deluge.

Explosion pressures were measured in a range of monitor points. Maximum pressure measured in any monitor point in the different experiments in the module, ranged from less than 0.05 to above 2.5 barg, depending on the variation of the parameters above. It may be noted that turbulent jets around the ignition resulted in nearly double peak pressure in M24, Arntzen (1995), but had nearly no effect in the MERGE geometries presented in Subsection 8.2.6.

FLACS simulations of explosions in this module, with the parameters above varied, gave peak pressures which agreed well with the experiments, as shown in Figures 8.15 and 8.16.

8.3.2 SCI

The SCI large scale experiments were conducted as a part of the Blast and Fire Engineering Project, which was presented by SCI (1996). The SCI geometry is to some degree a full scale version of the M24 geometry presented in the previous subsection. The dimensions of the SCI module is approximately 28m x 12(8)m x 8m, which is 3.2 times larger than the M24 module. The experiments were done with a representative natural gas.

A range of parameters were varied in the experiments:

- Ignition location, at the centre and at one end.
- Gas concentration, different equivalence ratios.
- Low and high density geometry configuration.
- Different degree of confinement through different side wall venting.
- Different width of the module, 8 and 12 m.
- With and without water deluge

Explosion pressures were measured at twenty-five positions throughout the module.

Figure 8.15 shows the high density SCI module and the flame location from a simulation with FLACS-96. The pressure distribution on the walls, from the same simulations, is also shown in this figure.

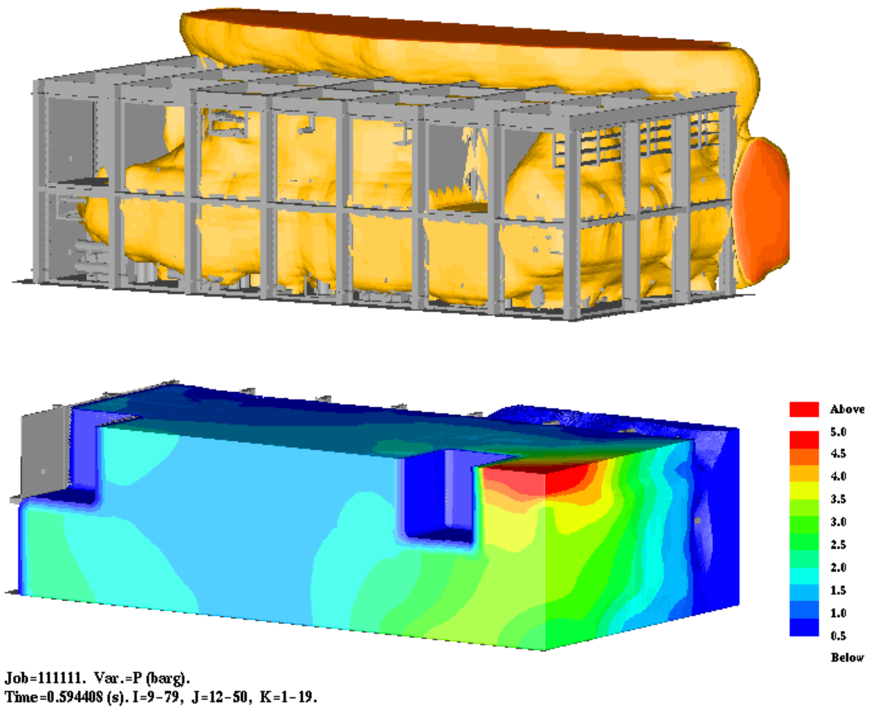

Figure 8.14 Simulation of explosion in the high density SCI module with FLACS-96. Flame location above and pressure distribution below.

.

The explosion experiments in the SCI module have been used to gauge the accuracy and consistency of the 12 mostly used gas explosion models. This was a sort of world championship in prediction of gas explosions, where the simulations were performed first and the experiments were done later. FLACS-96 was here the code showing the best trends.

Since pressures were measured in 25 monitor points, it may be difficult to compare simulated and experimental peak pressures directly. Figure 8.17 shows a comparison between FLACS 96 and experiments for average peak pressures from all monitor points from in the SCI module. Figure 8.18 shows a comparison between FLACS 96 and experiments for maximum peak pressures found in any monitor point in the SCI module.

8.4 Simulated versus experimental peak pressures

The submodels present in different versions of the FLACS code have been adjusted to obtain agreement between peak pressures from experiments and simulations. The submodels have been improved and new models have been introduced to each version. The submodels are therefore adjusted with different constants in different FLACS versions. Some of the main differences in submodels included in different FLACS versions are described in Section 2.7.

The ability of simulations with FLACS-94 and FLACS-96 to obtain peak pressures as seen in the explosion experiments presented in the previous sections are shown in Figure 8.15 and Figure 8.16. Simulation of different explosion experiments with FLACS-93 is described by Hansen et al. (1995). The grid dependency of FLACS-93 was studied by Hansen (1994).

The FLACS-96 submodels were also adjusted to obtain less grid dependency and better agreement for pressure pulse length and time of arrival. The SCI experiments, which have the most representative offshore geometry, with respect to both scale and geometry, were also included in the FLACS-96 validation/adjustment. In the SCI experiments pressures were measured in a range of monitor points. Experiments and simulations can then be compared based on an average of the peak pressures in all monitor points, as shown in Figure 8.15, or based on maximum peak pressure in any monitor, as shown in Figure 8.16.

FLACS-96*, which includes SIF and necessary improvements in submodelling found in the analysis in the previous chapters, as improved turbulence modelling and a new pressure dependency on the turbulent burning velocity, has been used for simulation of a range of explosion experiments. These includes geometries as the SCI and M24 modules, the SOLVEX box, MERGE geometries and the British Gas 180 m^3 explosion chamber. The simulations showed low grid dependency and agreed well with the experiment. FLACS-96* is not shown compared with experiments since the submodels may need some adjustment and not all explosion experiments have been simulated. FLACS-96* gives however about the same agreement between experiment and simulations as FLACS-96, and will after adjustment likely give a (much) better agreement.

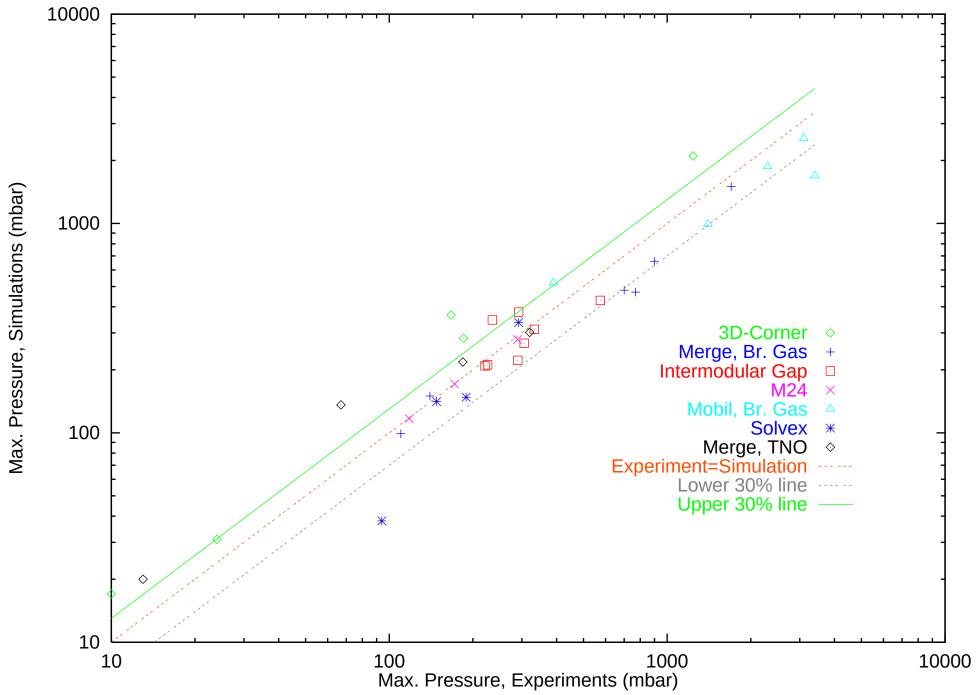

Figure 8.15 Peak pressures from FLACS 94 and medium scale experiments

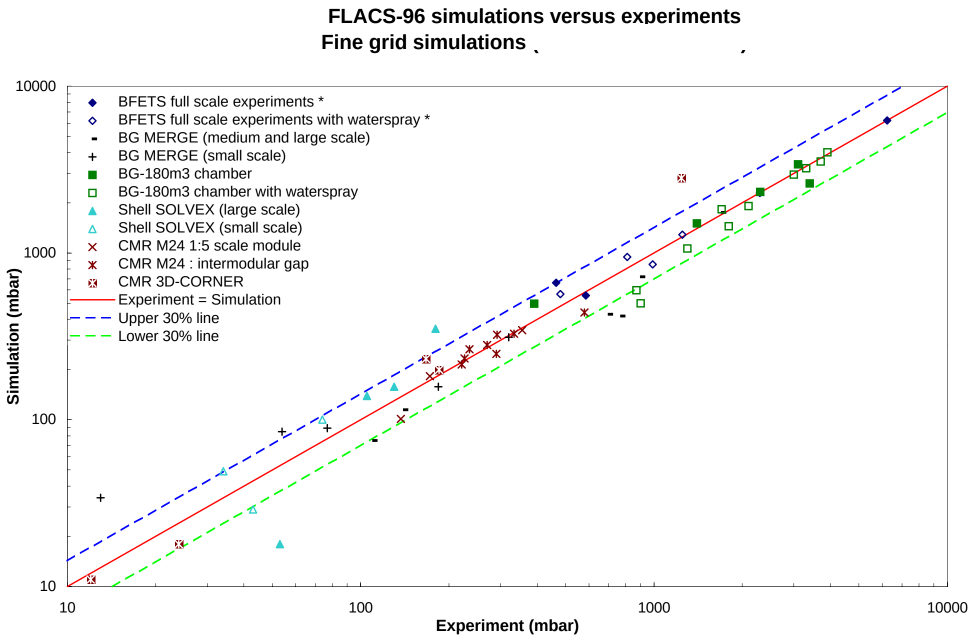

Figure 8.16 Peak pressures from FLACS 96 and medium scale experiment)

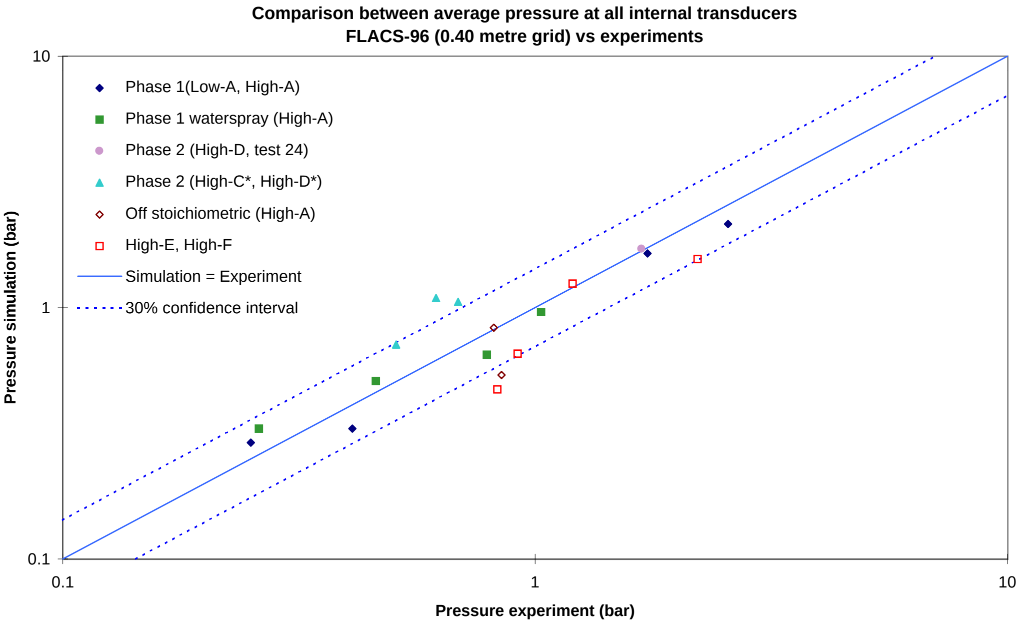

Figure 8.17 Average peak pressures from FLACS 96 and experiments in SCI module

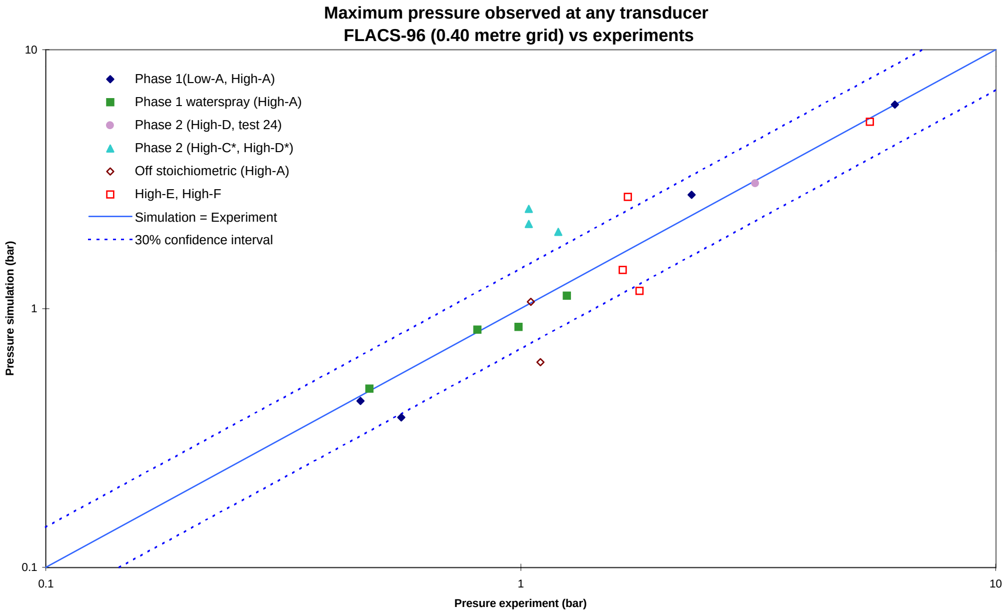

Figure 8.18 Maximum peak pressures from FLACS 96 and experiments in SCI module

8.5 Prediction of explosions

There are several ways to compare simulated and experimental peak pressures. The figures shown above and used by CMR are the most widely used for comparison.

In the SCI project the simulated and experimental results were also compared in several other graphs. Two of these graphs, the model performance measure and the cumulative plot, are shown in Fig 8.19, for one of the explosion models taking part in the SCI project. The model performance graph also shows the confidence limits and is often used for model evaluations. A perfect model will be placed at the origin (1,1) and this model predict the correct answer 100% of the time. A model located higher up on the centre line has a tendency to over and underpredict. A model to the right of the centre line has a tendency to overpredict and a model to the left has a tendency to underpredict.

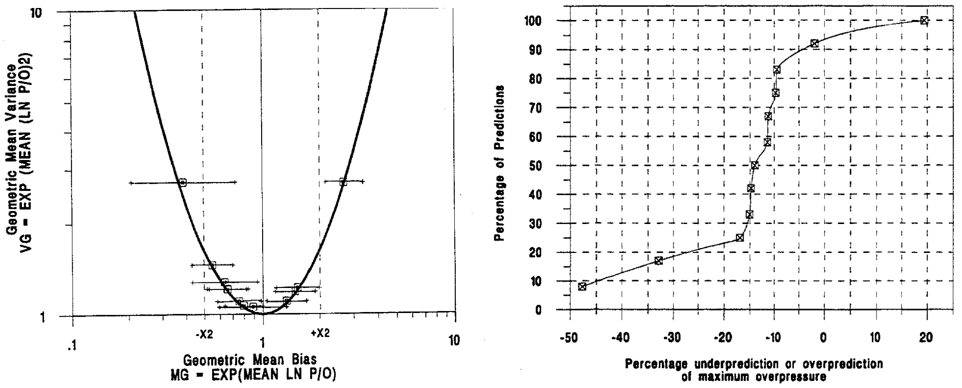

Figure 8.19 Performance measures (left) and cumulative plot (right)

The most important with a code is that it shows the correct trends. A code which give too high or too low pressures, but with correct trends, may only need adjustment of constants in submodels (e.g. for flamefolding or the extrapolation of turbulent burning velocities) to achieve more accuracy. A code with wrong trends, however needs an evaluation of the submodels used.

The reported accuracy of the explosion code is only valid for the geometries, scales and fuel mixtures where they have been compared with experimental results. In more complex (real) geometries and at larger scales the validity of the accuracy depends on how well the models in the code represents the physics of a gas explosion.

Most experiments have been done in a smaller scale typically 1/5 and 1/33 of real offshore modules. The codes are therefore mostly validated at this scale. Most codes have a large grid dependency. In prediction of pressures in real geometries, in full scale, the question for grid dependent codes will be, should the grid size or the number of grid cells be kept constant. It is therefore important that the explosion codes, and the submodels in the codes, are nearly grid independent.

The accuracy of results from an explosion code are dependent of both scenario and grid resolution. A estimate of accuracy should therefore ideally be given from whether, and to which degree, extrapolated submodels, as the turbulent burning velocity model, have been used. The larger the extrapolation, with respect to special fuels, elevated pressures and higher turbulent intensities and lengths, the larger is the uncertainty.

8.5.1 Predictions with FLACS

FLACS is used of by oil, gas and engineering companies in the design of process areas and offshore platforms in order to minimize the risk from gas explosions. In the simulations a range of parameters can be varied, as fuel type, size and location. The geometry can be changed in an attempt of lowering the explosion pressures, by changing the localization of objects, increasing vent openings, or introducing louvres and explosion panels. The simulations can also include mitigation of the explosion with water spray or inert gases.

8.5.2 Dubious trends from FLACS

The trends found from FLACS simulations, where the effect of geometrical changes is investigated may in some situations have limited validity. In connection to prediction of explosions in real offshore modules, the question is, how small geometrical details must be included in simulations to get a representative prediction? FLACS-96 predictions where the degree of smaller details (like small pipes) have been varied, showed that small details may be very important. This may, however, not be correct, since FLACS-96 handles small scale geometry wrongly, with the result of overprediction of turbulence and burning velocity, and thereby over prediction of pressures. Smaller objects are given too large turbulence production (subsection 7.6.1), the subgrid turbulence model contains no length scale information, so the dissipation of turbulence is too small. The burning rate around smaller objects is also overestimated since the length scale dependency is based on the module dimensions, instead of the dimensions of the small objects, and the effect of quenching is not included.

FLACS-96 explosion simulations, after a gas leakage into an offshore module, where the time between the stop of the leakage and the ignition is varied, shows that the calculated peak pressures increases with this time. In reality, the peak pressures are more likely to decrease with time. The reason for this faulty trend is that the turbulent length scale increases with time and that the false turbulence generation in the reaction zone increases with this length as presented in Subsection 4.6. Overprediction of turbulence often results in overprediction of burning velocities and pressures.

FLACS-96* simulations are, however, believed to give correct trends in investigation of the two scenarios above, as well as other scenarios.

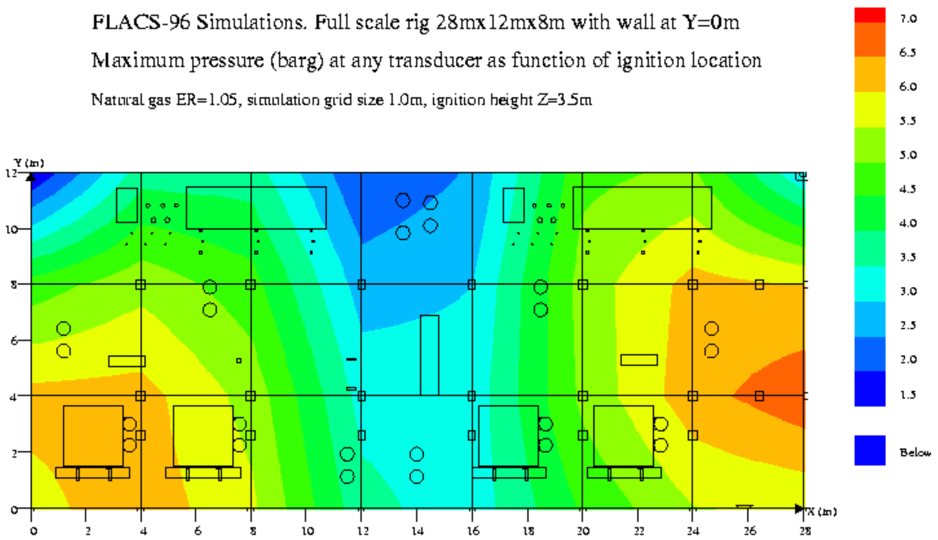

Figure 8.20 Peak pressure as function of ignition location

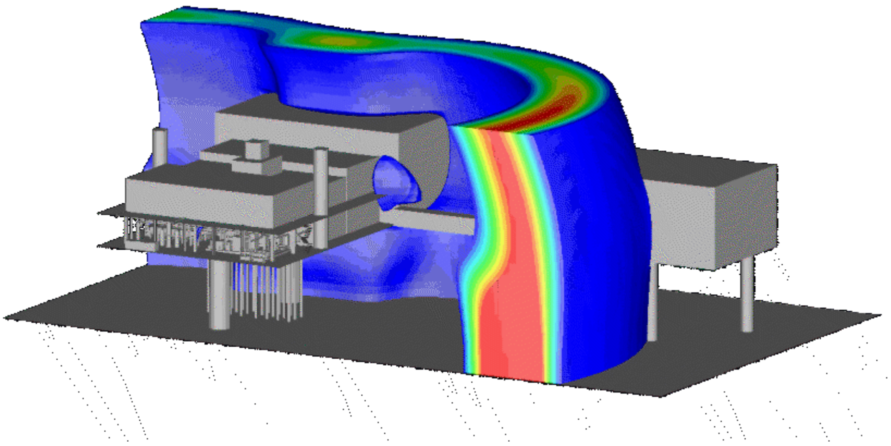

Figure 8.21 Blast wave around an offshore structure which has an explosion

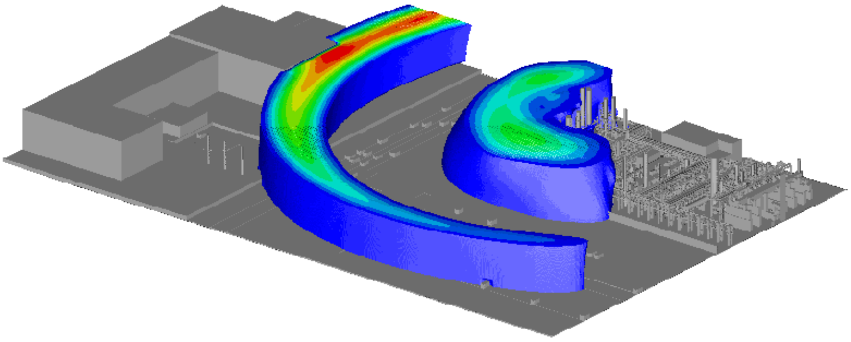

Figure 8.22 Pressure wave from simulation of the explosion accident at Beek

8.5.3 Peak pressure as function of ignition location

The simulations can be repeated several times, but with different ignition location each time. The peak pressures can then be presented as function of ignition location as shown from FLACS simulations in Fig. 8.20. The data from such figures can then be used, together with data for ignition probability as function of location, to calculate the distribution (frequency) of maximum overpressures, as presented by Høiset et al. (1997) and Høiset (1998). Such frequency of maximum pressures can also be calculated, based on the distribution of sizes and compositions of fuel clouds, and simulated explosion pressures from these clouds, as shown by Høiset (1998).

8.5.4 Blast waves

A gas explosion in one offshore structure may also result in damage on other structures located nearby. Inclusion of surrounding structures in the calculation domain gives a prediction of the blast wave affecting surrounding structures, as shown in Figure 8.21.

8.5.5 Explosion in landbased process industry

The FLACS code is mainly used for prediction of explosion effects in offshore geometries, but it is also used for calculations in land based installations. Since full-scale experiments are very expensive to perform, well-documented accidents have been simulated. The pressure impulse in explosion accidents can normally be estimated from the damage on and around the plant. Figure 8.22 shows the blast wave in a simulation of the explosion accident in the naphtha-cracker installation located at Beek in the Netherlands. Simulation of this accident was used to estimate fuel type, fuel cloud size and location, Wingerden (1995).

8.5.6 Explosion in the TWA-flight-800 air plane

The FLACS-96 code was used for the National Transportation Board in the evaluation on whether the TWA flight-800 accident in 1996 could have been caused by a gas explosion in one of the fuel tanks. The FLACS simulations showed that this was a possible scenario under the present conditions. Partly on background of these simulations the investigation concluded that the accident was caused by a gas explosion. The FLACS code was later used in the evaluation of ignition location in the accident, to find the reason for ignition.

8.5.7 Prediction with other CFD codes

The results of explosion calculations with other CFD codes depends largely on the submodels included. As shown in the presentation of the SOLVEX experiments in subsection 8.2.8, the CFD code PHONICS, which is one of the most popular codes for general use, was not able to calculate the experiments.

Another popular CFD code is FLOW-3D, which was used by Freeman (1995) for simulation of simple experiments in a rectangular box with baffles, open at one end. The experiments were performed with ignition at the closed end, with stoichiometric propane and methane. The simulated peak pressures were significantly lower than the experimental, which was explained with too slow turbulence buildup, due to weaknesses of the k-ε turbulence model. AEA Technology argued they had solved this turbulence buildup problem by implementation of something they named a Rayleigh Taylor instability modification to the turbulence model in their CFX code (Pritchard et al. 1996). This modification resulted in higher turbulence levels (through the faster buildup) which resulted in high enough pressures.

This shows that general CFD codes need implementation of tailor made submodels, to describe the physics in explosions, to be able to calculate explosions with a more satisfactory accuracy. The CFD models described above need e.g. a turbulence model for transient flows. It is also doubtful that they can represent flame propagation or subgrid geometry properly. The CFD codes developed especially for calculation of explosions, as FLACS, EXSIM, REAGAS and Cobra, described in Chapter 1, have all had an evolution where submodels which should describe some of the physics in an explosion have been developed and included.

8.6 Summary

CFD explosion codes used for calculation of gas explosions in complex geometries like offshore modules, need submodels to describe phenomena as combustion and representation of subgrid geometry. Some of these submodels will be based on extrapolated data, so their validity are uncertain. When adding together a range of models into a large CFD code, it is also easy to do some mistakes. The codes must therefore be verified against explosion experiments to secure that the simulation of explosions is relatively representative.

Some of the submodels could be wrong or uncertain, and have wrong trends. These wrong submodels may however be tuned by adjusting some constant, so the CFD codes give some correct results, as peak pressure for one or more explosion experiments (for a given grid resolution). In other, more real geometries and experiments and grid resolutions, one can assume that the probable uncertainty in predictions will depend on the uncertainty in the submodels. The defect of one submodel may in most situations lead to too high peak pressures, whereas another submodel may lead to too low pressures. Together these submodel can have been adjusted so the explosion code gives representative explosion pressures for some experiments and grid resolutions. Therefore, after correction of one submodels also other poor submodels must be corrected, or at least adjusted, to secure an improvement of the explosion code.

Predicted pressures from FLACS simulations were compared with measured values from a range of explosion experiments. The capability of FLACS and other explosion codes to predict gas explosions was discussed.

9 Conclusions and Recommendations

9.1 Conclusions

The work behind this thesis consists of two parts. The first part was to find the deficiencies in existing CFD models, when they are used in the description of transient reactive flows between complex geometry resolved on a coarse grid, as gas explosions in offshore modules. The second part was related to the development of improved models, avoiding the shortcomings of the present models. The work was concentrated on improvements in the CFD code FLACS, which is the most widely used code for simulation of gas explosions.

Most of the deficiencies were related to the turbulence and combustion modelling, but also other parts of the explosion modelling needed improvement. The volume expansion calculated by FLACS was inaccurate. A thermodynamical model, which included equilibrium chemistry was therefore developed and implemented in FLACS-96. The pressure correction equation in FLACS was only for compressible flows, so the equation of state was not satisfied in the reaction zone. A version for reactive compressible flows was therefore developed.

The turbulence models' ability to give representative turbulence field in complex, transient and reactive flows, where the geometry was represented both ongrid and subgrid, was tested. The k-ε turbulence model used is not intended for transient or reactive flows. It was therefore necessary to modify the model for reactive flows and develop an extension of the model to secure a representative rapid transient build-up of turbulence fields. The subgrid turbulent energy generation model used, gave representative turbulent energy production, but the turbulent length depended on grid size instead of obstruction size. A turbulent energy and length generation model which was developed solved this problem.

The combustion model in FLACS-89, as well as other combustion models analysed, was extremely grid dependent unless the numerical grid resolved the integral turbulence length scale. The representation of flame propagation was therefore poor in simulations in offshore modules, where the grid cell is typically an order or two larger than this length scale. Modelling of combustion with a flame model and a burning velocity model based on experimentally found data gave a much better and less grid dependent representation of the flame propagation. Two flame models and several burning velocity models were therefore developed. The β flame model represents the flame satisfactorily, and has been used in FLACS-93 and later versions. The β flame is however several grid cells thick and needs correction models for small flame radii and for burning towards walls. Representation of the flame as an interface, with the SIF model, gives a better representation of the flame, and was implemented as an option in FLACS-96 and later versions.

The turbulent burning velocity is modelled as a function of the turbulent velocity and length, and the laminar burning velocity, based on extrapolation of data found in experiments. Analyses of turbulent burning velocity data indicate that they correlate better against a chemical time scale based on activation and product temperature, than a time scale based on laminar burning velocities. The turbulent burning velocity correlation used is only valid at atmospheric pressure. At elevated pressures, new experiments shows that the correlation give too low values. A new correlation with improved pressure dependence is therefore needed. Flamefolding models had to be developed and included, to take into account the fraction of the flame area which is not represented by the numerical grid.

Simulations of gas explosion experiments, with the improvements in modelling described in this thesis included, show a significant improvement in the description of gas explosions. The simulated results have a low grid dependency and agree well with most experiments, especially when the uncertainty of the experiments is taken into account.

9.2 Recommendations for further work

The present work was concentrated on development of models which give satisfactory representation of the turbulence field, flame representation and volume expansion. Further improvements are needed in the modelling of the burning velocity of the flame, as function of turbulence field, gas composition, pressure and temperature. Simulation of gas explosion experiments may now be used in adjustment of the extrapolation of the burning velocity models, since other sub models in the explosion model now should give relatively representative turbulence fields and flame descriptions. The improvements in turbulent burning velocity modelling should have emphasis on the following four items:

- Implementation of a parabolic dependence, instead of power functions, in the extrapolation of turbulent burning data. This will also include the effect of flame quenching.
- Development of a turbulent burning velocity model, which takes into account the higher burning rate of gas mixtures containing fuels like ethylene, acetylene and hydrogen.
- Improvement of the turbulent burning velocity model at elevated pressures.
- Implementation of a chemical time scale based on product temperature, instead of laminar burning velocity.

Further work recommended for improvements in gas explosion modelling, may be represented by the following four points:

- Application of the flame model SIF and all the improvements in turbulence modelling in all further validation and prediction with FLACS.
- Expansion of the combustion modelling so it also includes shock/compression induced ignition, transition to detonation and flame acoustics interactions.
- Better representation of flame propagation around subgrid geometry, with some emphasis on common obstructions like grated floors.
- Improved modelling of release and dispersion of fuel leeks to obtain more representative fuel-air clouds.

Bibliography

Abdel-Gayed R.G.,Bradley D., Hamid, M.N., Lawes M.(1984a)
Lewis number effects on turbulent burning velocity
21: Symp. (Int.) on Combustion, The Comb. Institute, pp. 497-504

Abdel-Gayed R.G.,Bradley D.,Lawes M. (1984b)
Turbulent burning velocities and flame straining in explosions
Proc. Roy. Soc. London, A414, p. 389

Abdel-Gayed R.G.,Bradley D.,Lawes M., Lung F.K-K. (1986)
Premixed turbulent burning during explosions
21: Symp. (Int.) on Combustion, The Comb. Institute, pp. 497-504

Abdel-Gayed R.G.,Bradley D.,Lawes M. (1987)
Turbulent burning velocities: a general correlation in terms of straining rates
Proc. Roy. Soc. London, A414, p. 389

Abdel-Gayed R.G.,Bradley D. (1989)
Combustion Regimes and the Straining of Turbulent Premixed Flames
Combustion and Flame 76: 213-218

Aldredge (1992)
The propagation of wrinkled premixed flames in spatially periodic shear flow
Combustion and Flame 90: 121-133

Arntzen B.J. (1985)
Modelering av turbulens i jetstrøm (in norwegian)
Prosjekt, IMTF, NTNU, Trondheim, Norway, 1985

Arntzen B.J. (1992)
Enhancement of FLACS, Gas mixture explosions, Progress report for 1991
Ref. CMI-92-F25010, Christian Michelsen Institute, Bergen, Norway

Arntzen B.J., (1993a)
Final report on modelling in MERGE
CEC MERGE project report, STEP CT90/91.0111 (SMA)
Ref. CMR-93-F25042, Christian Michelsen Research, Bergen, Norway

Arntzen B.J., (1993b)
Combustion Modelling in FLACS 93
Ref. CMR-93-F25043

Arntzen, Linga, Hansen, Sand, Wilkins, Wingerden, Kong (1995)
EMERGE, final summary report
CEC EMERGE project report, EV5VCT930274
Ref. CMR-96-F20005

Arntzen, B.J. (1996)
Modelling of steady and transient turbulent flows
CEC EMERGE project report, EV5V - CT93 - 0274 (DG 12 FZPA)
Ref.No.: CMR-96-F20004

Arntzen, B.J., Hansen, O.R. (1997)
Improved thermodynamics in FLACS, modelling the effect of inert gases
Ref. No.: CMR-97-F30009

Arntzen, B.J. (1997a)
Flame modelling in FLACS 96; SIF, the Simple Interface Flame model
Ref.No.: CMR-96-F20020

Arntzen, B.J. (1997b)
Turbulence and drag in complex flows
FABIG presentation of EMERGE in London 9. Oct. 97, http://www.steel-sci.org/fabig

Baker W.E.,Cox, P.A., Westine, P.S., Kulesz, J.J., Strelow, R.A. (1983)
Explosion hazards and evaluation,
Elsevier Scientific Publishing Company

Bakke J.R. (1986)
Numerical simulation of gas explosions in two dimensional geometries
Dr. scient thesis, University of Bergen, Norway, CMI Report No. 865403-8

Bakke J.R., Bjeketvedt, D., Bjørkhaug, M. (1990)
FLACS as a tool for safe design against accidental gas explosions
I. Chem. E. Symposium series no. 122

Ballal, D.R. (1979)
The influence of laminar burning velocity on structure and propagation of turbulent flames.
Proc. Roy. Soc. London, A367, p. 485-502

Barr, P.K., Ashurst, W.T. (1984)
An interface scheme for turbulent flame propagation
SAND82-8773, Sandia National Laboratories, Livermore

Baulch D.L., Drysdale D.D., Duxbury J., Grant (1976)
Evaluated kinetic data for high temperature reactions
Butterworths, London

Begue C., B. Cardot, C. Pares, O. Pironneau (1990)
Simulation of turbulence with transient mean
Int. J. Num. Meth. in Fluids, Vol. 11, 1990

Bielert, U., Klug, M., Adomeit, G. (1996)
Application of front tracking technique to the turbulent combustion processes in a single stroke device
Combustion and Flame 106: 11-28 (1996)

Bimson, S.J., Bull, D.C., Cresswell, T.M., Marks, P.R., Masters, A.P., Prothero, A. Puttock, J.S., Rowson, J.J., Samuels, B. (1993)
An experimental study of the physics of gaseous deflagration in a very large vented enclosure
Proposed paper for the 14th International colloquium on the dynamics of explosions and reactive systems, Coimbra, Portugal, August 1st-6th, 1993

Bjerketvedt, D., Bakke, J.R., Wingerden, K. (1993)
Gas Explosion Handbook
Journal of hazardous materials, vol. 52-no.1, Elsevier, Amsterdam, 1997
Alternatively: Ref. CMR-93-A25034 or
http://www.cmr.no/english/gexcon/Handbook/GEXHBforewd.htm

Bjørkhaug (1986)
Flame acceleration in obstructed radial geometries
Ph.D. thesis, Ref. CMI No. 865403-9

Bradley, B., Lau, A.K.C., Lawes, M. (1992)
Flame stretch rate as a determinant of turbulent burning velocity
Phil. Trans. R. Soc. London A (1992) 338, 359-387

Bradley, B. (1992)
How fast can we burn
24: Symp. (Int.) on Combustion, The Comb. Institute, pp. 247-262

Bradley, B., Chen, Z., Swithenbank, J.R. (1988)
Burning rates in turbulent fine dust-air explosions
22: Symp. (Int.) on Combustion, The Comb. Institute, pp. 1767-1775

Bray K.N.C. (1990)
Studies of the turbulent burning velocities
Proc. R. Soc. Lond. A 431, 315-335

Bray, K.N.C. (1996)
The challenge of turbulent combustion
26’th Symposium on combustion, the combustion institute, pp1-26, 1996

Butler, T.D., Cloutman, J.K., Dukowich J.K., Ramshaw, J.R.
Multidimensional numerical simulation of reactive flow in internal combustion engines
Prog. Energy Combust. Sci., Vol. 7, 293-315

Cant R.S., Bray K.N.C. (1988)
Strained laminar flamelet calculations of premixed turbulent combustion in a closed vessel
22: Symp. (Int.) on Combustion, The Comb. Institute, p.791

Catlin C.A., Lindstedt R.P. (1991)
Premixed turbulent burning velocities derived from mixing controlled reaction models with cold front quenching
Combustion and Flame 85: 427-439

Catlin C.A., Faiweather, M., Ibrahim, S.S. (1995)
Prediction of turbulent, premixed flame propagation in explosion tubes
Combustion and Flame 102: 115-128 (1995)

Cato, M., Launder, B.E. (1993)
The modelling of turbulent flow around stationary and vibrating square cylinders
9. Symp. Turbulent shear flows, Kyoto, Japan, 1993

Chieng, C.C., Launder, B.E.(1980)
On the calculation of turbulent heat transport downstream from an abrupt pipe expansion
Numerical heat transfer, Vol. 3, pp. 189-207, 1980

Chomiak, J., Nisbet, J.R. (1995)
Modelling variable density effects in turbulent flames - some basic considerations
Combustion and flame 102: 371-386 (1995)

Chorin, A.J. (1980)
Flame advection and propagation algorithms
Journal of computational physics 35, 1-11

Cordes, J. Rodi, W., Cho, N.H. (1993)
Calculation of separated flows with a two-layer turbulence model
Physics of separated flows - Numerical, experimental and theoretical aspects, Vieweg, Braunschweig, Germany (1993)

Eckhoff, R.K.(1991)
Dust explosions in the process industries
Butterworth, London

Fernholz, H.H.
Turbulence
Springer-Verlag, editor Bradshaw, 2nd edition, 1978

Franke, R., Rodi, W (1991)
Calculation of vortex shedding past a square cylinder with various turbulence models
Turbulent Shear Flows 8, Springer -Verlag, Berlin

Freeman, D.J.
Validation of CFD prediction of gas explosions
Trans IChemE, vol.73, part B, Feb. 1995

Fukutani S., Jinnot H. (1985)
Simulation of stoichiometric acetylene/ethylene/ethane/ and methane/air premixed flames
Dynamics of reactive systems, Progress in astronautics and aeronautics, vol. 105

Gardner. D.J. Hulme, G. Hughes, D.J.(1993)
A survey of current predictive methods for explosion hazard assessments in the UK offshore industry
I, Chem. E. Symp. series no. 134

Gaydon, A.G. (1979)
Flames, Their structure, radiation and temperature
Chapman and Hall, London

Ghoniem, A.F., Chorin, A.J., Oppenheim (1982)
Numerical modelling of turbulent flow in a combustion tunnel
Phil. Trans. R. Soc. Lond. A 304, 303-325 (1982)

Gibbs, G.J., Calcote, H.F. (1959)
Effect of molecular structure on burning velocity
Journal of chemical and engineering data, vol. 4, no. 3, July 1959

Gjesdal T., (1996)
Calculation of flame area in the simple interface flame model
Ref. No.: CMR-96-F20021

Glassman, I., (1977)
Combustion
Academic press. London, 1977

Glastone, S. (1946)
Thermodynamics for chemists
D. Van Nostrand, Princeton N.J.

Gran, I.R. (1994)
Mathematical modelling and numerical simulation of chemical kinetics in turbulent combustion
Dr. Ing. thesis, University in Trondheim, 1994

Grimsmo, B. (1991)
Numerical simulation of turbulent flow and combustion in a four stroke homogeneous charge internal combustion engine
Dr. Ing. thesis, University in Trondheim, 1991

Gulder, O.L. (1990)
Turbulent premixed flames for different combustion regimes
23: Symp. (Int.) on Combustion, The Comb. Institute, pp. 743-750

Hakberg B., Gosman A.D. (1982)
Analytical determination of turbulent flame speed from combustion models
20: Symp. (Int.) on Combustion, The Comb. Institute, pp. 225-232

Hansen, O.R. (1994)
Length scale for turbulent combustion in FLACS93
Ref.: CMR-94-F25030

Hansen, O.R. (1994b)
Grid dependency study using FLACS
Ref.: CMR-94-F25047

Hansen, O.R., Åsheim, O. (1995)
Simulation of explosion experiments using FLACS93 version 2.0
Ref.: CMR-95-F20004

Heritage, J.R. (1996)
A model for Industrial CFD Application
ESPRIT project 20966: MICA

Hinze (1975)
Turbulence
McGraw-Hill, Inc.

Hjertager, B.H. (1982)
Simulation of transient compressible turbulent reactive flows
Comb. sci. & tech. vol. 27, pp. 159-170

Hjertager, B.H. (1986)
Handbook of heat and mass transfer, p. 1308
Gulf Publishing Company, Houston

Hjertager, B.H., Fuhre, K., Bjørkhaug, M.(1988)
Gas explosion experiments in 1:33 and 1:5 scale offshore separator and compressor modules using stoichiometric homogeneous fuel/air clouds
J. Loss prevention process industries, vol. 1, pp. 197-205, 1988

Hjertager, B.H. Sæter, O., Solberg, T. (1993)
Computer modelling of turbulent gas explosions in complex 2D and 3D geometries
Journal of hazardous materials, 34 /1993, 173-197

Høiset, S., Hjertager, B.H., Solberg, T., Malo, K.A. (1997)
Statistical estimation of loads from explosions
J. Loss Prev. Process Ind. Vol. 10. No. 4. pp. 271-283,1997

Høiset, S. (1998)
Statistical estimation of loads from explosions
Dr. Ing. thesis, NTNU Trondheim / Høgskolen i Telemark, 1998

JANAF Thermochemical Data
The Dow Chemical Company, Thermal Laboratory, Midland, Mich.

Kato and Launder (1993)
The modelling of turbulent flow around stationary and vibrating square cylinders.
9. Symp. on Turbulent Shear Flows, Kyoto, Japan

Kee R.J., Miller J.A., Jefferson (1980)
CHEMKIN: A general purpose, problem-independent, chemical kinetics code package
Sandia report, SAND80-8003, Livermore, California 94551

Kee R.J., Grcar, J.F., Smooke, M.D., Miller J.A. (1985)
A Fortran Program for Modelling Steady Laminar One-Dimensional Premixed Flames
Sandia report, SAND85-8240, UC-4, Livermore, California 94551

Kee, R.J. (1987)
The Chemkin Thermodynamic Data Base
Sandia report, SAND87-8215B. UC-4, Livermore, California 94551

Khalil, E.E., Spalding, D.B., Whitelaw, J.H. (1975)
The Calculation of Local Flow Properties in Two-Dimensional Furnaces
Int. J. Heat Mass Transfer, 18: 775-791

Kobayashi, H., Tamura, T., Maruta, K., Niioka, T., Williams, F.A. (1996)
Burning velocity of turbulent premixed flames in a high pressure environment
26’th Symposium on Combustion, The Combustion Institute, 1996, pp. 389-396

Kobayashi, H., Nakashimi, T., Tamura, T., Maruta, K., Niioka, T. (1997)
Turbulence measurements and Observations of turbulent premixed flames at elevated pressures up to 3.0 MPa
Combustion and Flame 108:104-117

Kobayashi, H., Kawabata, Y., Maruta, K. (1998)
Experimental study on general correlation of turbulent burning velocity at high pressure
27’th Symposium on Combustion, The Combustion Institute, 1998

Kong, D.(1996)
An experimental study of certain aspects of initiation and turbulent propagation of gas explosions
Dr. scient thesis, Bergen University, Norway

Kwon, O.J., Hah, C. (1995)
Simulation of three-dimensional turbulent flows on unstructured meshes
AIAA Journal, Vol. 33, No. 6 (1995)

Kuo, K.K. (1986)
Principles of Combustion
John Wiley & Sons, New York

Launder and Spalding (1972)
Lectures in mathematical models of turbulence
Academic Press, London

Leschziner, M.A. (1991)
Two-equation models for high-Reynolds-number flows
Introduction to the modelling of turbulence, von Karman Institute lect. series, Belgium

Lees, F.P. (1996)
Loss prevention in the process industry:
Butterworth-Heinermann, Oxford, 2nd ed. 1996

Lewis, B., von Elbe, (1961)
Combustion Flames and Explosion of Gases
Academic press, New York

Lindstedt, R.P., Sakthitharan, V.
Transient flame growth in a developing shear layer
Turbulent shear flows 9, Springer-Verlag Berlin 1995

Linan, A., Williams, F.A. (1994)
Fundamental aspects of combustion
Oxford University Press

Lind, C.D., Whitson, J.C. (1994)
Explosion hazards associated with spills of large quantities of hazardous materials. phase 2
Report no. CG-D-85-77., U.S. Dept of transportation, Coast gard final report ADA 047585

Lutz A.E., Kee R.J., Miller J.A. (1986)
SENKIN: A fortran program for predicting homogeneous gas phase chemical kinetics with sensitivity analysis
Sandia report, SAND80-8003, Livermore, California 94551

Magnussen, B.F., Hjertager, B.J. (1976)
On mathematical modelling of turbulent combustion
16: Symp. (Int.) on Combustion, The Comb. Institute, pp. 719-729

Markatos, N.C. (1985)
Computer simulation techniques for turbulent flows
Encyclopedia of fluid mechanics, vol. 6, Gulf publishing company, London, (1985)

Melaaen (1990)
Analysis of curvilinear nonorthogonal coordinates for numerical calculation of fluid flow in complex geometries
Dr. ing thesis, NTH, Trondheim

Mercx, W.P.M. (1996)
Extended Modelling and Experimental Research into Gas Explosions,Final summary report
CEC EMERGE project report, EV5VCT930274 (TNO)

Metghalchi, M., Keck,J.C. (1980)
Laminar Burning Velocity of Propane-Air Mixtures at High Temperature and Pressure
Combustion and Flame 38: 143-154

Milton, B.E., Keck,J.C. (1984)
Laminar Burning Velocities in stoichiometric hydrogen and hydrocarbon gas mixtures
Combustion and Flame 58: 13-22

Mohammadi, M., Pironneau, O. (1994)
Analysis of the K-Epsilon turbulence model
Masson, Paris 1994, ISBN: 2 225-84391-0

Murphy, J.D. (1985)
Turbulence modelling
Encyclopedia of fluid mechanics, vol. 6, Gulf publishing company, London, (1985)

Nallasamy, M.(1987)
Turbulence models and their applications to the prediction of internal flows a review
Computers & Fluids Vol. 15, No. 2, pp. 151-194, 1987

NIST Chemical kinetics database (1989)
National institute of standards and technology, Gaithersburg, MD 20899

Noh, W.T., Woodward, P, (1976)
SLIC (Simple line interface calculation)
Proc. 5th Int. Conf. Numer. Math. Fluid Mech., pp. 330-339, Berlin: Springer-Verlag

Olson, R.M.
Essentials of engineering fluid mechanics
Harper & Row, New York, 1980

Patankar, S.V. (1980)
Numerical heat transfer and fluid flow
Hemisphere publishing corporation, London, 1980

Peters, N. (1986)
Laminar flamelet concepts in turbulent combustion
21: Symp. (Int.) on Combustion, The Comb. Institute, pp. 1231-1250

Phillips (1994)
Explosions in the process industries
Institution of chemical engineers, UK, 2nd ed., 1994

Poisant, T.J., Veynate, D., Candel, S.
J. Fluid Mech. 228:561-606 (1991)

Popat, N.R., Catlin, C.A., Arntzen, B.J., Lindstedt, R.P., Hjertager, B.H., Solberg, T., Sæter, O., Van den Berg, A.C., (1996)
Investigations to improve and assess the accuracy of computational fluid dynamic based explosion models
Journal of hazardous materials, vol. 45, pp 1-25, Elsevier, Amsterdam (1996)

Pritchard, D.K.,Freeman, D.J., Guilbert, P.W. (1996)
Prediction of explosion pressures in confided spaces
J. Loss Prev. Process Ind. Vol. 9. No. 3. pp 205-215, 1996, Elsevier Science Ltd

Rahibe, M., Aubry, N., Sivashinsky, G.I., Lima, R. (1995)
Formation of wrinkles in outwardly propagating flames
Physical Review, vol. 52, num. 4

Roach, P. E. (1987)
The generation of nearly isotropic turbulence by means of grids
Int. J. Heat & Fluid Flow 8 (2)

Rodi, W.(1993)
Turbulence models and their application in hydraulics
Balkema, Rotterdam, 3rd edition, 1993

Rogers, M. (1995)
Project EMERGE: Measurement of turbulence and drag loads on pipework obstacles
British Gas, GRC R 0610

Salvesen H.C. Sand, I,Ø., (1993)
Fine grid simulations with the CFD code FLACS of vortex shedding past different cylinder configurations in a wind tunnel
Ref. CMR-93-F25056

Sand, I.Ø., Arntzen, B.J. (1991)
Simulation of turbulent reactive flow
CMI Report No.CMI-90-25071, Christian Michelsen Institute, Bergen, Norway

Sand, I.Ø., Bakke, J.R. (1989)
Wall-function boundary conditions in the Navier-Stokes and the energy equations
CMI Report, CMI No. 25110-3 (1989)

Schlichting, H.
Boundary layer theory
Sixth edition, McGraw-Hill, 1968

SCI (1996)
Joint Industry project on blast & fire engineering for topside structures
The Steel Construction Institute, 7th May 1996

Selby, C.A., Yassin, M. (1996)
The evaluation of gas explosion models
Second international specialist meeting on fuel-air explosions at CMR in Bergen

Sethian, J.(1984)
Turbulent combustion in open and closed vessels
Journal of computational physics 54, 425-456 (1984)

Sha, W.T. Launder, B.E. (1979).
A model for turbulent momentum and heat transport in large rod bundles
ANL-77-73, 1979

Sher, E., Ozdor, N. (1992)
Laminar Burning Velocities of n-Butane/Air Mixtures Enriched with Hydrogen
Combustion and Flame 89: 214-220

Sokolik, A.S., Karpov, V.P., Semenov, E.S. (1967)
Turbulent combustion of gases
Fizika Gorenia i Vzryva, Vol. 3, No. 1, pp. 61-76, 1967

Sonntag, R.E., Wylen, G.J.v. (1982)
Introduction to Thermodynamics
John Wiley & Sons, New York

Storvik, I.E.,Ryum, S.R., Wingerden, K.v., Hansen, O.R., Salvesen, H.C. (1996)
FLACS-96 USER's GUIDE
Ref. No.: CMR-96-F20073

Strehlow, AR.A. (1979)
Fundamentals of Combustion
ISBN 0-88275-539-0, Robert E. Kreiger publishing company, New York

Sæter, O., Solberg, T.,Hjertager, B.H.
Validation of the EXSIM-94 gas explosion simulator
Int. conference and exhibition on offshore structures - hazards, safety and engineering working in the new area, London, 12 - 13 december (1995)

Tennekes, H., Lumley, J.L. (1972)
A first Course in Turbulence
The MIT Press, London

Townsend, A.A. (1976)
The structure of turbulent shear flow
Cambridge university press, 1976

van Wingerden, Storvik, Arntzen, Teigland, Bakke, Sand, Sørheim
FLACS-93, a new explosion simulator
Proc. of the 2nd Int Conference on offshore structural design against extreme loads, pp.5.2.1-5.2.14, 1993

van Wingerden, C.J.M. (1995)
Gas explosions in vented enclosures and in the open: mechanisms, prediction methods and mitigation
Dr. philos thesis, University of Bergen, Norway.

Vasey, M., Catlin, C. (1990)
Review of applicability of predictive methods to gas explosions in offshore modules
HMSO OTH 89 312

Vasey, M. (1995)
Gas explosion model evaluation protocol
MEGGE: 016

Warnatz J. (1982)
Experimental investigations and computational simulation of acetylene-oxygen flames from near stoichiometric to sooting conditions
19: Symp. (Int.) on Combustion, The Comb. Institute, pp. 197-209

Warnatz J. (1984)
Combustion chemistry, chapter 5. Rate coefficients in the C/H/O system
Springer- Verlag, New York, ed. Gardiner W.C.

Welty, J.R., Wicks, C.E., Wilson, R.E. (1984)
Fundamental of momentum, heat, and mass transfer
John Wiley & Sons, New York

Westbrook C.K., Dryer F.L., Schug, K.P. (1983)
Numerical modelling of ethylene oxidation in laminar flames
Combustion and Flame 52: pp. 299-313

Westbrook C.K., Pitz W.J. (1984)
Combust. Sci. Technol., 37:117-152

White, F. M. (1991)
Viscous fluid flow
Second edition, McGraw-Hill

White, F.M. (1994)
Fluid mechanics
Mcgraw-Hill, Inc. London

Williams, F.A. (1985)
Combustion theory
ISBN 0-8053-9801-5, The Benjamin/Cummings Publishing Company, California 94025

Williams, F.A., Liñán, A. (1993)
Fundamental aspects of combustion
Oxford University Press

Zabetakis, M.G. (1965)
Flammability characteristics of combustible gases and vapours
Bureau of Mines Bulletin 627, Pittsburgh